Order from Disorder: Control of Multi-Qubit Spin Registers in Diamond

Bradley, C.E.

DOI
10.4233/uuid:acafe18b-3345-4692-9c9b-05e970ffbe40

Publication date
2021

Document Version
Final published version

Citation (APA)
Bradley, C. E. (2021). *Order from Disorder: Control of Multi-Qubit Spin Registers in Diamond*. [Dissertation (TU Delft), Delft University of Technology]. Delft University of Technology. https://doi.org/10.4233/uuid:acafe18b-3345-4692-9c9b-05e970ffbe40

Important note
To cite this publication, please use the final published version (if applicable).
Please check the document version above.

ORDER FROM DISORDER:
CONTROL OF MULTI-QUBIT SPIN REGISTERS IN DIAMOND

Dissertation

for the purpose of obtaining the degree of doctor
at Delft University of Technology,
by the authority of the Rector Magnificus, Prof. dr. ir. T.H.J.J. van der Hagen,
Chair of the Board for Doctorates,
to be defended publicly on
Wednesday 6th October at 15:00 o'clock

by

Conor Eliot BRADLEY

Master of Science in Physics,
Imperial College London, United Kingdom,
born in Sheffield, United Kingdom.

This dissertation has been approved by the promotor:
Prof. dr. ir. R. Hanson

Composition of the doctoral committee:

Rector Magnificus	Chairperson
Prof. dr. ir. R. Hanson	Delft University of Technology, Promotor
Dr. ir. T. H. Taminiau	Delft University of Technology, Copromotor
Independent members:	
Prof. dr. F. Jelezko	Ulm University, Germany
Prof. dr. M. A. G. J. Orrit	Leiden University
Prof. dr. L. DiCarlo	Delft University of Technology
Prof. dr. S. Gröblacher	Delft University of Technology
Prof. dr. ir. L. M. K. Vandersypen	Delft University of Technology, Reserve member

Printed by: Gildeprint – Enschede

Cover design: Conor Eliot Bradley

Casimir PhD Series, Delft-Leiden 2021-21

ISBN 978-90-8593-487-5

An electronic version of this dissertation is available at
`http://repository.tudelft.nl/`.

CONTENTS

SUMMARY

Electron spin qubits associated with individual solid-state defects can exhibit exceptional coherence and bright optical interfaces. Furthermore, their magnetic interactions with nuclear spins in the host material present a resource for multi-qubit registers. They have thus emerged as powerful systems with which to develop quantum technologies. In this thesis, we develop a toolbox for the precise control of multi-qubit spin systems associated with single nitrogen-vacancy (NV^-) centres in diamond. We utilise this platform to explore a number of avenues in quantum science: networks, computation, sensing, and simulation. Our findings provide new insights towards the goal of distributed quantum computation, and establish a programmable solid-state-spin quantum simulator for studying many-body physics.

NV-based optical quantum networks have made great progress in recent years, demonstrating protocols such as entanglement distillation and entanglement swapping. However, the consequences of stochastic ionisation events during their operation are largely unstudied. Therefore, we first investigate the NV^0 centre by developing novel techniques to herald the charge-state (Ch. 3). We directly observe the fine structure, and characterise the orbital and spin dynamics. Importantly, we realise that unmitigated ionisation events will decohere nuclear-spin quantum memories.

We then investigate the use of a ^{13}C qubit in isotopically-engineered diamond as a memory for network protocols (Ch. 4). We show that the qubit decoheres slower than previously demonstrated optical entangling rates, paving the way for key primitives such as deterministic non-local quantum logic. We also show that it is robust to an NV ionisation and recharging event, providing promise that this error channel can be overcome.

Next, we turn to the control of multi-qubit registers for quantum information processing (Ch. 5). We design and implement a novel two-qubit gate for high-fidelity control over hitherto inaccessible ^{13}C spins. We demonstrate a fully connected 10-qubit register with minute-long coherence times and realise 7-qubit entanglement. These results display the potential of multi-qubit spin registers in diamond for quantum computation.

In Ch. 6, we combine these techniques with multi-dimensional spectroscopy to precisely measure individual nuclear-nuclear couplings. We characterise a system of 27 ^{13}C spins, and find the spatial structure of this system with sub-angstrom resolution. This experiment constitutes a proof-of-principle demonstration towards the goal of atomic-scale imaging of individual spin-complexes extrinsic to the diamond, and provides a precise characterisation method for multi-qubit quantum processors.

Finally, we leverage this knowledge to construct a quantum simulator based upon individually controllable ^{13}C spins (Ch. 7). We isolate a 1D chain of 9 spins, and implement the driven Ising model. Utilising novel initialisation, control, and read-out techniques, we synthesise a many-body-localised discrete-time-crystal and observe its hallmark characteristics. This work gives insights into thermalisation in many-body quantum systems and establishes a novel simulation platform based on solid-state spins.

SAMENVATTING

Elektron spin qubits geassocieerd met individuele defecten in vaste-toestand materialen hebben exceptionele coherentie-eigenschappen en heldere optische interfaces. Bovendien biedt de magnetische interactie met kernspins in het materiaal een bron voor registers bestaande uit meerdere qubits. Daarom zijn individuele defecten komen bovendrijven als een veelbelovend systeem om quantumtechnologie mee te ontwikkelen. In dit proefschrift ontwikkelen we methodes voor de precieze controle over spinsystemen rondom een enkel stikstof-gat defect (nitrogen vacancy, NV^-) in diamant. We gebruiken dit platform om een aantal richtingen binnen de quantumwetenschap te onderzoeken: netwerken, computers, sensoren en simulaties. Onze bevindingen bieden nieuwe inzichten op de weg naar gedistribueerde quantum berekeningen, en brengen een programmeerbare spin quantum simulator tot stand om veeldeeltjesfysica te bestuderen.

Optische quantumnetwerken gebaseerd op stikstof-gat defecten hebben de laatste jaren geweldige progressie geboekt met de demonstratie van protocollen zoals de distillatie en teleportatie van verstrengeling. Echter, de consequentie van de stochastische ionisatie tijdens operaties is grotendeels onverkend gebleven. Daarom onderzoeken we eerst het neutrale stikstof-gat defect (NV^0) met nieuwe technieken om de ladingstoestand te prepareren (Hoofdstuk 3). We meten direct de fijnstructuur, en karakteristeren de orbitale en spin dynamica. Deze resultaten laten ook zien dat ionisatie decoherentie van kernspins veroorzaakt.

Dan bestuderen we een ^{13}C kernspin qubit in isotopisch-bewerkte diamant om quantumtoestanden op te slaan tijdens netwerkprotocollen (Hoofdstuk 4). Onze bevindingen laten zien dat willekeurige quantumtoestanden langer bewaard kunnen blijven dan de tijd die nodig is om netwerkknooppunten te verstrengelen. Dit maakt de weg vrij voor belangrijke demonstraties zoals niet-lokale quantum logica. We laten ook zien dat het geheugen robuust is tegen veranderingen van de ladingstoestand van het NV, wat hoop biedt dat dergelijke fouten opgelost kunnen worden.

Hierna bekijken we de controle van qubitregisters voor quantuminformatie doeleinden (Hoofdstuk 5). We ontwerpen en implementeren nieuwe twee-qubit operaties met hoge betrouwbaarheid op eerder ontoegankelijke kernspins. We demonstreren een volledig verbonden 10-qubit register met coherentietijden van een minuut en realiseren een verstrengelde toestand met 7 qubits. Deze resultaten laten de potentie van qubit spin registers in diamant voor quantumberekeningen zien.

In Hoofdstuk 6 combineren we deze technieken met multi-dimensionale spectroscopie om individuele kern-kern koppelingen precies te meten. We karakteriseren een systeem van 27 ^{13}C spins, en vinden de ruimtelijke structuur van dit systeem met subangstrom resolutie. Dit experiment vormt een eerste demonstratie richting het op atomair niveau afbeelden van spin-complexen buiten de diamant en is een methode om quantumprocessoren te karakteriseren.

Tenslotte bouwen we op deze vergaarde kennis om een quantumsimulator te realiseren gebaseerd op individueel controleerbare ^{13}C spins (Hoofdstuk 7). We isoleren een eendimensionale ketting van 9 spins, en implementeren het gedreven Ising model. Gebruikmakend van nieuwe initialisatie-, controle- en uitleestechnieken synthetiseren we de veel-deeltjes-gelokaliseerde discrete-tijd-kristallijne fase en observeren we de bijbehorende eigenschappen. Dit werk levert inzicht op in de thermalisatie van veeldeeltjes quantumsystemen en brengt een nieuw quantumsimulatieplatform gebaseerd op spins in de vaste stof tot stand.

1

INTRODUCTION

1.1. QUANTUM 2.0

The field of quantum mechanics is often associated with the philosophical debates of the first half of the twentieth century. However, applied in practice, it shaped the latter half. Technologies made possible only through an understanding of quantum physics are ubiquitous in our daily lives. Quantisation lead to the comprehension of band structure [1] and population inversion [2,3], critical to realising the semiconductor and laser devices which drive modern technology.

Despite the immense impact of these so-called 'Quantum 1.0' technologies, their operation is not reliant on the manipulation of individual quantum states [4–6]. Over the past few decades, a series of ground-breaking experiments have enabled the isolation, control, and measurement of individual quantum systems, such as atoms, photons, superconducting circuits, and solid-state spins [7–11]. A central question remains: do these intrinsically quantum systems enable a new class of 'Quantum 2.0' technologies which go beyond current possibilities?

Quantum 2.0 technologies are often grouped into four categories: quantum communication, quantum sensing and metrology, quantum simulation, and quantum computation [5]. Of these categories, quantum computation is the most intensively explored, due to the widespread claim that a large-scale quantum computer will be capable of solving some of the most pressing challenges for humankind, such as drug discovery and materials design [12,13]. In the last two years, experiments using 53 superconducting qubits [14] and 50 photonic squeezed states [15] have claimed 'quantum computational supremacy': the capability to run a known calculation on a quantum mechanical system which is intractable using any conventional computing device [16,17]. This advantage stems from the immense Hilbert space associated with such systems, which scales exponentially with the number of contributing quantum bits or 'qubits'. However, despite these impressive results, in both cases the task performed has no known practical applications. Realizing useful quantum computation will require quantum systems to be increasingly isolated from noise while simultaneously maintaining interfaces for control and measurement. Meeting this requirement while scaling the system to the large numbers of qubits required is a formidable challenge, even when aided by error-suppressing schemes such as quantum error mitigation [18] or, ultimately, quantum error correction [10,19,20].

1

Simulating the dynamics of interacting many-body quantum systems is a hard task for classical computers[21,22]. Analog quantum simulators rely on the capability to engineer specific interactions which match those of a physical system of interest, such that their dynamics can be reconstructed. Experimental quantum simulators using ultracold atoms, trapped ions, photons, superconducting circuits, and solid-state spins have been used to generate novel phases of matter, to study strongly correlated systems of bosons or fermions, and to investigate fundamental particle and gravitational physics[23,24]. Quantum simulations have now been performed with up to 256 individually probed Rydberg atom qubits[25,26], for which the description of the full quantum state requires more memory than there exists global data capacity. However, limits to the coherence of present experiments may mean that the system dynamics can be approximated by simplified state descriptions (such as matrix product states[27]). Reaching unambiguous quantum advantage in this setting remains an open target.

Quantum communication enables provably secure transfer of information[28]. That is, any adversarial attempt to intercept information can be detected before deciding to transmit the data. The ultimate level of security is proven by a so-called 'loophole-free Bell test'[29]. Such tests were first demonstrated by three distinct experiments in 2015[30–32]. Quantum communication typically employs flying photonic qubits, due to their fast travel speeds and low decoherence rates either in free-space or optical fibre. The ability to create quantum entanglement between static matter qubits (such as atoms or electrons) and flying qubits gives rise to the field of quantum networks. Within such systems, a wide range of protocols have been proposed, such as clock synchronisation with unprecedented accuracy[33]. This capability can also be used to link quantum computational modules, allowing for the creation of larger systems without the need to create a single monolithic device[34]. To implement such protocols, high-quality light-matter interfaces[35] must be realised, whose communication rate is ideally enhanced by multiplexing in the spatial-, frequency- or time-domain (or any combination thereof), in analogy with classical communications technology. Furthermore, each node must contain well-controlled qubits that can store and process quantum information while entanglement is distributed across the network.

Quantum sensing and metrology exploit the sensitivity of individual quantum systems to perturbations, such as magnetic, electric, or gravitational fields[36]. Conversely, extremely environmentally-insensitive qubits — atomic clocks — serve as frequency (time) standards which are of critical importance for technologies such as GPS[37]. The use of quantum entangled states can enable sensitivity beyond the standard quantum limit (shot noise limit), as famously demonstrated in the LIGO experiments[38]. Moreover, unique capabilities, such as the preparation of increasingly macroscopic objects in well-defined quantum states, may be used to probe fundamental question such as the quantum mechanical nature of gravity[39,40]. Finally, as we will explore in this thesis, the nanoscale nature of many qubit hosts makes them ideal probes of microscopic environments and their dynamics[41].

These four classes of technologies have differing requirements. However, at their heart, each relies on the ability to manipulate and measure quantum systems with exquisite precision. Within this thesis, we will focus upon the use of spin qubits in diamond towards these goals.

1.2. QUANTUM TECHNOLOGY WITH SOLID-STATE SPINS

Spins in solid-state materials have been identified as promising systems for quantum technologies[11,42,43]. Optically-active defects ('colour centres') in wide-bandgap semiconductors are of particular interest due to the ability to initialise and read-out the electron spin qubit using optical excitation. Devices based on solid-state spins offer a number of practical advantages. Their solid-state nature avoids the need for ultra-high vacuum and complex laser cooling systems. Furthermore, a number of colour centres have relatively high operating temperatures (demonstrating optical coherence between 1-20 K, and long-lived spin coherence up to room temperature), where cooling power is more abundant[11]. Finally, the ability to create on-chip photonic structures can be used to enhance the interface between spin qubits and light[44].

In recent years, great progress has been made in the isolation and control of a range of optically-active defect spins[45–53]. One of the most prominent examples is the nitrogen-vacancy (NV) centre in diamond. Building on developments in single molecule spectroscopy[54], individual NV centres were first optically addressed in 1997[55]. Since these first measurements, developments in device quality and control techniques have lead to fast and high-fidelity electron spin initialization and read-out (>99.8%[56] and >97%[30] in <5 μs, respectively), high-fidelity spin manipulation within tens of nanoseconds using direct microwave drives[57,58], and coherence times up to one second[59–61].

The realisation of quantum technologies generally requires access to more than one qubit. Importantly, magnetic coupling from the NV electron spin to the native nitrogen nuclear spin and to proximal ^{13}C spins in the diamond lattice provides access to additional qubits which can be used for computation, memory, or sensing[62–68]. An outstanding challenge, however, is to extend this platform beyond the control of a few spins, realising increasingly larger systems which will eventually be capable of performing computations and simulations that are intractable for classical technologies.

One promising approach towards this goal is via distributed quantum information processing (DQIP). Independent multi-qubit registers ('nodes') can be linked using photonic entanglement (Fig. 1.1(a))[33,34,69,70]. These entanglement links can then be consumed to perform quantum logic operations between nodes, forming them into a larger architecture.

A number of first steps have been made towards this architecture. Photonic entanglement has been demonstrated between NV centres separated by up to 1.3 km[30,71,72]. Moreover, the use of a single ^{13}C nuclear spin 'data qubit' (or 'quantum memory') in each node has led to demonstrations of entanglement distillation in a two-node network[73], and entanglement swapping in a three-node network[74], both of which are important primitives for DQIP. Within individual nodes, control over a few nuclear spins has been realised (Fig. 1.1(b))[75]. Such systems have been used to probe fundamental questions in physics such as the existence of contextuality[76], and observations of quantum Darwinism[77]. Furthermore, in the context of quantum computing, primitive error-correctable logical qubits have been demonstrated[68,75,78,79].

Building a truly large-scale architecture requires further improvements. In particular, the efficiency of the optical links[80,81], the number of data qubits in each node and their lifetime[56,74,82,83], and the fidelity of quantum logic operations must all increase. In this

thesis, we address a number of challenges on this path, by elucidating and mitigating the effects of optical excitation on the NV-^{13}C system, and by realizing unprecedented control over multi-qubit spin systems in diamond.

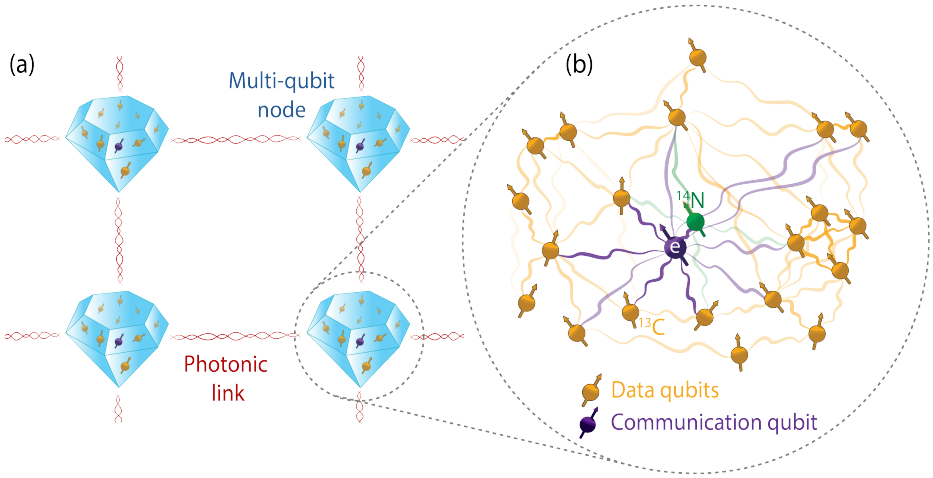

Figure 1.1: **Architecture for distributed quantum information processing using spins in diamond. (a)** Each diamond node hosts at least one optically-active defect (purple spin, 'Communication qubit'), such as an NV centre as used in this thesis. Coherently emitted photons are interfered to create entanglement between remote electron spins ('Photonic link'). The presence of additional spin qubits within each node, such as ^{13}C nuclear spins (yellow spins, 'Data qubits'), provides a resource for the manipulation and storage of complex quantum states. The four nodes shown here serve as a unit-cell for a large scale system operating a distributed surface code for quantum error correction [34,69,70]. **(b)** Schematic of a quantum network node based upon an NV centre within an interacting nuclear spin bath. The central electron spin (purple) exhibits magnetic couplings (purple lines) to the intrinsic ^{14}N spin of the NV centre (green), and to proximal ^{13}C spins in the diamond lattice (yellow). Prior to the work of this thesis, a few of the most strongly-coupled ^{13}C spins (dark purple lines) had been controlled as prototype qubits. In this thesis, we will explore the larger spin environment by first developing techniques to address ^{13}C spins with weaker electron-nuclear couplings (light purple lines). We will then investigate the couplings between nuclear spins themselves (yellow and green lines) and utilise these for further qubit control. These techniques provide access to spin registers comprising tens of qubits as a resource for quantum technologies. Figure (b) adapted from Abobeih [79].

1.3. THESIS OVERVIEW

The text is broken down into the following chapters:

In **Chapter 2**, I summarise the key properties of the NV centre in diamond. I then give an overview of the experimental techniques utilised and developed within this thesis, along with the underlying theoretical models. I also outline the fabrication procedures used to create devices akin to those used in this work.

In **Chapter 3**, we investigate the properties of the neutrally-charged NV centre. Using resonant excitation spectroscopy, we reveal the fine structure, and use this knowledge to selectively address individual spin-orbit states. We measure the timescales associated with spin- and orbital-dynamics. Finally, we perform high-fidelity read-out of the spin

state. Our findings suggest that — without intervention — stochastic ionisation will lead to rapid dephasing of ^{13}C data qubits in NV-based quantum networks. However, both the knowledge gained of the NV^0 level structure, and the capability to perform single-shot read-out, provide avenues to mitigate such dephasing.

In **Chapter 4**, we investigate isotopic engineering of diamond as an avenue for realising robust quantum-network memories. We characterise a weakly-coupled (~80 Hz) ^{13}C spin, and find that it retains its quantum state for >1e5 repetitions of the primitive used to create remote entanglement between NV centres, a two order-of-magnitude improvement upon the state of the art. We assess the robustness of the memory qubit to NV centre ionisation, with favourable results. Finally, we numerically investigate rudimentary distributed quantum information protocols combining NV-NV photonic entanglement and robust ^{13}C quantum memories. We find that key primitives for distributed quantum information processing — deterministic two-qubit gate operations and four-node GHZ-state creation — are now within reach for NV-based quantum networks.

In **Chapter 5**, we develop novel decoherence-protected two-qubit gates for the selective control of ^{13}C nuclear spins surrounding a single NV centre. We utilise these new capabilities to realise a fully connected 10-qubit register with two-qubit gate fidelities of up to 99.1(9)% and coherence times of up to one minute. Furthermore, we create genuine multipartite entanglement between 7 qubits. Our findings show that the combination of the NV centre and surrounding nuclear spins is a promising platform for quantum information processing.

In **Chapter 6**, we demonstrate atomic-scale imaging of a cluster of 27 ^{13}C nuclear spins surrounding a single NV centre in diamond. By combining the methods developed in Ch. 5 with multidimensional spectroscopy based upon double-resonance techniques, we isolate individual interactions between nuclear spins in the cluster. Using 171 measured coupling strengths, we develop numerical methods to extract the three-dimensional structure of all 27 spins with sub-ångström resolution. This is a proof-of-principle demonstration towards the goal of magnetic imaging of single molecules or spin complexes outside the diamond. Moreover, this precise characterisation of the local environment of a single NV centre gives unprecedented understanding for improved quantum control of a nuclear spin register.

In **Chapter 7**, we implement a quantum simulation of the driven-Ising model using a 1D chain of 9 interacting nuclear spins. We combine the knowledge of the nuclear-spin environment developed in Ch. 6 with novel control techniques to isolate, manipulate, and measure a carefully chosen subset of spins. These spins have the required properties to synthesise the discrete-time-crystalline phase: an out-of-equilibrium phase of matter which exhibits robust spatiotemporal order protected by many-body-localization. We show the hallmark characteristics of the many-body-localised discrete-time-crystal for the first time, establishing ^{13}C spins in diamond as a novel and promising quantum simulation platform for studying exotic states of matter.

In **Chapter 8**, I summarise the findings of this thesis. I discuss opportunities for near-term experiments which build upon the work shown here. Finally, I give a broader outlook for quantum technologies based on solid-state spins in diamond.

1

REFERENCES

[1] C. Kittel and P. McEuen, *Introduction to solid state physics* (Wiley New York, 1996).

[2] A. L. Schawlow and C. H. Townes, *Infrared and optical masers,* Phys. Rev. **112**, 1940 (1958).

[3] T. Maiman, *Stimulated optical radiation in ruby,* Nature **187**, 493 (1960).

[4] J. P. Dowling and G. J. Milburn, *Quantum technology: the second quantum revolution,* Philos. Trans. Royal Soc. A **361**, 1655 (2003).

[5] A. Acín *et al.*, *The quantum technologies roadmap: a european community view,* New J. Phys. **20**, 080201 (2018).

[6] J. Preskill, *Quantum computing in the nisq era and beyond,* Quantum **2**, 79 (2018).

[7] J.-M. Raimond, M. Brune and S. Haroche, *Manipulating quantum entanglement with atoms and photons in a cavity,* Rev. Mod. Phys. **73**, 565 (2001).

[8] D. Leibfried, R. Blatt, C. Monroe and D. Wineland, *Quantum dynamics of single trapped ions,* Rev. Mod. Phys. **75**, 281 (2003).

[9] P. Kok *et al.*, *Linear optical quantum computing with photonic qubits,* Rev. Mod. Phys. **79**, 135 (2007).

[10] M. H. Devoret and R. J. Schoelkopf, *Superconducting circuits for quantum information: an outlook,* Science **339**, 1169 (2013).

[11] D. D. Awschalom, R. Hanson, J. Wrachtrup and B. B. Zhou, *Quantum technologies with optically interfaced solid-state spins,* Nat. Photonics **12**, 516 (2018).

[12] A. Montanaro, *Quantum algorithms: an overview,* NPJ Quantum Inf. **2**, 1 (2016).

[13] Y. Alexeev *et al.*, *Quantum computer systems for scientific discovery,* PRX Quantum **2**, 017001 (2021).

[14] F. Arute *et al.*, *Quantum supremacy using a programmable superconducting processor,* Nature **574**, 505 (2019).

[15] H.-S. Zhong *et al.*, *Quantum computational advantage using photons,* Science **370**, 1460 (2020).

[16] S. Aaronson and A. Arkhipov, *The computational complexity of linear optics,* in *Proceedings of the forty-third annual ACM symposium on Theory of computing* (2011) pp. 333–342.

[17] J. Preskill, *Quantum computing and the entanglement frontier,* arXiv:1203.5813 (2012).

[18] A. Kandala *et al.*, *Error mitigation extends the computational reach of a noisy quantum processor,* Nature **567**, 491 (2019).

[19] P. W. Shor, *Scheme for reducing decoherence in quantum computer memory,* Phys. Rev. A **52**, R2493 (1995).

[20] B. M. Terhal, *Quantum error correction for quantum memories,* Rev. Mod. Phys. **87**, 307 (2015).

[21] R. P. Feynman, *Simulating physics with computers,* Int. J. Theor. Phys **21** (1982).

[22] Y. Manin, *Computable and uncomputable,* Sovetskoye Radio, Moscow **128** (1980).

[23] I. M. Georgescu, S. Ashhab and F. Nori, *Quantum simulation,* Rev. Mod. Phys. **86**, 153 (2014).

[24] E. Altman *et al.*, *Quantum simulators: Architectures and opportunities,* PRX Quantum **2**, 017003 (2021).

[25] S. Ebadi *et al.*, *Quantum phases of matter on a 256-atom programmable quantum simulator,* Nature **595**, 227 (2021).

[26] P. Scholl *et al.*, *Quantum simulation of 2d antiferromagnets with hundreds of rydberg atoms,* Nature **595**, 233 (2021).

[27] D. Perez-Garcia, F. Verstraete, M. M. Wolf and J. I. Cirac, *Matrix product state representations,* arXiv preprint quant-ph/0608197 (2006).

[28] N. Gisin, G. Ribordy, W. Tittel and H. Zbinden, *Quantum cryptography,* Rev. Mod. Phys. **74**, 145 (2002).

[29] A. Acín *et al.*, *Device-independent security of quantum cryptography against collective attacks,* Phys. Rev. Lett. **98**, 230501 (2007).

[30] B. Hensen *et al.*, *Loophole-free bell inequality violation using electron spins separated by 1.3 kilometres,* Nature **526**, 682 (2015).

[31] M. Giustina *et al.*, *Significant-loophole-free test of bell's theorem with entangled photons,* Phys. Rev. Lett. **115**, 250401 (2015).

[32] L. K. Shalm *et al.*, *Strong loophole-free test of local realism,* Phys. Rev. Lett. **115**, 250402 (2015).

[33] S. Wehner, D. Elkouss and R. Hanson, *Quantum internet: A vision for the road ahead,* Science **362** (2018).

[34] N. H. Nickerson, J. F. Fitzsimons and S. C. Benjamin, *Freely scalable quantum technologies using cells of 5-to-50 qubits with very lossy and noisy photonic links,* Phys. Rev. X **4**, 041041 (2014).

[35] D. Awschalom *et al.*, *Development of quantum interconnects (quics) for next-generation information technologies,* PRX Quantum **2**, 017002 (2021).

[36] C. L. Degen, F. Reinhard and P. Cappellaro, *Quantum sensing,* Rev. Mod. Phys. **89**, 035002 (2017).

[37] A. D. Ludlow, M. M. Boyd, J. Ye, E. Peik and P. O. Schmidt, *Optical atomic clocks,* Rev. Mod. Phys. **87**, 637 (2015).

[38] J. Aasi *et al.*, *Enhanced sensitivity of the ligo gravitational wave detector by using squeezed states of light,* Nat. Photonics **7**, 613 (2013).

[39] S. Bose *et al.*, *Spin entanglement witness for quantum gravity,* Phys. Rev. Lett. **119**, 240401 (2017).

[40] C. Marletto and V. Vedral, *Gravitationally induced entanglement between two massive particles is sufficient evidence of quantum effects in gravity,* Phys. Rev. Lett. **119**, 240402 (2017).

[41] F. Casola, T. van der Sar and A. Yacoby, *Probing condensed matter physics with magnetometry based on nitrogen-vacancy centres in diamond,* Nat. Rev. Mater. **3**, 1 (2018).

[42] F. A. Zwanenburg *et al.*, *Silicon quantum electronics,* Rev. Mod. Phys. **85**, 961 (2013).

[43] A. Morello, J. J. Pla, P. Bertet and D. N. Jamieson, *Donor spins in silicon for quantum technologies,* Adv. Quantum Technol. **3**, 2000005 (2020).

[44] A. Sipahigil *et al.*, *An integrated diamond nanophotonics platform for quantum-optical networks,* Science **354**, 847 (2016).

[45] D. J. Christle *et al.*, *Isolated electron spins in silicon carbide with millisecond coherence times,* Nat. Mater. **14**, 160 (2015).

[46] T. Iwasaki *et al.*, *Germanium-vacancy single color centers in diamond,* Sci. Rep. **5**, 12882 (2015).

[47] H. Seo *et al.*, *Quantum decoherence dynamics of divacancy spins in silicon carbide,* Nat. Commun. **7**, 12935 (2016).

[48] D. D. Sukachev *et al.*, *Silicon-vacancy spin qubit in diamond: a quantum memory exceeding 10 ms with single-shot state readout,* Phys. Rev. Lett. **119**, 223602 (2017).

[49] P. Siyushev *et al.*, *Optical and microwave control of germanium-vacancy center spins in diamond,* Phys. Rev. B **96**, 081201 (2017).

[50] B. Pingault *et al.*, *Coherent control of the silicon-vacancy spin in diamond,* Nat. Commun. **8**, 15579 (2017).

[51] J. N. Becker *et al.*, *All-optical control of the silicon-vacancy spin in diamond at millikelvin temperatures,* Phys. Rev. Lett. **120**, 053603 (2018).

[52] M. E. Trusheim *et al.*, *Transform-limited photons from a coherent tin-vacancy spin in diamond,* Phys. Rev. Lett **124**, 023602 (2020).

[53] A. E. Rugar, C. Dory, S. Sun and J. Vučković, *Characterization of optical and spin properties of single tin-vacancy centers in diamond nanopillars,* Phys. Rev. B **99**, 205417 (2019).

[54] W. E. Moerner and M. Orrit, *Illuminating single molecules in condensed matter,* Science **283**, 1670 (1999).

[55] A. Gruber *et al., Scanning confocal optical microscopy and magnetic resonance on single defect centers,* Science **276**, 2012 (1997).

[56] N. Kalb, P. C. Humphreys, J. Slim and R. Hanson, *Dephasing mechanisms of diamond-based nuclear-spin memories for quantum networks,* Phys. Rev. A **97**, 062330 (2018).

[57] G. Fuchs, V. Dobrovitski, D. Toyli, F. Heremans and D. Awschalom, *Gigahertz dynamics of a strongly driven single quantum spin,* Science **326**, 1520 (2009).

[58] G. De Lange, Z. Wang, D. Riste, V. Dobrovitski and R. Hanson, *Universal dynamical decoupling of a single solid-state spin from a spin bath,* Science **330**, 60 (2010).

[59] G. Balasubramanian *et al., Ultralong spin coherence time in isotopically engineered diamond,* Nat. Mater. **8**, 383 (2009).

[60] N. Bar-Gill, L. M. Pham, A. Jarmola, D. Budker and R. L. Walsworth, *Solid-state electronic spin coherence time approaching one second,* Nat. Commun. **4**, 1 (2013).

[61] M. H. Abobeih *et al., One-second coherence for a single electron spin coupled to a multi-qubit nuclear-spin environment,* Nat. Commun. **9**, 1 (2018).

[62] L. Childress *et al., Coherent dynamics of coupled electron and nuclear spin qubits in diamond,* Science **314**, 281 (2006).

[63] P. Neumann *et al., Multipartite entanglement among single spins in diamond,* science **320**, 1326 (2008).

[64] P. Neumann *et al., Single-shot readout of a single nuclear spin,* Science **329**, 542 (2010).

[65] T. Taminiau *et al., Detection and control of individual nuclear spins using a weakly coupled electron spin,* Phys. Rev. Lett. **109**, 137602 (2012).

[66] S. Kolkowitz, Q. P. Unterreithmeier, S. D. Bennett and M. D. Lukin, *Sensing distant nuclear spins with a single electron spin,* Phys. Rev. Lett. **109**, 137601 (2012).

[67] N. Zhao *et al., Sensing single remote nuclear spins,* Nat. Nanotechnol. **7**, 657 (2012).

[68] G. Waldherr *et al., Quantum error correction in a solid-state hybrid spin register,* Nature **506**, 204 (2014).

[69] N. H. Nickerson, Y. Li and S. C. Benjamin, *Topological quantum computing with a very noisy network and local error rates approaching one percent,* Nat. Commun. **4**, 1756 (2013).

[70] S. de Bone, R. Ouyang, K. Goodenough and D. Elkouss, *Protocols for creating and distilling multipartite ghz states with bell pairs,* IEEE Trans. Quantum Eng. **1**, 1 (2020).

[71] H. Bernien *et al.*, *Heralded entanglement between solid-state qubits separated by three metres,* Nature **497**, 86 (2013).

[72] P. C. Humphreys *et al.*, *Deterministic delivery of remote entanglement on a quantum network,* Nature **558**, 268 (2018).

[73] N. Kalb *et al.*, *Entanglement distillation between solid-state quantum network nodes,* Science **356**, 928 (2017).

[74] M. Pompili *et al.*, *Realization of a multinode quantum network of remote solid-state qubits,* Science **372**, 259 (2021).

[75] T. H. Taminiau, J. Cramer, T. van der Sar, V. V. Dobrovitski and R. Hanson, *Universal control and error correction in multi-qubit spin registers in diamond,* Nat. Nanotechnol. **9**, 171 (2014).

[76] S. B. van Dam, J. Cramer, T. H. Taminiau and R. Hanson, *Multipartite entanglement generation and contextuality tests using nondestructive three-qubit parity measurements,* Phys. Rev. Lett. **123**, 050401 (2019).

[77] T. K. Unden, D. Louzon, M. Zwolak, W. H. Zurek and F. Jelezko, *Revealing the emergence of classicality using nitrogen-vacancy centers,* Phys. Rev. Lett. **123**, 140402 (2019).

[78] J. Cramer *et al.*, *Repeated quantum error correction on a continuously encoded qubit by real-time feedback,* Nat. Commun. **7**, 1 (2016).

[79] M. Abobeih, *From atomic-scale imaging to quantum fault-tolerance with spins in diamond,* Ph.D. Thesis, TUDelft (2021).

[80] D. Riedel *et al.*, *Deterministic enhancement of coherent photon generation from a nitrogen-vacancy center in ultrapure diamond,* Phys. Rev. X **7**, 031040 (2017).

[81] M. Ruf, M. J. Weaver, S. B. van Dam and R. Hanson, *Resonant excitation and purcell enhancement of coherent nitrogen-vacancy centers coupled to a fabry-perot microcavity,* Phys. Rev. Appl. **15**, 024049 (2021).

[82] M. Blok, N. Kalb, A. Reiserer, T. Taminiau and R. Hanson, *Towards quantum networks of single spins: analysis of a quantum memory with an optical interface in diamond,* Faraday Discuss. **184**, 173 (2015).

[83] A. Reiserer *et al.*, *Robust quantum-network memory using decoherence-protected subspaces of nuclear spins,* Phys. Rev. X **6**, 021040 (2016).

2

METHODS FOR QUANTUM CONTROL WITH NV CENTRES IN DIAMOND

In this chapter, I summarise the key properties of the nitrogen-vacancy (NV) centre in diamond, and outline the experimental methods used to initialise, manipulate, and measure the electron spin of a single NV centre at 4 Kelvin. I then describe how the NV centre can be used to probe nuclear spins in its local environment and to realise universal quantum control over those spins. These methods form the foundations of the work presented in the rest of the thesis.

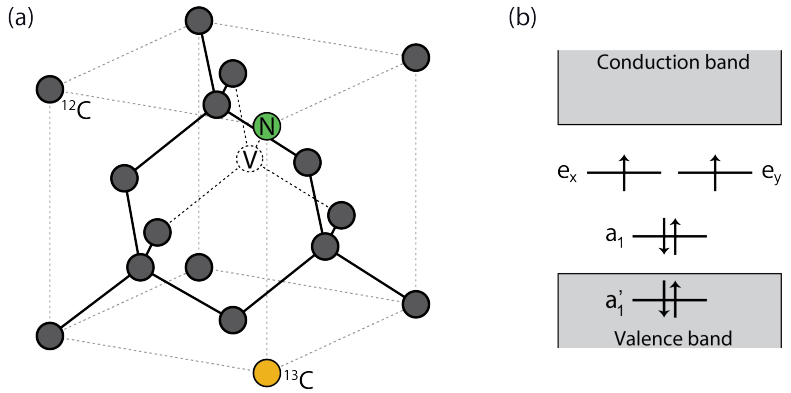

Figure 2.1: **Crystal structure and molecular orbitals of the NV centre. (a)** Crystal structure of an NV centre within a cubic unit cell of the diamond lattice. A nitrogen atom impurity (green) is adjacent to a vacant site (white). Under natural abundance (all work in this thesis aside from Ch. 4), 1.1% of the ^{12}C atoms (grey) are replaced by the spin-1/2 ^{13}C isotope (yellow) **(b)** NV^- centre molecular orbitals and their ground-state filling. Figures adapted from Pfaff[1], Bernien[2].

2.1. THE NV CENTRE IN DIAMOND

Diamond is host to a number of defects (or 'colour centres'), many of which have favourable properties for quantum technologies[3]. Of these, the nitrogen-vacancy (NV) centre was the first to be individually detected[4], and remains the most widely studied. An NV centre is manifested by a substitutional nitrogen atom impurity next to a vacant lattice site (Fig. 2.1(a)). All experiments performed in this thesis make use of naturally occurring NV centers in type-IIa chemical-vapour-deposition (CVD) grown substrates. In these substrates, exceptionally low impurity concentrations of a few parts-per-billion minimise unwanted background fluorescence and electronic spin-bath noise. Consequently, the NV concentration is also very low.

If desired, there are typically two approaches to increase the concentration of NV centres. While not used for the substrates employed in this thesis, they are described here for completeness. First, a greater fraction of intrinsic nitrogen impurities can be converted to NV centres by creating additional vacant sites. Subsequent annealing of the diamond at high temperature (1200 °C) induces migration of these vacancies until they form bound states (such as NV centres)[5]. Vacancy creation can be performed, for example, by electron irradiation[6–8], or by laser writing[9–11], both of which have been shown to produce NV centres with coherent optical transitions as required for quantum network protocols.

The second approach is to introduce additional nitrogen into the diamond. Ion implantation and subsequent annealing offers the potential to create NV centres localised to within a few tens of nanometres[12], but current techniques used to perform this process induce significant lattice damage which deteriorates NV centre properties[13,14]. These issues may be addressed in future work by performing shallow (low energy) implantation and subsequent diamond overgrowth[15,16]. Nitrogen can also be deliberately

grown into the diamond, though this can come at the cost of a significant background electron spin bath. This can be mitigated by the use of more advanced growth techniques, such as 'δ-doping', which localises the impurities at particular depths [16–18].

The nitrogen-vacancy centre typically occurs in either the negatively-charged (NV^-) or neutrally-charged (NV^0) state. For NV^0, five electrons contribute to the filling of its molecular orbitals, of which two are inherent to the nitrogen atom, and the other three arise from the dangling bonds of the vacancy-neighbouring carbon atoms [19–21]. Conversion between the $NV^0 \leftrightarrow NV^-$ states occurs only by capturing an additional electron from a local charge trap [21,22], which can be stimulated by optical excitation [23–26]. The majority of protocols based upon NV centres utilise the NV^- state, which we will hereafter refer to as NV, and which we will focus on for the remainder of this chapter. In Ch. 3 we will further investigate the properties of the NV^0 centre.

2.2. LEVEL STRUCTURE OF THE NV CENTRE

We begin with an overview of the NV centre fine structure and optical properties. The composition of the NV centre molecular orbitals and their ground-state filling is shown in Figure 2.1(b). These molecular orbitals are formed from linear combinations of the neighbouring nitrogen and carbon orbitals under the C_{3v} symmetry of the NV complex [19–21]. The $^3A_2$ ground state is characterised by two doubly occupied orbitals (a_1' and a_1) and a pair of degenerate orbitals each hosting a single unpaired electron (e_x and e_y). These unpaired electrons form a spin-triplet ($S = 1$) ground state due to Coulomb repulsion. From this ground state, optical excitation can promote a single electron from the a_1 orbital to either of the e orbitals, creating one of six orbital-doublet spin-triplet excited states. As the unoccupied orbitals of both the ground and first-excited states of the NV centre lie within the diamond bandgap, optical transitions between these states do not induce charge transfer between the NV and the diamond lattice [21,27]. The NV centre optical properties are thus akin to a trapped ion in vacuum, albeit hosted in a solid-state matrix.

Figure 2.2(a) shows the energy levels of the NV centre and the allowed transitions. At zero magnetic field, the ground state $m_s = \pm 1$ levels are degenerate, but are split from the $m_s = 0$ level by spin-spin interactions, with a zero-field-splitting of $\Delta_{ZFS} = 2.88$ GHz [28–30]. An external magnetic lifts the degeneracy of the $m_s = \pm 1$ levels, with the Zeeman term following the electronic gyromagnetic ratio of $\gamma_e = 2.802$ MHz/G (Fig. 2.2(c)). The ground-state electronic Hamiltonian is thus:

$$H_e = \Delta_{ZFS} S_z^2 + \gamma_e (\mathbf{B} \cdot \mathbf{S}). \tag{2.1}$$

Here, $\mathbf{S} = (S_x, S_y, S_z)$, where S_α are the electron spin-1 operators, and $\mathbf{B} = (B_x, B_y, B_z)$ is the magnetic field vector. Throughout this thesis we work with axially aligned fields such that $B_x \approx B_y \approx 0$. We have neglected second order spin-orbit coupling and effects from electric (or strain) fields [28,29], alongside hyperfine interaction terms which we will discuss in Sec. 2.6.

Lifting the degeneracy of the $m_s = \pm 1$ levels provides access to a choice of isolated qubit states, which we typically choose to be the $m_s = \{0,\text{-}1\} = \{|0\rangle, |1\rangle\}$ basis. Microwave (MW) driving at the associated transition frequency realises high-fidelity manipulation of the ground-state qubit within tens of nanoseconds [31,32].

Optical excitation enables transitions to the six spin-triplet orbital-doublet first-excited states. At room temperature, the excited states are mixed by two-phonon Raman processes, leading to broad homogeneous linewidths ~15 THz[33,34]. However, at cryogenic temperatures (<10 K), the individual transitions are resolved, with typical few-GHz energy separations compared with their lifetime-limited linewidths of 13 MHz[33,35]. Optical selection rules give rise to the transitions shown in Figure 2.2(a). The degeneracy of the pairs of states $\{E_x,E_y\}$ and $\{E_1,E_2\}$ is lifted under lateral strain (Fig. 2.2(b))[19,21]. Further tuning of the different excited-state energies can be achieved through a combination of magnetic, electric and strain fields[19,35–38], but these techniques are not utilised in this work. For all experiments in this thesis, a specific magnetic field is chosen to aid in the control of the spin environment (discussed in Sec. 2.7), a (random) lateral strain occurs inherently for each NV centre, and electric fields are not applied.

We now identify a set of transitions which can be used for spin initialisation and read-out. As each step has differing requirements, we choose distinct optical transitions based upon their properties. Due to the presence of spin-orbit coupling, the A_1, E_1, and E_2 states all have a significant probability (>40% per cycle at 4 K[39,40]) to undergo an inter-system crossing (ISC) to the singlet states ($^1A_1$)[40,41]. The $^1A_1$ singlet states rapidly decay to the metastable ^1E states, which then decay back to the ground states. Importantly, this final decay preferentially populates the $m_s = 0$ state (with a ratio of {6(1):1:1} into m_s = {0:-1:+1} for strain fields of 2-5 GHz and working at 4 K[39]). Exciting a chosen subset of A_1, E_1, and E_2 pumps population out of the spin-±1 projections, leading to rapid spin initialisation (spin-pumping, SP) into the $m_s = 0$ state, with achievable fidelities >99.7% within 3 μs[39,42].

Conversely, the ISC rates from the states A_2, E_x, and E_y are much reduced[40,41]. Exciting the $m_s = 0$ ground state on either the E_x or E_y transition leads to highly cycling behaviour, with an average of ~100 cycles before a spin-flipping process occurs[39]. There is thus a significant contrast in the number of emitted photons for the $|0\rangle$ and $|1\rangle$ states when exciting on either of these transitions, enabling single-shot read-out[42]. Figure 2.3(b) shows example histograms of the number of detected photons after preparing a single NV centre in each of these states and attempting read-out (see Sec. 2.4 for details of the experimental setup). The quality of the read-out process is described by the single-shot read-out fidelity:

$$F_{\mathrm{SSRO}} = \frac{1}{2}(F_{0|0} + F_{1|1}), \tag{2.2}$$

where $F_{i|j}$ is the probability to assign the state $|i\rangle$ after attempting initialization in the state $|j\rangle$. Note that this is a lower bound, as it assumes perfect state initialisation. In Figure 2.3(c) we plot the calculated read-out fidelity for this data. A value of 94.3(1)% is achieved, as typical for the experiments performed in Chs. 5, 6 and 7.

Note that F_{SSRO} is a strict metric for the case that we assign an outcome after every read-out. By taking a probabilistic approach to measurement (discarding ambiguous results), it is possible to assign certain outcomes with higher fidelities. An example is seen in the histogram shown in Figure 2.3(b). If at least one photon is detected in this experiment, there is a 99.1(1)% probability that the pre-measurement state was $|0\rangle$, even though F_{SSRO} is only 94.3(1)%. We denote this probability the 'conditional read-out fidelity', F_{CRO}. As we will discuss in Sec. 2.9, probabilistic measurements can be a useful

tool to improve the quality of certain operations, and are especially useful for heralded state preparation. A related metric is the 'projectivity' of the measurement: the probability that the post-measurement state of the electron spin corresponds to the assigned state[43]. The projectivity becomes important when we wish to use the post-measurement state, as, for example, in Ch. 5.

Without tuning of the energy levels, the main considerations when selecting optical transitions are spectral isolation and read-out cyclicity (the number of optical cycles before a change of the spin state). First, we pick transitions which are well-isolated, such that off-resonant excitation of other states is minimised. If the E_x and E_y transitions are both isolated, we then consider their cyclicity. This is dependent on lateral strain and magnetic field, but typically the E_x transition is preferred[20,44].

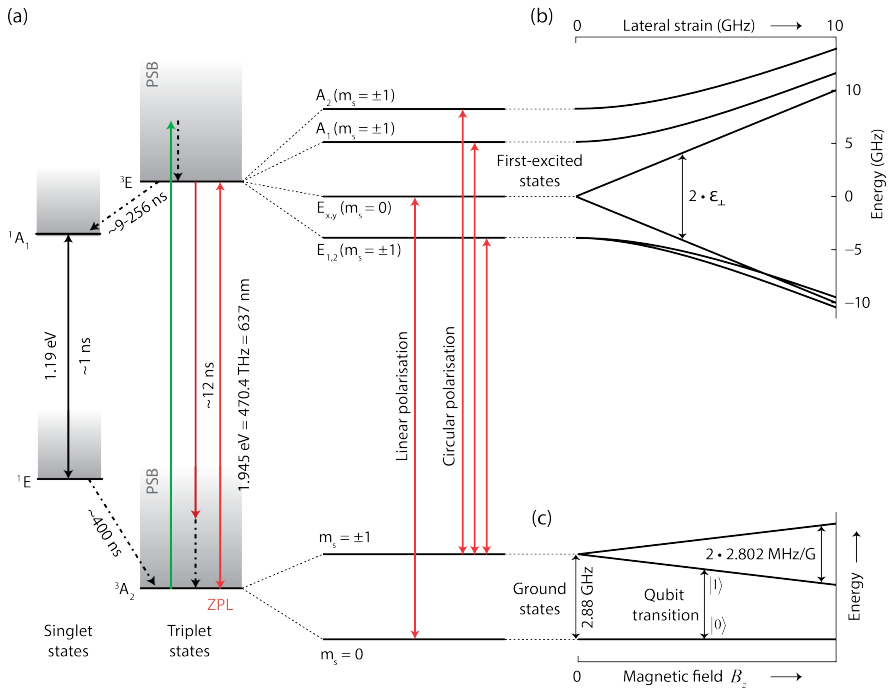

Figure 2.2: **Level structure of the NV$^-$ centre in diamond.** **(a)** Energies of the ^{3}A$_2$ orbital-singlet spin-triplet ground states ($S = 1$), the ^{3}E orbital-doublet spin-triplet first-excited states, and the ^{1}A$_1$ and ^{1}E singlet manifolds ($S = 0$). All energies are shown in the absence of external fields. Under the appropriate optical selection rules, laser excitation can drive transitions between the ground and first-excited spin-triplet states. Subsequent decay can occur either coherently in the zero-phonon line (ZPL), in conjunction with a phonon in the phonon-sideband (PSB), or for the A_1, E_1 and E_2 states, via an intersystem crossing (ISC) to the singlet manifolds. **(b)** Level steering of the first excited states under lateral strain (or equivalent applied electric field). In this thesis, all used NV centres have natural lateral strains of $\epsilon_\perp$ = 2-5 GHz, and no external electric fields are applied. **(c)** Ground state fine structure. A zero-field-splitting of 2.88 GHz arises due to spin-spin interactions. The application of an external magnetic field lifts the degeneracy of the $m_s = \pm1$ states, and a qubit is defined between the $m_s = 0$ ($|0\rangle$) and $m_s = -1$ ($|1\rangle$ states. The hyperfine structure is discussed later in this chapter. Figures adapted from Pfaff[1], Bernien[2], Hensen[29].

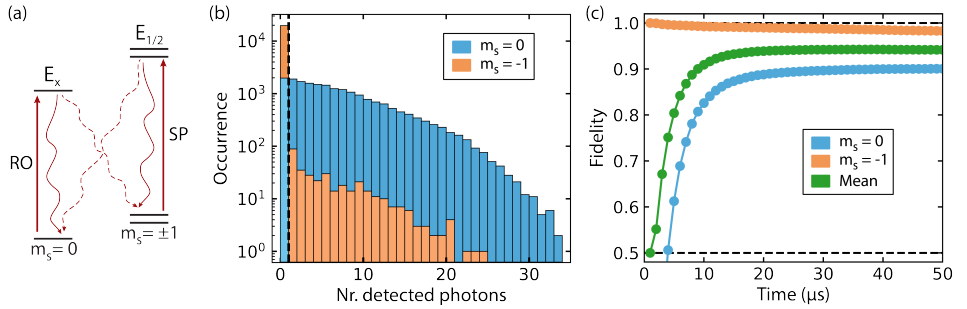

Figure 2.3: **NV centre single-shot read-out: (a)** Energy levels and optical transitions selected for read-out (RO) and spin-pumping (SP). Solid (dashed) wiggled lines represent spin-conserving (non-conserving) decay channels. **(b)** Histograms of the number of detected photons after spin-pumping into each of the $m_s = 0$ ($|0\rangle$) and $m_s = -1$ ($|1\rangle$) states, and performing single-shot read-out for a duration of 38 μs (see (c)). The mean number of detected photons is $\langle n \rangle = 6.84(4)$ $(0.10(1))$ for the $|0\rangle$ ($|1\rangle$) state. Dashed line at $n = 1$ indicates the state-discrimination threshold. **(c)** Single-shot read-out fidelity as a function of the read-out duration. A maximal fidelity of $F_{\mathrm{SSRO}} = 94.3(1)\%$ is reached for 38 μs. Panel (a) adapted from Robledo *et al.*[42].

2.3. DEVICE FABRICATION

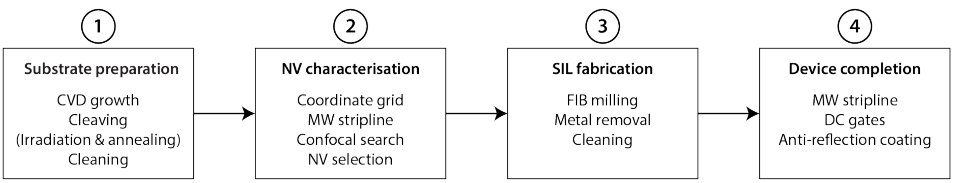

Figure 2.4: **Process flow for fabrication of diamond devices.** Details for each box are given in the text.

For the experiments performed in this thesis, a number of device capabilities are required to enable high-fidelity quantum control. The process for device fabrication is outlined in Figure 2.4: we now discuss the details of each step.

In this work, we use naturally-occurring single NV centres in ultrapure CVD-grown diamond substrates from Element Six (**Box 1** of Fig. 2.4). Except where specified otherwise, all of these substrates contain a natural abundance of ^{13}C isotope, 1.1%, and have been cleaved along the $\langle 111 \rangle$ crystal axis (having been grown along the $\langle 100 \rangle$ orientation). This has the benefit that — for NVs which are oriented in the $\langle 111 \rangle$ direction — a well-aligned external magnetic field can be produced by simply placing a permanent magnet at the back of the substrate.

If it is desirable to increase the NV concentration, electron irradiation is employed with an electron energy of 2 MeV and a fluence of 10^{13} e^-/cm^2s to create vacancies (performed at the Reactor Institute Delft). Subsequently, a three-step annealing process[8] is performed under high vacuum ($< 10^{-6}$ mbar), reaching a peak temperature of 1100 °C, inducing vacancy migration and NV formation. Irrespective of performing irradiation and annealing, the substrate is cleaned using a triacid process, 1:1:1 $H_2SO_4(97\%)$:$HNO_3(60\%)$:$HClO_4(60\%)$ at 120°C for one hour in a re-flux setup[8]. The

diamond is then mounted onto a silicon carrier wafer using rubber cement (Marabu Fixogum) for ease of handling during the fabrication process.

Subsequently (**Box 2**), we create a marker (coordinate) grid and a gold stripline on the diamond surface via electron-beam lithography (EBL). We use a single-layer EBL resist (PMMA A8 950, spun at 3250 RPM to produce a layer ~1 μm thick), followed by evaporation of a 15 nm chrome layer for electron-beam conduction. After exposure and development of the resist, and wet-etching of the chrome layer, we use a short oxygen plasma etch to ensure a pristine surface for metal evaporation. We first evaporate a 7 nm titanium adhesion layer, followed by 150 nm of gold. After a lift-off procedure in acetone, the sample is removed from the carrier wafer and mounted on a printed circuit board (PCB) using conductive silver paint, before wire-bonding for delivery of MW fields.

An automated search for suitable NV centres is performed using a room-temperature confocal microscope. Example confocal images at the diamond surface (showing marker positions for localisation) and at a depth[†] of ~5 μm (showing candidate NVs) are exhibited in Figures 2.5(a) and (b). The depth of 5 μm is chosen to ensure bulk properties of the NVs (avoiding surface effects[45]), while limiting the size of the solid-immersion lenses (SILs) which will be written in the next phase. NVs are selected on having a $\langle 111 \rangle$ orientation (determined by polarisation-dependence of fluorescence), and showing no strongly-coupled (>1 MHz) ^{13}C spins in optically-detected magnetic resonance.

Once a number of suitable NV centres have been identified, we begin fabricating the device itself (**Box 3**). First, a 15 nm chrome layer is evaporated for conduction in scanning electron microscopy (SEM). SILs are then milled into the diamond surface at the detected positions using a 30 kV gallium focused ion beam (FIB) combined with an SEM (Fig. 2.5(c))[42,46]. These micro-structures enhance the collection efficiency from diamond by suppressing total internal reflection. This enhanced collection efficiency improves the signal-to-noise ratio for high-fidelity single-shot read-out[42], and also directly translates into improved remote-entanglement rates for quantum network experiments[47]. After SIL writing, the gold structures are removed using a KI wet-etch, before a second triacid clean is used to remove the remaining materials. An oxygen plasma etch then strips the top layer (~20-30 nm) of the diamond, removing any remaining gallium contamination (Fig. 2.5(d)).

Next (**Box 4**), the substrate is again mounted on a silicon carrier for a two-step EBL process, each step following the recipe described above. The first step is used to create a number of 20x20 μm^2 alignment markers, while the second step uses these markers to finely align a microwave stripline and electrodes for DC Stark-tuning (not employed in this thesis) to the solid-immersion lens positions. As before, a 7 nm titanium layer is evaporated for adhesion, followed by 150 nm of gold. After lift-off, atomic layer deposition (ALD) is used to create an Al_2O_3 anti-reflection coating[48]. A thickness of ~102 nm is deposited (measured refractive index 1.61 for a 105°C deposition process), reducing the natural reflection of ~17% to a residual value of ~0.5-1%, which can be used for phase-stabilisation measurements in single-photon remote-entanglement protocols[49,50]. An example device after the ALD and evaporation processes is shown in Figure 2.5(e).

Finally, the sample is mounted on a PCB using silver paint, and the stripline and gates are wirebonded for delivery of MW fields and DC voltages (or grounding), respectively.

[†]This depth is corrected for refraction at the diamond surface[20].

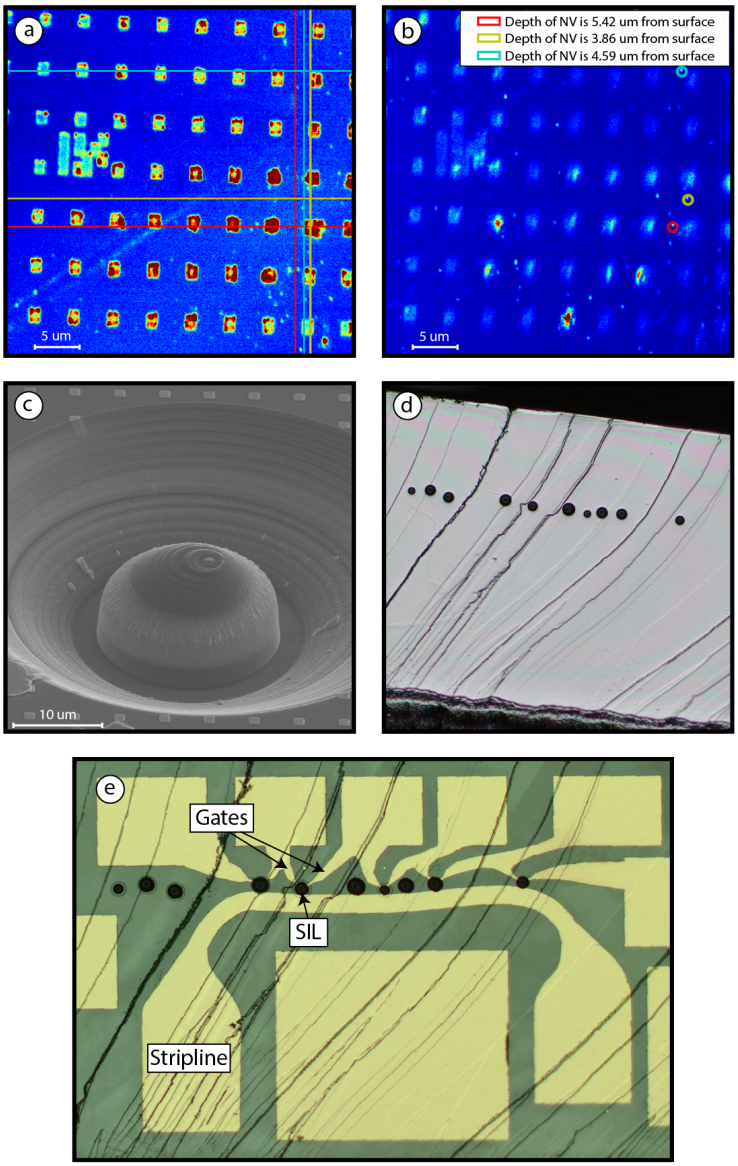

Figure 2.5: **Nanofabrication of NV diamond devices. (a)** Confocal microscope image of the diamond surface after writing of a gold alignment grid. At the surface, a uniquely-identifiable pattern is observed (mid-left), along with an array of 1x1 μm^2 markers. Crosshairs give the positions of localised $\langle 111 \rangle$ NV centres (see (b)). **(b)** Confocal image of the diamond at a depth of ~5 μm (corrected for refraction at the diamond surface). Three identified $\langle 111 \rangle$-oriented NV centres are located. Other bright spots did not pass the NV selection criteria. **(c)** SEM image of a solid-immersion lens (SIL), milled into the diamond surface using a gallium focused ion beam. Small localisation markers are seen outside the trench. **(d)** Substrate prior to two-step EBL and ALD processes. After SIL writing, the diamond has been triacid cleaned, a PMMA resist layer has been applied (leading to the observed interference pattern), and a 15 nm layer of chrome has been deposited for conduction in the electron-beam. **(e)** Completed device, prior to wire-bonding. A single gold stripline is used to deliver microwaves to all SILs, but each SIL has its own pair of electrodes (or 'gates') for Stark-tuning of the optical transitions. In this case, the stripline and gates were evaporated on top of the ALD layer due to poor metal adhesion to the diamond surface. Shown device was pre-characterised by A. J. Stolk and M. Teng, and fabricated by C.E.B. and S. Baier.

2.4. EXPERIMENTAL SETUP

2.4.1. HARDWARE COMPONENTS

All experimental data presented in this thesis was measured on diamond devices in closed-cycle cryostats (Montana Cryostation S50) at ~4 K. Three distinct hardware setups and devices were used, as described in Table 2.1, but the majority of features are common to these setups. In Figure 2.6, we show a typical schematic for one of the measurement setups. Generally, experimental sequences are programmed via a Python interface (QTLab) and then executed on the hardware via a microcontroller (ADwin Pro II). Each hardware setup comprises optical elements for NV charge- and spin-state initialisation and readout[47], and MW and radio-frequency (RF) components for NV ground-state spin manipulation and nuclear spin control (detailed in Sections 2.7-2.9). Pulse sequences are created using an arbitrary waveform generator with 1 ns precision (Tektronix AWG5014C).

Chapter	Setup name	B_z (G)	Device name	^{13}C concentration	Crystal axis
3	LT3	1850	Hans	1.1%	⟨111⟩
4	M2	47	Gretel	0.01%	⟨100⟩
5	M1	403	111_no_1	1.1%	⟨111⟩
6	M1	403	111_no_1	1.1%	⟨111⟩
7	M1	403	111_no_1	1.1%	⟨111⟩

Table 2.1: Experimental setups and devices used throughout this thesis. Setup and device names are an internal reference. B_z is the externally applied magnetic field along the NV axis (in Gauss). Crystal axis gives the direction parallel to the axis of optical irradiation.

2.4.2. DYNAMIC CONTROL

A central feature of the hardware is the capability to perform real-time (1 μs clock-cycle) conditional logic using the microcontroller and AWG. Conditional logic based upon photon detection events is used for a number of protocols, such as to herald the NV in a particular charge or spin state[26,47]. Details of individual implementations are given in the chapters where they are used.

In a broader context beyond this thesis, active-feedback capabilities are key to a number of NV-based experiments, including quantum error correction[51,52], complex state preparation[53,54], adaptive quantum sensing[55], and quantum network protocols such as teleportation[56,57], entanglement distillation[58] and entanglement swapping[50]. All of these schemes are made possible by the combination of fast electronics, non-destructive measurements, and long relaxation and coherence times of the addressed spins, as we will discuss in the next section.

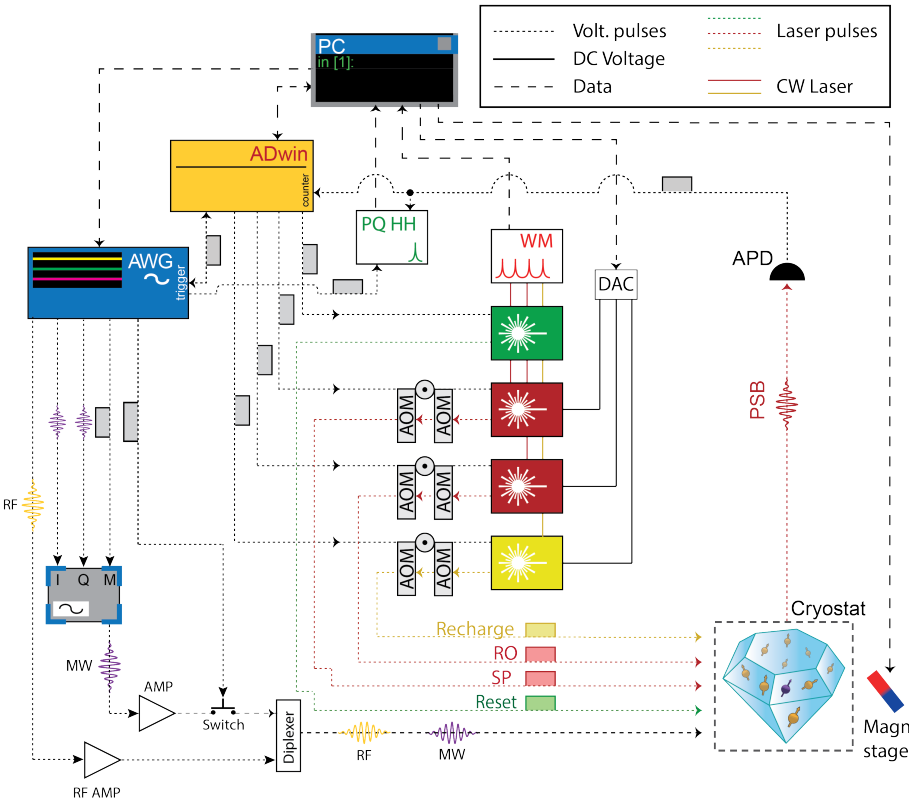

Figure 2.6: **Experimental setup. Laser systems:** A 515 nm laser (Cobolt MLD, current modulated, >135 dB on/off ratio) is used for charge-resonance reset [47]. A pair of 637 nm lasers (Toptica DL-pro and New Focus TLB-6704-P) are used for resonant spin initialisation (SP) and read-out (RO). A 575 nm laser (Toptica DL-SHG-pro) is used for resonant excitation spectroscopy of the NV^0 centre (Ch. 3) and for resonant recharging (Chs. 3, 4). The 637 nm and 575 nm laser frequencies are stabilised using a wavemeter (HF-Ångstrom WS/U-10U) and associated PID loop to 2 MHz accuracy. For the resonant lasers, we cascade two acousto-optic modulators (AOMs, G&H FibreQ) to achieve >100 dB on/off ratios. AOMs can be modulated either by the microcontroller or by the AWG. For the latter the control lines are omitted from the schematic to maintain readability. **Optical elements:** Light is focused onto and collected from the diamond using a 0.9 NA microscope objective (Olympus MPLFLN 100x) held under vacuum. The objective is movable in three dimensions using piezo-electric stages (PI Q545 or similar) for fine alignment to a single NV centre. NV phonon-sideband (PSB) emission is separated from reflected laser light using a long-pass filter (640 nm) and collected on an avalanche photodiode (APD, Laser Components). Detected photons are counted with the microcontroller. For time resolved measurements (Ch. 3), the times-of-arrival of these photons are recorded using a time-to-digital converter (Picoquant HydraHarp) which is synchronised to the AWG pulse sequence. **Microwave electronics:** Microwave (MW) pulses (for NV ground state manipulation) are produced with a vector source (R&S SGS100A), for which the frequency, duration, waveform and phase are determined by a pre-programmed AWG using IQ- and pulse-modulation. Single-sideband modulation at 250 MHz is used to spectrally isolate the control pulses from low-frequency noise of the AWG, which is filtered using a 175 MHz high-pass filter. The output of the vector source is passed through an amplifier (AR25S1G6 or similar), and through a MW switch (TriQuint TGS2355-SM, 40 dB on/off ratio) which is also controlled by the AWG. Video leakage noise of the switch is filtered using a 175 MHz high-pass filter. **RF electronics:** Radio-frequency (RF) pulses for nuclear spin control are directly synthesised by the AWG. This signal is passed through an RF amplifier (Analog Devices ADA4870), and filtered using a 52 kHz high-pass filter and 10 MHz low-pass filter. Finally, the MW and RF signals are combined using a diplexer and enter the cryostat. **Magnetic field:** Axial magnetic fields at the NV centre are produced using permanent neodymium magnets, which are mounted on motorised stages (Newport UTS100PP or similar). Coarse field alignment is performed by minimising the mean transition frequency of the $m_s = 0 \leftrightarrow -1$ and $m_s = 0 \leftrightarrow +1$ transitions. Fine field alignment (uncertainty of 0.07°) can be performed using thermal echo sequences as in Ch. 6. Figure adapted from Pfaff [1], Kalb [59], Abobeih [52].

2.5. SPIN RELAXATION AND COHERENCE OF NV CENTRES

With the ability to initialise and read-out the electronic spin state of a single NV centre via optical addressing, we now give an overview of the characteristic decoherence timescales for the ground-state spin. Measuring these processes requires manipulation of the electron qubit states, which is realised by resonant microwave driving. To achieve high-fidelity single-qubit gates, we employ spectrally-broad Hermite pulse envelopes[60,61] with maximal Rabi frequencies of ~25 MHz.

First, we consider spin relaxation (T_1) processes. Under ambient conditions, spin-lattice relaxation from two-phonon Raman processes limits the characteristic decay time, T_1, to ~5 ms[62,63]. However, with decreasing temperature, these Raman processes (scaling $\propto T^5$) are strongly suppressed. Below ~30 K, two-phonon Orbach processes are also frozen[63]. In ultrapure samples, cross-relaxation ('flip-flop' interactions) with other NV centres is negligible. Consequently, leakage of the microwave and optical control fields is often the dominant relaxation process at low temperatures. As discussed in the previous section, our hardware setups incorporate cascaded AOMs to ensure >100 dB on/off ratios for all lasers, and a microwave switch to suppress electronic noise (40 dB on/off ratio)[64]. In Figure 2.7(a), we show the measured spin-relaxation time for the device used in Chs. 5, 6, 7[64], averaged over the three ground-state spin states. The fitted decay time is $T_1 = 3.6(3) \cdot 10^3$ s. For practical purposes, this shows that spin relaxation of the NV^- electron spin plays no role in the results presented in this thesis. Surprisingly, the measured T_1 times even exceed theoretically-proposed limits set by single-phonon processes[65,66], suggesting that the exact spin-phonon dynamics are not yet fully understood.

We now turn to the coherence times of the electron spin, T_2^* and T_2. With natural abundance of ^{13}C isotopes, and working in the high B_z regime (see Sec. 2.7), Ramsey-type measurements of the electron spin reveal typical dephasing (T_2^*) times of ~5 μs. This dephasing arises from interactions between the NV and the surrounding nuclear spin environment, which effectively creates a quasi-static magnetic field at the point of the NV centre[67]. Due to the slow nature of the nuclear spin-bath dynamics, the use of dynamical decoupling sequences (repeated spin-echo pulses) can significantly extend the coherence time[64,68]. Applying such sequences to the same device as mentioned above, an arbitrary quantum state can be preserved for times >1 s (Fig. 2.7(b)). The electron-spin coherence can be extended by more than five orders of magnitude, reaching a T_2 time of 1.58(7) s after N=10240 pulses[64]. Crucially, this coherence time is sufficient to probe weakly coupled spins in the local spin environment (coupling $\ll 1/T_2^*$).

2.6. NV INTERACTING WITH A MANY-BODY SPIN-SYSTEM

The majority of quantum protocols rely on the ability to create and manipulate multi-qubit entangled states. Within the diamond lattice, a large number of nuclear spins magnetically couple to the NV electron spin. In this thesis, we will show that such nuclear spins can be used as a resource to realise prototype quantum network memories (Ch. 4), multi-qubit registers (Ch. 5), and quantum simulators (Ch. 7). In the following sections, I review the basic ideas and methods that those chapters are built upon,

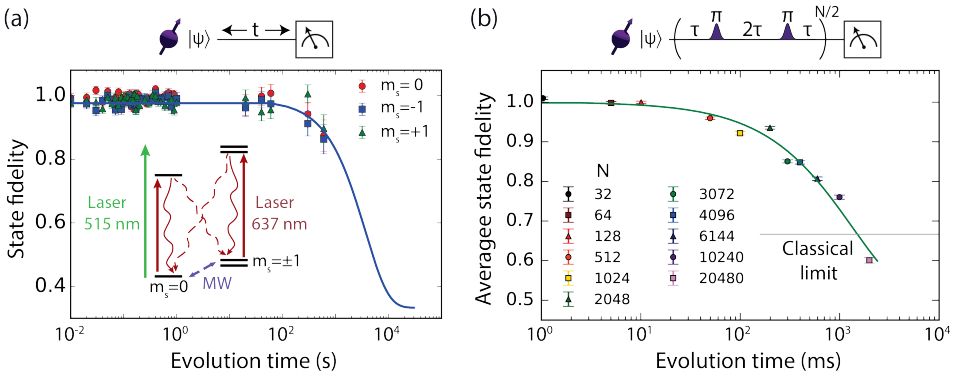

Figure 2.7: **Electron spin T_1 and T_2 times: (a)** Measured spin relaxation after preparing each of the three m_s spin projections and waiting for a time, t. Solid line is a fit to $f(t) = 1/3 + 2/3\exp[-t/T_1]$, from which we extract $T_1 = 3.6(3) \cdot 10^3$ s. The inset shows the potential spin-relaxation channels due to optical or microwave leakage (dashed lines). **(b)** Average state fidelity for the six cardinal states after a total evolution time, $t = 2N\tau$, following the sequence schematised above the figure. For each evolution time, the number of decoupling pulses N is optimised to maximise the mean state fidelity. The mean fidelity exceeds the classical bound of 2/3 for at least 1 s: the fitted exponential decay (solid line) crosses this bound at 1.46 s. All decoupling is performed at time values commensurate with the ^{13}C Larmor period to minimise interactions with the spin bath, and the π-pulse phases follow the XY8 scheme to mitigate pulse errors [69]. Figures adapted from Abobeih *et al.* [64].

beginning with the interaction Hamiltonian.

The complete spin-system comprises the intrinsic electron spin and ^{14}N nuclear spin of the NV centre, and a surrounding bath of (many) ^{13}C nuclear spins. We can write the total system Hamiltonian (for the electronic ground state) as a sum over the following contributions:

$$H_{\text{sys}} = H_{\text{e}} + H_{\text{N}} + H_{\text{e-N}} + H_{\text{C}} + H_{\text{e-C}} + H_{\text{C-C}} + H_{\text{N-C}}. \tag{2.3}$$

Here, H_{i} denote the Hamiltonian terms for the individual spin species: electron (e, H_{e} already given in Eq. 2.1), ^{14}N (N) and ^{13}C (C). $H_{\text{i-j}}$ denote the pairwise interactions.

For the nitrogen spin and its interaction with the electron spin, we have [21,70]:

$$\begin{aligned} H_{\text{N}} &= -Q I_{z,\text{N}}^2 + \gamma_{\text{N}}(\mathbf{B}\cdot\mathbf{I}_{\text{N}}), \\ H_{\text{e-N}} &= \mathbf{S}\cdot\mathbf{A}_{\text{N}}\cdot\mathbf{I}_{\text{N}} \approx A_{\parallel,\text{N}} S_z I_{z,\text{N}}. \end{aligned} \tag{2.4}$$

Here, $Q = 4.95$ GHz is the quadrupole splitting [70], $\gamma_{\text{N}} = 0.3077$ kHz/G is the nitrogen-spin gyromagnetic ratio. $\mathbf{I}_{\text{N}} = (I_{x,\text{N}}, I_{y,\text{N}}, I_{z,\text{N}})$ are the ^{14}N spin-1 operators. $\mathbf{A}_{\text{N}}$ is the hyperfine tensor for the electron-nitrogen interaction, with components $A_{\alpha\beta,\text{N}}$ for $\alpha,\beta \in \{x,y,z\}$. Under the secular approximation (denoted by the '$\approx$' sign throughout this section), this interaction reduces to a purely ZZ coupling of $A_{\parallel,\text{N}} = 2.2$ MHz.

The Hamiltonian terms for the ^{13}C spins and their interaction with the electron are given by:

$$\begin{aligned} H_{\text{C}} &= \sum_i \gamma_{\text{C}}(\mathbf{B}\cdot\mathbf{I}_{\text{C}}^{(i)}), \\ H_{\text{e-C}} &= \sum_i \mathbf{S}\cdot\mathbf{A}_{\text{C}}^{(i)}\cdot\mathbf{I}_{\text{C}}^{(i)} \approx \sum_i (A_{\parallel,C}^{(i)} S_z I_{z,\text{C}}^{(i)} + A_{\perp,C}^{(i)} S_z I_{x,\text{C}}^{(i)}). \end{aligned} \tag{2.5}$$

Here, $\gamma_C = 1.0705$ kHz/G is the carbon-spin gyromagnetic ratio. $\mathbf{I}_C^{(i)} = (I_{C,x}^{(i)}, I_{C,y}^{(i)}, I_{C,z}^{(i)})$ are the ^{13}C spin-1/2 operators acting on spin i. $\mathbf{A}_C^{(i)}$ is the hyperfine tensor for the interaction between the electron and the i^{th} ^{13}C spin. Formally, in the regime $(\gamma_C B_z \pm A_{\parallel,C}^{(i)}) \gg A_{\perp,C}^{(i)}$ as studied in this thesis, the term $A_{\perp,C}^{(i)} S_z I_{x,C}^{(i)}$ can also be discarded under the secular approximation. However, as we will see in the following section, carefully designed pulse sequences can enhance the contribution from this term as a tool for quantum control. Note that each ^{13}C spin experiences a unique interaction with the electron, owing to its individual lattice position. This interaction is composed of a combination of dipole-dipole and Fermi contact terms[71]. For simplicity, we denote the hyperfine component perpendicular to the NV-axis, $A_{\perp,C}^{(i)}$, to act along the x-axis of the given ^{13}C spin. That is, in this formulation, each ^{13}C spin has a unique coordinate system defined by the spatial orientation of its hyperfine interaction. In Ch. 6 we develop and demonstrate a method to recover the global coordinate system for a system of 27 ^{13}C spins.

Finally, we have dipolar interactions between nuclear spins:

$$\begin{aligned} H_{\text{C-C}} &= \sum_{i,j} \mathbf{I}_C^{(i)} \cdot \mathbf{C}_{i-j} \cdot \mathbf{I}_C^{(j)}, \\ H_{\text{N-C}} &= \sum_{i} \mathbf{I}_N \cdot \mathbf{C}_{N-j} \cdot \mathbf{I}_C^{(i)}. \end{aligned} \tag{2.6}$$

Here, $\mathbf{C}_{i-j}$ and $\mathbf{C}_{N-j}$ are the ^{13}C-^{13}C and ^{14}N-^{13}C interaction tensors. Note that, when combining all of the Hamiltonian contributions, the resulting ('effective') nuclear-nuclear interaction strengths are modified due to the presence of the electron spin[72,73]. This effect is discussed further in Ch. 6.

Owing to the difference in gyromagnetic ratios between the electron spin and the nuclear spins, the electron-nuclear coupling are typically 3-4 orders of magnitude stronger than nuclear-nuclear couplings (typically tens of kHz vs few-to-tens of Hz for the spins considered in this thesis).

2.7. TWO-QUBIT INTERACTIONS VIA DYNAMICAL DECOUPLING

As described in the previous section, the electron spin interacts with single nuclear spins through the hyperfine interaction. The first pioneering multi-qubit experiments in diamond utilised the electron spin along with the nitrogen nuclear spin (~ 2.2 MHz hyperfine coupling), and/or 1-2 strongly coupled ($A_{\parallel,C}^{(i)} \gg 1/T_2^*$) ^{13}C spins[42,56,74–78]. For such spins, hyperfine-split transitions can be resolved in the electron spin resonance (ESR) spectrum, and conditional logic can be realised by applying weak microwave pulses which selectively drive those individual transitions. However, the statistical likelihood of observing several strongly-coupled ^{13}C spins for a single NV becomes very small[78]. A breakthrough was made in 2012, where three independent experiments[79–81] showed that tailored dynamical decoupling (DD) sequences can be used to detect and control individual nuclear spins with coupling strengths $A_{\parallel,C}^{(i)} \ll 1/T_2^*$, providing access to many more spins surrounding a single NV centre. We will now discuss the mechanism behind this capability.

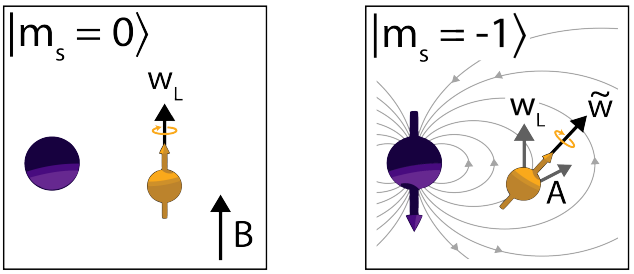

Figure 2.8: **Electron-^{13}C interaction:** for the $m_s = 0$ (left) and $m_s = -1$ (right) states of the electron spin (purple). In the $m_s = 0$ state, the hyperfine interaction is turned off, and the nuclear spin (yellow) simply precesses at the Larmor frequency (ω_L) around the axis set by the external magnetic field (**B**=(0,0,B_z)). In the $m_s = -1$ state, the hyperfine interaction is turned on. Under the secular approximation, the interaction is described by two terms which define the axis **A**=($A_\perp$,0,$A_\parallel$). The interaction leads to a shift of the ^{13}C precession frequency to $\tilde{\omega}$ (see text) and a tilting of the precession axis by an angle $\theta = \arctan(A_\perp/(\omega_L - A_\parallel))$ from the normal. Figure adapted from Ch. 4.

We first consider the Hamiltonian terms given in Eq. 2.5. For the electron spin and a single ^{13}C, we have[62,79]:

$$H = \omega_L I_z + A_\parallel S_z I_z + A_\perp S_z I_x. \tag{2.7}$$

Here, we assume a well-aligned magnetic field, and are considering the interaction picture for the electron energy splitting ($|0\rangle \leftrightarrow |1\rangle$). We have neglected the far-detuned $m_s = +1$ level. For simplicity, we have dropped the indices i and C from the hyperfine components and ^{13}C-spin operators. $\omega_L = \gamma_C B_z$ is the ^{13}C Larmor frequency.

Note that Eq. 2.7 can be written in the form:

$$\begin{aligned} H &= |0\rangle\langle 0|\, H_0 + |1\rangle\langle 1|\, H_1, \\ H_0 &= \omega_L I_z, \\ H_1 &= (\omega_L - A_\parallel) I_z + A_\perp I_x. \end{aligned} \tag{2.8}$$

That is, the nuclear spin experiences differing evolution dependent on the state of the electron spin (Fig. 2.8). In the $m_s = 0$ state, the nuclear spin undergoes simple Larmor precession around the axis defined by the external magnetic field (B_z, aligned along the NV axis). However, in the $m_s = -1$ state, the nuclear spin rotates around a tilted axis, at a modified frequency $\tilde{\omega} = \sqrt{(\omega_L - A_\parallel)^2 + A_\perp^2}$. Importantly, for non-zero $A_\perp$, the two rotation axes do not commute. Therefore, by toggling between these two axes at a frequency which is periodic with the nuclear spin precession dynamics (i.e., by toggling the electron spin state), it is possible to realise non-trivial rotations which are controlled by the initial state of the electron spin.

To realise these non-trivial rotations, we consider a dynamical decoupling sequence of primitive form: $(\tau - \pi - 2\tau - \pi - \tau)$. The corresponding nuclear spin unitary evolution is given by[62,79]:

$$\begin{aligned} V_0 &= \exp[-iH_0\tau]\cdot\exp[-2iH_1\tau]\cdot\exp[-iH_0\tau] = \exp[-i\theta(\mathbf{I}\cdot\mathbf{n_0})], \\ V_1 &= \exp[-iH_1\tau]\cdot\exp[-2iH_0\tau]\cdot\exp[-iH_1\tau] = \exp[-i\theta(\mathbf{I}\cdot\mathbf{n_1})]. \end{aligned} \tag{2.9}$$

Here, the subscript denotes the initial state of the electron prior to application of the sequence. $\mathbf{n}_\psi$ is the effective rotation axis about which the nuclear spin has rotated by an angle θ at the end of the primitive. Critically, the rotation axes are dependent on the choice of decoupling time, τ. If τ is perfectly resonant with the dynamics of a particular nuclear spin, the axes $\mathbf{n}_\psi$ are anti-parallel ($\mathbf{n_0} \cdot \mathbf{n_1}$ = -1). Under this condition, and setting $\theta = \pi/2$, the canonical form of a maximally entangling controlled-rotation gate ('CRx($\pm\pi/2$)' gate) is realised between the electron and nuclear spin:

$$U_{\mathrm{CRx}}(\pm\pi/2) = |0\rangle\langle 0| \otimes R_x(+\pi/2) + |1\rangle\langle 1| \otimes R_x(-\pi/2), \tag{2.10}$$

where $R_x(\theta)$ is a rotation about the x-axis by an angle θ. In the high-field regime ($\omega_L \gg A_\perp, A_\parallel$), this condition is met for:

$$\tau_k \approx \frac{(2k-1)\pi}{2\omega_L - A_\parallel} \tag{2.11}$$

with integer k > 0.

We make a few comments on these DD-mediated interactions. First, meeting the exact resonance condition is not a strict requirement for a maximally-entangling electron-nuclear gate. Writing the rotation axes as $\mathbf{n}_\psi = n_{x,\psi}\hat{x} + n_{z,\psi}\hat{z}$, it can be shown that any set of axes satisfying $n_{0,x} = -n_{1,x}$ and $|n_x|>|n_z|$ is sufficient to reproduce Eq. 2.10 (up to a single-qubit z-rotation on the nuclear spin)[82]. Thus it is possible to work at moderately detuned τ values if desired.

Second, in the above example, we set $\theta = \pi/2$. In practice, the rotation angle θ is dependent on both the number of decoupling pulses, N ($N/2$ applications of V_ψ), and the perpendicular hyperfine coupling component, $A_\perp$. In the high-field regime, and at exact resonance, this relationship is described by[79] $\theta = (N \cdot A_\perp)/\widetilde{\omega}$. As N takes integer values, the set of achievable rotation angles for a given τ value is discretised. Such discretisation errors can typically be mitigated by choosing an appropriate (detuned) τ value. The smaller the value of $A_\perp$, the slower the gate speed. For small $A_\perp$, this leads to reduced control fidelities due to nuclear spin dephasing within the gate duration.

Finally, we note that the choice of external magnetic field plays a role in the DD gate dynamics. We focus on the high-field regime. Here, the number of decoupling pulses required to realise the $\pi/2$ rotation scales linearly with the magnetic field[79]. While the required interpulse delay scales as the inverse of the magnetic field, and so the absolute gate times should not change significantly, a large number of pulses can lead to loss of fidelity due to pulse errors. Moreover, the linewidth of the resonance also scales inversely with the magnetic field. At very high magnetic fields, sub-ns temporal resolution is required to accurately address the resonances. For these reasons, we choose to work at a magnetic field of 403 G, which offers a good trade-off between these factors. This field choice also remains far from the NV ground-state level anti-crossing at ~1024 G[83], and ensures that the NV MW transitions ($m_s = 0 \leftrightarrow m_s = -1$, $m_s = 0 \leftrightarrow m_s = +1$) are far from degeneracy and so free of crosstalk which would induce leakage out of the qubit subspace.

In Ch. 5, we develop novel two-qubit gates which combine resonant radio-frequency driving with similar dynamical decoupling sequences ('DDrf' gates) to enable high-fidelity operations to spins with weak $A_\perp$ ($\ll \widetilde{\omega}$). This approach may enable high-magnetic field operation with greater ease in future work.

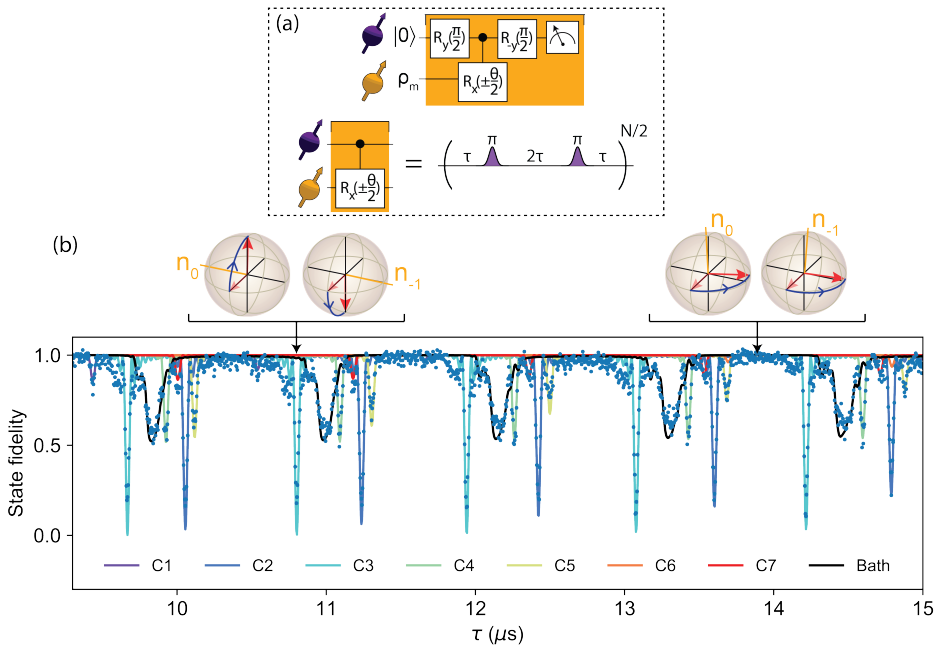

Figure 2.9: **Dynamical decoupling (DD) spectroscopy:** (a) Quantum circuit for DD spectroscopy. At particular τ values, a dynamical decoupling sequence of N π pulses realises entangling interactions with individual nuclear spins (controlled-$R_x(\pm\theta/2)$ gates, Eq. 2.10), resulting in a loss of coherence (see text). (b) Measured DD spectrum for $N = 32$ at a magnetic field of 403 G. Solid lines are fitted signals for seven individual ^{13}C spins and a bath of 200 generated spins with sampled hyperfine couplings < 10 kHz[64]. Bloch spheres presented above the data show the nuclear spin rotation axes $\mathbf{n}_\psi$ (see text) for C3 upon resonance (τ ~10.8 μs) and at a value commensurate with the Larmor period (τ ~13.9 μs). At resonance the $\mathbf{n}_\psi$ are anti-parallel, enabling maximally entangling operations with the electron spin. Off-resonance, the nuclear spin undergoes simple precession around (or close to) the z-axis, and no entanglement is generated. Figure (b) adapted from Taminiau *et al.*[62] and Abobeih *et al.*[64].

2.8. DYNAMICAL DECOUPLING SPECTROSCOPY

For an unstudied NV centre to be used for multi-qubit experiments, the first step is to perform preliminary (coarse) characterisation of the nuclear spin environment. This gives information about individual ^{13}C spins and the suitable τ values for their DD-based control. A detailed characterisation will be performed in Ch. 6. In this first approach, we use the following scheme, labelled dynamical decoupling spectroscopy.

The sequence is shown in Figure 2.9(a). First, we prepare the electron in a superposition state by spin pumping and subsequently applying a MW $\pi/2$ pulse. Next, we apply a number $N/2$ repetitions of the decoupling primitive (N π pulses). Finally, we measure the remaining coherence by applying a second $\pi/2$ pulse and then reading out the electron spin optically. In Figure 2.9(b), we plot the measured coherence as a function of the dynamical decoupling delay, τ. We observe a rich structure hosting a number of periodically-occurring coherence dips. Such collapses arise due to entanglement between the electron spin and nuclear spins at the given τ value.

To formally describe the measured signal, we now revert to the scenario of the electron spin interacting with a number of nuclear spins. The probability to retrieve the initial superposition state is given by[79] $P_x = (M+1)/2$, where:

$$\begin{aligned} M &= \prod_i M_i \\ M_i &= \mathrm{Re}[\mathrm{Tr}[V_{0,i}^{N/2}(V_{1,i}^{N/2})^\dagger]]. \end{aligned} \tag{2.12}$$

M can be written in this form, as a product of single-nuclear-spin M_i, under the approximation that the nuclear spins are non-interacting. In the case of stronger nuclear-nuclear interactions, this no longer holds. Such cases are analysed in detail in Refs.[54,64,84,85], but in this work the approximation only incurs minor perturbations to the signal.

From the measured spectrum, it is already possible to identify candidate single spins which can be well controlled. Points at which $M = 0$ indicate complete loss of coherence of the electron. In the case of an interaction with a single spin, this corresponds to a maximally-entangling operation: a gate of the form of Eq. 2.10 has been achieved. Overlapping or very broad resonances (such as those shown in black in Fig. 2.9(b)) usually indicate interactions with multiple spins, which is undesired for selective qubit control. Therefore, we look for well isolated and narrow resonances, such as the highlighted resonance at $\tau \sim 10.8$ μs in Figure 2.9(b).

There are a number of methods by which one can extract the nuclear spin hyperfine parameters from DD spectra to gain information about the nuclear spin environment. The simplest is to measure these spectra for a wide range of τ and a few values of N. It is then possible to match simulated signals with the measured values. This gives a reasonable estimate for the hyperfine parameters of the most strongly-coupled ^{13}C spins, but is a relatively cumbersome and otherwise imprecise approach. In Ch. 6, we develop an alternate methodology to precisely characterise a system of 27 ^{13}C spins. Since that work, the analysis of DD spectra has been revisited, using novel algorithmic[86] and deep-learning methods[87]. Remarkably, using the latter approach, accurate extraction of the hyperfine parameters of at least 23 of those 27 nuclear spins was achieved. While this technique does not acquire the nuclear-nuclear couplings (which *are* obtained by the methods of Ch. 6), it is a powerful tool for efficient preliminary characterisation of the nuclear spin environments of new NVs.

Note that there are a number of alternate approaches to perform nuclear-spin spectroscopy, each with their own advantages and drawbacks. For example, this task can be performed using DDrf gates as shown in Ch. 5, or via weak measurement sequences[88,89].

2.9. UNIVERSAL CONTROL OF ^{13}C SPINS

In the previous two sections, we have discussed how dynamical decoupling can enable electron-nuclear entangling gates, and how these are identified in practice. We now discuss how to implement universal single- and two-qubit control. We will first show how read-out and initialisation of nuclear spins can be performed by coherently mapping spin states to-and-from the electron spin, before discussing single-qubit operations and two-qubit gate optimisation.

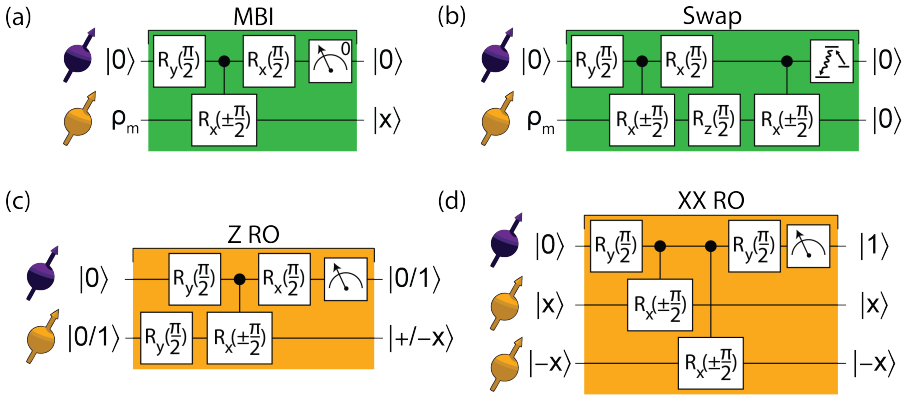

Figure 2.10: **Quantum circuits for ^{13}C initialisation and read-out:** For all circuits, the output states correspond to the result of the sequence applied to the corresponding input states, assuming perfect operations. (a) Measurement-based initialisation. This sequence of gates maps the x-basis spin projection of the nuclear-spin to the z-basis of the electron, after which a measurement heralds the $|x\rangle$ nuclear state conditioned on the outcome '0' . (b) Swap initialisation. Compared with (a), an additional single-qubit gate and two-qubit gate realise a partial-swap operation of the electron and nuclear spin states, deterministically preparing the nuclear spin in the $|0\rangle$ state without the need for conditioning on measurement. Finally, the electron spin is reset. (c) Z-basis nuclear-spin read-out. Following the same protocol as in (a), but with an additional single-qubit operation to map the nuclear-spin z-basis to the x-basis for read-out, and utilising full (unconditional) measurement of the electron spin to reveal the nuclear state. (d) Multi-qubit read-out of the XX operator. Concatenating two-qubit gates between the electron and two separate nuclear spins within the sequence reveals information about the joint state of the two nuclear spins. In this case, the XX-parity is odd, and so the electron spin outcome is $|1\rangle$.

2.9.1. INITIALISATION

Consider the electron spin interacting with only a single nuclear spin, under application of the sequence shown in Figure 2.10(a). After spin pumping the electron spin, we have the initial state $\rho_{\text{init}} = |0\rangle\langle 0|_e \otimes \rho_{m,C}$. The nuclear spin is initially mixed ($\rho_m = I/2$), as we work in the regime $k_B T \gg \hbar\omega_L$.

In succession, we then apply $R^{\pi/2}_{y,e}$ (a $\pi/2$ pulse around the y-axis on the electron spin), the two-qubit entangling gate CRx($\pm\pi/2$), and finally $R^{\pi/2}_{x,e}$. The final state is given by[62,90]:

$$\rho_{\text{MBI}} = (|0\rangle\langle 0|_e \otimes |x\rangle\langle x|_C + |1\rangle\langle 1|_e \otimes |-x\rangle\langle -x|_C)/2, \tag{2.13}$$

where $|\pm x\rangle = (|0\rangle \pm |1\rangle)/\sqrt{2}$. That is, the electron and nuclear spin states are classically correlated. Measuring the state of the electronic spin projects the nuclear spin in the state $|x\rangle_C$ (for the outcome $|0\rangle_e$) or $|-x\rangle_C$ (for $|1\rangle_e$). We denote this scheme 'measurement-based initialisation' (MBI).

To maximise the nuclear spin initialisation fidelity, we here use a conditional approach for the electron spin measurement (as discussed in Sec. 2.2). Specifically, we proceed with the experiment only upon detecting a single photon (F_{CRO} >99%). Furthermore, we turn off the excitation light within 2 μs of such an event to increase the projectivity. There is then a very high probability (also >99%[51]) that the electron spin is indeed in the $|0\rangle$ state after measurement, minimising dephasing of the nuclear spin.

While this approach can enable high fidelity initialisation of the $|x\rangle_C$ state, conditioning on a certain outcome makes it probabilistic. Therefore, it does not scale well when initialising a number of spins. An alternative approach is to apply the scheme shown in Figure 2.10(b), which realises a swap gate. Taking the state ρ_{MBI}, we apply a single-qubit rotation $R^{\pi/2}_{z,C}$ (method described below) followed by another CRx($\pm\pi/2$) gate. The final state is now[62,90]:

$$\rho_{\text{swap}} = (|0\rangle\langle 0|_e \otimes |0\rangle\langle 0|_C + |1\rangle\langle 1|_e \otimes |0\rangle\langle 0|_C)/2. \tag{2.14}$$

The nuclear spin is deterministically prepared in the $|0\rangle_C$ state, while the electron spin is left in a mixed state. We thus complete the protocol by spin-pumping the electron back into a known state with high fidelity.

Beyond the methods described here, alternative schemes based on polarisation transfer ('dynamic nuclear polarisation') can also be used to initialise nuclear spins[16,91,92]. Such techniques are utilised and discussed in Ch. 7.

2.9.2. READ-OUT

As can be inferred from the name 'measurement-based initialisation', the scheme of Figure 2.10(a) also enables read-out of the nuclear spin via the electron spin: an 'ancilla-based' measurement[93].

We consider an arbitrary nuclear spin state that we wish to measure along the x-basis, with the electron prepared in the $|0\rangle_e$ state prior to this measurement:

$$\rho_{\text{meas}} = \rho_e \otimes \rho_C = \begin{pmatrix} 1 & 0 \\ 0 & 0 \end{pmatrix} \otimes \begin{pmatrix} a & b \\ c & d \end{pmatrix}. \tag{2.15}$$

Here, like ρ_e, ρ_C is Hermitian, positive, and has unit trace, but the parameters $\{a,b,c,d\}$ are otherwise unconstrained[93].

We then apply the same sequence of operations as for MBI (Fig. 2.10(a)). However, we now assign a measurement outcome in every experimental shot (rather than discarding instances in which a photon is not detected). The nuclear-spin single-shot read-out fidelity is thus bounded by F_{SSRO} (Eq. 2.2). Prior to the read-out of the electron, the electronic state (after tracing over the nuclear spin) is:

$$\rho_{\mathrm{RO,e}} = \frac{1}{2}\begin{pmatrix} 1+b+c & 0 \\ 0 & 1-b-c \end{pmatrix} \tag{2.16}$$

Reading out the electron spin, we find $\langle Z \rangle = \mathrm{Tr}[\sigma_z \rho_{\mathrm{RO,e}}] = (b+c)$, where σ_i are the Pauli matrices. This is the same expectation value as expected from an ideal x-basis measurement on the arbitrary nuclear state ρ_C, showing that the mapping scheme works as expected. Measuring an arbitrary nuclear spin basis is achieved by rotating the target basis to the x-basis using an appropriate single-qubit gate: an example for a z-basis measurement is shown in Figure 2.10(c).

Alongside single-qubit measurements, it is possible to measure multi-qubit operators by concatenating two-qubit gates within the sequence, as exemplified for the $\langle XX \rangle$ operator in Figure 2.10(d). The compilation of these measurements is described in detail by Cramer *et al.*,[51,82] and Abobeih *et al.*[52]. Note that the capability to perform multi-qubit measurements in a non-destructive manner (called parity, or stabiliser measurements) lies at the heart of quantum error correction, for which demonstrations of the key elements have been achieved within this system[43,51,52].

In Ch. 7 we also develop a novel read-out scheme for nuclear spins which can not be addressed using two-qubit gates due to weak electron-nuclear couplings. This scheme concatenates the DD-based read-out described here with a secondary mapping sequence which utilises the nuclear-nuclear couplings to transfer the spin projection of a distant spin to one with a stronger electron-nuclear coupling.

2.9.3. SINGLE-QUBIT ROTATIONS

Strong microwave driving enables high-fidelity manipulation of the electron spin independent of the state of the nuclear spins (Sec. 2.5), while tailored dynamical decoupling sequences enable electron-nuclear two-qubit gates (Sec. 2.7). Alongside these gates, universal control of an electron-nuclear register requires single-qubit operations on the nuclear spins, which we will discuss here.

The critical requirement for single-qubit gates is that they should not create entanglement. So far, for the nuclear spins, we have only encountered one such case: in Eq. 2.10 we see that we can perform an $R^{\pi}_{x,C}$ gate for $\theta = \pi$. For any other θ, however, this gate is entangling with the electron spin. The question arises, therefore, whether it is possible to create dynamical decoupling sequences which preserve the electron spin coherence while generating unconditional nuclear spin rotations. Within the framework presented in Sec. 2.7, it can be shown that there *are* τ values for which the $\mathbf{n}_\psi$ are parallel ($\mathbf{n}_0 \cdot \mathbf{n}_1 = 1$) and have non-zero x-components[62]. At the resonance condition:

$$\tau_m \approx \frac{m\pi}{2\omega_L - A_\parallel} \tag{2.17}$$

for even integer m, we have $n_{0,x} = n_{1,x} = \pm 1$, where the sign alternates from an initial value of $+1$ at $m = 2$ (-1 at $m = 4$ and so forth). The rotation angle θ is again dependent

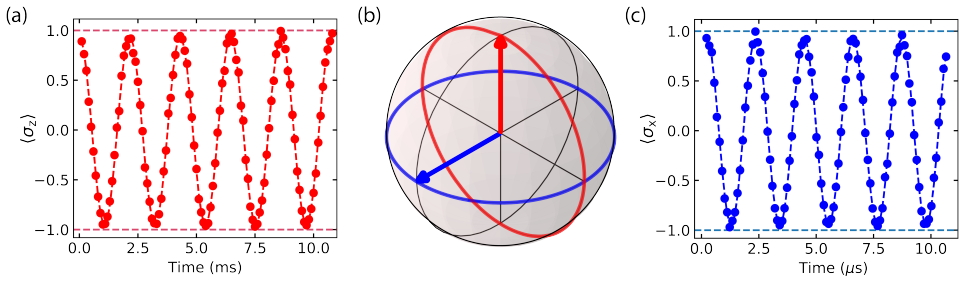

Figure 2.11: **^{13}C single-qubit gates:** (a) RF driving of a single nuclear spin around the x-axis after preparation in the $|\uparrow\rangle$ state. The fitted Rabi frequency is 464.2(1) Hz. (b) Bloch sphere evolution of the nuclear spin for Rabi driving (red, see (a)) and free precession (blue, see (c)). (c) Free precession of a single nuclear spin around the ~z-axis after preparation in the $|x\rangle$ state. The fitted precession frequency is 470.3(2) kHz. For both (a) and (c), the electron remains in the $|1\rangle$ state during the ^{13}C evolution time. The data is corrected for imperfect optical read-out of the electron spin but not for gate errors in the preparation and read-out of the ^{13}C spin. Error-bars are smaller than the markers.

on both the number of decoupling pulses N and the perpendicular hyperfine coupling $A_\perp$ of the targeted spin. As for conditional rotations, the range of possible θ depends on the values of n_x. For realising unconditional $\pi/2$ gates, it is possible to work at a detuned τ value, for which the desired rotation will be achieved up to an additional single-qubit phase. Note that, while the effective rotation axis is along x (in the frame of the target nuclear spin), arbitrary rotations can be achieved by compilation with $R^{\phi}_{z,C}$ gates (see below). In Ch. 5, we will show that DDrf gates also enable $R^{\theta}_{\phi,C}$ gates.

$R^{\phi}_{z,C}$ gates can also be implemented via dynamical decoupling sequences. This is achieved for τ values for which the $\mathbf{n}_\psi$ are again parallel, but now lie along the z-axis (i.e. have negligible x-components). Such a condition is generically met for τ values close to integer multiples of the Larmor period, $\tau_L = 2\pi/\omega_L$ (Fig. 2.9(b)). For a given number of decoupling pulses, N, the acquired phase, ϕ, is:

$$\phi = (2\omega_L - A_\parallel)N\tau \tag{2.18}$$

Together, all the discussed operations realise a universal gate-set: arbitrary quantum circuits can be implemented on electron-nuclear systems, independent of the states of each spin. However, we can also consider scenarios in which the electron spin is only being used as an ancilla qubit. That is, it is not hosting quantum information itself, and can be freely prepared in a chosen state. In such cases, nuclear spin single-qubit gates can also be implemented via simpler means.

For the $R^{\theta}_{\phi,C}$ gates, we follow two further approaches. First, we revisit the conditional DD resonances (Eq. 2.11). Notably, by preparing the electron spin in either $|0\rangle$ or $|1\rangle$ prior to the DD sequence, it does not entangle with the target spin, enabling single-qubit gates also for these τ values. This additional flexibility can reduce crosstalk.

Second, we can use direct RF driving, without any decoupling pulses. If the electron is prepared in the $|1\rangle$ state prior to the pulse, each nuclear spin can be addressed individually via its unique hyperfine shift ($\approx A_\parallel$). The RF drive is synthesized via the AWG

with an arbitrary phase, duration and amplitude (arbitrary ϕ, θ). This has a number of benefits. First, the Rabi frequency only weakly depends on $A_\perp$ [74], such that control of ^{13}C spins with weak perpendicular couplings is still possible. Second, the gates do not require dynamical decoupling pulses on the electron spin, which are a potential source of infidelity. Finally, it is easier to achieve resonance using RF driving than it is for DD sequences, especially at larger magnetic fields where the DD resonances become increasingly narrow. In Figure 2.11(a), we show high-fidelity RF driving of a single ^{13}C spin. The measured Rabi oscillations enable calibration of pulse durations (or amplitudes) to implement desired $R^\theta_{\phi,C}$ rotations.

$R^\phi_{z,C}$ gates can be implemented by preparing the electron in the $|0\rangle$ or $|1\rangle$ state and subsequently waiting. The nuclear spin then precesses either around the z-axis at ω_L, or around a slightly tilted axis at $\widetilde{\omega}$ (Sec. 2.7). This approach also avoids the need for decoupling pulses. In Figure 2.11(c), we show free precession of a single ^{13}C spin, from which arbitrary $R^\phi_{z,C}$ rotations can be calibrated.

Note that in this thesis, the nuclear spins phases are generally defined in the laboratory frame (unlike for the electron spin, where the phases are defined with respect to a free-running microwave oscillator), and so each spin is acquiring phase at all times. The initial phase of a nuclear spin superposition state is defined by the operation used to create it. Thereafter, the relative phase is tracked at a rate dependent on whether the electron is in a known eigenstate or is being decoupled. This ensures that all gates maintain well-defined phase relations.

A summary of the single- and two-qubit gate schemes is given in Table 2.2.

Gate type	Technique	Gate duration	Conditions
$R^\theta_{\phi,e}$	MW driving	$\propto \Omega_{\text{Rabi}}$, ~100 ns	Any
$R^\phi_{z,e}$	Virtual	-	Compiled via MW phase (I/Q mod)
$R^\theta_{x,C}$	DD	$\propto A_\perp$, ~1 ms	Any
$R^\theta_{\phi,C}$	DDrf (Ch. 5)	$\propto \Omega_{\text{Rabi}}$, ~1 ms	Any
$R^\theta_{\phi,C}$	RF driving	$\propto \Omega_{\text{Rabi}}$, ~1 ms	Electron in $\|1\rangle$
$R^\phi_{z,C}$	DD	$\propto \gamma_C B_z$, ~1 μs	Any
$R^\phi_{z,C}$	Wait	$\propto \gamma_C B_z$, ~1 μs	Electron in known eigenstate
$R^\phi_{z,C}$	Virtual	-	Compiled via RF phase (AWG)
CRx(θ)	DD	$\propto A_\perp$, ~1 ms	Any
CRϕ(θ)	DDrf (Ch. 5)	$\propto \Omega_{\text{Rabi}}$, ~1 ms	Any

Table 2.2: Summary of gate operations, the techniques used for their application, their associated durations, and the conditions under which they may be used.

2.9.4. TWO-QUBIT GATE OPTIMISATION

The toolset described in the previous sections also provides a mechanism for calibrating electron-nuclear two-qubit gates. As both initialisation and read-out of the ^{13}C spins are based upon two-qubit operations, their combined signal gives information about those

gate fidelities. This signal can be used as a proxy for the two-qubit gate fidelity.

The calibration sequence is shown in Figure 2.12(a). After identification of promising resonances from DD spectroscopy, we estimate the parameters which realise a CRx($\pm\pi/2$) gate. This gate is then used in two ancilla-based measurements of the nuclear spin. The first measurement corresponds to MBI (using a conditional read-out), whereas the second measurement uses complete single-shot read-out. For the second measurement, we measure along both the x- and y-basis of the nuclear spin. The combined outcomes give the coherence, $C = \sqrt{\langle X\rangle^2 + \langle Y\rangle^2}$, giving the full signal independent of any nuclear spin z-rotations induced by a detuned two-qubit gate. We repeat this experiment for a range of τ and N values close to the identified resonance. Figure 2.12(b) shows example outcomes from this measurement, from which an optical set of parameters are chosen to maximise the gate fidelity.

At present the maximum DD-based two-qubit gate fidelities achieved are ~ 99% [58,94]. These numbers are not thought to be fundamentally limited, but rather arise from a combination of factors including residual electron spin decoherence (primarily from electronic noise), nuclear spin decoherence (which may be mitigated by nuclear spin bath polarisation [16,91,92,95]) and crosstalk (which may be suppressed by improved gate designs [96–99]). In Chs. 4 and 5 we will further discuss these effects alongside the decoherence mechanisms of individual ^{13}C spins, which exhibit rich physics due to the presence of the frozen core phenomenon [94,100,101].

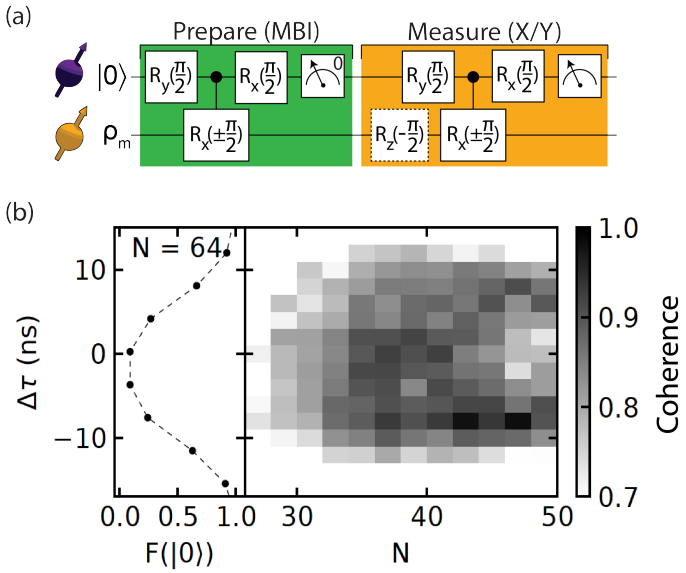

Figure 2.12: **Two-qubit gate optimisation:** (a) Quantum circuit used to initialise a single ^{13}C spin and measure the resulting expectation values $\langle X\rangle$ and $\langle Y\rangle$. For the latter basis, the dashed $R_z(-\pi/2)$ gate is incorporated. The '0' in the first electron measurement indicates that the sequences continues conditioned on receiving that outcome. (b) Measured coherence ($C = \sqrt{\langle X\rangle^2 + \langle Y\rangle^2}$) as a function of the number of decoupling pulses N and the adjustment of the interpulse delay from resonance, $\Delta\tau$. Combinations which produce the highest coherence correspond to the highest-fidelity two-qubit gates. Figure adapted from Kalb [59].

REFERENCES

[1] W. Pfaff, *Quantum measurement and entanglement of spin quantum bits in diamond,* Ph.D. Thesis, TUDelft (2013).

[2] H. Bernien, *Control, measurement and entanglement of remote quantum spin registers in diamond,* Ph.D. Thesis, TUDelft (2014).

[3] D. D. Awschalom, R. Hanson, J. Wrachtrup and B. B. Zhou, *Quantum technologies with optically interfaced solid-state spins,* Nat. Photonics **12**, 516 (2018).

[4] A. Gruber *et al., Scanning confocal optical microscopy and magnetic resonance on single defect centers,* Science **276**, 2012 (1997).

[5] S. Chakravarthi *et al., Window into nv center kinetics via repeated annealing and spatial tracking of thousands of individual nv centers,* Phys. Rev. Mater. **4**, 023402 (2020).

[6] D. Twitchen *et al., Electron paramagnetic resonance (epr) and optical absorption studies of defects created in diamond by electron irradiation damage at 100 and 350 k,* Physica B Condens. **273**, 628 (1999).

[7] B. Campbell and A. Mainwood, *Radiation damage of diamond by electron and gamma irradiation,* Phys. Status Solidi A **181**, 99 (2000).

[8] M. Ruf *et al., Optically coherent nitrogen-vacancy centers in micrometer-thin etched diamond membranes,* Nano Lett. **19**, 3987 (2019).

[9] Y.-C. Chen *et al., Laser writing of coherent colour centres in diamond,* Nat. Photonics **11**, 77 (2017).

[10] Y.-C. Chen *et al., Laser writing of individual nitrogen-vacancy defects in diamond with near-unity yield,* Optica **6**, 662 (2019).

[11] C. Stephen *et al., Deep three-dimensional solid-state qubit arrays with long-lived spin coherence,* Phys. Rev. Appl. **12**, 064005 (2019).

[12] Y. Chu *et al., Coherent optical transitions in implanted nitrogen vacancy centers,* Nano Lett. **14**, 1982 (2014).

[13] S. B. van Dam *et al., Optical coherence of diamond nitrogen-vacancy centers formed by ion implantation and annealing,* Phys. Rev. B **99**, 161203 (2019).

[14] M. Kasperczyk *et al., Statistically modeling optical linewidths of nitrogen vacancy centers in microstructures,* Phys. Rev. B **102**, 075312 (2020).

[15] A. E. Rugar *et al., Generation of tin-vacancy centers in diamond via shallow ion implantation and subsequent diamond overgrowth,* Nano Lett. **20**, 1614 (2020).

[16] T. Unden *et al., Coherent control of solid state nuclear spin nano-ensembles,* NPJ Quantum Inf. **4**, 1 (2018).

[17] K. Ohno *et al., Engineering shallow spins in diamond with nitrogen delta-doping,* Appl. Phys. Lett. **101**, 082413 (2012).

[18] B. A. Myers *et al., Probing surface noise with depth-calibrated spins in diamond,* Phys. Rev. Lett. **113**, 027602 (2014).

[19] J. R. Maze *et al., Properties of nitrogen-vacancy centers in diamond: the group theoretic approach,* New J. Phys. **13**, 025025 (2011).

[20] B. Hensen, *Measurement-based quantum computation with the nitrogen-vacancy centre in diamond,* M.Sc. Thesis, TUDelft (2011).

[21] M. W. Doherty *et al., The nitrogen-vacancy colour centre in diamond,* Phys. Rep. **528**, 1 (2013).

[22] N. B. Manson *et al.,* NV—N+ *pair centre in 1b diamond,* New J. Phys. **20**, 113037 (2018).

[23] G. Waldherr *et al., Dark states of single nitrogen-vacancy centers in diamond unraveled by single shot nmr,* Phys. Rev. Lett. **106**, 157601 (2011).

[24] N. Aslam, G. Waldherr, P. Neumann, F. Jelezko and J. Wrachtrup, *Photo-induced ionization dynamics of the nitrogen vacancy defect in diamond investigated by single-shot charge state detection,* New J. Phys. **15**, 013064 (2013).

[25] M. S. Barson, E. Krausz, N. B. Manson and M. W. Doherty, *The fine structure of the neutral nitrogen-vacancy center in diamond,* Nanophotonics **8**, 1985 (2019).

[26] S. Baier *et al., Orbital and spin dynamics of single neutrally-charged nitrogen-vacancy centers in diamond,* Phys. Rev. Lett. **125**, 193601 (2020).

[27] J. Weber *et al., Quantum computing with defects,* Proc. Natl. Acad. Sci. **107**, 8513 (2010).

[28] M. Doherty *et al., Theory of the ground-state spin of the nv- center in diamond,* Phys. Rev. B **85**, 205203 (2012).

[29] B. J. Hensen, *Quantum nonlocality with spins in diamond,* Ph.D. Thesis, TUDelft (2016).

[30] V. Ivády, I. A. Abrikosov and A. Gali, *First principles calculation of spin-related quantities for point defect qubit research,* NPJ Comput. Mater. **4**, 1 (2018).

[31] G. Fuchs, V. Dobrovitski, D. Toyli, F. Heremans and D. Awschalom, *Gigahertz dynamics of a strongly driven single quantum spin,* Science **326**, 1520 (2009).

[32] G. De Lange, Z. Wang, D. Riste, V. Dobrovitski and R. Hanson, *Universal dynamical decoupling of a single solid-state spin from a spin bath,* Science **330**, 60 (2010).

[33] K.-M. C. Fu *et al., Observation of the dynamic jahn-teller effect in the excited states of nitrogen-vacancy centers in diamond,* Phys. Rev. Lett. **103**, 256404 (2009).

[34] R. Albrecht, A. Bommer, C. Deutsch, J. Reichel and C. Becher, *Coupling of a single nitrogen-vacancy center in diamond to a fiber-based microcavity,* Phys. Rev. Lett. **110**, 243602 (2013).

[35] P. Tamarat *et al.*, *Stark shift control of single optical centers in diamond,* Phys. Rev. Lett. **97**, 083002 (2006).

[36] L. Bassett, F. Heremans, C. Yale, B. Buckley and D. Awschalom, *Electrical tuning of single nitrogen-vacancy center optical transitions enhanced by photoinduced fields,* Phys. Rev. Lett. **107**, 266403 (2011).

[37] M. W. Doherty, N. B. Manson, P. Delaney and L. C. Hollenberg, *The negatively charged nitrogen-vacancy centre in diamond: the electronic solution,* New J. Phys. **13**, 025019 (2011).

[38] H. Bernien *et al.*, *Two-photon quantum interference from separate nitrogen vacancy centers in diamond,* Phys. Rev. Lett. **108**, 043604 (2012).

[39] N. Kalb, P. C. Humphreys, J. Slim and R. Hanson, *Dephasing mechanisms of diamond-based nuclear-spin memories for quantum networks,* Phys. Rev. A **97**, 062330 (2018).

[40] M. L. Goldman *et al.*, *Phonon-induced population dynamics and intersystem crossing in nitrogen-vacancy centers,* Phys. Rev. Lett. **114**, 145502 (2015).

[41] M. L. Goldman *et al.*, *State-selective intersystem crossing in nitrogen-vacancy centers,* Phys. Rev. B **91**, 165201 (2015).

[42] L. Robledo *et al.*, *High-fidelity projective read-out of a solid-state spin quantum register,* Nature **477**, 574 (2011).

[43] S. B. van Dam, J. Cramer, T. H. Taminiau and R. Hanson, *Multipartite entanglement generation and contextuality tests using nondestructive three-qubit parity measurements,* Phys. Rev. Lett. **123**, 050401 (2019).

[44] S. Loenen, *Improving single-shot readout for diamond quantum processors,* M.Sc. Thesis, TUEindhoven (2019).

[45] S. Sangtawesin *et al.*, *Origins of diamond surface noise probed by correlating single-spin measurements with surface spectroscopy,* Phys. Rev. X **9**, 031052 (2019).

[46] J. Hadden *et al.*, *Strongly enhanced photon collection from diamond defect centers under microfabricated integrated solid immersion lenses,* Appl. Phys. Lett. **97**, 241901 (2010).

[47] H. Bernien *et al.*, *Heralded entanglement between solid-state qubits separated by three metres,* Nature **497**, 86 (2013).

[48] T. Yeung, D. Le Sage, L. M. Pham, P. Stanwix and R. L. Walsworth, *Anti-reflection coating for nitrogen-vacancy optical measurements in diamond,* Appl. Phys. Lett. **100**, 251111 (2012).

[49] P. C. Humphreys *et al.*, *Deterministic delivery of remote entanglement on a quantum network,* Nature **558**, 268 (2018).

[50] M. Pompili *et al.*, *Realization of a multinode quantum network of remote solid-state qubits,* Science **372**, 259 (2021).

[51] J. Cramer *et al.*, *Repeated quantum error correction on a continuously encoded qubit by real-time feedback,* Nat. Commun. **7**, 1 (2016).

[52] M. Abobeih, *From atomic-scale imaging to quantum fault-tolerance with spins in diamond,* Ph.D. Thesis, TUDelft (2021).

[53] M. Degen *et al.*, *Entanglement of dark electron-nuclear spin defects in diamond,* Nat. Commun. **12**, 1 (2021).

[54] H. Bartling *et al.*, *Coherence and entanglement of inherently long-lived spin pairs in diamond,* arXiv:2103.07961 (2021).

[55] C. Bonato *et al.*, *Optimized quantum sensing with a single electron spin using real-time adaptive measurements,* Nat. Nanotechnol. **11**, 247 (2016).

[56] W. Pfaff *et al.*, *Unconditional quantum teleportation between distant solid-state quantum bits,* Science **345**, 532 (2014).

[57] S. L. N. Hermans *et al.*, *Qubit teleportation between non-neighbouring nodes in a quantum network,* In preparation (2021).

[58] N. Kalb *et al.*, *Entanglement distillation between solid-state quantum network nodes,* Science **356**, 928 (2017).

[59] N. Kalb, *Diamond-based quantum networks with multi-qubit nodes,* Ph.D. Thesis, TUDelft (2018).

[60] W. S. Warren, *Effects of arbitrary laser or nmr pulse shapes on population inversion and coherence,* J. Chem. Phys. **81**, 5437 (1984).

[61] L. M. Vandersypen and I. L. Chuang, *Nmr techniques for quantum control and computation,* Rev. Mod. Phys. **76**, 1037 (2005).

[62] T. H. Taminiau, J. Cramer, T. van der Sar, V. V. Dobrovitski and R. Hanson, *Universal control and error correction in multi-qubit spin registers in diamond,* Nat. Nanotechnol. **9**, 171 (2014).

[63] A. Jarmola, V. Acosta, K. Jensen, S. Chemerisov and D. Budker, *Temperature-and magnetic-field-dependent longitudinal spin relaxation in nitrogen-vacancy ensembles in diamond,* Phys. Rev. Lett. **108**, 197601 (2012).

[64] M. H. Abobeih *et al.*, *One-second coherence for a single electron spin coupled to a multi-qubit nuclear-spin environment,* Nat. Commun. **9**, 1 (2018).

[65] T. Astner *et al.*, *Solid-state electron spin lifetime limited by phononic vacuum modes,* Nat. Mater. **17**, 313 (2018).

[66] A. Norambuena *et al.*, *Spin-lattice relaxation of individual solid-state spins,* Phys. Rev. B **97**, 094304 (2018).

[67] G. Balasubramanian *et al.*, *Ultralong spin coherence time in isotopically engineered diamond,* Nat. Mater. **8**, 383 (2009).

[68] N. Bar-Gill, L. M. Pham, A. Jarmola, D. Budker and R. L. Walsworth, *Solid-state electronic spin coherence time approaching one second,* Nat. Commun. **4**, 1 (2013).

[69] T. Gullion, D. B. Baker and M. S. Conradi, *New, compensated carr-purcell sequences,* J. Magn. Reson. **89**, 479 (1990).

[70] B. Smeltzer, J. McIntyre and L. Childress, *Robust control of individual nuclear spins in diamond,* Phys. Rev. A **80**, 050302 (2009).

[71] A. P. Nizovtsev *et al.*, *Non-flipping 13c spins near an nv center in diamond: hyper-fine and spatial characteristics by density functional theory simulation of the c510 [nv] h252 cluster,* New J. Phys. **20**, 023022 (2018).

[72] M. G. Dutt *et al.*, *Quantum register based on individual electronic and nuclear spin qubits in diamond,* Science **316**, 1312 (2007).

[73] M. Abobeih *et al.*, *Atomic-scale imaging of a 27-nuclear-spin cluster using a quantum sensor,* Nature **576**, 411 (2019).

[74] L. Childress *et al.*, *Coherent dynamics of coupled electron and nuclear spin qubits in diamond,* Science **314**, 281 (2006).

[75] P. Neumann *et al.*, *Single-shot readout of a single nuclear spin,* Science **329**, 542 (2010).

[76] G. Fuchs, G. Burkard, P. Klimov and D. Awschalom, *A quantum memory intrinsic to single nitrogen–vacancy centres in diamond,* Nat. Phys. **7**, 789 (2011).

[77] W. Pfaff *et al.*, *Demonstration of entanglement-by-measurement of solid-state qubits,* Nat. Phys. **9**, 29 (2013).

[78] G. Waldherr *et al.*, *Quantum error correction in a solid-state hybrid spin register,* Nature **506**, 204 (2014).

[79] T. Taminiau *et al.*, *Detection and control of individual nuclear spins using a weakly coupled electron spin,* Phys. Rev. Lett. **109**, 137602 (2012).

[80] N. Zhao *et al.*, *Sensing single remote nuclear spins,* Nat. Nanotechnol. **7**, 657 (2012).

[81] S. Kolkowitz, Q. P. Unterreithmeier, S. D. Bennett and M. D. Lukin, *Sensing distant nuclear spins with a single electron spin,* Phys. Rev. Lett. **109**, 137601 (2012).

[82] J. Cramer, *Quantum error correction with spins in diamond,* Ph.D. Thesis, TUDelft (2016).

[83] A. Wickenbrock *et al.*, *Microwave-free magnetometry with nitrogen-vacancy centers in diamond,* Appl. Phys. Lett. **109**, 053505 (2016).

[84] N. Zhao, J.-L. Hu, S.-W. Ho, J. T. Wan and R. Liu, *Atomic-scale magnetometry of distant nuclear spin clusters via nitrogen-vacancy spin in diamond,* Nat. Nanotechnol. **6**, 242 (2011).

[85] F. Shi *et al.*, *Sensing and atomic-scale structure analysis of single nuclear-spin clusters in diamond,* Nat. Phys. **10**, 21 (2014).

[86] H. Oh *et al.*, *Algorithmic decomposition for efficient multiple nuclear spin detection in diamond,* Sci. Rep. **10**, 1 (2020).

[87] K. Jung *et al.*, *Deep learning enhanced individual nuclear-spin detection,* NPJ Quantum Inf. **7**, 1 (2021).

[88] K. Cujia, J. M. Boss, K. Herb, J. Zopes and C. L. Degen, *Tracking the precession of single nuclear spins by weak measurements,* Nature **571**, 230 (2019).

[89] M. Pfender *et al.*, *High-resolution spectroscopy of single nuclear spins via sequential weak measurements,* Nat. Commun. **10**, 1 (2019).

[90] M. Bakker, *Frozen core spin dynamics in diamond,* M.Sc. Thesis, TUDelft (2015).

[91] P. London *et al.*, *Detecting and polarizing nuclear spins with double resonance on a single electron spin,* Phys. Rev. Lett. **111**, 067601 (2013).

[92] I. Schwartz *et al.*, *Robust optical polarization of nuclear spin baths using hamiltonian engineering of nitrogen-vacancy center quantum dynamics,* Sci. Adv. **4**, eaat8978 (2018).

[93] M. A. Nielsen and I. Chuang, *Quantum computation and quantum information,* (2002).

[94] C. E. Bradley *et al.*, *A ten-qubit solid-state spin register with quantum memory up to one minute,* Phys. Rev. X **9**, 031045 (2019).

[95] J. Randall *et al.*, *Observation of a many-body-localized discrete time crystal with a programmable spin-based quantum simulator,* arXiv:2107.00736 (2021).

[96] V. Mkhitaryan, F. Jelezko and V. Dobrovitski, *Highly selective detection of individual nuclear spins with rotary echo on an electron spin probe,* Scientific reports **5**, 1 (2015).

[97] J. Casanova, Z.-Y. Wang, J. Haase and M. Plenio, *Robust dynamical decoupling sequences for individual-nuclear-spin addressing,* Phy. Rev. A **92**, 042304 (2015).

[98] T. K. Unden, D. Louzon, M. Zwolak, W. H. Zurek and F. Jelezko, *Revealing the emergence of classicality using nitrogen-vacancy centers,* Phys. Rev. Lett. **123**, 140402 (2019).

[99] W. Dong, F. Calderon-Vargas and S. E. Economou, *Precise high-fidelity electron–nuclear spin entangling gates in nv centers via hybrid dynamical decoupling sequences,* New J. Phys. **22**, 073059 (2020).

[100] G. Khutsishvili, *Spin diffusion and magnetic relaxation of nuclei,* Sov. Phys. JETP **15**, 909 (1962).

[101] R. Guichard, S. Balian, G. Wolfowicz, P. Mortemousque and T. Monteiro, *Decoherence of nuclear spins in the frozen core of an electron spin,* Phys. Rev. B **91**, 214303 (2015).

3

ORBITAL AND SPIN DYNAMICS OF SINGLE NV^0 CENTRES IN DIAMOND

S. Baier*, C. E. Bradley*, T. Middelburg, V. V. Dobrovitski, T. H. Taminiau, R. Hanson

The neutral charge state plays an important role in quantum information and sensing applications based on nitrogen-vacancy centres. However, the orbital and spin dynamics remain unexplored. Here, we use resonant excitation of single centres to directly reveal the fine structure, enabling selective addressing of spin-orbit states. Through pump-probe experiments, we find the orbital relaxation time (430 ns at 4.7 K) and measure its temperature-dependence up to 11.8 K. Finally we reveal the spin relaxation time (1.5 s), and realise projective high-fidelity single-shot readout of the spin state (≥ 98%).

The results of this chapter have been published in Phys. Rev. Lett. **125**, 193601 (2020).
*Equally contributing authors.

3.1. INTRODUCTION

Defect centres in solids are a promising class of systems for quantum science and technology[1,2]. They combine bright optical transitions, access to long-lived electronic- and nuclear-spin registers and compatibility with solid-state device engineering. Of particular prominence is the negatively-charged nitrogen-vacancy centre (NV^-) in diamond, which has enabled recent advances in quantum information science[3,4] and quantum sensing[5–7].

Alongside NV^-, the nitrogen-vacancy defect can exist in both the neutral- (NV^0) and — with sufficient Fermi-level engineering — positive- (NV^+) charge states. These additional charge states can be used as a resource in a number of applications, such as spin-to-charge conversion for improved spin-state read-out[8,9], classical data storage in NV ensembles[10], and deliberate charge-state switching for improved nuclear-spin coherence under ambient conditions[11,12].

Conversely, for experiments based upon NV^-, undesired conversion to NV^0 can be a hindrance: active charge-state initialisation protocols have been used to counter this[13,14]. For quantum networks, stochastic conversion from NV^- to NV^0 is an important decoherence mechanism for nuclear-spin quantum memories[15].

Despite the importance of NV^0, understanding of many of its properties remains elusive. In particular, the orbital- and spin-dynamic timescales are unknown. Also, while recent magnetic circular dichroism (MCD) measurements on ensembles[16,17] give insight into the NV^0 fine structure, no direct observation has been reported. Building an understanding of the system and its associated dynamic processes is important for improving control in NV quantum devices. Moreover, the knowledge gained may offer new insights into the physics of other impurities in solids[18]. Finally, NV^0 may prove to be a powerful quantum system in its own right.

Here, we develop protocols combining resonant excitation of both NV^0 and NV^-. We apply these novel protocols to reveal the orbital and spin dynamics of single NV^0 centres in diamond, as well as to realise initialisation and single-shot readout of the NV^0 spin state. We perform our measurements on single NV centres at cryogenic temperatures, see Fig. 3.1(a) and Sec. 3.7.1. The NV centre is addressed with microwave (MW) pulses (NV^- ground-state spin transitions) as well as with polarisation-controlled $\lambda_{\mathrm{red}} = 637\,\mathrm{nm}$ (NV^- zero-phonon line (ZPL)) and $\lambda_{\mathrm{yellow}} = 575\,\mathrm{nm}$ (NV^0 ZPL) laser light. We apply an axial magnetic field of $B_z = 1890(5)\,\mathrm{G}$ to induce significant Zeeman splitting.

3.2. EXCITATION SPECTROSCOPY OF THE NV^0 CENTRE

The ZPL of the NV^0 centre has been conclusively attributed to this defect[19–24]. A combination of ab-initio calculations and symmetry arguments led to the proposal of ground states of $^2\mathrm{E}$ symmetry, which can be optically excited to a $^2\mathrm{A}_2$ manifold[25,26]. An additional metastable $^4\mathrm{A}_2$ quartet state was also predicted, and has been observed by electron paramagnetic resonance (EPR) measurements under excitation of the NV^0 ZPL[27]. A splitting of the transitions of the two orbital states E_x and E_y has been measured[26,28]. However, the associated fine structure has not been observed in PL or EPR measurements.

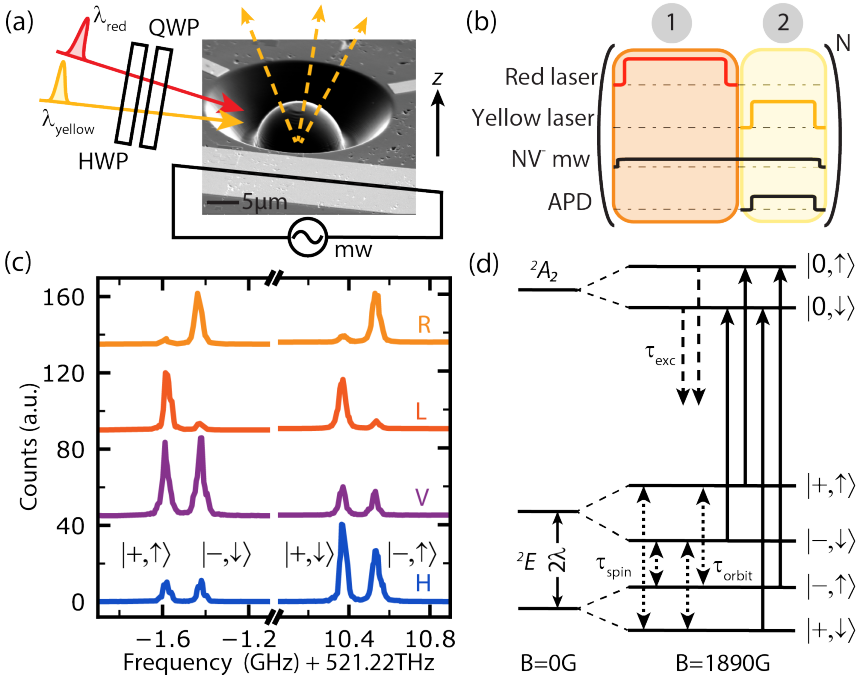

Figure 3.1: Direct observation of the fine structure of the NV^0 centre. (a) Electron microscope image of a solid-immersion lens fabricated around the NV centre. Optical (λ_{yellow}, λ_{red}) and mw control are indicated. (b) Experimental sequence for spectroscopy consisting of a preparation (1) and measurement (2) part. (c) Spectra obtained with linear (H,V) and circular (L,R) polarisations ($P_{\text{yellow}} = 500\,\text{pW}$), offset for clarity (see Sec. 3.7.2). (d) Ground and excited state level structure. Spin-conserving optical transitions (solid arrows), excited state decay (dashed arrows) and spin/orbital relaxations (dotted arrows) are indicated.

We start by performing spectroscopy using the experimental procedure sketched in Fig. 3.1(b). For each frequency step, we (1) probabilistically prepare the emitter in NV^0 by applying strong laser excitation resonant with the NV$^-$ ZPL, in combination with weak mw driving (see Sec. 3.7.1) to induce the conversion NV$^-$ → NV^0. We then (2) apply polarised yellow light, during which time all single-photons above 650 nm are integrated.

The measured spectra (Fig. 3.1(c)) show four transitions — the first direct spectroscopic observation of the NV^0 fine structure. These observations validate the model of Barson *et al.*[16], and we hence follow their theoretical description below. Under the secular approximation, the ground-state Hamiltonian of NV^0 can be described by

$$\begin{aligned} H = {} & g\mu_B \hat{S}_z B_z + l\mu_B \hat{L}_z B_z + 2\lambda \hat{L}_z \hat{S}_z \\ & + \epsilon_\perp (\hat{L}_- + \hat{L}_+). \end{aligned} \tag{3.1}$$

g is the spin g-factor, μ_B is the Bohr magneton, l is the orbital g-factor, λ is the spin-orbit interaction parameter and $\epsilon_\perp$ is the perpendicular strain parameter. $\hat{L}_z = \sigma_z$ and $\hat{S}_z = \frac{1}{2}\sigma_z$ are the orbital and spin operators defined in terms of the Pauli matrix σ_z, while $\hat{L}_\pm = |\pm\rangle\langle\mp|$ with $|\pm\rangle = \mp(1/\sqrt{2}(|X\rangle \pm i|Y\rangle))$ are the orbital operators defined within the

basis of the strain eigenstates $\{|X\rangle, |Y\rangle\}$. The z-axis is defined parallel to the NV axis.

The resulting level structure is presented in Fig. 3.1(d). The ^{2}E ground state is composed of a pair of doublet states with opposite spin-orbit parity (lower spin-orbit branch: $\{|+,\downarrow\rangle, |-,\uparrow\rangle\}$; upper spin-orbit branch: $\{|-,\downarrow\rangle, |+,\uparrow\rangle\}$). The degeneracy of each doublet is lifted by orbital- and spin-Zeeman contributions under the applied magnetic field. Conversely, the $^2A_2$ excited state exhibits no spin-orbit structure, but is rather split by the spin-Zeeman effect alone. These contributions lead to four spin-conserving transitions. The contributing ground state for each observed transition is indicated in Fig. 3.1(c).

We find that the luminescence of the transitions depend significantly on the polarisation of the excitation light (see Fig. 3.1(c)). Differing transition amplitudes for orthogonal polarisations can be attributed to optical selection rules that are strongly dependent on $\epsilon_\perp$ (see Sec. 3.7.3 and Ref. [16]). Based upon these observations, we develop a method to extract $\epsilon_\perp$ and simultaneously the fine structure parameters of the NV^0 Hamiltonian (Sec. 3.7.3). By fitting spectra from three individual NV centres against our theoretical model, we find $l = 0.039(11)$ and $\lambda = 4.9(4)$ GHz. These values are roughly a factor of 2 larger than those found previously using NV-ensemble MCD measurements[†].

Crucially, the data in Fig. 3.1(c) shows that resonant optical excitation in this magnetic field regime allows for state-resolved addressing, enabling the heralded preparation of specific states and investigation of the system dynamics. To date, only the excited-state lifetime, τ_{exc}, of 21 ns has been reported[30]. Here, we investigate the orbital- and spin-relaxation timescales of the ground state, τ_{orbit} and τ_{spin}, see Fig. 3.1(d).

3.3. TIME-RESOLVED FLUORESCENCE MEASUREMENTS

In order to unambiguously measure the dynamics of NV^0, we design and implement a charge-resonance (CR) protocol that realises high-fidelity heralded preparation into NV^0, with the $\lambda = 575$ nm laser resonant with a chosen optical transition, see Fig. 3.2(a). The CR protocol (1) can be broken down as follows. First, a heralding signal confirms preparation in NV^-, with the $\lambda = 637$ nm lasers on resonance with the NV^- transitions. Next, a strong red optical pulse induces charge state conversion, after which a chosen NV^0 transition is excited with yellow light. If the photon counts obtained during the 'NV^0 check' exceed a pre-set threshold, the protocol is completed. Further details are given in Sec. 3.7.4.

After the CR protocol, we perform the experimental sequence on NV^0 (2). Finally, we detect whether undesired conversion to NV^- occurred during the experimental sequence, and then perform read-out of the NV^0 state (3). The number of repetitions of the experimental sequence (2) is chosen to minimise the overhead from the CR protocol while maintaining an NV^0 population above 85%, and ranges from N=15-1000 dependent upon the used yellow power. Note that the CR protocol prepares a specific spin state of the NV^0 centre. For circular polarisation we typically start the experiment by heralding the $|\downarrow\rangle$ spin state. For linear polarisation, however, due to their close spectral vicinity, the CR check heralds either the $|\downarrow\rangle$ or $|\uparrow\rangle$ spin state.

In Fig. 3.2(b) we show time-resolved pump measurements. Here, the yellow

[†]A re-assessment of the procedures of Barson *et al.* concluded that it can not be excluded that an error in documenting the data is the cause of this discrepancy[29].

laser is gated by an acousto-optic modulator (AOM), with measured rise-/fall-time of 30(5)/7(1) ns. Upon opening the AOM, we observe a rapid increase in fluorescence due to optical cycling, which is then damped as population is pumped out of the driven state. By fitting the steady-state fluorescence counts for L/H polarisation we extract a saturation power of 2.5(2)/1.8(1) nW and saturation counts of 105(2)/103(2) kcts/s, see Fig. 3.2(c). As the optical power is increased, coherent optical Rabi oscillations are observed. In Fig. 3.2(d), we plot the fitted frequency of these oscillations, revealing the expected $\sqrt{P_{\text{yellow}}}$ dependence. When the AOM is closed the fluorescence decays with $\tau_{\text{exc}} = 22(1)$ ns (inset Fig. 3.2(b)), which is consistent with literature[30].

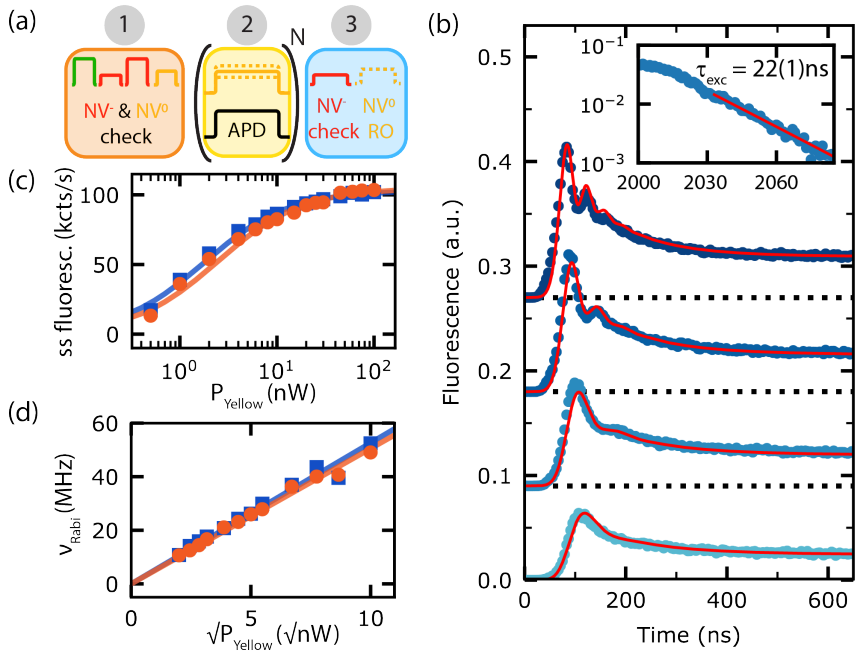

Figure 3.2: Time-resolved resonant pump measurements. (a) Experimental sequence consisting of preparation (1), measurement (2) and readout (3) parts. (b) Fluorescence of NV^0 when driving the lower spin-orbit branch with H polarisation for $P_{\text{yellow}} = 2, 4, 10, 20$ nW (bottom to top) averaged over at least 1×10^6 repetitions. Measurements have a timing resolution of 250 ps and are offset for clarity. Solid red lines are simulations of the full system dynamics with our theoretical model (Sec. 3.7.5). Inset: decay of fluorescence counts after the AOM is closed. (c) Steady state (ss) fluorescence counts as a function of P_{yellow}, for H (squares) and L polarisation (circles). The data is fit with a saturation curve $f(P) = A(P/(P + P_{\text{sat}}))$. (d) Optical Rabi frequency as a function of $\sqrt{P_{\text{yellow}}}$. Fits yield a slope of 5.3(1)/5.1(1) MHz/$\sqrt{\text{nW}}$ for L/H polarisation.

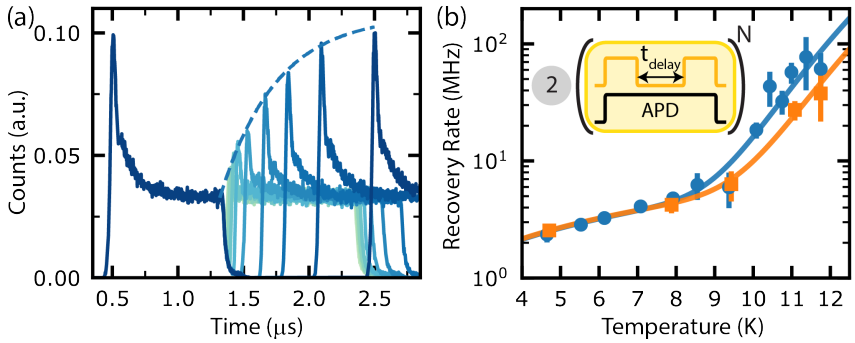

Figure 3.3: Time-resolved pump-probe spectroscopy. The experimental sequence after state preparation is given in the inset of (b). (a) Example traces for a range of t_{delay} (light to dark for increasing t_{delay}), at a temperature of 5.5(1) K, integrated over 5×10^6 acquisitions each, measured with H polarisation. The dashed line is a fit to the recovery behaviour (Sec. 3.7.7). (b) Recovery rate R_{recovery} as a function of the cryostat temperature. Circles (squares) describe data measured on the lower (upper) spin-orbit branch. Error bars for R_{recovery} correspond to 1 s.d. fit errors. The solid lines are fits of form $f(T) = A\,T + B\exp[-\Delta/k_B T]$, giving $A = 0.53(3)$ MHz/K ($A = 0.54(2)$ MHz/K) and $B = 1(1) \times 10^7$ MHz ($B = 1(4) \times 10^7$ MHz) for the lower (upper) branch.

3.4. ORBITAL DYNAMICS OF THE NV^0 CENTRE

To uncover the recovery timescale after pumping we turn to pump-probe spectroscopy. Example time-traces are shown in Fig. 3.3(a). The resulting data is well described by an exponential recovery with a single timescale associated with how fast the system relaxes once illumination is turned off (see Sec. 3.7.7). At base temperature of our cryostat ($T = 4.65(3)$ K), we extract $\tau_{\text{recovery}} = 0.43(6)\,\mu$s. We attribute these fast dynamics to orbital relaxation processes, i.e. $|+\rangle \leftrightarrow |-\rangle$ and $\tau_{\text{orbit}} = \tau_{\text{recovery}}$.

We repeat the pump-probe measurements across a range of temperatures. The fitted recovery times are shown as rates $R_{\text{recovery}} = 1/t_{\text{recovery}}$ in Fig. 3.3(b). After an initial linear increase a rapid increase is observed at higher temperatures. At these higher temperatures, the required time resolution exceeds the AOM switching time constants, which we take into account in the fitting procedure (see Sec. 3.7.7).

The initial linear increase ($\propto T$) can be attributed to single-phonon processes, while high-order processes appear to govern the recovery rate at higher temperatures[31,32]. Here, we fit individually to a two-phonon Raman process ($\propto T^n$) and a two-phonon Orbach process ($\propto \exp[-\Delta/k_B T]$), with k_B being the Boltzmann constant. For the Raman process the fit returns $n = 13(2)$ (14(3)) for the lower (upper) spin-orbit branch; a physical explanation for such values is currently lacking. For the Orbach process we find a characteristic energy scale of $\Delta = 12(2)$ meV ($\Delta = 13(4)$ meV) extracted from a fit to the lower (upper) spin-orbit branch. Δ is associated to the energy splitting to the first vibronic level of the NV^0 ground state, predicted to be a Jahn-Teller system[19,33]. The value found here agrees with the bulk absorption measurements of Davies[19] (13.6(7) meV), and with recent density-functional theory calculations (21.4 meV)[33], suggesting that the measured increase of R_{recovery} is predominantly due to two-phonon Orbach processes. While a detailed model is beyond the scope of this work, we expect that our findings will aid in the further understanding of the vibronic structure of NV^0.

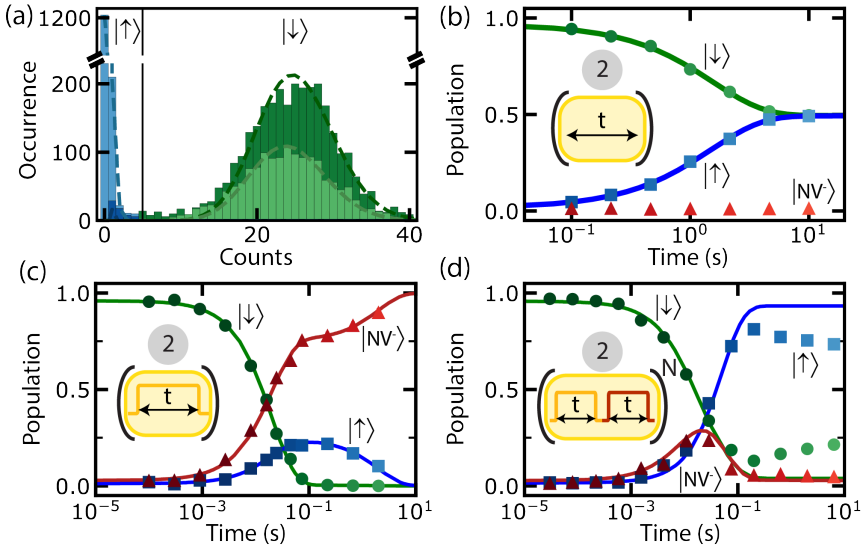

Figure 3.4: Single-shot readout and spin pumping. (a) Histograms after preparation of the NV^0 $|\downarrow\rangle$ state (dark colors) and mixed (light colors) spin states. (b) Relaxation (T_1) measurement for the $|\downarrow\rangle$ (circles) and $|\uparrow\rangle$ (squares) states, fitted with an exponential decay (recovery). The NV$^-$ population (triangles) remains negligible in the dark. The data is averaged over 3×10^3 repetitions each. (c) Spin-pumping: NV^0 spin- and total NV$^-$ populations as a function of yellow illumination time. Solid lines are fits to solutions for the underlying 3-level rate equations (Sec. 3.7.8). (d) Spin-pumping with charge-cycling: same as (c) but with stroboscopic red illumination. The time axis is the yellow illumination time (half of the total sequence time).

3.5. SPIN DYNAMICS OF THE NV^0 CENTRE

Now we turn to the spin dynamics of NV^0. Here, we exploit polarisation control to selectively prepare, address, and readout the NV^0 spin state. These measurements are all performed on timescales $\gg \tau_{\text{orbit}} = 0.43(6)\,\mu$s and thus average over the orbital basis; we will therefore only refer to the spin states. In all experiments below, we use L polarisation, addressing the $|\downarrow\rangle$ state. We herald the preparation of $|\downarrow\rangle$ by applying 25 nW for 250 μs, and proceed when more than 25 photons are detected. After a delay of 0.1 ms, we perform a charge-state check with red excitation, followed by a second yellow readout (again, 25 nW for 250 μs), see Fig. 3.2(a)(3). We then repeat this experiment, but with a delay of 10 s between the yellow readouts, allowing for relaxation processes to occur. The resulting histograms are shown in Fig. 3.4(a).

In the first case (dark colors), we observe a single dominant population which can be modelled by a Poissonian distribution with mean photon count 25.2(2), and that we attribute to $|\downarrow\rangle$. In the second case (light colors), we additionally observe a second distribution, again modelled as a Poissonian distribution with mean photon count 0.171(4). A charge-state measurement of NV$^-$ performed before each read-out shows that only a small fraction of the population ($P_{\text{NV}^-} \sim 1\%$) is found in the unwanted charge state — which we discard from the histograms — and that the majority of low-count events can be attributed to a dark state of NV^0. As the populations evolve without laser excitation,

the dark state must be part of the ground state manifold; we therefore assign this state to the second spin state $|\uparrow\rangle$. A read-out threshold of 5 photons (solid line, Fig. 3.4(a)) discriminates the two spin states.

We now sweep the delay time between initialisation and read-out. The measured populations of $|\downarrow\rangle$ ($P_\downarrow$) and $|\uparrow\rangle$ ($P_\uparrow$) are plotted in Fig. 3.4(b), showing relaxation to a mean population of 0.494(6). The data is consistent with a spin-1/2 T_1 process of characteristic timescale $\tau_{\text{spin}} = 1.51(1)$ s. Note that the observed value is a lower bound of the intrinsic spin relaxation, as it may be limited by leakage of resonant laser light. By setting the initial and long-time population in $|\downarrow\rangle$ to be 1 and 0.5 respectively, we obtain a lower-bound for the single-shot read-out fidelity, $F_{RO} = \frac{1}{2}(F_{|\downarrow\rangle} + F_{|\uparrow\rangle}) \geq 98.2(9)\%$, where $F_{|s\rangle}$ is the probability to assign $|s\rangle$ after preparing $|s\rangle$ (see Sec. 3.7.10).

To investigate the cycling nature of the driven optical transition we now repeat the measurement under 5 nW of resonant yellow excitation, see Fig. 3.4(c). We find that $P_\downarrow$ decreases on a timescale faster than can be explained by spin-relaxation alone, showing that the optical excitation induces spin pumping. Possible spin-mixing channels are given either in the $^2A_2$ excited state or via an intersystem crossing, which might be offered by the $^4A_2$ state. We also find a significant increase of P_{NV^-} due to optically-induced charge conversion (see Sec. 3.7.6 and Ref.[34]). However, this slows once $|\downarrow\rangle$ is depleted as $|\uparrow\rangle$ is a dark state for optical excitation. Beyond this, $P_\uparrow$ reduces with τ_{spin}, and charge conversion continues. We find a high state preparation fidelity for $|\uparrow\rangle$ of 99^{+1}_{-10} % after 600 ms, but with an absolute population in the NV^0 $|\uparrow\rangle$ state of only 22(2) %.

To reveal the respective rates we develop a three-level-rate equation model that we fit to our data, using the measured spin-relaxation time as a fixed input (solid lines, Fig. 3.4(c)) (see Sec. 3.7.8). For the applied power of 5 nW, we extract characteristic timescales of 27(1) ms (90(4) ms) for the charge conversion (spin pumping) process. From this we can estimate the cyclicity of the $|\downarrow\rangle$ state within this regime to be $0.98(8) \times 10^5$ cycles, mainly limited by recharging to NV^- (see Sec. 3.7.9).

In a second experiment the 5 nW yellow excitation is stroboscopically interleaved with strong $NV^- \rightarrow NV^0$ ionisation pulses, see Fig. 3.4(d) and Sec. 3.7.8. Again we observe a gradual decrease of $P_\downarrow$, and an increase of both $P_\uparrow$ and P_{NV^-}, but then P_{NV^-} growth stops and even inverts. This observation can be explained via the picture that the removal of an electron from NV^- prepares a random spin-state in NV^0, eventually populating the dark state $|\uparrow\rangle$. Competing rates between this spin-selection process and spin relaxation lead to the observed steady state populations. We again fit a three-level rate equation model, using the previously obtained parameters as fixed inputs, and extract a timescale for ionisation of 18(4) ms. The rate equation model does not accurately describe the behaviour at long timescales, which is likely due to a reduction of the NV^0 spin-relaxation time under red excitation and strong NV^- microwave driving.

As a final step, we develop a master equation simulation to capture the full dynamics of the NV^0 centre (see Sec. 3.7.5). In Fig. 3.2(b) we plot the simulated excited state population (solid line), using the uncovered NV^0 timescales and spectral properties. We match the Rabi frequency to the measured optical power and further include a spectral average over a Gaussian distribution of detuning values with FWHM = $2\pi \times 20$ MHz. We find excellent agreement with our experimental fluorescence data, emphasising a consistent understanding of the NV^0 dynamics.

3.6. CONCLUSION

In conclusion, we have developed a novel toolbox for the study and control of single neutrally-charged NV centres in diamond. We have uncovered the dynamic timescales and demonstrated single-shot readout and initialisation-by-measurement of the NV^0 spin, each with high fidelity. In future investigations, coherent control of the spin states may be obtained. Detailed modelling of the defect may give new insights into the observed temperature-dependence of the orbital dynamics. On the application side, protection of nuclear spin quantum memories from dephasing by NV^0 may be achieved by microwave spin locking in both orbitals, or by feedback based upon the NV^0 spin read-out demonstrated here. Finally, at reduced temperatures that suppress the orbital dynamics, NV^0 may prove to be a powerful system for quantum technologies in its own right.

3.7. SUPPLEMENTARY MATERIALS

3.7.1. EXPERIMENTAL SETUP

Our experiments are performed on single nitrogen-vacancy (NV) centres in type-IIa bulk diamond (Element Six, CVD grown, <111> oriented), using a cryogenic (Montana Cryostation, 4 K) home-built confocal microscope setup. Enhanced photon-collection efficiency is achieved by fabrication of solid-immersion lenses[35] and an anti-reflection coating[36]. For phonon-sideband (PSB) detection, a dichroic mirror (Semrock, pass above 650 nm) and an additional long-pass filter are used to block reflections of the excitation lasers. Photon emission is detected via an avalanche photo-diode (APD, Laser components, quantum efficiency ~ 80%), with a total collection efficiency of ~ 3% (~ 10%) of the NV^0 (NV^-) PSB.

We apply a magnetic field of $B_z = 1890(5)$ G along the symmetry axis z of the NV centre via a permanent magnet. A slight misalignment of the field leaves a small perpendicular magnetic field component of $B_\perp = 10(5)$ G. As the ratio $B_\perp / B_z$ is small, we neglect the effect of the perpendicular magnetic field. In addition to the magnetic field, local strain and electric fields can alter the NV centre level-structure[37]. For the NV centre used in the main text we observe the level structures as depicted in Fig. 3.5.

To address the NV^0 charge state we apply resonant optical excitation of the NV^0 zero-phonon-line (ZPL) ($\lambda = 575.17$ nm, $\omega = 2\pi \times 521.22$ THz). The laser frequency can be manually tuned to each ^2E to $^2A_2$ transition. In the NV^- charge state, selective excitation of ZPL transitions ($\lambda = 637.25$ nm, $\omega = 2\pi \times 470.45$ THz) enables optical readout (RO, $m_s = 0 \leftrightarrow E_x$) and spin-pumping (SP, $m_s = \pm 1 \leftrightarrow E_{1,2}$). The ground state spin levels ($m_s = 0 \leftrightarrow m_s = -1$; 2.4 GHz) can be coherently adressed with microwave (mw) pulses delivered via gold strip lines on top of the diamond surface. For the NV used in the main text (NV A), we extract an NV^- perpendicular strain of $\epsilon_{NV^-} = 4.2(1)$ GHz, from the observed optical transition frequencies, see Fig. 3.5. We note that it is unclear how this relates to the strain in NV^0, as the susceptibility of the NV^0 states to electric fields is currently unknown. Further, charge state conversion may result in differing local charge environments for the two charge states[38].

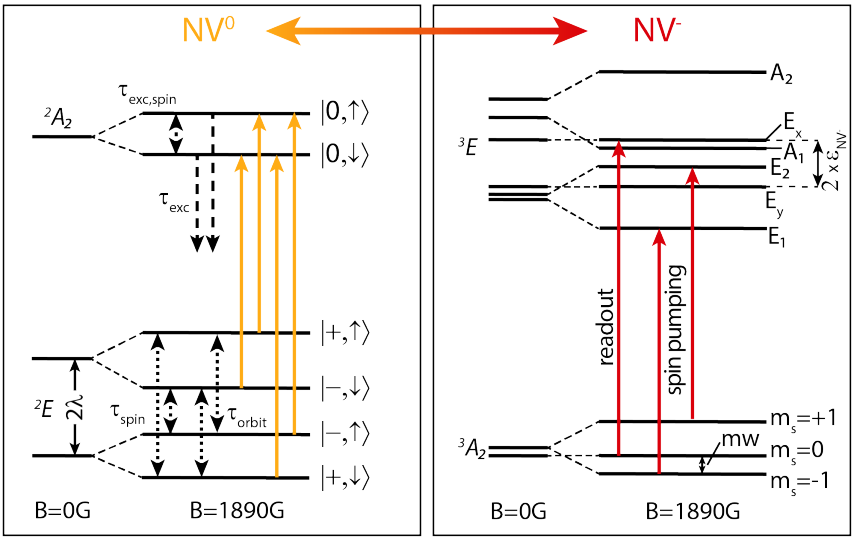

Figure 3.5: Level structure for the two charge states NV^0 and NV$^-$ of a single NV centre. The optical transitions used within this work are indicated by yellow (red) solid arrows for NV^0 (NV$^-$). Charge-state switching between the two charge states is achieved via two-photon absorption of the respective ZPL laser[34].

3.7.2. PHOTO-LUMINESCENCE MEASUREMENTS

For the photo-luminescence (PL) measurements presented in Fig. 3.1, the following methodology was used. First, the NV centre is prepared in the neutral charge state by application of a 50 μs optical SP pulse (1 μW) in combination with weak mw driving ($\nu^{\mathrm{mw}}_{\mathrm{Rabi}} \sim 150$ kHz) of the NV$^-$ $m_s = 0 \leftrightarrow m_s = -1$ ground-state spin transition. This method prevents optical spin-pumping into a NV$^-$ dark state ($m_s = 0$). Second, 500 pW of yellow light (P_{yellow}) is applied for 15 μs at the NV^0 ZPL transition, during which all single-photon detection is integrated. The red-yellow procedure is repeated $N = 150$ times before the frequency is stepped by 1 MHz. For these measurements the weak NV$^-$ mw driving (off-resonant for NV^0) is kept active throughout the experiment due to technical reasons, but this is not expected to affect the NV^0 dynamics.

A total of 20 full scans were made for each polarisation setting, which were collated to produce the final PL data. For each PL scan, the fluorescence maxima are found via a peak finding routine (python, scipy.signal.find_peaks_cwt). Further, all data sets are shifted to the mean frequency of all fluorescence maxima and summed. We typically observe shifts of the maxima by up to 200 MHz due to spectral diffusion. PL scans of the lower and upper spin-orbit branches were done in two separate measurements. To avoid systematic shifts of the splitting between the two spin-orbit branches, the NV centre is reset by strong green ($\lambda = 515$ nm, 10 μW) illumination in between these two measurements, cancelling potentially accumulating effects of spectral diffusion from the red-yellow scans.

In a second set of experiments, we study the linewidth of the observed optical transitions for various values of P_{yellow}, see Fig. 3.6(a). We observe a broadening of the

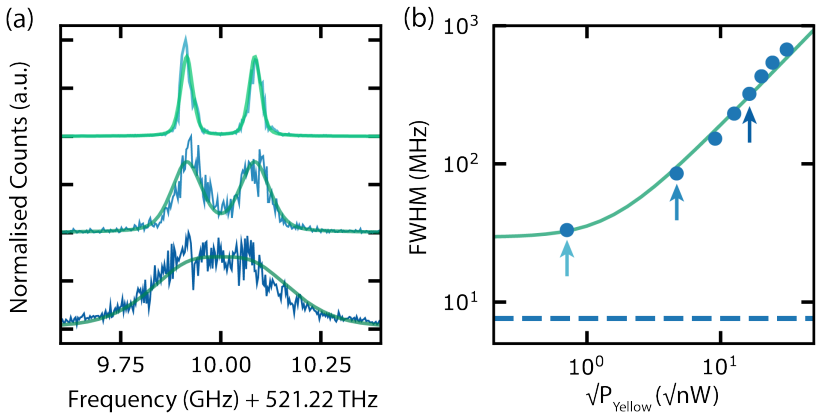

Figure 3.6: Power broadening of NV^0 optical transitions. (a) Example PL spectra for the lower spin-orbit branch, measured at powers of 0.5 nW, 22 nW, and 160 nW (light to dark blue) with H polarisation. Each spectrum consists of 20 individual scans which have been shifted on top of one another and summed. A pair of Voigt profiles is fitted. The spectra have been normalised and offset for clarity. (b) FWHM of the fitted Voigt profiles, as a function of $\sqrt{P_{\text{yellow}}}$. The solid line is a fit to the data (see text), from which we extract $a = 18.6(1)\,\text{MHz}/\sqrt{\text{nW}}$ and $b = 25.1(3)\,\text{MHz}$. The transform limit, 7.6 MHz, arising from the excited state lifetime, $\tau_{\text{exc}} = 21\,\text{ns}$, is shown as a dashed line.

lines with increasing power. As a result, in the high power regime the fine structure is no longer resolved. The extracted full width at half maximum (FWHM) is plotted in Fig. 3.6(b) as a function of $\sqrt{P_{\text{yellow}}}$ (i.e. $\propto$ optical Rabi frequency). For power broadening, a linear dependence on the Rabi frequency is expected, while at low powers the FWHM is limited by the intrinsic linewidth of the defect. In Fig. 3.6(b) we fit the dependence under the assumption that the linewidth can be described by a convolution of a lifetime-limited Lorentzian profile ($f_{\text{L}} = 1/(2\pi \times \tau_{\text{exc}}) = 7.6\,\text{MHz}$) with Gaussian broadening terms. The resulting Voigt FWHM can be approximated by[39] $f \approx 0.5446 f_{\text{L}} + \sqrt{0.2166 f_{\text{L}}^2 + f_{\text{G}}^2}$. The Gaussian component is given by the convolution of a power-dependent term from power-broadening, and a power-independent term arising from spectral diffusion: $f_{\text{G}} = \sqrt{a^2 P_{\text{yellow}} + b^2}$. The fit shows good agreement with the observed behaviour. We find a spectral-diffusion-limited linewidth of 30.3(3) MHz, a factor of 4 above the transform limit.

3.7.3. EXTRACTION OF THE NV^0 FINE STRUCTURE PARAMETERS

The obtained PL measurements carry information of the parameters of the ground and excited state Hamiltonians. Based on these measurements we develop a methodology to extract the NV^0 orbital g-factor l and spin-orbit interaction parameter λ.

Beside the fine-structure constants, the PL spectrum of the NV^0 centre depends on both magnetic field and strain (stress within the crystal and electric fields). These de-

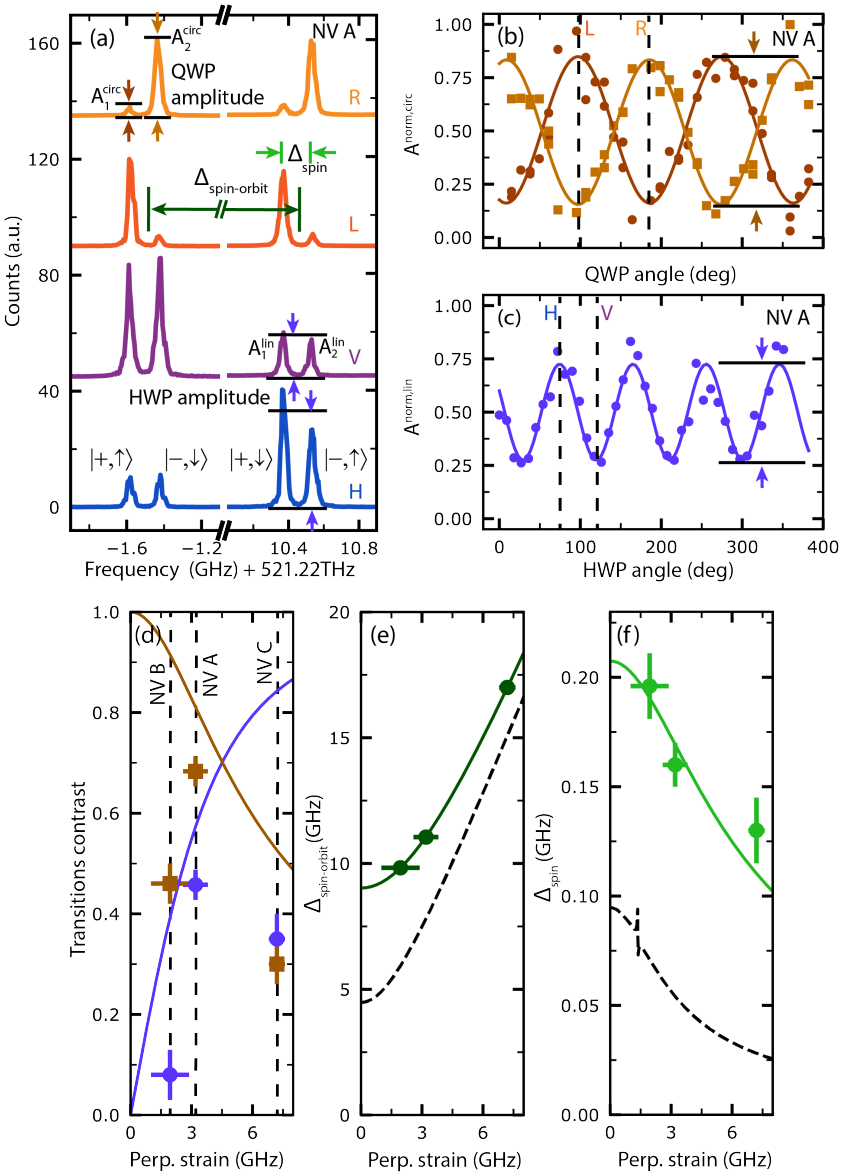

Figure 3.7: Extraction of finestructure constants. (a) PL spectra for four different excitation light polarisations (R, L, V, H) for NV A. (b) NV A: Example traces for extracted and normalised PL amplitudes $A_1^{\mathrm{circ,norm}}$ (circles) and $A_2^{\mathrm{circ,norm}}$ (squares) for varying angles of the quarter-wave plate (QWP). (c) Same as (b) but for $A^{\mathrm{lin,norm}}$ when varying the angle of the half-wave plate (HWP). The dashed lines in (b,c) indicate the angles for which the PL scans in (a) are taken. Solid lines show fits with a sine function. (d) Transition contrast for circular ('orbit contrast', squares) and linear ('spin-orbit contrast', circles) polarisation extracted from the normalised amplitudes, as indicated by the vertical arrows in (b,c), determined for three NV centres (dashed lines). (e,f) $\Delta_{\mathrm{spin\text{-}orbit}}$ and Δ_{spin} for the same NV centres as in (d). The data of (d-f) is simultaneously fitted against the Hamiltonians. The data is shown together with the best fit (solid lines) as a function of perpendicular strain $\epsilon_\perp$. Dashed lines in (e,f) show the expected transition energy splittings for the fine structure constants of Barson *et al.*, see Ref. [16].

pendencies are captured within the NV^0 Hamiltonian of the ^2E ground state, see Ref. [16]:

$$H = g\mu_B \hat{S}_z B_z + l\mu_B \hat{L}_z B_z + 2\lambda \hat{L}_z \hat{S}_z + \epsilon_\perp (\hat{L}_- + \hat{L}_+). \tag{3.2}$$

Here, g is the spin g-factor, μ_B is the Bohr magneton, $\hat{L}_z = \sigma_z$ and $\hat{S}_z = \frac{1}{2}\sigma_z$ are the orbital and spin operators defined in terms of the Pauli matrix σ_z. The last term of the Hamiltonian shows the influence of perpendicular strain $\epsilon_\perp$, where $\hat{L}_\pm = |\pm\rangle\langle\mp|$ with $|\pm\rangle = \mp(1/\sqrt{2}(|X\rangle \pm i|Y\rangle))$ and $\{|X\rangle, |Y\rangle\}$ is the basis for the strain eigenstates. Note that parallel strain is not included as it does not affect the relative energy of the ground state levels. For the excited state $^2A_2$, the Hamiltonian reads as

$$H = g\mu_B \hat{S}_z B_z \tag{3.3}$$

and does not show a dependency on strain.

These two Hamiltonians lead to the energy level structure as presented in Fig. 3.5. The four resulting transition frequencies are shown in the PL spectra in Fig. 3.7(a). The corresponding eigenstates in the ground state are indicated. Depending on the polarisation (circular right (R) or left (L); linear horizontal (H) or vertical (V)), the amplitude of the observed PL varies. From Voigt fits to the individual PL lines we extract the transition frequencies and PL amplitudes. From the transition frequencies, we determine the energy splitting, Δ_{spin}, between the two spin-states, $|\uparrow\rangle$ and $|\downarrow\rangle$, associated with each spin-orbit branch, and the energy splitting $\Delta_{\text{spin-orbit}}$ between the two spin-orbit branches.

Further, the PL amplitudes can be directly related to the transition strength for a given polarisation and transition. In the absence of strain, circularly-polarised transitions are expected, as one quantum of orbital angular momentum has to be transferred upon excitation. Accordingly, under such excitation, full PL contrast would be expected between the transitions within each spin-orbit branch ('orbit contrast'). However, under large strain, the ground state is better described within the strain eigenbasis [16], with associated linearly-polarised transitions. In this scenario, full contrast would instead be expected between the spin-orbit branches ('spin-orbit contrast'), whilst no 'orbit contrast' would be expected within each branch. As a consequence the observed contrasts can be used to determine the strain.

To extract the contrast, we repeat PL scans of a spin-orbit branch for several angles of the quarter-wave plate (QWP) and half-wave plate (HWP). In the case of circular polarisation, we normalise each PL scan by the respective integrated total counts. The fitted amplitudes A_1^{circ} and A_2^{circ} for the transitions of two spin states are then normalised by the mean of the sum of the two amplitudes for all measured angles, $A_i^{\text{circ,norm}} = A_i^{\text{circ}} / \overline{A_1^{\text{circ}} + A_2^{\text{circ}}}$ with $i \in \{1,2\}$. For linear polarisation, for each angle we take the mean amplitude of the transitions within a spin-orbit branch, $A^{\text{lin}} = (A_1^{\text{lin}} + A_2^{\text{lin}})/2$. We then normalise each angle by the mean for all measured angles, $A^{\text{lin,norm}} = A^{\text{lin}} / \overline{A^{\text{lin}}}$. Figure 3.7(b,c) shows example plots for the resulting normalised amplitudes for varying circular and linear polarisations. Measurements on the respective other spin-orbit branch give similar results.

As a next step we extract the transition contrast for circular polarisations (Fig. 3.7(b), 'orbit contrast') and linear polarisations (Fig. 3.7(c), 'spin-orbit contrast') from the amplitudes of fits with a sine function. These contrasts are plotted in Fig. 3.7(d) for three

independently measured NV centres, NV A, NV B, and NV C. Further, we plot the mean transition energy splittings $\Delta_{\text{spin-orbit}}$ and Δ_{spin} in Fig. 3.7(e) and (f).

The four data sets, ('orbit contrast', 'spin-orbit contrast', $\Delta_{\text{spin-orbit}}$, Δ_{spin}), from the three NV centres are now simultaneously fitted against the Hamiltonian with $\epsilon_{\perp,i}$ for each NV, l, and λ as free fitting parameters. Our results are summarised in Tab. 3.1 (method 1). The fitted strain results are used to place the experimental data points in Fig. 3.7(d-f), see dashed lines in Fig. 3.7(d). Solid lines show the result of our fit. The transition energy splittings Δ_{spin} and $\Delta_{\text{spin-orbit}}$ are well described by our theoretical model. While a good match of the transition contrast for NV A is found, NV B and C show a discrepancy. A possible explanation could be non ideal polarisation settings at the position of the NV for these data sets, resulting in less clean rotation around the Poincaré sphere, i.e. mixed circular and linear polarisations when rotating the QWP/HWP. A mixed polarisation leads to both reduced 'orbit contrast' and reduced 'spin-orbit contrast'.

As a second method we repeat our fitting procedure, but this time fixing the individual strain values to ϵ_{NV^-} of each NV, obtained from NV^-, see Fig. 3.5. While it is not known how the NV^- strain translates to strain in NV^0, a correlation is expected. From the fit we obtain l and λ, see Tab. 3.1 (method 2). Within error the two methods give the same values. In Sec. 3.2 we report the mean of the two values: $l_{\text{mean}} = 0.039(11)$, $\lambda_{\text{mean}} = 4.9(4)$ GHz.

method	$\epsilon_\perp^{\text{A}}$ (GHz)	$\epsilon_\perp^{\text{B}}$ (GHz)	$\epsilon_\perp^{\text{C}}$ (GHz)	l	λ (GHz)
1	3.2(6)	1.9(9)	7.2(4)	0.040(8)	4.5(4)
2	4.15	1.05	4.35	0.037(14)	5.2(4)

Table 3.1: Ground state Hamiltonian parameters extracted from a fit to our experimental data for the three NV centres NV A, NV B, and NV C. For method 1 the measured contrasts of NV^0 is used as an input to fit the strain values, while method 2 uses the strains extracted from NV^- as fixed parameters.

We now compare our data to the transition frequencies calculated using the fine structure parameters of Barson *et al.* [16], $l_{\text{lit}} = 0.0186(5)$, $\lambda_{\text{lit}} = 2.24(5)$ GHz, (dashed lines, Fig. 3.7(e,f)). Strikingly, with these parameters, our data for Δ_{spin} cannot be reproduced for *any* strain value, strongly indicating that the discrepancy in fine structure parameters cannot be explained by systematic errors in our method to extract the strain of the NV.

We note that Barson *et al.* have used NV ensemble magnetic-circular dichroism measurements while we here observe PL of single NV centres.

3.7.4. CHARGE-RESONANCE CHECK

As described in Sec. 3.3, one of the key components of the experiments in this work is the introduction of a charge-resonance (CR) check for NV^0. This check allows heralded preparation of the NV in the neutral charge state, while also preparing the red lasers on resonance with the NV^- optical transitions, and the yellow laser on resonance with one of the four NV^0 transitions. The full procedure is shown in Fig. 3.8 and outlined in the following.

We first prepare the negatively-charged state. A strong green pulse (12 μW) is applied for 300 μs in order to prepare the system ('reset'). Next, we simultaneously apply a combination of the red RO (1 nW) and SP (3 nW) light for a duration of 70 μs, during which time we integrate all single-photon counts incident on an avalanche photo-diode (APD) ('check NV^-'). If a set photon-count threshold is exceeded, we have high confidence that the red lasers are well on resonance with their associated transitions and that the NV is in NV^-, and proceed to the next step. If the count is below the threshold, but above zero, then it is assumed that the NV is in the negative charge state and close to resonance, but not yet in a satisfactory regime. In this case, the red check is repeated until the threshold is passed. In the case that any red check produces a zero photon-count, the green pulse ('reset') is reapplied to reset the charge state or to induce significant spectral diffusion bringing the NV^- transitions back in resonance with the red lasers. We note that the low powers used for resonant excitation itself cause minimal spectral diffusion.

After the NV^- check, an ionisation pulse is applied to prepare NV^0 ('ionise'). Here, we apply 5 nW (10 nW) of RO (SP) light respectively, for a total duration of 1 ms. While the ionisation probability is low ($\sim$ 2%), the chosen powers ensure that spectral diffusion is minimal.

To verify that the NV has been successfully transferred to the neutral charge state and to confirm that the yellow light is on resonance with a single transition we apply 25 nW of yellow light for 250 μs ('check NV^0'). In this check, we either exceed the threshold, in which case we proceed to the main experiment, or we return to the 'check NV^-' step. The counts of each successful 'check NV^0' step are saved.

In our experiments, we use a single yellow laser only. We note that polarisation of this laser affects the spin-state prepared after the CR check. When exciting with linear polarisation, one of the two spin states is prepared in each experimental repetition. Which spin state is prepared may vary due to spectral diffusion between repetitions in combination with the close spectral vicinity between the spin states (see Fig. 3.7(a)). However, when exciting with circular polarisation, a single NV^0 spin-state is selectively addressed and heralded throughout: the probability to false-herald a non-targeted transition is negligible. While the laser frequency corresponds to a transition associated with a specific spin-orbit state, the check heralds a mixed orbital state as it takes significantly longer than the orbital relaxation time. We note that a general (not spin-selective) resonance check with higher efficiency could be achieved by adding a second laser to address a NV^0 transition corresponding to the opposite spin-state.

Finally, after the experiment has been completed, we perform the 'check NV^- after' step, which can be used to detect transfer from NV^0 to NV^- during the experiment. This is enabled by the fact that transfer between the NV charge states induces minimal spectral diffusion, as witnessed by our recharging data (Sec. 3.7.6).

We then return to the 'check NV^0' step due to two reasons. First, the detected counts can be used to readout the NV^0 spin state in the case recharging has not happened. Second, for most experimental repetitions we remain in NV^0, leaving a high probability that the 'check NV^0' step is passed again. In such cases, it is not necessary to repeat the 'check NV^-' step, reducing measurement overhead time.

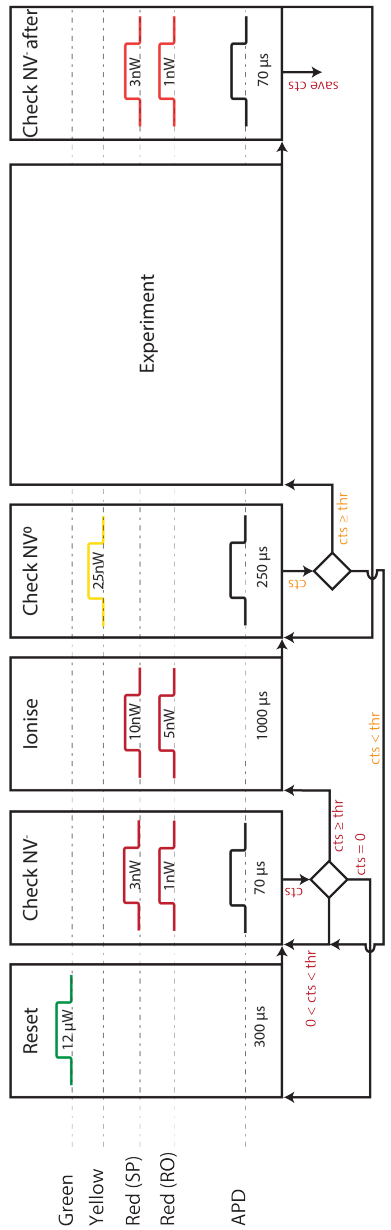

Figure 3.8: NV$^-$ and NV^0 CR check. The application of laser pulses, counting of PSB photons, and decisions depending if the measured counts (cts) have passed the preset thresholds (thr) are all performed via a microprocessor (ADWIN).

3.7.5. LINDBLAD MASTER EQUATION SIMULATIONS

In order to capture the full dynamics of the NV^0 system we develop a theoretical model based on the Lindblad master equation. In Eq. 3.4, we describe the initial (mixed) state of the system, whose populations are parameterised by probabilities p_i for $i \in \{0,..,5\}$. Eq. 3.5 describes the non-unitary time evolution of that state, $\rho(t)$:

$$\rho_0 = p_0 |+,\downarrow\rangle\langle+,\downarrow| + p_1 |-,\uparrow\rangle\langle-,\uparrow| + p_2 |-,\downarrow\rangle\langle-,\downarrow| + p_3 |+,\uparrow\rangle\langle+,\uparrow| + p_4 |0,\downarrow\rangle\langle0,\downarrow| + p_5 |0,\uparrow\rangle\langle0,\uparrow| \tag{3.4}$$

$$\dot{\rho}(t) = -\frac{i}{\hbar}[H(t),\rho(t)] + \sum_n C_n \rho(t) C_n^\dagger - \frac{1}{2}[\rho(t) C_n^\dagger C_n - C_n^\dagger C_n \rho(t)]. \tag{3.5}$$

Here, $H(t)$ is the time-dependent Hamiltonian, $\hbar$ the Planck constant and $C_n = \sqrt{\gamma} A_n$ the collapse operator capturing relaxation processes. A_n is the coupling operator and $\gamma = 1/\tau_{\text{relax}}$ the corresponding decay rate with relaxation time constant τ_{relax}.

We now show an example case for dynamics under optical pumping (see Fig. 3.2). In the experiment, we herald a specific spin-orbit state via the 'check NV^0' step, simultaneously bringing the yellow laser on resonance with the respective transition. As an example, we can herald the $|+,\downarrow\rangle$ state. However, due to orbital relaxation dynamics being much faster then the duration of the state check we effectively herald an orbitally mixed $|\downarrow\rangle$ state, i.e.

$$\rho_0 = \frac{1}{2}\left(|+,\downarrow\rangle\langle+,\downarrow| + |-,\downarrow\rangle\langle-,\downarrow|\right). \tag{3.6}$$

Under optical pumping, we can describe the (rotating frame) system Hamiltonian, $H(t)$, and the total collapse operator, $\sum_n C_n$ as:

$$H(t) = 2\pi \begin{array}{c} \begin{matrix} |+,\downarrow\rangle & |-,\uparrow\rangle & |-,\downarrow\rangle & |+,\uparrow\rangle & |0,\downarrow\rangle & |0,\uparrow\rangle \end{matrix} \\ \begin{pmatrix} 0 & 0 & 0 & 0 & \frac{\Omega(t)}{2} & 0 \\ 0 & 0 & 0 & 0 & 0 & \frac{\Omega(t)}{2} \\ 0 & 0 & 0 & 0 & 0 & 0 \\ 0 & 0 & 0 & 0 & 0 & 0 \\ \frac{\Omega(t)}{2} & 0 & 0 & 0 & \delta & 0 \\ 0 & \frac{\Omega(t)}{2} & 0 & 0 & 0 & \Delta+\delta \end{pmatrix} \end{array} \begin{matrix} \langle+,\downarrow| \\ \langle-,\uparrow| \\ \langle-,\downarrow| \\ \langle+,\uparrow| \\ \langle0,\downarrow| \\ \langle0,\uparrow| \end{matrix} \tag{3.7}$$

$$\sum_n C_n = \frac{1}{\sqrt{2}} \begin{array}{c} \begin{matrix} |+,\downarrow\rangle & |-,\uparrow\rangle & |-,\downarrow\rangle & |+,\uparrow\rangle & |0,\downarrow\rangle & |0,\uparrow\rangle \end{matrix} \\ \begin{pmatrix} 0 & 0 & \sqrt{\frac{1}{\tau_{\text{orbit}}}} & \sqrt{\frac{1}{\tau_{\text{spin}}}} & \sqrt{\frac{1}{\tau_{\text{exc}}}} & 0 \\ 0 & 0 & \sqrt{\frac{1}{\tau_{\text{spin}}}} & \sqrt{\frac{1}{\tau_{\text{orbit}}}} & 0 & \sqrt{\frac{1}{\tau_{\text{exc}}}} \\ \sqrt{\frac{1}{\tau_{\text{orbit}}}} & \sqrt{\frac{1}{\tau_{\text{spin}}}} & 0 & 0 & \sqrt{\frac{1}{\tau_{\text{exc}}}} & 0 \\ \sqrt{\frac{1}{\tau_{\text{spin}}}} & \sqrt{\frac{1}{\tau_{\text{orbit}}}} & 0 & 0 & 0 & \sqrt{\frac{1}{\tau_{\text{exc}}}} \\ 0 & 0 & 0 & 0 & 0 & \sqrt{\frac{1}{\tau_{\text{exc,spin}}}} \\ 0 & 0 & 0 & 0 & \sqrt{\frac{1}{\tau_{\text{exc,spin}}}} & 0 \end{pmatrix} \end{array} \begin{matrix} \langle+,\downarrow| \\ \langle-,\uparrow| \\ \langle-,\downarrow| \\ \langle+,\uparrow| \\ \langle0,\downarrow| \\ \langle0,\uparrow| \end{matrix} \tag{3.8}$$

The diagonal elements in the Hamiltonian of Eq. 3.7 correspond to the detuning of each transition with respect to the laser frequency, while the off-diagonal elements enable Rabi driving between respective levels. In our example, the laser is on resonance with the $|+,\downarrow\rangle \leftrightarrow |0,\downarrow\rangle$ transition. The transition $|-,\uparrow\rangle \leftrightarrow |0,\uparrow\rangle$ has a detuning of $\Delta = 160\,\text{MHz}$. An additional detuning, δ, is randomly sampled from a Gaussian distribution with FWHM $= 2\pi \times 20\,\text{MHz}$, to account for the effects of imperfect laser resonance checks or small spectral diffusion. The Rabi frequency is given by $\Omega(t) = \alpha\sqrt{P(t)}$, with α being a proportionality factor and $P(t)$ the time dependent laser power. Note that we neglect driving of the (far-detuned) upper spin-orbit states and thus omit the corresponding terms. In our simulations we implement $P(t)$ with rise/fall times as independently measured in our experiment, see Fig. 3.9(a). The elements in Eq. 3.8 correspond to relaxation processes between certain levels, see Fig. 3.5. Here we use the respective timescales as extracted in Sections 3.3-3.5.

In Fig. 3.9(b-c) we plot the simulated expectations values for two different temperature scenarios, both for a driving power of 5 nW. In both cases we observe that the $|+,\downarrow\rangle$ state is depopulated, while population in the opposite orbital state, $|-,\downarrow\rangle$, grows via the excited state, $|0,\downarrow\rangle$. Initially, a damped Rabi oscillation between $|+,\downarrow\rangle$ and $|0,\downarrow\rangle$ is observed, before a steady state population is reached. In the case of lower temperature and hence a slower orbital relaxation constant, τ_{orbit}, a stronger orbital pumping is observed. After the laser light is switched off, the excited state decays with τ_{exc}, while the two orbital states relax back to an equal population with the time constant τ_{orbit}.

In Fig. 3.2 we plot the expectation value of the excited state $|0,\downarrow\rangle$, and find an excellent agreement with the experimental fluorescence counts. This confirms the accuracy of our theoretical model, and shows that the observed NV^0 dynamics are well understood. We note that the timescales for spin relaxation, τ_{spin}, and spin pumping, $\tau_{\text{exc,spin}}$, are much longer than the pumping duration, and hence are not observed in this set of experiments.

3.7.6. RECHARGING DYNAMICS

An important feature of our experiments is the ability to switch between the NV^- and NV^0 charge states through resonant excitation. Ionisation ($NV^- \rightarrow NV^0$) under resonant excitation has previously been experimentally studied [34,40], and an ionisation mechanism was proposed that combines a two-photon and an Auger process [34]. While a mechanism for the recharging process ($NV^0 \rightarrow NV^-$) was also proposed, the power dependence under resonant excitation has not been measured [34]. Here we present such measurements.

We first herald the defect in the NV^0 state, see 'check NV^0' step in the previous section, with the yellow laser resonant to a single transition in the lower spin-orbit branch. We then apply yellow recharging light for a certain time, before we read-out the NV^- population via the 'check NV^- after' step. In Fig. 3.10(a) (Fig. 3.10(b)) we plot the NV^- population as a function of recharging time for linear (circular) polarisation, for a few selected powers. For all powers we observe a growth in NV^- population that eventually approaches unity both under high- and low-power excitation. This important observation shows both that high-fidelity switching can be achieved, and that the red read-out is robust: spectral diffusion remains minimal even for second long experiments. Addition-

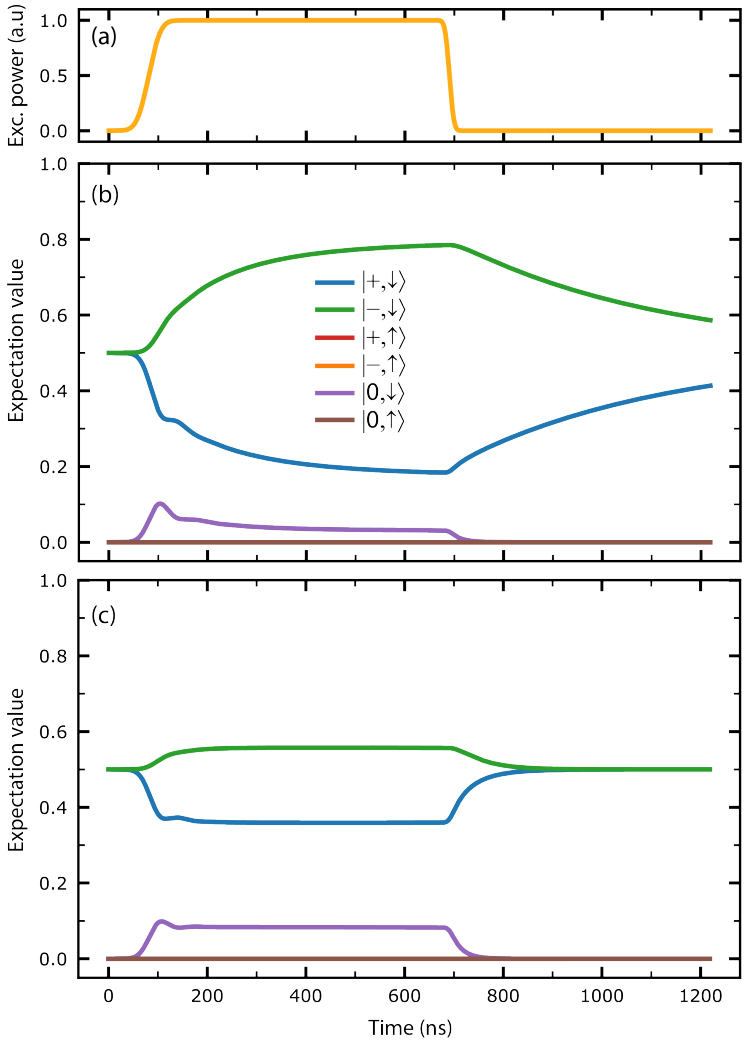

Figure 3.9: Master equation simulations. (a) Shape of the experimental yellow pulse with measured AOM rise and fall times of 30(5) and 7(1) ns, respectively. (b,c) Simulated expectation value for the relevant NV^0 levels (inset) under resonant excitation of $|+,\downarrow\rangle$ for $\tau_{\text{orbit}} = 425\,\text{ns}$ ($T = 4.65\,\text{K}$) (b) and $\tau_{\text{orbit}} = 50\,\text{ns}$ ($T = 10.1\,\text{K}$) (c). For the chosen power, population of the $|\uparrow\rangle$ spin levels remains zero throughout the simulation.

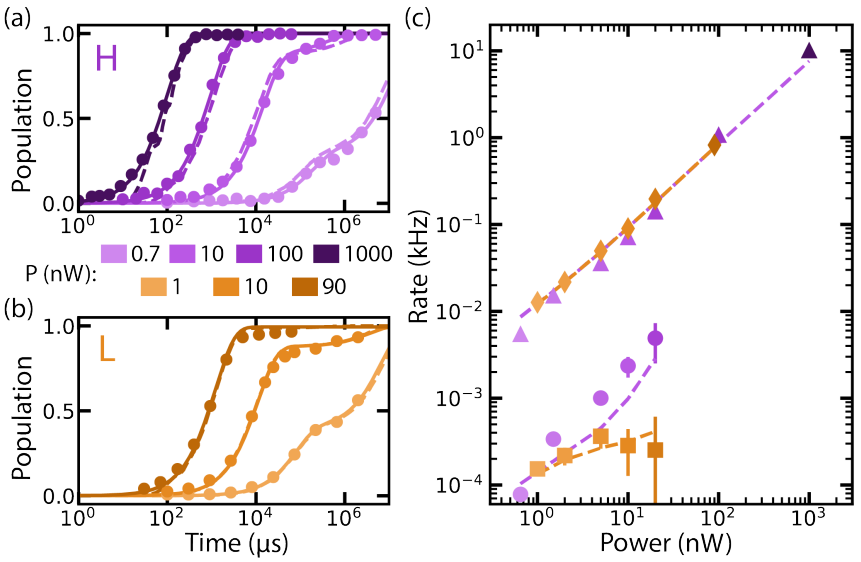

Figure 3.10: NV$^-$ population as a function of recharging time after initialisation into NV^0, for horizontal (a), and left circular (b) polarisation, respectively. Solid lines are fits following a double-exponential growth function, while dashed lines are populations obtained by Master equation simulations (see text). (c) Fitted fast and slow timescales as a function of the recharging power. Markers correspond to measured data for linear (triangles and circles) and circular (diamonds and squares) polarisation, while the dashed lines connect the values obtained from numerical simulations.

ally, the ability to reach near-unity NV$^-$ population within a few-hundred μs suggests that significant population is not trapped in the $^4A_2$ level of NV^0. Possible explanations for this observation are that the inter-system crossing rate is small, the $^4A_2$ lifetime is short, or the recharging process can also occur from the $^4A_2$ level itself.

For a range of recharging powers, we perform sweeps as exemplified in Figure 3.10(a) and (b), and fit with growth functions. For comparison, we additionally perform Master equation simulations, for which we can fit the same growth functions. In the simulations the NV$^-$ state is implemented as a dark state that can be populated via an excitation of the $^2A_2$ NV^0 state to the conduction band. Orbital dynamics are neglected as their corresponding timescales are much faster then the observed timescales for recharging. Further, in order to perform the simulations in reasonable computational time, the recharging rate, spin-pumping rate, and spin-relaxation rates are re-scaled by a fixed factor of four orders of magnitude. Remarkably, our simulations show both qualitative and quantitative agreement with the experimental data. At very short times small deviations arise as the (unmodified) excited-state lifetime becomes comparable to the re-scaled recharging process.

We generally anticipate two recharging timescales. A fast timescale, τ_{fast}, is associated with resonant recharging. A slow timescale, τ_{slow}, arises from NV^0 spin-pumping and spin-relaxation causing the driven transition to become dark, i.e. via a spin flip

$|\downarrow\rangle \leftrightarrow |\uparrow\rangle$. Recharging from the dark state occurs due to a combination of off-resonant excitation and relaxation back to the resonantly driven spin-state. Note that a slow timescale is expected for both linear and circular polarisation. The initial CR check prepares a single spin-state, and at low powers, both polarisations perform spin-selective driving as power-broadening is significantly less than the detuning between the $|\uparrow\rangle$ and $|\downarrow\rangle$ optical transitions. The behaviour can thus be described by a double-exponential growth function: $f(t_{\text{recharge}}) = Ae^{-t_{\text{recharge}}/\tau_{\text{fast}}} + (1-A)e^{-t_{\text{recharge}}/\tau_{\text{slow}}}$. Where it is not possible to fit a second timescale due to the dominance of the fast timescale (high powers), a single exponential growth function is used, $f(t_{\text{recharge}}) = Ae^{-t_{\text{recharge}}/\tau_{\text{fast}}}$.

In Fig. 3.10(c), we plot all of the fitted rates. Two key features are apparent. First, for both linear and circular polarisation, the fast timescales broadly overlap and follow a linear power-dependence, as expected for a two-photon process for which the first step is resonant and in saturation. From a linear fit we extract a recharging rate of 9.3(6) Hz/nW. Second, the slow timescale is seen to be significantly faster for linear than for circular polarisation. This difference arises from the fact that off-resonant excitation is strongly suppressed by circular polarisation, preventing both spin-pumping back to the resonant transition and off-resonant recharging. The extracted rates from the Master equation simulations are in good agreement with our experimental data both for the fast and the slow timescales.

Importantly, this characterisation can be used to determine the frequency of charge-resonance checks required in each experiment to ensure that the NV^0 population remains high.

3.7.7. PUMP-PROBE SPECTROSCOPY

Here, we describe the procedures followed for the pump-probe spectroscopy measurements, Fig. 3.3.

For each set temperature of the cryostat, we measure a series of time traces as exemplified in Fig. 3.3(a). For each time trace, we integrate the total photon counts during the first 40 ns after opening the AOM for the probe and pump measurements, respectively, and take their ratio. We then fit the recovery behaviour against the delay time, t_{delay}, following the function $f(t_{\text{delay}}) = a + A(1 - e^{-(t_{\text{delay}}-t_0)/T})$, where a is the steady-state fluorescence under pumping, A is the peak fluorescence of the mixed state, t_0 is the time at which the pump is turned off, and T is the characteristic recovery time. Between subsequent pump-probe experiments, there is a minimum delay of 3 μs, which is more than five times longer than the longest observed recovery time, ensuring that the system is reset between measurements.

At higher temperatures, a challenge for these measurements arises as the required time resolution exceeds that of the AOM rise- and fall-times, see Fig. 3.9(a), and hence the optical pulse is not turned off for the entirety of the set t_{delay}. We correct for this systematic error by calibrating the delay times as those for which the optical pulse falls below 90% of the full amplitude, measured using a fast photodiode. However, we note that some corrections may remain, which may lead to an underestimate of the orbital relaxation rates in those measurements. In future work, such measurements could be improved using a fast electro-optic modulator to gate the pulses.

3.7.8. RATE EQUATIONS

In order to extract the timescales for recharging and spin-pumping, as shown in Fig. 3.4, we develop a three-level model for which we can derive analytic solutions for use in a fitting routine.

We start with the scenario of Fig. 3.4(c). Given the relatively slow timescales under consideration (for 5 nW of yellow excitation), we choose to neglect the orbital basis (which is effectively mixed, see Eq. 3.6). This leaves three levels, $|\uparrow\rangle$, $|\downarrow\rangle$ and NV$^-$, which we denote as $U(t)$, $D(t)$, $N(t)$. We consider the processes of resonant recharging (r, from $D \rightarrow N$), resonant spin-pumping (p, from $D \rightarrow U$) and spin-relaxation (s, from $D \leftrightarrow U$), and neglect off-resonant recharging (from $U \rightarrow N$), off-resonant spin-pumping (from $U \rightarrow D$), and ionisation (from $N \rightarrow D, U$), which are all expected to have negligible rates in this parameter regime. The dynamics between these levels are thus described by the following coupled equations:

$$N(t) + D(t) + U(t) = 1 \tag{3.9}$$

$$\frac{dN(t)}{dt} = r\,D(t) \tag{3.10}$$

$$\frac{dD(t)}{dt} = -(r+s+p)\,D(t) + s\,U(t) \tag{3.11}$$

$$\frac{dU(t)}{dt} = +(s+p)\,D(t) - s\,U(t) \tag{3.12}$$

We impose initial conditions

$$D(0) = c_1 \tag{3.13}$$

$$U(0) = c_2 \tag{3.14}$$

$$N(0) = 1 - c_1 - c_2 \tag{3.15}$$

and derive analytic solutions to these equations (solutions available in code form upon request), which we then use as fitting functions for the measured populations. The spin relaxation time is fixed to the independently measured time of 1.51(1) s. All other parameters are free in the optimisation, leading to the following best-fit values:

τ_{spin} (s)	τ_{recharge} (s)	τ_{pump} (s)	c_1	c_2
1.51	0.027(1)	0.090(4)	0.960(6)	0.012(5)

Here, $\tau_{\text{spin}} = 1/s$, $\tau_{\text{recharge}} = 1/r$, $\tau_{\text{pump}} = 1/p$, and c_1 and c_2 are the respective populations in $|\downarrow\rangle$ and $|\uparrow\rangle$ after initialisation.

We now move to the scenario shown in Fig. 3.4(d). In this case, we stroboscopically interleave periods of 5 nW yellow excitation with periods of 500 nW of red NV$^-$ spin-pumping excitation coupled with hard microwave π-pulses regularly spaced by 1.25 μs. To simplify this into a rate-equation model, we make the following assumptions (along with those already made for the previous case). First, we combine the stroboscopic driving into continuous driving with averaged resonant recharging (r, from $D \rightarrow N$) and ionisation (i, from $N \rightarrow D, U$) rates. We assume that charge conversion from NV$^-$ to NV^0

results in a completely mixed NV^0 spin state: that is, the rate, i, equally couples to both D and U. We note that analytic solutions incorporating an asymmetry in these couplings were derived, but that any asymmetry could not be constrained by the fitting procedure. Finally, we assume that the microwaves only couple the (not-described) spin levels of NV^- — preventing spin-pumping in that charge state — and so only influence the rate i. Under this model, we arrive at the following set of coupled equations:

$$N(t) + D(t) + U(t) = 1 \tag{3.16}$$

$$\frac{dN(t)}{dt} = r\,D(t) - i\,N(t) \tag{3.17}$$

$$\frac{dD(t)}{dt} = -(r+s+p)\,D(t) + s\,U(t) + \frac{i}{2}\,N(t) \tag{3.18}$$

$$\frac{dU(t)}{dt} = +(s+p)\,D(t) - s\,U(t) + \frac{i}{2}\,N(t) \tag{3.19}$$

We again impose initial conditions

$$D(0) = c_1 \tag{3.20}$$

$$U(0) = c_2 \tag{3.21}$$

$$N(0) = 1 - c_1 - c_2 \tag{3.22}$$

and derive analytic solutions to these equations (solutions available in code form upon request), which we then use as fitting functions for the measured populations. For this scenario, we fix r, p, c_1 and c_2 to the values obtained from the fit to the previous case, as the initialisation step and yellow excitation parameters are unchanged. The spin-relaxation rate, s, is fixed to twice its previous value ($t_{\text{spin}} = 1.51/2$), as the time-axis on this plot is the total yellow excitation time, which is half of the total sequence time. This leaves only the ionisation rate unfixed, for which we obtain a fitted value of $\tau_{\text{ion}} = 1/i = 0.018(4)$ s. While the behaviour at short times is well described by the model, the long-time behaviour is not well captured. If all fit parameters are unconstrained, we find that the long-time behaviour is well described, and still obtain agreement to within 50% for all values, aside from for τ_{spin}, for which we now fit 0.14(1) s. This could indicate that the presence of red excitation and/or strong microwave driving induces an additional NV^0 spin-relaxation mechanism.

3.7.9. SPIN CYCLICITY

In order to extract the cyclicity of the $|\downarrow\rangle$ transition under resonant excitation as reported in Sec. 3.5 we use the following procedure. Here, we are interested on how many photons are scattered before the $|\downarrow\rangle$ spin state is left, i.e. before leaving the three-level system $\{|+,\downarrow\rangle, |-,\downarrow\rangle, |0,\downarrow\rangle\}$. The experiment starts when $|+,\downarrow\rangle$ is heralded, which can then be excited to $|0,\downarrow\rangle$ (for $P_{\text{yellow}} = 5$ nW a Rabi flop takes about 42 ns). From here the electron decays ($\tau_{\text{exc}} = 22(1)$ ns) either to $|+,\downarrow\rangle$ or to $|-,\downarrow\rangle$, each with a 50% probability. If it decays to $|+,\downarrow\rangle$ it can immediately be excited again, while $|-,\downarrow\rangle$ corresponds to a dark state that can only relax back to $|+,\downarrow\rangle$ via orbital relaxation ($\tau_{\text{orbit}} = 0.43(6)$ μs). This process continues until either a charge- or spin-flip event happens. From Fig. 3.4(c) we have extracted characteristic timescales of 27(1) ms (90(4) ms) for the charge conversion (spin

pumping) process. Within this regime the cyclicity is limited by charge conversion, for which we calculate $0.98(7) \times 10^5$ scattered photons before leaving the $|\downarrow\rangle$ manifold.

We note that at lower powers the recharging process, which requires a two-photon excitation, is expected to be suppressed. Here, the cyclicity will then be limited by a spin-flip process, enabling $3.2(2) \times 10^5$ cycles.

3.7.10. READOUT FIDELITY

In Sec. 3.5, we report single-shot read-out (RO) of the NV^0 spin state with fidelity, $F_{\text{RO}} \geq 98.2(9)\%$. Here we outline the characterisation procedure.

The readout fidelity is defined by the relation $F_{\text{RO}} = \frac{1}{2}(F_{\downarrow|\downarrow} + F_{\uparrow|\uparrow})$, where $F_{i|j}$ is the probability to assign the spin state $|i\rangle$ after preparing $|j\rangle$. Note that this assumes that each spin state can be initialised perfectly. Imperfect initialisation will lead to a decrease in the achievable fidelity: the calculated RO fidelities are thus a lower bound.

In the presented experiments, we use a single yellow laser for both state initialisation and readout. As this means that we are only able to herald the $|\downarrow\rangle$ state with high fidelity, we use the intrinsic spin relaxation process of NV^0 to prepare a mixed state, which can also be used to calculate the fidelity for $|\uparrow\rangle$ read-out. The histograms presented in Fig. 3.4(a) are used for this calculation.

First, to calculate $F_{\downarrow|\downarrow}$ and $F_{\uparrow|\downarrow}$, we herald $|\downarrow\rangle$ using a threshold of 25 photons for the 'check NV^0' step of Fig. 3.8. After a brief delay (0.1 ms), we check for any residual population in NV$^-$ ('check NV$^-$ after'), which is discarded. We then perform the 'check NV^0' step again to read out the spin population. From 3000 experimental shots, we discard 52 cases, corresponding to an NV$^-$ population of 1.7(2)%. Of the remainder, 98.4(2)% of cases match or exceed the chosen threshold of 5 photons (Sec. 3.5). We thus have: $F_{\downarrow|\downarrow}$ = 98.4(2)%, and $F_{\uparrow|\downarrow}$ = 1.6(2)%. We note that the initialisation fidelity of the $|\downarrow\rangle$ heralding step (25 nW for 250 μs) is likely limited by spin pumping to $|\uparrow\rangle$. From independent spin-pumping measurements we expect a reduction of that population by ~ 0.8% over the 250 μs, though this is partially mitigated by the initialisation threshold of 25 photons. Note that, while in this work the same parameters for initialisation and single-shot read-out are used, further optimisation of the heralding pulse may increase the state preparation fidelity in the future.

To calculate $F_{\uparrow|\uparrow}$ and $F_{\downarrow|\uparrow}$, we repeat the procedure, but now wait for 10 s between the first 'check NV^0' step and the 'check NV$^-$ after' step, preparing the mixed state. We anticipate a state preparation infidelity of < 0.2% arising from the finite waiting time.

After preparation of the fully mixed state, the RO outcomes are described by:

$$F_{\downarrow} = \frac{1}{2}(F_{\downarrow|\uparrow} + F_{\downarrow|\downarrow}) \tag{3.23}$$

$$F_{\uparrow} = \frac{1}{2}(F_{\uparrow|\uparrow} + F_{\uparrow|\downarrow}) \tag{3.24}$$

where $F_{\downarrow}$ ($F_{\uparrow}$) is the probability to obtain ≥ 5 photons (< 5 photons). In this experiment, we discard 35 cases attributed to NV$^-$, estimating the NV$^-$ population to be 1.2(2)%. From the remaining cases, we find $F_{\uparrow}$ = 49.8(9)% and $F_{\downarrow}$ = 50.2(9)%. Using the values previously obtained for $F_{\downarrow|\downarrow}$ and $F_{\uparrow|\downarrow}$, we obtain $F_{\uparrow|\uparrow}$ = 98(2)%, $F_{\downarrow|\uparrow}$ = 2(2)%.

Combining the results we arrive at a single-shot read-out fidelity, $F_{RO} \geq 98.2(9)\%$.

REFERENCES

[1] M. Atatüre, D. Englund, N. Vamivakas, S.-Y. Lee and J. Wrachtrup, *Material platforms for spin-based photonic quantum technologies,* Nat. Rev. Mater. **3**, 38 (2018).

[2] D. D. Awschalom, R. Hanson, J. Wrachtrup and B. B. Zhou, *Quantum technologies with optically interfaced solid-state spins,* Nat. Photonics **12**, 516 (2018).

[3] P. C. Humphreys *et al.*, *Deterministic delivery of remote entanglement on a quantum network,* Nature **558**, 268 (2018).

[4] C. E. Bradley *et al.*, *A ten-qubit solid-state spin register with quantum memory up to one minute,* Phys. Rev. X **9**, 031045 (2019).

[5] N. Aslam *et al.*, *Nanoscale nuclear magnetic resonance with chemical resolution,* Science **357**, 67 (2017).

[6] D. R. Glenn *et al.*, *High-resolution magnetic resonance spectroscopy using a solid-state spin sensor,* Nature **555**, 351 (2018).

[7] M. Abobeih *et al.*, *Atomic-scale imaging of a 27-nuclear-spin cluster using a quantum sensor,* Nature **576**, 411 (2019).

[8] B. J. Shields, Q. P. Unterreithmeier, N. P. de Leon, H. Park and M. D. Lukin, *Efficient readout of a single spin state in diamond via spin-to-charge conversion,* Phys. Rev. Lett. **114**, 136402 (2015).

[9] D. A. Hopper, H. J. Shulevitz and L. C. Bassett, *Spin readout techniques of the nitrogen-vacancy center in diamond,* Micromachines **9**, 437 (2018).

[10] S. Dhomkar, J. Henshaw, H. Jayakumar and C. A. Meriles, *Long-term data storage in diamond,* Sci. Adv. **2**, e1600911 (2016).

[11] P. C. Maurer *et al.*, *Room-Temperature Quantum Bit Memory Exceeding One Second,* Science **336**, 1283 (2012).

[12] M. Pfender *et al.*, *Protecting a Diamond Quantum Memory by Charge State Control,* Nano Lett. **17**, 5931 (2017).

[13] H. Bernien *et al.*, *Heralded entanglement between solid-state qubits separated by three metres,* Nature **497**, 86 (2013).

[14] D. A. Hopper, J. D. Lauigan, T.-Y. Huang and L. C. Bassett, *Real-time charge initialization of diamond nitrogen-vacancy centers for enhanced spin readout,* Phys. Rev. Appl. **13**, 024016 (2020).

[15] N. Kalb, P. C. Humphreys, J. Slim and R. Hanson, *Dephasing mechanisms of diamond-based nuclear-spin memories for quantum networks,* Phys. Rev. A **97**, 062330 (2018).

[16] M. S. Barson, E. Krausz, N. B. Manson and M. W. Doherty, *The fine structure of the neutral nitrogen-vacancy center in diamond,* Nanophotonics **8**, 1985 (2019).

[17] D. Braukmann, E. R. Glaser, T. A. Kennedy, M. Bayer and J. Debus, *Circularly polarized zero-phonon transitions of vacancies in diamond at high magnetic fields,* Phys. Rev. B **97**, 195448 (2018).

[18] L. C. Bassett, A. Alkauskas, A. L. Exarhos and K.-M. C. Fu, *Quantum defects by design,* Nanophotonics **8**, 1867 (2019).

[19] G. Davies, *Dynamic Jahn-Teller distortions at trigonal optical centres in diamond,* J. Phys. C **12**, 2551 (1979).

[20] Y. Mita, *Change of absorption spectra in type-Ib diamond with heavy neutron irradiation,* Phys. Rev. B **53**, 11360 (1996).

[21] T. A. Kennedy, J. S. Colton, J. E. Butler, R. C. Linares and P. J. Doering, *Long coherence times at 300 k for nitrogen-vacancy center spins in diamond grown by chemical vapor deposition,* Appl. Phys. Lett. **83**, 4190 (2003).

[22] T. Gaebel *et al.*, *Photochromism in single nitrogen-vacancy defect in diamond,* Appl. Phys. B **82**, 243 (2006).

[23] G. Waldherr *et al.*, *Dark states of single nitrogen-vacancy centers in diamond unraveled by single shot nmr,* Phys. Rev. Lett. **106**, 157601 (2011).

[24] N. Aslam, G. Waldherr, P. Neumann, F. Jelezko and J. Wrachtrup, *Photo-induced ionization dynamics of the nitrogen vacancy defect in diamond investigated by single-shot charge state detection,* New J. Phys. **15**, 013064 (2013).

[25] A. Gali, *Theory of the neutral nitrogen-vacancy center in diamond and its application to the realization of a qubit,* Phys. Rev. B **79**, 235210 (2009).

[26] N. B. Manson *et al.*, *Assignment of the NV^0 575-nm zero-phonon line in diamond to $a\,^2E$-$^2A_2$ transition,* Phys. Rev. B **87**, 155209 (2013).

[27] S. Felton *et al.*, *Electron paramagnetic resonance studies of the neutral nitrogen vacancy in diamond,* Phys. Rev. B **77**, 081201 (2008).

[28] B. J. Hensen, *Quantum nonlocality with spins in diamond,* Ph.D. Thesis, TUDelft (2016).

[29] Private communication with M. Barson, ANU Canberra, Australia (2020).

[30] K. Beha, A. Batalov, N. B. Manson, R. Bratschitsch and A. Leitenstorfer, *Optimum Photoluminescence Excitation and Recharging Cycle of Single Nitrogen-Vacancy Centers in Ultrapure Diamond,* Phys. Rev. Lett. **109**, 097404 (2012).

[31] R. Orbach and B. Bleaney, *Spin-lattice relaxation in rare-earth salts,* Proc. R. Soc. A **264**, 458 (1961).

[32] A. Abragam and B. Bleaney, *Electron paramagnetic resonance of transition ions* (OUP Oxford, 2012).

[33] J. Zhang, C.-Z. Wang, Z. Zhu, Q. H. Liu and K.-M. Ho, *Multimode jahn-teller effect in bulk systems: A case of the* NV^0 *center in diamond,* Phys. Rev. B **97**, 165204 (2018).

[34] P. Siyushev *et al.*, *Optically Controlled Switching of the Charge State of a Single Nitrogen-Vacancy Center in Diamond at Cryogenic Temperatures,* Phys. Rev. Lett. **110**, 167402 (2013).

[35] J. Hadden *et al.*, *Strongly enhanced photon collection from diamond defect centers under microfabricated integrated solid immersion lenses,* Appl. Phys. Lett. **97**, 241901 (2010).

[36] H. Bernien, *Control, measurement and entanglement of remote quantum spin registers in diamond,* Ph.D. Thesis, TUDelft (2014).

[37] M. W. Doherty *et al.*, *The nitrogen-vacancy colour centre in diamond,* Phys. Rep. **528**, 1 (2013).

[38] N. B. Manson *et al.*, NV—N+ *pair centre in 1b diamond,* New J. Phys. **20**, 113037 (2018).

[39] J. J. Olivero and R. Longbothum, *Empirical fits to the voigt line width: A brief review,* J. Quant. Spectrosc. Radiat. Transf. **17**, 233 (1977).

[40] L. Robledo, H. Bernien, I. van Weperen and R. Hanson, *Control and coherence of the optical transition of single nitrogen vacancy centers in diamond,* Phys. Rev. Lett. **105**, 177403 (2010).

4

ROBUST QUANTUM-NETWORK MEMORY IN ISOTOPICALLY ENGINEERED DIAMOND

C. E. Bradley, S. W. de Bone, P. F. W. Möller, S. Baier, M. J. Degen, S. J. H. Loenen, H. P. Bartling, M. Markham, D. J. Twitchen, R. Hanson, D. Elkouss, T. H. Taminiau

Optical quantum networks can enable long-range quantum communication and modular quantum computation. A powerful approach is to use network nodes that host additional qubits, which provide the quantum memory and computational power to perform entanglement distillation, quantum error correction, and information processing. Nuclear spins associated with optically-active defects in diamond are a promising candidate for this role. However, dephasing of these spin qubits during the creation of the optical network links hinders scaling to larger networks. In this work, we show that a single ^{13}C spin in isotopically engineered diamond offers a long-lived quantum memory that is robust to the optical link operation. The measured memory lifetime is improved by two orders-of-magnitude over the longest reported value, and exceeds the best reported times for making remote photonic entanglement. We identify ionisation of the NV centre as a newly limiting decoherence mechanism. As a first step towards overcoming this limitation, we demonstrate that the nuclear spin state can be retrieved with high fidelity after a complete cycle of ionisation and recapture. Finally, we use numerical simulations to show that the combination of this improved memory lifetime with previously demonstrated entanglement links and gate operations can enable key primitives for quantum networks, such as deterministic non-local two-qubit logic operations and GHZ state creation across four network nodes. Our results pave the way for test-bed diamond-based quantum networks capable of investigating complex algorithms and error correction.

The results of this chapter are in preparation for peer review.

4.1. INTRODUCTION

Optical quantum networks have the potential to enable a wealth of applications that go beyond classical technologies, including secure communication, quantum sensor networks, and distributed quantum computation [1–3]. Such a network consists of nodes with 'communication' qubits that are connected together by entanglement through photonic channels (Fig. 4.1(a)). Each node ideally contains multiple additional 'data' qubits that can be used to store and process quantum states. Universal operations over the network can then be performed by repeatedly distributing entangled states and subsequently consuming them [2].

Large-scale networks and universal quantum computation become possible if imperfections can be overcome through entanglement distillation and quantum error correction [2,3]. Besides high-fidelity operations, this requires the faithful storage of quantum states while new entangled states are repeatedly distributed over the network [2–4]. We capture this capability by a parameter that we term the 'network number', $N_{\text{network}} = r_{\text{ent}}/r_{\text{mem}}$, given by the ratio of the inter-node entanglement generation rate r_{ent} and the decoherence rate r_{mem} of the data qubits during network operation[†]. Without error correction, N_{network} sets the available number of cycles of entanglement distribution, and thereby the depth of protocols and computations that can be performed efficiently. While quantum error correction can ultimately increase achievable circuit depths, this will require $N_{\text{network}} \gg 1$ [2,3,6].

Various systems have demonstrated basic building blocks for optical quantum networks [5,7–15]. The nitrogen-vacancy (NV) centre in diamond is a promising platform because it combines a spin-photon interface for heralded remote entanglement [16–18], with access to multiple ^{13}C nuclear-spin data qubits that can store quantum states for long times [19–25]. Entanglement generation rates r_{ent} larger than the idle qubit decoherence rate have been shown, enabling a single cycle of entanglement delivery deterministically on a clock cycle [5]. As a first step towards exploiting additional computational power in the nodes, experiments with up to two qubits per node demonstrated two-cycle network protocols such as entanglement distillation [26] and entanglement-swapping in a three-node network [27]. However, in all these experiments $N_{\text{network}} < 0.1$. The resulting network operation is inherently probabilistic — if entanglement generation cycles do not succeed early enough, all previously established quantum states stored in the network memory are lost — hindering the scaling to larger systems operating over many cycles. Realizing large N_{network} will require higher entanglement rates r_{ent} through efficient spin photon interfaces [28–31] and/or reducing the dephasing of the nuclear spin qubits during network operation (r_{mem}) [26,32].

In this work, we focus on the latter challenge. We demonstrate that ^{13}C spin qubits in isotopically engineered diamond provide robust data qubits for NV-based quantum networks. We develop control and single-shot readout of an individual ^{13}C spin that is weakly coupled to a single NV centre. We then show that an arbitrary quantum state

[†]A related metric is the 'link efficiency' η_{link}, which has been defined as the ratio of the entanglement rate over the *idle* qubit decoherence rate, rather than the qubit decoherence during network operation [4,5]. This parameter η_{link} sets an upper bound on N_{network}, and a large η_{link} is a necessary, but not sufficient condition for realizing large-scale quantum networks.

can be stored in this data qubit for over $1{\cdot}10^5$ repetitions of the remote entanglement sequence. For current entanglement link success rates, this would imply $N_{\text{network}} \approx 10$. We show through numerical network simulations that this high N_{network} value can enable a next generation of network protocols, including deterministic two-qubit gates over the network and the distillation of entangled states over a four-node network, which provides a primitive for surface-code quantum error correction (Fig. 4.1(a)). Finally, we identify ionisation of the NV centre as the limiting mechanism and show that the data qubit can be protected through fast controlled resetting of the NV charge state. When combined with recent progress with optical cavities towards enhanced entanglement rates[29,31] and high-fidelity quantum gates[21,25,33], these results indicate that nuclear spins in isotopically engineered samples provide a promising path towards quantum networks.

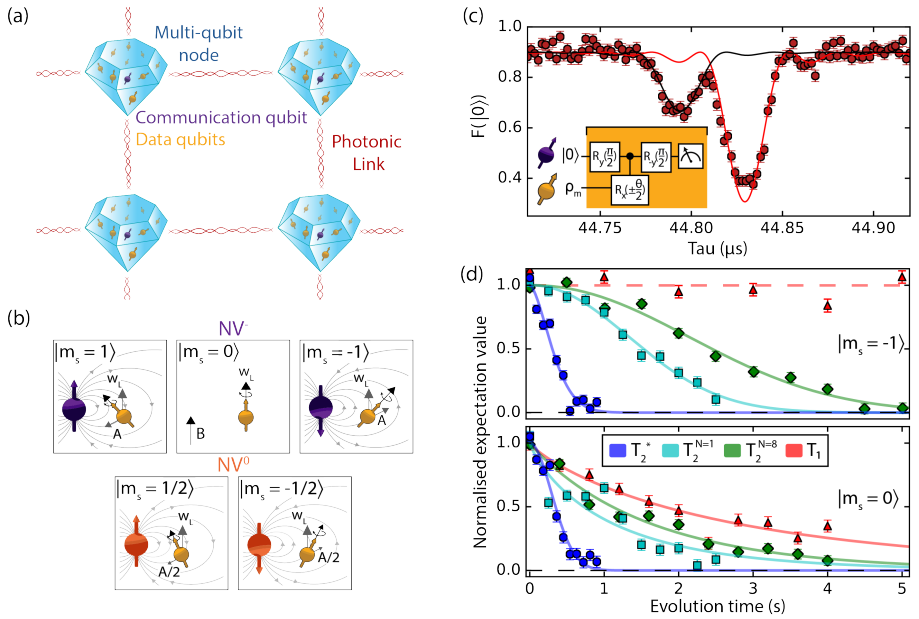

Figure 4.1: (a) Architecture for distributed quantum information processing using spins in diamond. Multi-qubit nodes are formed from electron spin 'communication' qubits (purple) which magnetically couple to nuclear spin 'data' qubits (yellow), allowing universal control. The coherent spin-photon interface of the link qubits enables the heralded creation of remote photonic entanglement between nodes. The data qubits enable long-lived storage and processing of quantum information. The network portrayed here forms a unit cell for distributed quantum error correction based on the surface code[2,3,6]. (b) Electron-nuclear hyperfine coupling: nuclear-spin precession at the Larmor frequency around an external magnetic field $\vec{B}$ is perturbed by the presence of the electron spin. Depending on the NV charge and spin states: NV^- (purple), $m_s = \{-1, 0, +1\}$, or NV^0 (orange), $m_s = \{-1/2, +1/2\}$, the precession frequency and axis are modified. (c) Dynamical decoupling spectroscopy of the NV centre[34]. The resonance at 44.832 μs (red) reveals a single ^{13}C spin with hyperfine parameters $A_\parallel = 2\pi \cdot 80(1)$ Hz and $A_\perp = 2\pi \cdot 271(4)$ Hz. The resonance at 44.794 μs (black) corresponds to the ^{13}C spin bath. Solid lines correspond to a theoretical model (Sec. 4.9.1). (d) Intrinsic decoherence timescales of the nuclear spin for differing electron states. Solid lines are fits (Sec. 4.8). Dashed lines are guides to the eye. N denotes the number of spin-echo pulses. All error bars are one standard error.

4.2. SYSTEM OVERVIEW

We consider quantum network nodes consisting of a single NV centre coupled to multiple ^{13}C nuclear spins (Fig. 4.1(a)). The optically active NV electron spin acts as a communication qubit and the ^{13}C nuclear spins are additional data qubits that also function as quantum memory to store states while new entanglement links between NV centres are established. A key feature of this system is that the ^{13}C spin dynamics depend on the NV electron spin state (Fig. 4.1(b)). This is captured by the Hamiltonian for a single ^{13}C spin:

$$H = \omega_L I_z + A_\parallel m_s I_z + A_\perp m_s I_x. \tag{4.1}$$

Here, we have made the secular approximation. $\omega_L = \gamma_C B_z$ is the nuclear spin Larmor frequency, where γ_C is the ^{13}C gyromagnetic ratio and B_z is the external magnetic field along the NV axis (here $B_z = 47$ G). I_α are the nuclear spin-1/2 operators, while m_s is the spin-z projection of the electron spin. In the NV$^-$ charge state that is used for network operation, $m_s \in \{-1, 0, 1\}$, from which we define a qubit in the $\{-1, 0\}$ basis ($:= \{|1\rangle, |0\rangle\}$). Additionally, however, stochastic ionisation events can convert NV$^-$ to the NV^0 state with $m_s \in \{-1/2, +1/2\}$.

As seen from Eq. 4.1, the ^{13}C spin undergoes differing precession dependent on the electron charge- and spin-state. This conditional precession enables complete control over the ^{13}C spins by controlled inversions of the electron NV spin[21]. Uncontrolled electron-spin dynamics, however, induce additional dephasing of the ^{13}C spin, which sets a limit on the achievable network number N_{network}[20,32,35]. Our approach to creating robust memory is to reduce the coupling between the NV electron spin and the ^{13}C data qubits by reducing the ^{13}C concentration. While this approach results in slower gate speeds, these are not the rate-limiting step in current network experiments[27]. Note that, in the case of ^{13}C-spin-bath-limited decoherence, the coherence times increase proportionally with the reduction in coupling strength, such that no intrinsic reduction in gate fidelity is expected[36,37].

Our experiments are performed on a single NV centre in a type-IIa isotopically-purified diamond (targeted ^{13}C concentration of 0.01%) at a temperature of 4 K. The hardware setup and NV centre properties are described in Sec. 4.8.

Dynamical decoupling (DD) spectroscopy with the NV centre[34] reveals coupling to an isolated ^{13}C spin, along with the wider spin bath (Fig. 4.1(c)). We characterise the electron-nuclear hyperfine components parallel (perpendicular) to the NV axis to be $A_\parallel = 2\pi \cdot 80(1)$ Hz ($A_\perp = 2\pi \cdot 271(4)$ Hz)[34,38]. In comparison to previous studies in natural ^{13}C abundance samples[20,32], the electron-nuclear coupling strength is reduced by approximately two orders of magnitude, as expected from the isotopic concentration.

We realise universal control over the electron-^{13}C two-qubit system by microwave (MW) and radio-frequency (RF) single-qubit gates, and a DD-based electron-nuclear two-qubit gate[21,39]. Furthermore, we develop repetitive readout of the nuclear spin to improve the single-shot readout fidelity[19,40–44], giving a maximum state preparation and measurement (SPAM) fidelity of 91(1)% (Sec. 4.9.1). For the measurements reported here we focus on the system dynamics rather than maximising the fidelities, and thus use a faster initialisation procedure to optimise the signal-to-noise ratio, with lower SPAM fidelity of 79.4(9)% (Sec. 4.9.1). The fidelities are predominantly limited by electron-spin

decoherence during two-qubit gates, likely arising from the high concentration of P1 centre impurities in this specific device (~ 75 ppb[45]). Multi-qubit registers with comparable two-qubit gate fidelities to those achieved in natural-abundance ^{13}C devices (~99%[21]) are expected to be feasible with reduced impurity concentration in future diamond growth.

4.3. MEMORY ROBUSTNESS WHILE IDLING

We first investigate the intrinsic decoherence processes of the ^{13}C nuclear spin, i.e. when the electron spin is idle. The electron spin state affects spin-bath dynamics, as flip-flop interactions between nuclear spins are suppressed when the hyperfine interaction is present (the 'frozen core' effect)[21,46,47]. Therefore, we separately characterise the decoherence timescales with the NV electron in the $|1\rangle$ or $|0\rangle$ states.

Figure 4.1(d) summarises the measured timescales. The observation of vastly longer $T_{1,e=|1\rangle}$ ($\gg$ 5 s) than $T_{1,e=|0\rangle}$ (= 2.8(2) s) indicates that the spin relaxes primarily through flip-flop interactions with other ^{13}C spins. The measured $T_{1,e=|0\rangle}$ is approximately 30-100 times longer than typical values for natural abundance samples, consistent with the expectation of a linear dependence on isotopic concentration[36,37].

The measured dephasing times are $T^*_{2,e=|1\rangle}$ = 0.38(1) s and $T^*_{2,e=|0\rangle}$ = 0.42(2) s. We first isolate the timescale associated with couplings to the nuclear spin bath by performing a spin-echo experiment on all ^{13}C spins, decoupling the ^{13}C bath from other processes but leaving their mutual interactions unperturbed. We find a characteristic timescale, $T^*_{2,^{13}\mathrm{C-bath}}$ = 0.66(3) s (Sec. 4.9.2). The contribution from P1 impurities can similarly be estimated using the NV electron dephasing time during double electron-electron resonance measurements with the P1 impurities, $T^{*,e}_{2,\mathrm{P1-bath}}$ = 230 μs[45]. From the respective gyromagnetic ratios, γ_C, γ_e, we infer $T^*_{2,\mathrm{P1-bath}}$ = 0.61 s. Combining these processes gives an estimate for T_2^* ~ 0.45 s, close to the measured values.

We finally consider the application of spin echoes which mitigate quasi-static noise. The single-echo $T^{N=1}_{2,e=|0\rangle}$ (= 1.11(8) s) and eight-echo $T^{N=8}_{2,e=|0\rangle}$ (= 1.62(9) s) are likely limited by the m_s = 0 nuclear T_1. The observation of some underlying structure in these measurements is likely due to the dynamics of other proximal ^{13}C spins[18]. However, in the electron $|1\rangle$ state, the nuclear spin frozen core has previously been shown to significantly enhance ^{13}C spin-echo times[21]. While $T^{N=1}_{2,e=|1\rangle}$ (= 1.82(6) s) and $T^{N=8}_{2,e=|1\rangle}$ (= 2.91(8) s) do exceed $T^{N=1,8}_{2,e=|0\rangle}$ respectively, they are shorter than would be predicted from the ^{13}C concentration alone (~ 1 minute). We ascribe this to the presence of the P1 bath, which exhibits faster dynamics which are not well mitigated by echo pulses.

4.4. MEMORY ROBUSTNESS DURING NETWORK OPERATION

Armed with a characterisation of the intrinsic decoherence processes, we now turn to the remote entanglement sequence shown in Figs. 4.2(a,b). This entangling primitive is compatible with single-photon schemes used in recent NV network experiments[5,27,48]. In this work, we implement the protocol on a single network node to investigate its effect on the ^{13}C data qubit.

As discussed in the previous sections, imperfect knowledge of the electron spin state

leads to spurious phases acquired by the nuclear spin. Within each entangling attempt, there are a number of processes which can lead to such dephasing: the stochastic nature of the electronic spin reset time, infidelities in the initialised electron spin state, excited state spin-flips after the optical π-pulse, and MW pulse errors. Reducing the electron-nuclear coupling strength enhances the robustness to such events.

We implement the entangling protocol experimentally. For simplicity, we omit the optical π-pulses, but note that the small associated electron spin-flip probability is expected to play a negligible effect on the ^{13}C decoherence[20,32]. As a trade-off between the optical reset rate and stochastic ionisation to NV^0 [49,50], spin reset is performed using 30 nW of optical power for 5 μs, resulting in an initialisation fidelity $\geq$ 98% (Sec. 4.9.3). For the MW pulse used to create the electron superposition state, we implement a weak multi-tone driving pulse ($\Omega_{\text{Rabi}} \sim 93$ KHz) (Sec. 4.9.4). This comes at the expense of a time overhead, but mitigates heating. We set the MW rotation angle to $\pi/2$, for which dephasing due to the entangling primitive is expected to be maximal for the given sequence (Sec. 4.9.6). Finally, as we are considering networks for distributed quantum computation, we assume that the distance between network nodes is small (< 100 m). Thus, any decision logic can be completed within 1 μs. With these choices, the total duration of each primitive is 9 μs.

We prepare the nuclear spin in each of the six cardinal states ($\Psi_i \in \{|x\rangle,|-x\rangle,|y\rangle,|-y\rangle,|\uparrow\rangle,|\downarrow\rangle\}$), apply N repetitions of the primitive, and measure the expectation value in the associated eigenbasis, $\langle\hat{\sigma}_j\rangle = \text{Tr}(\rho\,\hat{\sigma}_j)$, where σ_j are nuclear spin Pauli operators, j $\in$ {x,y,z} (Fig. 4.2(c)). We interleave one cycle of XY8 decoupling pulses on the nuclear spin to mitigate dephasing. Without any post-selection of the data we find that the data qubit can preserve an arbitrary quantum state for $N_{1/e} = 1.33(4)\cdot10^5$ entangling primitives (1.20(4) s of continuous entanglement attempts).

We now consider the effects of ionisation and spectral diffusion on the data. After each experimental run, we perform two-laser probe measurements (E', E_y transitions), denoted charge-resonance (CR) checks (Sec. 4.9.7)[17]. The number of photons detected in this check is used to verify that the NV remained in NV^- and on resonance throughout the experiment. By varying the post-selection threshold for the CR check, we can reject measurements in which the NV ionised or underwent spectral diffusion with increasing confidence. We find a further improvement in the data qubit lifetime when omitting these cases, showing that they are currently a significant limitation (Fig. 4.2(c)). After accounting for ionisation and spectral diffusion, we fit a decay time $N_{1/e} = 2.07(8)\cdot10^5$. Considering spin superposition- and eigen-states separately, we find $N_{1/e,xy} = 1.90(8)\cdot10^5$ [1.71(7) s] and $N_{1/e,z} = 2.6(2)\cdot10^5$ attempts [2.4(2) s].

In Sec. 4.9.5, we additionally present results for the decay of a superposition state when using strong microwave pulses, so that the sequence is shorter (primitive duration 6.3 μs). We find a further improved corrected decay constant of $N_{1/e,x} = 4(1)\cdot10^5$ attempts [2.6(6) s]. However, in this case, we cannot rule out that heating due to the strong pulses changes the repumping dynamics, although the observation of similar ionisation statistics suggests that this is not the case. Such heating can be addressed by improved device engineering in future work.

For both primitive durations (6.3 μs and 9 μs), the measured decoherence timescales are comparable to those arising from intrinsic spin-bath dynamics. This suggests that

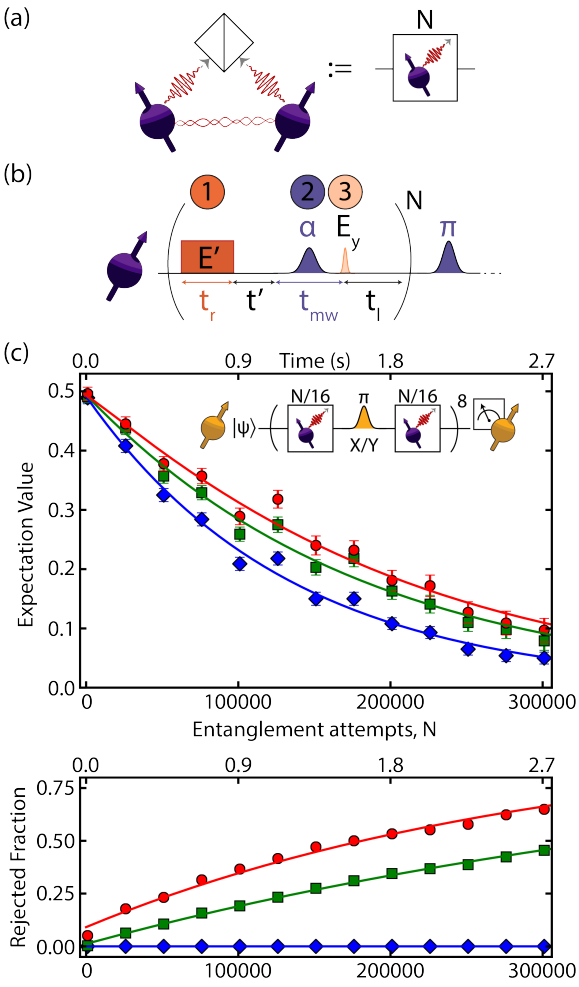

Figure 4.2: Memory robustness under remote-entanglement generation: (a) Sketch of a remote-entanglement process. After generation of local spin-photon entanglement at each node (see (b)), a detection event at a central beamsplitter heralds remote entanglement. Due to loss processes, the protocol is probabilistic. (b) Remote entanglement primitive: (1) The electron spin is reset by an optical pulse of duration $t_r = 5\ \mu$s. (2) After a time $t' = 200$ ns, a microwave pulse of duration $t_{mw} = 2.8\ \mu$s prepares a spin superposition state. (3) An optical π-pulse generates spin-photon entanglement, after which a time $t_l = 1\ \mu$s is required to determine whether the attempt succeeded. In case of success, a microwave π-pulse is used to preserve the electron coherence. E' and E_y denote optical transitions (Sec. 4.8). (c) Data qubit expectation value in the encoded state eigenbasis, as a function of the number of applied primitives (see (b)), averaged over the six cardinal states. Diamonds (squares and circles) correspond to no post-selection (post-selection on measuring ≥1 and ≥5 photons in a CR check performed at the end of the sequence). Solid lines are fits (see Sec. 4.8). Lower panel shows the fraction of rejected data for the three cases.

the entanglement sequence only weakly increases the dephasing of the ^{13}C spin.

We use Monte Carlo simulations to model the nuclear spin dephasing induced by

the entanglement attempts, taking into account all known control errors (Sec. 4.9.6) but neglecting the intrinsic decoherence rates[20]. We find that even using pessimistic parameters, an $A_{\parallel} = 2\pi \cdot 80$ Hz coupled nuclear spin is predicted to retain a fidelity of 77.6(4)% with respect to an initial superposition state after 10^6 entangling attempts. This finding is consistent with the interpretation of spin-bath limited decoherence in the present experiment.

Our simulations also show that the dephasing infidelity after 10^6 entangling attempts can be reduced below 1% by using optimised primitives incorporating an additional electron spin echo (Sec. 4.9.6). Further improvement of the performance can be realised by reducing the entangling primitive duration, such that more attempts can be performed within the intrinsic decoherence timescales. These intrinsic timescales may themselves be extended by optimised decoupling schemes[51] as well as using samples with lower nitrogen defect concentrations. It is clear, however, that ionisation currently is a limiting factor. We next probe the nuclear spin dynamics after such ionisation events to understand if they can be mitigated.

4.5. MITIGATING IONISATION

The above section indicates that ionisation of the NV centre limits achievable memory performance. In the above experiments, and in all work up to now[20,27,32], an ionisation event ($NV^- \rightarrow NV^0$) at some point in the sequence causes complete dephasing of the ^{13}C spins. This is because such events occur stochastically, the subsequent electron spin dynamics are unknown, and, as discussed above (see Eq. 4.1 and Fig. 4.1(b)), each electron spin state causes different ^{13}C spin evolution. Ionisation rates lower than those presented here can be achieved, because single-photon entangling schemes typically use unbalanced spin-superposition states for which the optical excitation probabilities are much smaller[5,27]. However, because weaker optical powers result in longer sequence times and the optical π-pulses cannot be removed, it is challenging to completely prevent ionisation. A promising approach is to develop techniques which make the data qubit robust to this process.

In order to study the effect of charge-state switching, we implement resonant optical pulses that induce ionisation ($NV^- \rightarrow NV^0$, 1 ms) and recharging ($NV^0 \rightarrow NV^-$, 1 ms). Combining these pulses with CR checks, we can use heralding and post-selection to perform verified charge-state switching from $NV^- \rightarrow NV^0 \rightarrow NV^-$ (Sec. 4.9.7).

We first combine the verified charge-state switching protocol with nuclear spin control to investigate the properties of the ^{13}C spin for the NV^0 state. After preparing NV^- and initialising the nuclear spin in the state $|\uparrow\rangle$, we apply the ionisation pulse, and proceed with the experiment if a subsequent CR check heralds preparation in NV^0. We then apply a nuclear spin RF π-pulse with a Rabi frequency of 5.4(2) Hz, for which we sweep the carrier frequency f. After applying the recharge pulse, we read out the nuclear spin in the Z-basis and post-select the data on finding the NV in NV^-. As shown in Fig. 4.3(a), we observe a single nuclear spin resonance at a frequency of 50229.8(1) Hz, which matches the ^{13}C Larmor frequency. The observation of a single transition, rather than two transitions at $f = \omega_L \pm A_{\parallel}/2$, suggest a fast averaging over the two NV^0 electron spin states, akin to motional narrowing[19].

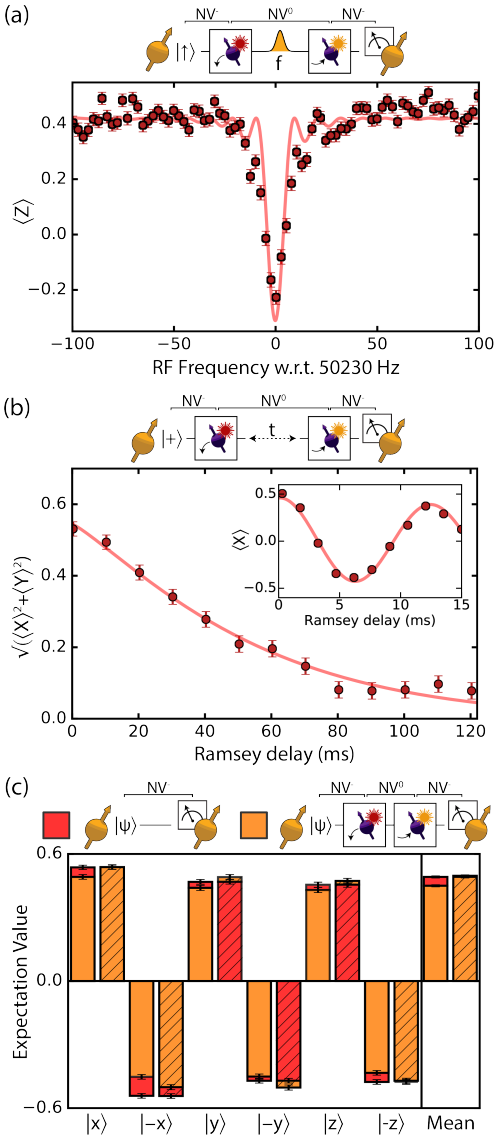

Figure 4.3: (a) Nuclear magnetic resonance spectroscopy after heralded preparation of NV^0. Solid line is a fit (Sec. 4.8). (b) Free induction decay of the nuclear spin coherence in NV^0. Inset: Ramsey fringes measured during the first 15 ms of free evolution (artificial detuning of 80 Hz with respect to 50230 Hz). Solid lines are fits (Sec. 4.8). (c) Protection of an arbitrary data qubit state under NV charge cycling. Orange (red) bars correspond to measurements with a charge-state cycle (idling in NV^-) between nuclear spin initialisation and readout. Solid (hatched) bars correspond to all measured data (post-selection on finding the NV in the negative charge state).

To characterise the nuclear spin dephasing, we prepare the nuclear spin in a superposition state, and let it evolve freely while switching to NV^0 for a variable time. The inset of Fig. 4.3(b) reveals coherent oscillations, corresponding to precession of the nuclear spin at a frequency of 50231(1) Hz. The nuclear spin coherence $(\langle X\rangle^2 + \langle Y\rangle^2)^{1/2}$ decays as $T^*_{2,\mathrm{NV0}} = 57(3)$ ms. This dephasing time is significantly shorter than for NV^- ($T^*_{2,\mathrm{NV-}} \sim 0.4$ s, Fig. 4.1(d)), indicating that the NV^0 state introduces an additional dephasing mechanism. The fitted decay exponent of $n = 1.2(1)$ (Sec. 4.8) matches the value of $n = 1$ expected for the motional-narrowing-like regime [19].

The observation of a single nuclear spin frequency and a decreased T_2^* are consistent with a rapidly fluctuating NV^0 electron spin state. In this regime, the dephasing time scales as $T_2^* = 8/(A_\parallel^2 \cdot T_1^{\mathrm{NV0}})$ [19,52]. Thus, we can extract $T_1^{\mathrm{NV0}} = 570(30)$ μs. This value deviates from another recent cryogenic measurement ($T_1^{\mathrm{NV0}} = 1.51(1)$s) [53]. It is likely that this discrepancy is either due to the much higher magnetic field ($B_z = 1850$ G) or absence of a P1 bath in that work.

The observed nuclear spin dephasing time in NV^0 is much longer than the time needed to recharge to NV^-. We now show that this enables the protection of the data qubit from ionisation events. We prepare the ^{13}C in each of the six cardinal states, and compare the expectation values obtained when applying the ionisation and recharging process prior to measurement, or when measuring immediately after state preparation. Here, to minimise dephasing during the ionisation and recharging processes, we shorten the ionisation pulse length to 0.3 ms, and use a higher-power 0.5 ms recharging pulse (Sec. 4.9.7).

Without post-selecting cases in which the NV returned to the bright state, we find a reduction of the spin expectation values of 8(1)% (averaged over the cardinal states) when applying the charge-state cycle (Fig. 4.3(c)). Upon post-selection, we find a negligible difference between the cases (the charge-cycle scenario outperforms immediate measurement by 1(1)%). We thus attribute the majority of the current infidelity to the finite recharging probability, which is likely limited by spectral diffusion arising from the high impurity concentration in the present sample (Sec. 4.9.7). We estimate that the NV is in the NV^0 state for an average of ~ 500 μs, for which the ^{13}C dephasing from the measured $T^*_{2,\mathrm{NV0}}$ is $\sim 0.5\%$, within the uncertainty of the present measurements.

Incorporating such ionisation protection within a network protocol requires a few further considerations. First, the average nuclear spin precession frequency during the entangling primitives should match the precession for NV^0, else additional dephasing will occur at the difference frequency until recharging occurs. This can be realised by alternating the choice of NV^- qubit-basis $m_s = \{0,-1\},\{0,+1\}$ between entangling attempts. Second, re-charging within the entangling sequence can be realised by adding auxiliary 575 nm excitation during all NV^- spin-reset pulses, which prevents extended periods in which the NV resides in the neutral charge-state [5]. A drawback of this approach is that extensive application of yellow light may induce spectral diffusion due to ionisation of the P1 bath or other impurities [54]. A second, less intrusive approach is to interleave periodic CR checks within the entangling sequence. Efficiently scheduling such checks into a full remote entangling protocol is non-trivial, but the timescales associated with ionisation, data qubit dephasing in NV^0, CR-checking and recharging suggest that such an approach is feasible.

We note that the NV^0 spin-T_1 may increase with reduction of impurities, or under different magnetic fields, which would result in faster nuclear spin dephasing. This challenge might be overcome by either inducing fast NV^0 spin-flips using microwave driving, or by performing feedback correction using recently demonstrated NV^0 optical spin-readout at high magnetic fields[53].

4.6. NUMERICAL ANALYSIS OF QUANTUM NETWORK PROTOCOLS

Finally, we investigate the projected performance of a number of quantum network protocols when combining the improved memory lifetime demonstrated in this work with previously demonstrated entanglement links and gate operations. We focus on non-local two-qubit operations and the creation of distributed four-qubit GHZ states, a key building block for the distributed surface-code[2,3] (Fig. 4.1(a)).

These investigations are based upon density-matrix simulations of noisy quantum circuits. We use the following set of parameters to model the dominant error sources, which are either the measured state-of-the-art (on a variety of devices) or near-term predictions (denoted by *): two-qubit gates (1% infidelity[21]), NV optical measurement (1% infidelity*[9]), and networked (NV-NV) Bell-pair creation (10% infidelity*[27]). We account for the finite duration associated with each operation, including probabilistic NV-NV remote entanglement (duration 6 μs, success probability 0.01%*[27]), and for decoherence of electron and nuclear spin qubits across all operations[18,21]. We do not take NV ionisation into account. A detailed summary of the models and parameters used can be found in Sec. 4.9.8.

In Figs. 4.4(a,b,c), we show the quantum circuit and simulated average fidelity F_{av}[55] for a deterministic CNOT operation between nuclear spins in separate network nodes. For $N_{1/e} = 2{\cdot}10^3$ (achieved in previous work[27]), the projected average fidelity is $F_{\text{av}} \approx 0.33$, close to that of a completely random operation ($F_{\text{av}} = 0.25$); the nuclear spin decoheres on a timescale shorter than the average time taken to create an entangled resource state. In contrast, for the $N_{1/e} = 2{\cdot}10^5$ as obtained here, we find a projected gate fidelity of $F_{\text{av}} \approx 0.86$, which approaches the limit of $F_{\text{av}} \approx 0.89$ set by the quality of the NV-NV Bell-pair resource state, local two-qubit gate operations, and measurement errors. These results indicate that deterministic two-qubit gate operations across optical quantum networks are within reach.

We next turn to protocols for GHZ state synthesis between four network nodes. We compare three protocols, which are schematically depicted in Fig. 4.4(d). First, we have the 'Plain' protocol, the simplest known approach which fuses three distributed Bell pairs into a GHZ state. Second, we have the recently identified 'Modicum' protocol[6], which extends the Plain protocol by one additional Bell pair creation step between two otherwise idling nodes to realise a single step of entanglement distillation. Finally, we have the 'Expedient' protocol introduced by Nickerson *et al.*[2], which uses 22 Bell pairs in total to perform additional rounds of distillation, and, in principle, can lead to high-quality GHZ states even in the presence of errors. Note, however, that previous work did not take into account the decoherence of the data qubits during entangling sequences or idling[2].

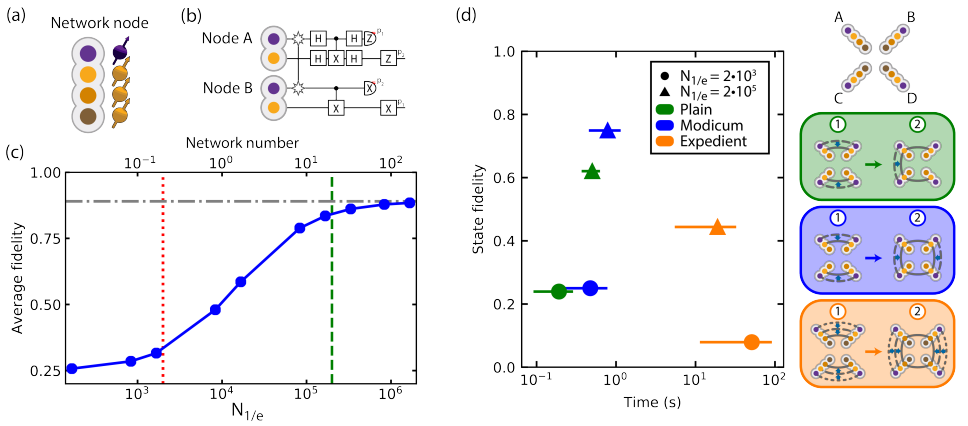

Figure 4.4: (a) Diagram of a single network node comprising an electron spin (purple) and up to three nuclear spins (orange tones). (b) Quantum circuit for a CNOT operation between nuclear spins in separate network nodes. $p_{1,2}$ are feed-forward operations. The gate is performed deterministically: the nuclear-spin states are prepared, then entanglement is distributed, and the gate is performed independent of the number of entanglement attempts required and for all measurement outcomes. (c) Simulated performance of the non-local CNOT protocol (see (b)) for a range of data qubit lifetimes. With the improvements achieved in this work ($N_{1/e}$ = $2{\cdot}10^5$), the average CNOT fidelity, $F_{av} \approx 0.86$ approaches the limit of 0.89 set by other error sources (grey line), see text. Conversely, the longest previously measured lifetime ($N_{1/e} = 2{\cdot}10^3$, Ref.[27]) would only enable a CNOT fidelity of $F_{av} \approx 0.33$. Error bars are smaller than markers. (d) Simulated performance for creation of a GHZ state between four network nodes, for three different protocols as schematised on the right. Further details of each protocol are given in Sec. 4.9.8. In all cases, the progress made in this work ($N_{1/e} = 2{\cdot}10^5$) leads to significant fidelity improvements, at the cost of a increase in protocol duration due to the slower two-qubit gates. The horizontal error bars in (d) indicate the distribution of durations taken for each protocol to succeed (68.2% confidence intervals).

In Fig. 4.4(d), we plot the simulated GHZ state fidelities ($F_{state} = \langle\Psi_{GHZ}|\rho|\Psi_{GHZ}\rangle$) for each protocol, alongside the average duration to prepare the state. For each scheme, there are two data points, which show the fidelities obtained when considering the data qubit lifetimes of $N_{1/e} = 2{\cdot}10^3$ and $N_{1/e} = 2{\cdot}10^5$ respectively. The first observation is that, for all the tested schemes, the improved lifetimes lead to significantly higher fidelities. With the lifetime achieved in this work, the simulated GHZ fidelities for the Plain and Modicum protocols exceed $F = 0.5$, confirming genuine multipartite entanglement of four qubits.

The differences in performance between the schemes with $N_{1/e} = 2{\cdot}10^5$ give insights into the usefulness of entanglement distillation for the considered parameter regime. First, between the Plain and Modicum protocols, we see that the additional distillation step does improve the fidelity, from F=0.62 to F=0.75. However, this fidelity improvement is limited due to the need for an additional SWAP operation (three two-qubit gates). Furthermore, the probabilistic nature of distillation leads to a slight increase in the average duration of the protocol. For the Expedient protocol, we see that it takes significantly longer to successfully generate one GHZ state, and achieves lower fidelities. Additional rounds of entanglement distillation are only beneficial if the fidelity improvements (from distilling imperfect states) exceed the fidelity losses from decoherence of idle qubits. A

further increase in N_{network} is required to make use of such protocols.

Together, these results show that the lifetime of the robust quantum-network memory demonstrated in this work is sufficient to demonstrate key distributed quantum computation protocols, such as deterministic two-qubit gates and basic distillation schemes, across optical quantum networks.

4.7. CONCLUSION

We have demonstrated a robust quantum-network memory based upon a single ^{13}C spin qubit in isotopically-engineered diamond. Compared with previous work[20,27], the data qubit lifetime is improved by two orders-of-magnitude during network operation. Critically, the data qubit now decoheres more slowly than state-of-the-art entanglement rates between NV centre network nodes[5,27]. Using numerical simulations, we show that the corresponding parameter regime — with $N_{\text{network}} \sim 10$ — enables a range of novel protocols for optical quantum networks, including deterministic two-qubit logic and creation of genuinely-entangled four-qubit GHZ states. Additionally, such robust memory would greatly speed up recently demonstrated protocols such as entanglement distillation and entanglement swapping[26,27].

On the path towards reaching the fault-tolerance threshold for large-scale distributed quantum-information-processing, our simulations show that further improvements in N_{network} are needed. The ^{13}C decoherence rate r_{mem} is currently limited by spurious ionisation of the NV centre to NV^0. Our results show that arbitrary states can be protected while cycling the charge state back and forth with minimal loss of fidelity, suggesting that such events can be mitigated. Further improvements in r_{mem} are possible by further improving the intrisic coherence times, and reducing the time needed for the entanglement sequence. Additionally, an improvement of the optical entanglement success probability by a factor ~ 100 is feasible using Fabry-Pérot micro-cavities[29,31], which would also greatly speed up the overall operation speed. Together such improvements would yield $N_{\text{network}} \approx 1000$, which is anticipated to be sufficient to realise large-scale error corrected quantum networks[2].

4.8. METHODS

4.8.1. SAMPLE AND HARDWARE SETUP

Our experiments are performed on a type-IIa isotopically purified (targeted 0.01% ^{13}C) ⟨100⟩ diamond substrate (Element Six). We address a single NV centre using a cryogenic (4 K) confocal microscope. A solid immersion lens and anti-reflection coating are fabricated to increase optical collection efficiency[16,56,57]. An external magnetic field is applied along the NV symmetry axis using three orthogonal permanent neodymium magnets mounted on linear actuators (Newport UTS100PP). We measure the field vector to be $(B_x, B_y, B_z) = (0.3(1), 0.06(8), 46.801(1))$ G by spectroscopy of the P1 bath transition frequencies[45].

Resonant optical excitation of NV$^-$ at 637 nm (red, Toptica DLPro and New Focus TLB-6704-P) realises high-fidelity spin initialisation ($E_{1,2}$ transitions, := E') and single-

shot readout (E_y transition)[16]. We measure read-out fidelities of 68.5(2)% for the bright state ($m_s = 0, := |0\rangle$) and 99.3(3)% for the dark state ($m_s = -1, := |1\rangle$), giving $F_{\mathrm{SSRO}} = 0.839(3)$. We employ 515 nm (green, Cobolt MLD) excitation to prepare the NV in NV^- and on resonance with the 637 nm lasers[17]. Finally, for experiments involving the neutral charge state, NV^0, we use resonant 575 nm (yellow, Toptica DL-SHG Pro) light to realise fast recharging to NV^-. Through direct current modulation or cascaded acousto-optical modulators, we achieve on/off ratios > 100 dB for all lasers.

Microwave (MW) driving via a lithographically defined gold stripline enables coherent control between $|0\rangle \leftrightarrow |1\rangle$. Pulses are applied using Hermite envelopes with maximum $\Omega_{\mathrm{Rabi}} \sim 27$ MHz, aside from within the entangling primitive, where a multi-tone driving scheme is employed to mitigate heating (Sec. 4.9.4). Using a fast microwave switch (TriQuint TGS2355-SM, 40 dB) to suppress electronic noise, we measure long electron spin relaxation ($T_1 \gg 30$ s), dephasing ($T_2^* = 94(2)$ μs) and coherence ($T_2 = 0.992(4)$ ms) times, the latter of which is limited by the electron spin bath formed by the P1 centres (75 ppb[45]) which can be reduced in future diamond growth.

4.8.2. MAGNETIC FIELD STABILISATION

The presence of a number of 6-9 T magnetic field systems in adjacent laboratories leads to slow magnetic field drifts (measured to be ~ 200 mG peak-peak across all presented measurements). These drifts are first mitigated using a feedback-loop. We measure the electron spin resonance frequency approximately every 10 minutes, and compensate any deviation to within 3 kHz (~ 1 mG) of the set-point by moving the magnets. This comes at the cost of slight magnetic field misalignment. If this misalignment becomes too large, or nearby magnetic field systems are being swept too quickly, we observe degradation of the nuclear spin operations. To remove such effects from our results, during ^{13}C-related data-taking we interleave separate reference measurements of the nuclear spin expectation value after simple state-preparation and measurement. These reference measurements do not contribute to the presented data-sets, but are used to discard measurement runs in the case that the reference measurement falls below 75% of the calibrated value.

4.8.3. DATA ANALYSIS

Throughout this text, we do not correct the nuclear spin data for SPAM errors.

The intrinsic decoherence timescales of the ^{13}C data qubit, as presented in Fig. 4.1(d), are fitted as follows:

$F(t) = A\exp[-(t/T)^n]$			
Metric	A	T (s)	n
$T^*_{2,e=\|1\rangle}$	0.55(2)	0.38(1)	1.6(1)
$T^*_{2,e=\|0\rangle}$	0.46(1)	0.42(2)	2.0(2)
$T^{N=1}_{2,e=\|1\rangle}$	0.51(1)	1.82(6)	2.1(2)
$T^{N=1}_{2,e=\|0\rangle}$	0.52(2)	1.11(8)	0.9(1)
$T^{N=8}_{2,e=\|1\rangle}$	0.58(1)	2.91(8)	2.1(2)
$T^{N=8}_{2,e=\|0\rangle}$	0.60(2)	1.62(9)	1.0(1)
$T_{1,e=\|1\rangle}$	0.43(2)	-	-
$T_{1,e=\|0\rangle}$	0.49(2)	2.8(2)	0.9(1)

The decoherence timescale for the data qubit during network operation (upper panel of Fig. 4.2(c)) is fit according to:

$F(N) = A\exp[-(N/N_{1/e})^n]$			
CR threshold	A	$N_{1/e} \cdot$ 1e5	n
0	0.49(1)	1.33(4)	1.00(5)
1	0.49(1)	1.80(6)	1.09(8)
5	0.49(1)	2.07(8)	1.09(8)

while the fraction of rejected data (lower panel) is fit using:

$F(N) = 1 - A\exp[-(N/N_{\text{ion}})]$		
CR threshold	A	$N_{\text{ion}} \cdot$ 1e5
1	0.988(4)	5.03(7)
5	0.91(1)	3.0(1)

The ^{13}C nuclear magnetic resonance spectrum for the NV^0 state (Fig. 4.3(a)) is described by:

$F(f) = a - A[\Omega^2/2(\Omega^2 + (f-f_0)^2)]$ $\cdot[1-\cos(\sqrt{\Omega^2+(f-f_0)^2}\,t)]$		
a	A	f_0 (Hz)
0.421(3)	0.73(2)	50229.8(1)

where the measured Rabi frequency, Ω = 5.4(2) Hz, and the chosen pulse duration, t = 92 ms, are fixed parameters.

For the ^{13}C free induction decay in the NV^0 state (Fig. 4.3(b)), we fit:

$F(t) = A\exp[-(t/T_2^*)^n]$		
A	T_2^* (ms)	n
0.54(2)	57(3)	1.2(1)

Finally, for the free evolution of $\langle X\rangle$ (inset of Fig. 4.3(b)), we fit:

$F(t) = A\exp[-(t/T_2^*)^n]\cdot\cos(\omega t+\phi)$		
A	ω (Hz)	ϕ (°)
0.46(1)	81(1)	-4(3)

where T_2^* = 56 ms and n = 1.2 are fixed to the values found in the previous fit.

4.9. SUPPLEMENTARY MATERIALS

4.9.1. NUCLEAR SPIN CONTROL

Dynamical decoupling (DD) spectroscopy is used to characterise the nuclear spin environment of the NV centre[34]. The signal presented in Fig. 4.1(c) is modelled by the interaction of the NV with two individual ^{13}C spins, taking into account the decoherence of the electron spin during the decoupling sequence[34].

The resonance at 44.832 μs is associated with the single spin characterised as a data qubit in this work, for which we extract hyperfine interaction parameters of $A_\parallel = 2\pi\cdot$ 80(1) Hz and $A_\perp = 2\pi\cdot$ 271(4) Hz via Ramsey spectroscopy and DD nutation experiments respectively[38]. The resonance at 44.794 μs is, in reality, a sum over a number of spins associated with the ^{13}C bath. However, the signal is reasonably approximated by a single nuclear spin with $A_\parallel = 2\pi\cdot$ 0 Hz and $A_\perp = 2\pi\cdot$ 150 Hz.

We realise universal control over the electron-^{13}C system: an electron-nuclear two-qubit gate is implemented following the methods described in Taminiau *et al.*[39] (CRot duration ~ 25 ms), while selective radio-frequency driving and free precession enable arbitrary ^{13}C single-qubit gates[21]. Following the methods of Cramer *et al.*, we estimate

the two-qubit gate fidelity to be ~ 84%[58]. This is thought to be limited by the electron spin coherence, which is restricted by the P1 spin bath rather than the ^{13}C bath. Reduction of these impurities through improved diamond growth should enable high fidelity control over a larger number of nuclear spins, as demonstrated in natural abundance ^{13}C samples[21].

As the fidelity of the nuclear spin readout is limited by the electron spin coherence, it is possible to improve this readout fidelity by repeated measurements, as has previously been achieved for single ^{13}C nuclear spins under ambient conditions[19,40,41]. We implement the repetitive readout protocol shown in Fig. 4.5(a). As the electron-nuclear coupling is weak — $A_\parallel \ll 1/\tau_{RO}$, for τ_{RO} the combined readout and repumping time — electron spin flips during the optical readout induce minimal ^{13}C dephasing. We can thus repeat the mapping and readout procedure a number of times, from which we acquire histograms as exemplified in Fig. 4.5(b).

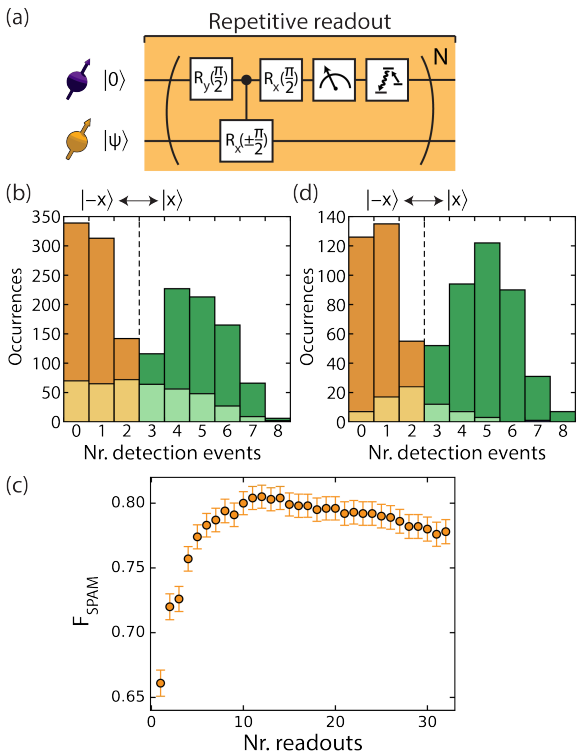

Figure 4.5: **Nuclear spin repetitive readout:** (a) Repetitive readout protocol: in each repetition, the nuclear X-basis spin-projection is mapped to the electron spin Z-basis, which is optically read out and then reset. (b) Example histograms obtained when preparing the |x⟩ and |−x⟩ states with a single projective measurement, followed by 8 X-basis readouts. Dashed line denotes the optimal state discrimination threshold. Dark (light) colours correspond to populations which are assigned to the targeted (erroneous) state. (c) Optimised state preparation and measurement fidelity as a function of the number of repetitive readouts. (d) Same as (b), but now using the outcomes of 8 prior readouts (≥5 read-outs with ≥1 photon for |x⟩ initialisation, no photons in any of the 8 readouts for |−x⟩ initialisation) as an additional initialisation step.

The histograms after preparation of $|x\rangle$ and $|-x\rangle$ respectively show two distinct populations. The state preparation and measurement process is quantified by $F_{\text{SPAM}} = \frac{1}{2}(F_{x|x} + F_{-x|-x})$, where $F_{i|j}$ is the probability to assign the spin state $|i\rangle$ after attempting initialisation in $|j\rangle$. In Fig. 4.5(c), we plot F_{SPAM} as a function of the number of repeated readouts, in each case using the optimal threshold to discriminate the two states. At an optimum number of 12 readouts, F_{SPAM} reaches 80.4(9)%. In all other nuclear spin data shown in the text, we utilise N = 8 readout repetitions (F_{SPAM} = 79.4(9)%) as a trade-off between optimal fidelity and measurement run-time. F_{SPAM} is predominantly limited by two mechanisms. First, the measurement sequence still induces some decoherence of the nuclear spin — as can be seen by the decrease in fidelity for >12 read-outs — reducing the extractable information. This effect would likely be mitigated by improvement of the two-qubit gate. Second, we prepare the $|x\rangle$ and $|-x\rangle$ states using a single projective measurement[58]. Repetitive measurements can also be used to initialise the spin: in Fig. 4.5(d) we additionally show the outcome of 8 repetitive readouts, conditioned on the outcome of 8 prior readouts. We find an achievable F_{SPAM} = 91(1)%, but do not employ it in this work due to the additional time overhead of >0.5 s per experimental shot.

4

4.9.2. HOMONUCLEAR ECHO

In Sec. 4.3, we report the nuclear spin dephasing timescale associated with nuclear spin bath dynamics to be $T^*_{2,^{13}\text{C-bath}}$ = 0.66(3) s. To identify this timescale, we prepare the electron in the $|0\rangle$ state and perform a homonuclear spin-echo at the ^{13}C Larmor frequency (Ω_{Rabi} = 120 Hz). Such a pulse inverts the local nuclear spin environment, decoupling it from other quasi-static noise sources but leaving the ^{13}C-^{13}C interactions unperturbed.

In Fig. 4.6 we present the measured data and experimental sequence.

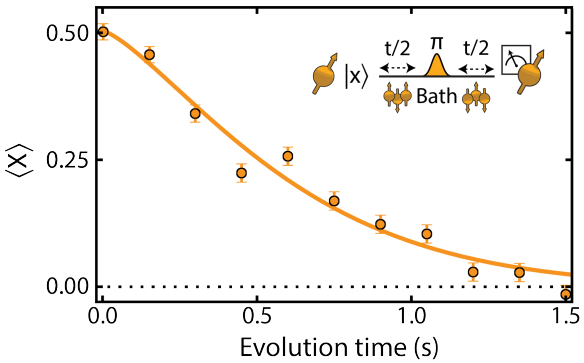

Figure 4.6: **Homonuclear Echo:** Measured nuclear spin dephasing when applying a homonuclear spin echo. The electron is initialised in the $|0\rangle$ state, such that the echo pulse simultaneously inverts the addressed ^{13}C along with the surrounding nuclear spin environment. The data are fit with an exponential decay, $f(t) = A\exp[-(t/T_2)^n]$, for which we find $T^*_{2,^{13}\text{C-bath}}$ = 0.66(3) s and n = 1.3(1).

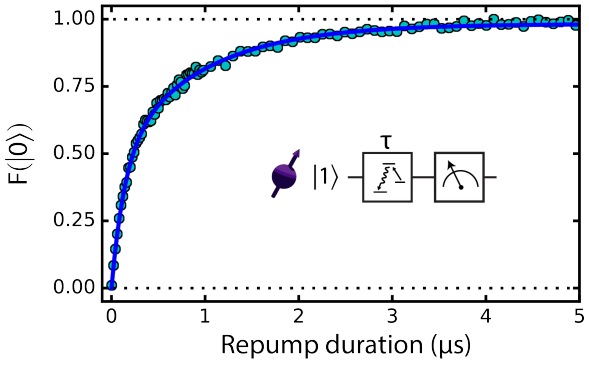

Figure 4.7: **Electron spin reset:** After initialisation in $|1\rangle$, the population in $|0\rangle$ is plotted as a function of the repumping duration (30 nW, E'). A delay of 10 μs between turning off the spin-pumping laser and turning on the readout laser ensures that minimal population resides in the metastable singlet states[20]. The data are well described by a two-timescale phenomenological model: $f(t) = A(1-\exp[-t/\tau_1]) + B(1-\exp[-t/\tau_2])$, for which we find A=0.480(15), B=0.503(14), τ_1=142(5) ns, τ_2=905(31) ns.

4.9.3. ELECTRON SPIN INITIALISATION

Electron spin initialisation constitutes a large fraction of the remote entanglement primitive duration[27]. Therefore, faster initialisation rates are desirable. This can be achieved by using higher laser powers, such that the NV centre is more frequently excited. However, higher laser powers also increase the ionisation rate[49,50]. Furthermore, as initialisation occurs primarily via the NV^- intersystem crossing[20], the ~ 370 ns lifetime of the singlet state, alongside the finite branching ratio from this state to the targeted $m_s = 0$ state, limit the extent to which higher laser powers increase the reset speed.

As a trade-off between these factors, we use 30 nW of E' excitation for the repumping process. This leads to initialisation fidelities ≥98% in a duration of 5 μs. In Fig. 4.7 we plot the measured reset dynamics for this power.

4.9.4. WEAK ELECTRON-SPIN PULSES

When implementing large numbers of repetitions of the remote entanglement protocol using strong microwave pulses, the mean number of detected photons during single-shot read-out was observed to decrease. This is attributed to heating of the sample.

The applied heat-load can be reduced by decreasing the MW Rabi frequency, but this is complicated by the presence of the nitrogen nuclear-spin. The electron-nitrogen hyperfine coupling, $A_\parallel S_z I_z$ ($A_\parallel = 2\pi \cdot 2.18$ MHz) causes a three-fold splitting of the transition frequency. For this reason, we usually employ strong, spectrally-broad Hermite pulses (Rabi frequency ~ 27 MHz) for high-fidelity (≫ 99%) manipulation of the electron spin, independent of the nitrogen spin state.

While prior initialisation of the nitrogen spin in a chosen state can relax this requirement[42], the large excited-state hyperfine coupling causes rapid depolarisation of the nuclear spin under repeated optical reset of the electron-spin, ruling out this method in

the presented experiments[59].

An alternative approach is to apply three separate drive tones, each addressing one of the nitrogen hyperfine levels. High-fidelity inversion is realised if the Rabi frequency of each tone, Ω, is large relative to the transition linewidth, which is described by a Gaussian distribution with $\sigma_f = 1/(\sqrt{2}\pi T_2^*) = 4.5$ kHz. Conversely, Ω should be small relative to the detuning between the transitions $A_\parallel$, such that AC-Stark frequency shifts remain small. We apply square pulse envelopes with $\Omega = 92$ kHz for each tone. The integrated power over the multi-tone pulse is ~ 80 (~ 40) times reduced for the π ($\pi/2$) pulse when compared to the strong Hermite pulses (Rabi frequency: π-pulse ~ 27 MHz, $\pi/2$-pulse ~ 16 MHz), enabling the repeated application of hundreds of thousands of MW pulses without observation of heating effects.

We numerically evaluate the electron spin dynamics using the QuTip python package[60]. Making the secular and rotating wave approximations, and transforming to the interaction picture $\omega_1 \hat{S}_z$, with $\omega_1 = D + \gamma_e B_z$, the Hamiltonian describing the evolution of the driven electron-nitrogen system is:

$$\begin{aligned} H' = {} & 2D\,|2\rangle\langle 2| + Q\hat{I}_z^2 + \gamma_N B_z \hat{I}_z + A_\parallel \hat{S}_z \hat{I}_z \\ & + \frac{1}{\sqrt{2}}\Omega(\cos(\phi_1)\hat{S}_x - \sin(\phi_1)\hat{S}_y) \\ & + \frac{1}{\sqrt{2}}\Omega(\cos(A_\parallel t + \phi_2)\hat{S}_x - \sin(A_\parallel t + \phi_2)\hat{S}_y) \\ & + \frac{1}{\sqrt{2}}\Omega(\cos(-A_\parallel t + \phi_3)\hat{S}_x - \sin(-A_\parallel t + \phi_3)\hat{S}_y). \end{aligned} \tag{4.2}$$

Here, $\hat{S}_i$ and $\hat{I}_i$ are the electron and nuclear spin-1 operators. D is the zero-field splitting, Q is the quadrupole splitting, γ_e and γ_N are the electron and nitrogen gyromagnetic ratios, and B_z is the external magnetic field component parallel to the NV axis. ϕ_i are the phases of the individual drive fields, while $|2\rangle\langle 2|$ is the projector on the state $|2\rangle$ of the electron spin: this term is a detuning of the non-driven electron spin transition. We have additionally assumed that the three drive tones are x-polarised.

In Fig. 4.8 we show the simulated and measured electron spin dynamics. A high-fidelity π-pulse is realised after ~ 5.5 μs of driving. The observed modulations arise due to slight relative AC-Stark shifts. Each drive tone induces a frequency shift approximately given by $\delta_{\text{AC-Stark}} \sim \Omega^2/2\Delta$, where Δ is the difference between the drive frequency and each detuned transition frequency. For the $m_I = 0$ transition, the shifts from the off-resonant tones are cancelled to first order. However, for the $m_I = \pm 1$ transitions, there is a frequency shift of $\sim \pm 2$ kHz.

We note that the parameters used here are not suitable for natural abundance samples, ($T_2^* \sim 5\,\mu$s, $1/(\sqrt{2}\pi T_2^*) \sim 45$ kHz), where the broader intrinsic linewidth leads to significant infidelity (simulated to be $\sim 33\%$ by Monte Carlo sampling, compared with $\sim 0.6\%$ for the present scenario). However, heating can alternatively be addressed by improved device engineering in future work, for example by fabricating the stripline using superconducting materials. This would enable the use of strong microwave pulses throughout the experiments and remove the time overhead required for weak pulses.

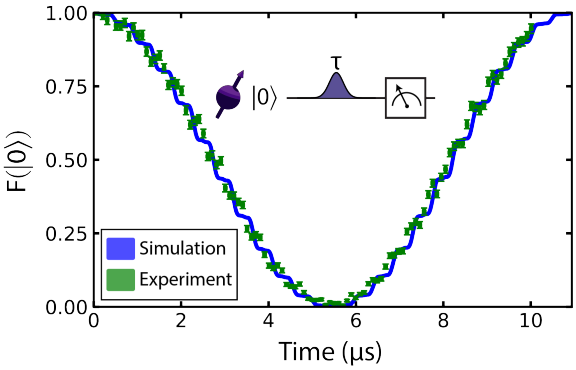

Figure 4.8: **Weak microwave pulses:** Electron spin dynamics under application of the three-tone microwave pulse. The solid line (circles) show the simulated (measured) dynamics after initialisation of the electron spin in $|0\rangle$. A π-pulse is realised after 5.5 μs.

4.9.5. QUANTUM NETWORK MEMORY PERFORMANCE USING STRONG PULSES

As discussed in the above section, the use of strong microwave pulses during the remote entanglement primitive led to the observation of heating effects. For this reason, we implemented the weak pulse scheme to ensure that optical processes were unaffected and thus would be compatible with remote entanglement generation. Nevertheless, we here study the data qubit decoherence when using strong pulses, which enables a shorter duration per entangling attempt.

The entangling primitive used here is identical to that used in Sec. 4.4 (t_r = 5 μs, t' = 200 ns, t_l = 1 μs), but with the weak MW $\pi/2$ pulse (t_{MW} = 2.8 μs) now replaced by a Hermite $\pi/2$ pulse (t_{MW} = 100 ns). The total duration is thus reduced from 9 μs to 6.3 μs. We measure the decay of the nuclear coherence, $(\langle X\rangle^2 + \langle Y\rangle^2)^{1/2}$, as a function of the number of entangling primitives after initialisation in $|x\rangle$. We again interleave one round of nuclear spin XY8 decoupling pulses. In Fig. 4.9 we plot the results, including different post-selection thresholds for the post-measurement CR checks. Importantly, the rejected fraction of events is similar to that observed when using the weak pulse scheme, suggesting that optical dynamics are relatively unchanged.

When compared with the data presented in Sec. 4.4, we observe an increase in data qubit robustness. With the most stringent filtering, we find a decay time of $419(96)\cdot10^3$ attempts (2.6(6) s). This compares favourably with the weak pulse case, where the equatorial states $\{|x\rangle,|y\rangle,|-x\rangle,|-y\rangle\}$ have a mean decay time of $190(8)\cdot10^3$ attempts (1.8(1) s).

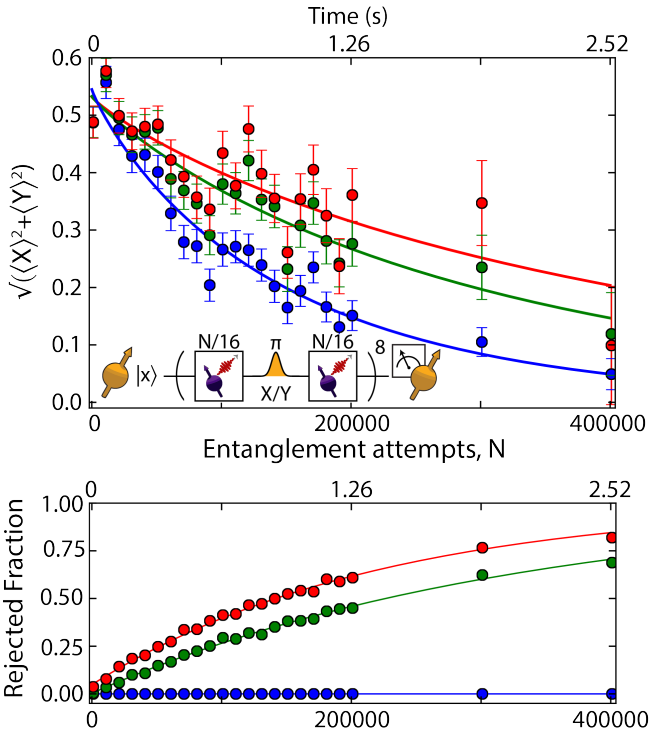

Figure 4.9: **Data qubit robustness using strong electron pulses:** Nuclear spin coherence as a function of the number of applied remote entangling primitives. Blue, green, red lines correspond to post-selection using a CR-check performed after the experiment, with thresholds of 0, 1, 5 respectively. The lower panel shows the corresponding fraction of rejected data.

4.9.6. SIMULATED NUCLEAR SPIN DEPHASING DUE TO THE REMOTE-ENTANGLEMENT PROTOCOL

In this section we numerically analyse the nuclear-spin dephasing induced by repeated remote entanglement attempts. Our analysis is based upon Monte Carlo simulations, adapted from the work of Kalb *et al.*[20]. Here, we will neglect the intrinsic dephasing timescales (T_2^* and T_2) of the nuclear spin, rather focusing on the limits imposed by the remote entanglement sequence alone. Further, we neglect the role played by ionisation. We will consider two sequences, the first following that implemented experimentally, and the second in which an additional electron spin-echo is incorporated within each attempt, see Figs. 4.10(a,b).

To build up a statistical distribution for the phase acquired by the nuclear spin after repeated application of the sequence, we generate a number of samples, K, each of N trials.

In each trial, a random number $0 \leq \mathrm{RN}_{\mathrm{init}} \leq 1$ is used to instantiate the NV electron in a given spin projection, $|s\rangle \in \{-1, 0, +1\}$, each with probability $p_{|s\rangle}$. The $p_{|s\rangle}$ are parameterised by a chosen initialisation error, p_{init}, such that $p_{|0\rangle} = (1 - p_{\mathrm{init}})$ and

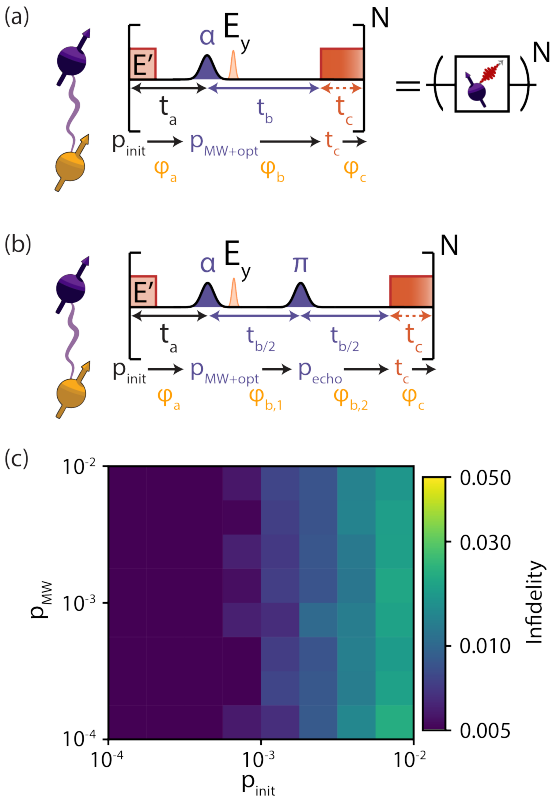

Figure 4.10: **Numerical analysis of nuclear spin dephasing:** (a) Sketch of the primitive remote entanglement unit used in experiment as formulated for Monte Carlo simulation. The nuclear spin (yellow) acquires spurious phases according to the dynamics of the electron spin (purple) and the $\hat{S}_z\hat{I}_z$ coupling $A_\parallel$. This phase is broken down into contributions from three imperfect operations, determined by initialisation infidelity (ϕ_a, parameterised by p_{init}), microwave inversion (ϕ_b, parameterised by p_{flip}) and stochastic reset time (ϕ_c, parameterised by t_c). (b) Sketch of the primitive remote entanglement unit when incorporating an additional electron spin-echo pulse (with failure possibility parameterised by p_{echo}). (c) Results of Monte Carlo simulations for the scenario given in (b), after application of $1 \cdot 10^6$ entangling primitives. $\alpha = \pi/2$, $p_{\text{MW}} = 0.5$, $p_{\text{opt}} = 0.01$, $t_a = 4.8$ μs, $t_{b/2} = 1$ μs and $\langle t_c \rangle = 200$ ns. Results are averaged over 600 samples.

$p_{|-1\rangle} = p_{|+1\rangle} = p_{\text{init}}/2$.

The nuclear spin is now evolved for a time, $t_a = (t_p - t_r + t_s)$, where t_p is the total optical pumping duration, t_r is the mean time to initialise ('reset') the spin, and t_s is the spacing between the end of the repump laser pulse and the centre of the 'α' microwave pulse (used to prepare the electron superposition for spin-photon entanglement). A phase, ϕ_a is acquired according to the initial state, at the difference frequency $\delta\omega = A_\parallel s$.

Next, the 'α' microwave pulse is applied, the effect of which is treated as instantaneous. While throughout this work we set $\alpha = \pi/2$, for which the sequence induces maximal dephasing noise on the data qubit, α is generally a free parameter which determines a rate-fidelity trade-off for remote spin-spin entanglement in the single-click entangling

protocol[5,27]. Another random number, $0 \leq \mathrm{RN}_{\mathrm{MW}} \leq 1$, is used to determine whether the electron spin is flipped between $|0\rangle \leftrightarrow |-1\rangle$ ($|+1\rangle$ is assumed to be unperturbed). The inversion is applied if $\mathrm{RN}_{\mathrm{MW}} < p_{\mathrm{MW}}$, the inversion probability of the chosen microwave pulse.

Immediately after the microwave pulse, we apply the effect of the optical π-pulse used to create spin-photon entanglement. A third random number, $0 \leq \mathrm{RN}_{\mathrm{opt}} \leq 1$, is used to determine whether the electron spin is flipped from $|0\rangle \rightarrow \{|-1\rangle, |+1\rangle\}$, each with equal probability. Again, the inversion is applied if $\mathrm{RN}_{\mathrm{opt}} < p_{\mathrm{opt}}$, which we set to be 0.01, according to the estimated spin-flip probability of the $\mathrm{E}_{x,y}$ transitions[20]. Note that the probability of this spin-flip is much smaller than that induced by the microwave pulse, justifying the omission of the optical pulses in the presented experiments.

In the case that we do not incorporate the electron spin-echo (Fig. 4.10(a)), the nuclear spin now simply acquires phase for a time t_b (ϕ_b), defined as the time between the centre of the microwave pulse and the onset of optical pumping. This time period allows for the decision logic for success or failure of the remote entanglement protocol (detection or loss of the optical photon). For short range (metre-scale) experiments, this timescale is typically $\sim 1\,\mu s$, limited by the current electronics used. The dephasing associated with t_b is dominant in this sequence: for $\alpha = \pi/2$, there is an extended period of time during which the electron has an approximately 50% chance to be in either the $|0\rangle$ or $|-1\rangle$ state.

We thus also consider the case in which it is possible to incorporate the echo (for example, because heating is mitigated by device engineering), see Fig. 4.10(b). In this case, the nuclear spin acquires phase for a time $t_b/2$ ($\phi_{b,1}$), before the echo is applied, and then for a further time $t_b/2$ ($\phi_{b,2}$). In case of successful application of the echo, $\phi_{b,1} + \phi_{b,2} = 0$. We account for a finite failure probability of the echo pulse using another random number, $0 \leq \mathrm{RN}_{\mathrm{echo}} \leq 1$. If $\mathrm{RN}_{\mathrm{echo}} < p_{\mathrm{echo}}$, the electron spin is flipped between $|0\rangle \leftrightarrow |-1\rangle$.

Finally, we account for the stochastic optical reset. In the case that the electron spin is in $|-1\rangle$ or $|+1\rangle$ at the onset of spin-pumping, a finite duration is required to prepare $|0\rangle$ for the start of the next repetition. A reset time, t_c, is sampled from the phenomenological two-timescale function fitted in Fig. 4.7, which determines the final evolution time before the end of the trial, during which time a phase ϕ_c is acquired.

Summing these phases, we find the total phase acquired by the nuclear spin for the i-th trial of the k-th sample: $\phi_{i,k}$. Repeating this process for N trials, we calculate the cumulative phases $\Phi_{n,k} = \sum_{i=1}^{n} \phi_{i,k}$ for $n = \{1, ..., N\}$.

For each sample, we can then calculate the state fidelity after each n trials:

$$F_{n,k} = \frac{1}{2} + \frac{1}{2}\cos\left(\Phi_{n,k} - \overline{\Phi_n}\right) \tag{4.3}$$

where $\overline{\Phi_n}$ is the mean phase after n trials, averaged over all samples. Finally, we find the characteristic n for which $\cos\left(\Phi_{n,k} - \overline{\Phi_n}\right)$ falls below $1/e$.

We consider two regimes. First, for the sequence excluding the spin-echo, we choose parameters that are as least as pessimistic as used in the experiments in Sec. 4.4. We have $t_a = 6.1$ μs, $t_b = 2.4$ μs, $\langle t_c \rangle = 535$ ns (following the two-timescale function fitted in Fig. 4.7), $p_{\mathrm{init}} = 0.03$, $p_{\mathrm{MW}} = 0.5$, $p_{opt} = 0.01$. We find that after application of $1 \cdot 10^6$ entangling

primitives, the expected fidelity with an initial superposition state is 0.776(4), averaged over 4000 samples. These calculations indicate that dephasing due to the entangling sequence is not limiting in the experiments.

We now turn to the case in which the echo is incorporated. We assume that strong MW pulses can be employed, enabling t_a = 4.8 μs, t_b = 2 μs. Further, we assume that faster spin reset can be achieved, as has been previously demonstrated with higher powers[20,32]: setting $\langle t_c \rangle$ = 200 ns (following a single exponential timescale). We set p_{MW} = 0.5, p_{opt} = 0.01. We now perform a 2D sweep of the fidelity after $1 \cdot 10^6$ trials as a function of p_{init} and p_{echo}. The results are plotted in Fig. 4.10. Even with 1% errors in the initialisation and echo operations, a fidelity of 96.7(2)% is achieved.

4.9.7. CONTROLLED CHARGE-STATE SWITCHING OF THE NV CENTRE

Throughout the experiments shown in this work, we make use of two-laser probe measurements ('CR checks') to detect the NV^- charge state[17]. During these checks, weak resonant light is applied on the NV^- E' (8 nW) and E_y (1.5 nW) transitions for 150 μs, during which we record all photon counts. By setting a threshold on the number of detected photons, it is possible to herald that the NV is in the negative charge-state, and that the spin-pumping and readout lasers are resonant. In the case of low counts a strong green pulse (515 nm, 30 μW, 50 μs) is used to scramble the local charge environment, before the check is repeated.

To investigate the effect of NV^- ionisation on the nuclear spin data qubit, we require fast switching of the NV charge state along with efficient detection. In this section we design and implement a protocol which enables such studies.

The protocol is shown in Fig. 4.11(a). We begin with a CR check, which we use to prepare the system in NV^- (Check NV^- (1)). At this point, we can utilise the previously described universal control to prepare the nuclear spin in a chosen state. Next, we apply a strong two-laser ionisation pulse. 50 nW of E_y and 500 nW of E' excitation are used, which are chosen to maintain predominantly NV^- $m_s = 0$ projection while attempting ionisation. After this pulse, a second CR check is performed (Check NV^- (2)). We proceed with the measurement only if this check returns 0 photon counts, which occurs with ~ 10% (40%) probability after a 300 μs (1 ms) pulse. This outcome heralds the system in a dark state of the NV, which can be associated with either NV^0 or a significant detuning of the NV^- transitions due to spectral diffusion.

We now perform the desired experiment on the nuclear spin, either allowing free evolution or applying RF driving. Next, we apply a strong yellow (575 nm) recharging pulse, using 500 nW for Figs. 4.3(a,b), and 1100 nW (the maximum attainable) for Fig. 4.3(c) to increase the recharging probability. After the recharging pulse, we apply spin-pump light to prepare the NV^- $m_s = 0$ state and subsequently read-out the nuclear spin. Finally, we perform one more CR check (Check NV^- (3)). The outcome of this check allows for post-selection of the nuclear spin read-out data upon finding the NV in the negative-charge state (retaining 82% of cases with the 575 nm pulse parameters used for Figs. 4.3(a,b): 1 ms, 500 nW, 85% for Fig. 4.3(c): 0.5 ms, 1100 nW). For post-selection, we discard data which lies close to the bright/dark discrimination threshold (see below). We only consider data for which the NV began in the negative charge-state (> 13 counts in (1)), transferred to a dark state (0 counts in (2)), and then returned to the negative

charge-state via the recharging pulse (≥ 5 counts in (3)).

In Fig. 4.11(b) we show example photon-count distributions from CR checks performed after preparing NV^- (1), after heralding the dark state (2), and after applying a 1.1 μW, 0.5 ms recharging pulse (3). The mean number of photons detected in each case is 16.9, 0.3, and 13.7 respectively, clearly demonstrating the ability to switch between the bright and dark states. However, the slight reduction of mean counts for case (3) compared to case (1) indicates that the recharging process does not achieve unity success. We now study this process more carefully.

We first quantify the charge-state read-out fidelity. Considering the data shown in panels (1) and (2) of Fig. 4.11(b), we maximise the quantity $F_{\text{charge}} = \frac{1}{2}(F_{\text{b|b}} + F_{\text{d|d}})$, where $F_{i|j}$ is the probability to assign the 'bright' (b, NV^-) or 'dark' (d, NV^0 or off-resonant) state after attempting initialisation in that state. With a threshold of 3 counts (assign bright if ≥ 3 photons detected), we find $F_{\text{charge}} = 98.81(4)\%$.

In Fig. 4.11(c) we plot the NV^- population after first preparing the dark state and then applying a 1 ms, 500 nW recharging pulse, for which we sweep the pulse frequency. The observation of two transitions corresponding to the spin-orbit branches of NV^0 confirms that this is the resonant recharging process[53,61]. Here, the broader line observed for the higher-frequency resonance (lower spin-orbit branch of NV^0) is likely due to the polarisation of the yellow laser — which is fixed at an arbitrary value in these experiments — being biased towards linear horizontal[53]. Optimal recharging is achieved when working at the central frequency for this branch, here 521.247 THz. Note that the lifetime of the NV^0 orbital-state is short even at 4 K (sub-μs), and so it is sufficient to only address a single spin-orbit branch.

We now turn to the temporal dependence. In Fig. 4.11(d) we show the NV^- population as a function of the recharge pulse length, now at a (maximal) power of 1.1 μW. The population grows rises quickly, with a fitted time constant of 71(2) μs. However, beyond a maximum population of 88.6(6)% at $t = 0.55$ ms, the signal again decays. A possible explanation for this decay is spectral diffusion, caused by ionisation of nearby P1 centres by the yellow laser[54]. Note that significantly higher recharging probabilities were achieved in Ref.[53], where the diamond substrate contained significantly fewer impurities. In Fig. 4.11(e), we focus on the first 500 μs of recharging, and probe the population in each of the NV^- spin states. We observe that the recharging laser induces fast spin-pumping into the $m_s = 0$ state, as expected due to the intersystem crossing. At $t = 500$ μs, the fraction of NV^- population in this state is 91.9(8)%. Note that this spin-pumping effect mitigates dephasing of the nuclear spin in the time between recharging and resonant spin-reset of the NV^- spin.

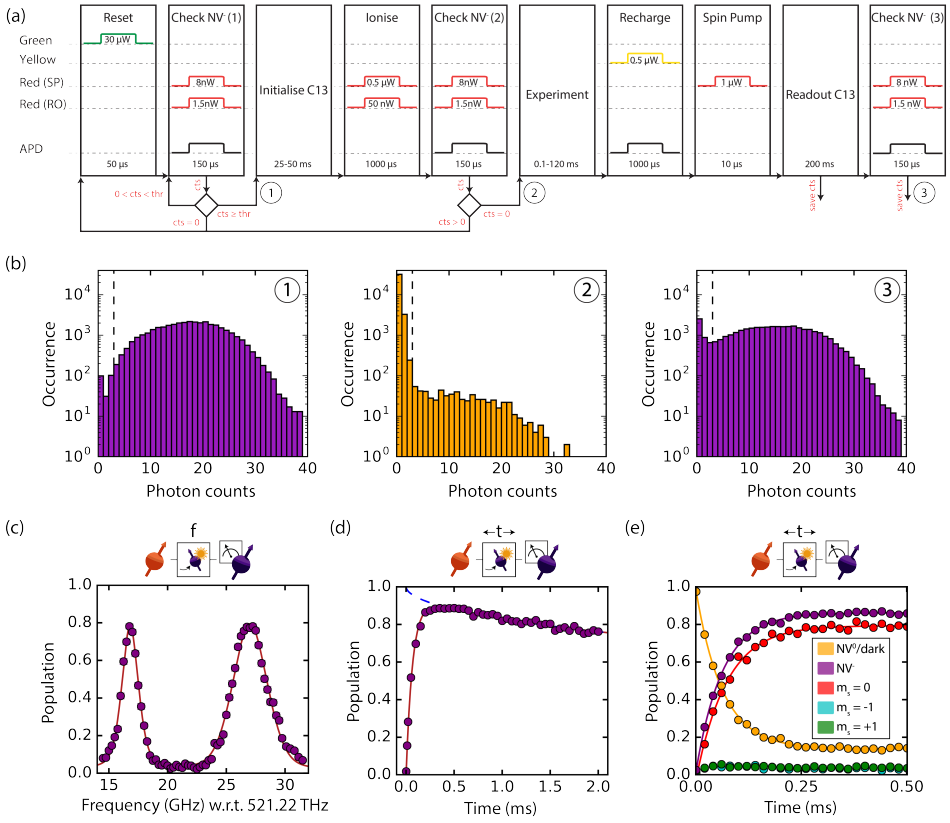

Figure 4.11: **Charge-state switching:** (a) Flow diagram for the charge-state switching protocol, showing the decision logic used for bright- and dark-state heralding and optional post-selection. (b) Distribution of photon-counts from CR checks performed at the points (1), (2), (3) indicated in panel (a). (c) NV^- population as a function of the recharging pulse frequency, using a 1 ms pulse of 500 nW. Solid line is a fit to the sum of two Voigt profiles. (d) NV^- state population as a function of the recharging pulse duration, at 521.247 THz and 1.1 μW. Solid line is a fit to $F(t) = (1-\exp[-t/\tau_1]) \cdot (\exp[-(t/\tau_2)^n]$, from which we find $\tau_1 = 71(2)$ μs, $\tau_2 = 22(4)$ ms and n=0.54(3). Dashed line shows the decay component, characterised by τ_2. (e) Populations in the NV^0/dark state, and in the differing spin-projections of the NV^- state as a function of the recharging pulse duration, again at 521.247 THz and 1.1 μW. Solid lines are fits to $F(t) = a + A\exp[-(t/\tau)^n]$. We find τ = {73(7),63(1),63(1)} μs, n.= {1.0(1),1.00(1),1.00(1)}, for the $m_s = 0$, NV^0 and NV^- populations respectively.

4.9.8. SIMULATED PERFORMANCE OF A WEAKLY-COUPLED ^{13}C FOR DISTRIBUTED QUANTUM INFORMATION PROCESSING

In Sec. 4.6, we present the simulated performance of two-qubit logic operations and generation of four-qubit GHZ states between nuclear spin qubits hosted in disparate quantum network nodes. Here we outline the models and methods used for these simulations. Further details can be found in the code implementation.

SIMULATION PARAMETERS

In Tables 4.1-4.3, we give the list of relevant parameters, which are described in the following sub-sections.

Parameter	Description	Values
General parameters		
$\mathbf{p_g}$	Gate error probability	0.01
$\mathbf{p_m}$	Measurement error probability	0.01
$\mathbf{p_n}$	Network error probability	0.1
$\mathbf{p_{RE}}$	RE success probability	0.0001
$\mathbf{T_{meas}}$	Measurement duration	$4.0 \cdot 10^{-6}$ s
$\mathbf{T_{RE}}$	RE duration	$6.0 \cdot 10^{-6}$ s
$\mathbf{T^e_X}$	Electron X gate duration	$0.14 \cdot 10^{-6}$ s
$\mathbf{T^e_Y}$	Electron Y gate duration	$0.14 \cdot 10^{-6}$ s
$\mathbf{T^e_Z}$	Electron Z gate duration	$0.10 \cdot 10^{-6}$ s
$\mathbf{T^e_H}$	Electron H gate duration	$0.10 \cdot 10^{-6}$ s

Table 4.1: General system parameters as used for the simulations presented in Figs. 4.4(c,d).

^{13}C decoherence parameters (Ref. [27])		
$\mathbf{T1^n_{idle}}$	^{13}C T_1 when idle	300 s
$\mathbf{T1^n_{RE}}$	^{13}C T_1 during RE attempts	0.03 s
$\mathbf{T2^n_{idle}}$	^{13}C T_2 when idle	10 s
$\mathbf{T2^n_{RE}}$	^{13}C T_2 during RE attempts	0.012 s
$\mathbf{T2^e_{idle}}$	Electron T_2 when idle	1.0 s
1.1% ^{13}C gate durations		
$\mathbf{T^C_X}$	^{13}C X gate duration	$1.0 \cdot 10^{-3}$ s
$\mathbf{T^C_Y}$	^{13}C Y gate duration	$1.0 \cdot 10^{-3}$ s
$\mathbf{T^C_Z}$	^{13}C Z gate duration	$0.5 \cdot 10^{-3}$ s
$\mathbf{T^C_H}$	^{13}C H gate duration	$0.5 \cdot 10^{-3}$ s
$\mathbf{T_{CNOT}}$	CNOT gate duration	$0.5 \cdot 10^{-3}$ s
$\mathbf{T_{CZ}}$	CZ gate duration	$0.5 \cdot 10^{-3}$ s
$\mathbf{T_{SWAP}}$	SWAP gate duration	$1.5 \cdot 10^{-3}$ s

Table 4.2: Decoherence timescales as measured in Ref. [27], and typical gate durations for such a device (1.1% ^{13}C) [21], as used for the simulations presented in Fig. 4.4(d) (labelled by $N_{1/e} = 2 \cdot 10^3$, the $T2^n_{RE}$ decay).

^{13}C decoherence parameters (this work)		
$\mathbf{T1^n_{idle}}$	^{13}C T_1 when idle	300 s
$\mathbf{T1^n_{RE}}$	^{13}C T_1 during RE attempts	1.2 s
$\mathbf{T2^n_{idle}}$	^{13}C T_2 when idle	10 s
$\mathbf{T2^n_{RE}}$	^{13}C T_2 during RE attempts	1.2 s
$\mathbf{T2^e_{idle}}$	Electron T_2 when idle	1.0 s
0.01% ^{13}C gate durations		
$\mathbf{T^C_X}$	^{13}C X gate duration	$13\cdot10^{-3}$ s
$\mathbf{T^C_Y}$	^{13}C Y gate duration	$13\cdot10^{-3}$ s
$\mathbf{T^C_Z}$	^{13}C Z gate duration	$6.5\cdot10^{-3}$ s
$\mathbf{T^C_H}$	^{13}C H gate duration	$6.5\cdot10^{-3}$ s
$\mathbf{T_{CNOT}}$	CNOT gate duration	$25\cdot10^{-3}$ s
$\mathbf{T_{CZ}}$	CZ gate duration	$25\cdot10^{-3}$ s
$\mathbf{T_{SWAP}}$	SWAP gate duration	$75\cdot10^{-3}$ s

Table 4.3: Decoherence timescales as measured in this work, and associated gate durations (0.01% ^{13}C device), as used for the simulations presented in Figs. 4.4(c) (see text) and 4.4(d) (labelled by $N_{1/e} = 2\cdot10^5$, the $T2^n_{RE}$ decay).

NODE TOPOLOGY

We assume that the NV centre has a star topology, where two qubit gates are only possible between the electron spin qubit and another qubit. Moreover, CNOT gates can only be carried out controlled by the electron spin qubit. Direct read-out is only possible for the electron spin qubit: other qubits must be read-out by first mapping their state to the electron spin. The protocols considered here require a maximum of three ^{13}C qubits in each node.

DECOHERENCE

Decoherence is modelled using two types of noise channels: the generalised amplitude damping channel and the phase damping channel[62] which have characteristic timescales of T_1 and T_2 respectively. We assign different T_1 and T_2 values to the nuclear spins dependent on whether their associated electron spin is being used to generate inter-node entanglement at a given point in the sequence.

The set of Kraus operators for the generalised amplitude damping channel is given by

$$
\begin{aligned}
K_{AD1} &= \sqrt{\frac{1}{2}}\begin{bmatrix}1 & 0\\ 0 & \sqrt{1-\gamma_1}\end{bmatrix},\\
K_{AD2} &= \sqrt{\frac{1}{2}}\begin{bmatrix}0 & \sqrt{\gamma_1}\\ 0 & 0\end{bmatrix},\\
K_{AD3} &= \sqrt{\frac{1}{2}}\begin{bmatrix}\sqrt{1-\gamma_1} & 0\\ 0 & 1\end{bmatrix},\\
K_{AD4} &= \sqrt{\frac{1}{2}}\begin{bmatrix}0 & 0\\ \sqrt{\gamma_1} & 0\end{bmatrix}.
\end{aligned}
\tag{4.4}
$$

where $\gamma_1 = 1 - \exp(-t/T_1)$.

The set of Kraus operators for the phase damping channel is given by:

$$K_{PD1} = \begin{bmatrix} 1 & 0 \\ 0 & \sqrt{1-\gamma_2} \end{bmatrix}, \; K_{PD2} = \begin{bmatrix} 0 & 0 \\ 0 & \sqrt{\gamma_2} \end{bmatrix}. \tag{4.5}$$

where $\gamma_2 = 1 - \exp(-t/\bar{T}_2)$.

In Tables 4.2 and 4.3, the T_1 times correspond to the experimentally measured decoherence times of the eigenstates of the Pauli-Z matrix ($|\uparrow\rangle$,$|\downarrow\rangle$), and correspond directly to the T_1 times used for the generalised amplitude damping channel of the model. The T_2 times correspond to the experimentally measured decoherence times of the eigenstates of the Pauli-X and Pauli-Y matrices ($|\mathrm{x}\rangle$,$|-\mathrm{x}\rangle$,$|\mathrm{y}\rangle$,$|-\mathrm{y}\rangle$). To account for the dephasing induced by the generalised amplitude damping channel, modified T_2 values must be used in the phase damping channel, which are given by:

$$\frac{1}{\bar{T}_2} = \frac{2}{T_2} - \frac{1}{T_1} \tag{4.6}$$

GATES

We model single-qubit gates as noiseless. We model noisy two-qubit gates using a depolarizing noise model:

$$N_{2Q}(\rho, p_g) = (1-p_g)\rho + \frac{p_g}{15} \sum_{\sigma_i, \sigma_j} (\sigma_i \otimes \sigma_j)\rho(\sigma_i \otimes \sigma_j)^\dagger. \tag{4.7}$$

where $\sigma_i, \sigma_j \in \{I, X, Y, Z\}$ and the sum is over all combinations of the Pauli operators σ_i, σ_j except for $\sigma_i = \sigma_j = I$.

For simplicity of compilation, we consider a native gate-set consisting of the Pauli gates, the Hadamard gate, the CNOT gate and the CZ gate. SWAP gates are carried out using three CNOT gates. All single- and two-qubit gates have associated durations: after each operation, the appropriate T_1 and T_2 decoherence is applied to all idle qubits.

NV-NV ENTANGLEMENT

We model the creation of remote-entanglement (RE) links (i.e. NV-NV Bell pairs) following the single-click protocol[48]. The protocol produces states that we assume are of the form

$$\rho_{NV,NV} = (1-p_n)\left|\psi\right\rangle\left\langle\psi\right| + p_n \left|11\right\rangle\left\langle 11\right|. \tag{4.8}$$

with $\left|\psi\right\rangle = (|01\rangle + |10\rangle)/\sqrt{2}$ and p_n a parameter that we call the network error, arising from events in which both NVs emitted a photon[5]. The single-click protocol is probabilistic and has success probability $p_{\text{success}} = 2p_{\text{det}}p_n$, where p_{det} is the probability to detect a photon.

In simulation, each time a RE link must be generated, Monte-Carlo methods are used to determine the number of entangling attempts n_{RE} before success. The decoherence channels are then applied to all idle qubits with an associated duration of $t_{RE} = n_{\text{RE}}\, t_{\text{ent}}$, where t_{ent} is the duration of each entangling primitive.

The results presented in Fig. 4.4(c) are averaged over 500,000 repetitions, whereas those in Fig. 4.4(d) use 100,000 repetitions, aside from the Expedient protocol for $N_{1/e} = 2{\cdot}10^3$, for which only 10,000 repetitions are used due to the low protocol success rate.

MEASUREMENT NOISE

We restrict measurements to the Z-basis. To measure the qubits in the X-basis, we apply a Hadamard gate before the measurement. The gate duration time of this additional operation is included in the simulations.

We model (single qubit) measurement errors by projecting onto the opposite eigenstate of the measured operator. Measurement errors are characterised by the probability p_m of an incorrect projection.

DYNAMICAL DECOUPLING

To mitigate dephasing of both communication and data qubits due to quasi-static noise sources (for example, due to spin-bath interactions or magnetic field fluctuations), a dynamical decoupling scheme is accounted for in the sequencing of all operations. We model this process by only applying operations at intervals of a basic echo sequence: $\tau - \pi - \tau$. Here, π denotes a π-pulse being applied to the system, and τ is the inter-pulse delay time. Operations are only allowed in between the echo sequences of each node; consecutive operations in the same node are allowed, after which the decoupling sequence is restarted. We set τ equal to the duration of 5000 entangling attempts for the purified sample and a τ equal to the duration of 500 entangling attempts for the natural abundance sample. The π-pulse duration is set to $13 \cdot 10^{-6}$ seconds for the purified sample and $1 \cdot 10^{-6}$ seconds for the natural abundance sample.

NON-LOCAL CNOT OPERATIONS

In Fig. 4.4(c), we present the average fidelity of a non-local CNOT operation. Here, we use the parameters given in Tables 4.1 and 4.3, but sweep the values of $T1^n_{RE} = T2^n_{RE} = N_{1/e} \cdot T_{RE}$. The average fidelity of the operation is calculated by determining the entanglement fidelity following the relation given in Ref.[55]. We do not show the results when using the faster gate and measurement durations (Table 4.2), because a negligible difference is observed. For example, for $N_{1/e}$ = 83,333, we find an average fidelity of 0.7899, compared with 0.7890 when using the slower durations.

GHZ-CREATION PROTOCOLS

In this section, we discuss the three GHZ creation protocols used in Fig. 4.4(d). The circuit diagrams of the protocols are depicted in Fig. 4.12. In each node, the first (purple) qubit indicates the electron qubit of the NV centre (i.e., the communication qubit), with the other qubits indicating ^{13}C spins ('memory' and 'data' qubits). The memory qubits are used to store intermediate states required to create the GHZ state. When the GHZ state is created, it can be consumed to non-locally perform a weight-4 Pauli measurement on qubits of a distributed error-correcting code, e.g., the surface code[2,3]. In the diagrams of Fig. 4.12, the inner-most ^{13}C is the data qubit of the code (i.e., it would be a constituent of an encoded logical qubit).

The Plain protocol is the most simple protocol to create a 4-qubit GHZ state out of Bell pairs: it only requires three pairs. The local operations of this protocol 'fuse' the three pairs into the GHZ state. Fusion takes place with Block B.2 from the legend: this operations fuses two entangled states that do not overlap in any of the nodes with the aid of a Bell pair that is consumed in the process. Feed-forward operations based on this Bell-state measurement lead to protocol success with unit probability.

As mentioned above, RE links can only be created between the electron qubits. Hence, the states of the electron qubits must be swapped with those of data qubits ('stored') at some point in all of the protocols. In the Plain protocol, this occurs after the first pair of RE links are created: the electron qubits of nodes A, C are stored such that it is possible to generate a third RE link between nodes A and C.

The Modicum protocol uses one additional Bell pair compared to Plain. This additional pair is used to distill the 4-qubit GHZ state. This distillation step is probabilistic; if successful it increases the state fidelity. However, if it fails, the GHZ state is discarded and the protocol restarts from scratch. Fusion of the Bell pairs takes place in Modicum with Block B.1 (both in nodes A and C in Fig. 4.12), which describes fusion of two entangled states that overlap in one network node. Distillation takes place with Block A.2 in nodes B and D, which essentially measures a stabilizer of the desired pure entangled state. In particular, Block A.2 is known in the literature as 'single selection'[63]. The operation is successful if the measurement results are even: in that case the correct stabilizer operation is measured. In case of an odd measurement combination, the distillation operation fails, and the protocol returns to the indicated 'failure reset level' (indicated with 'frl' in the legend). The Modicum protocol is found with the dynamic programming algorithm presented in Ref. [6].

The Expedient protocol[2] uses 22 Bell pairs to create the GHZ state. Compared to the Plain protocol, the additional 19 Bell pairs are used for distillation purposes. This can be either for distillation of Bell pairs before they are fused to form the GHZ state, or for distillation of the GHZ state after it is created. Distillation takes place with Block A.2, but also with Block C.1 and Block C.2. Block C.1 can be understood as an operation that performs two distillation steps by consuming two ancillary Bell pairs. This block is known in the literature as the 'double selection' distillation protocol[63]. Block C.2 essentially performs three distillation steps by consuming three Bell pairs. Depending on where in the circuit the distillation steps occur, failure of a step means the entire protocol has to start from scratch, or only a specific branch of the protocol has to be carried out again. Fusion again takes place with Block B.2.

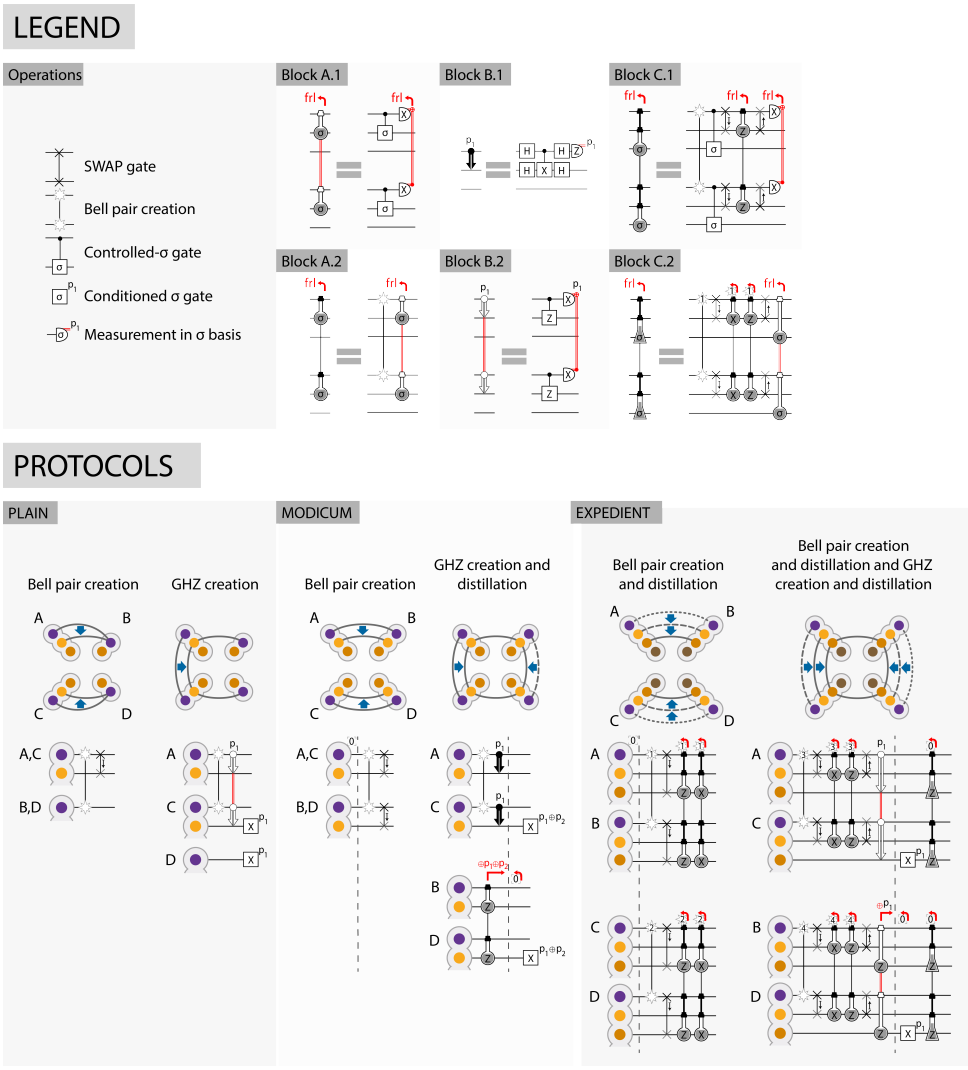

Figure 4.12: Circuit diagrams of the three GHZ creation protocols used in the simulations. Bell states are generated in the form of Eq. 4.8, followed by an X-gate on their second qubit to turn them into noisy versions of the $(|00\rangle + |11\rangle)/\sqrt{2}$ state. 'Plain' uses three Bell pairs to create a 4-qubit GHZ state. 'Modicum' uses a fourth Bell pair to increase the GHZ fidelity with a distillation step. 'Expedient'[2] uses 22 Bell pairs and has many (intermediate) distillation steps. Details of those steps are given in the text. The schematics above the circuits show four network nodes (A,B,C,D) comprising an electron spin (purple) and up to three nuclear spins (orange tones).

REFERENCES

[1] S. Wehner, D. Elkouss and R. Hanson, *Quantum internet: A vision for the road ahead,* Science **362** (2018).

[2] N. H. Nickerson, Y. Li and S. C. Benjamin, *Topological quantum computing with a very noisy network and local error rates approaching one percent,* Nat. Commun. **4**, 1756 (2013).

[3] N. H. Nickerson, J. F. Fitzsimons and S. C. Benjamin, *Freely scalable quantum technologies using cells of 5-to-50 qubits with very lossy and noisy photonic links,* Phys. Rev. X **4**, 041041 (2014).

[4] C. Monroe *et al.*, *Large-scale modular quantum-computer architecture with atomic memory and photonic interconnects,* Phys. Rev. A **89**, 022317 (2014).

[5] P. C. Humphreys *et al.*, *Deterministic delivery of remote entanglement on a quantum network,* Nature **558**, 268 (2018).

[6] S. de Bone, R. Ouyang, K. Goodenough and D. Elkouss, *Protocols for creating and distilling multipartite ghz states with bell pairs,* IEEE Trans. Quantum Eng. **1**, 1 (2020).

[7] S. Ritter *et al.*, *An elementary quantum network of single atoms in optical cavities,* Nature **484**, 195 (2012).

[8] D. Hucul *et al.*, *Modular entanglement of atomic qubits using photons and phonons,* Nat. Phys. **11**, 37 (2015).

[9] B. Hensen *et al.*, *Loophole-free bell inequality violation using electron spins separated by 1.3 kilometres,* Nature **526**, 682 (2015).

[10] W. Rosenfeld *et al.*, *Event-ready bell test using entangled atoms simultaneously closing detection and locality loopholes,* Phys. Rev. Lett. **119**, 010402 (2017).

[11] R. Stockill *et al.*, *Phase-tuned entangled state generation between distant spin qubits,* Phys. Rev. Lett. **119**, 010503 (2017).

[12] V. Krutyanskiy *et al.*, *Light-matter entanglement over 50 km of optical fibre,* NPJ Quantum Inf. **5**, 1 (2019).

[13] L. Stephenson *et al.*, *High-rate, high-fidelity entanglement of qubits across an elementary quantum network,* Phys. Rev. Lett. **124**, 110501 (2020).

[14] Y. Yu *et al.*, *Entanglement of two quantum memories via fibres over dozens of kilometres,* Nature **578**, 240 (2020).

[15] S. Daiss *et al.*, *A quantum-logic gate between distant quantum-network modules,* Science **371**, 614 (2021).

[16] L. Robledo *et al.*, *High-fidelity projective read-out of a solid-state spin quantum register,* Nature **477**, 574 (2011).

[17] H. Bernien *et al.*, *Heralded entanglement between solid-state qubits separated by three metres,* Nature **497**, 86 (2013).

[18] M. H. Abobeih *et al.*, *One-second coherence for a single electron spin coupled to a multi-qubit nuclear-spin environment,* Nat. Commun. **9**, 1 (2018).

[19] P. C. Maurer *et al.*, *Room-Temperature Quantum Bit Memory Exceeding One Second,* Science **336**, 1283 (2012).

[20] N. Kalb, P. C. Humphreys, J. Slim and R. Hanson, *Dephasing mechanisms of diamond-based nuclear-spin memories for quantum networks,* Phys. Rev. A **97**, 062330 (2018).

[21] C. E. Bradley *et al.*, *A ten-qubit solid-state spin register with quantum memory up to one minute,* Phys. Rev. X **9**, 031045 (2019).

[22] T. K. Unden, D. Louzon, M. Zwolak, W. H. Zurek and F. Jelezko, *Revealing the emergence of classicality using nitrogen-vacancy centers,* Phys. Rev. Lett. **123**, 140402 (2019).

[23] H. Bartling *et al.*, *Coherence and entanglement of inherently long-lived spin pairs in diamond,* arXiv:2103.07961 (2021).

[24] J. Randall *et al.*, *Observation of a many-body-localized discrete time crystal with a programmable spin-based quantum simulator,* arXiv:2107.00736 (2021).

[25] M. Abobeih *et al.*, *Fault-tolerant operation of a logical qubit in a diamond quantum processor,* arXiv preprint arXiv:2108.01646 (2021).

[26] N. Kalb *et al.*, *Entanglement distillation between solid-state quantum network nodes,* Science **356**, 928 (2017).

[27] M. Pompili *et al.*, *Realization of a multinode quantum network of remote solid-state qubits,* Science **372**, 259 (2021).

[28] A. Sipahigil *et al.*, *An integrated diamond nanophotonics platform for quantum-optical networks,* Science **354**, 847 (2016).

[29] D. Riedel *et al.*, *Deterministic enhancement of coherent photon generation from a nitrogen-vacancy center in ultrapure diamond,* Phys. Rev. X **7**, 031040 (2017).

[30] C. Nguyen *et al.*, *Quantum network nodes based on diamond qubits with an efficient nanophotonic interface,* Phys. Rev. Lett. **123**, 183602 (2019).

[31] M. Ruf, M. J. Weaver, S. B. van Dam and R. Hanson, *Resonant excitation and purcell enhancement of coherent nitrogen-vacancy centers coupled to a fabry-perot microcavity,* Phys. Rev. Appl. **15**, 024049 (2021).

[32] A. Reiserer *et al.*, *Robust quantum-network memory using decoherence-protected subspaces of nuclear spins,* Phys. Rev. X **6**, 021040 (2016).

[33] J. Casanova, Z.-Y. Wang, J. Haase and M. Plenio, *Robust dynamical decoupling sequences for individual-nuclear-spin addressing,* Phy. Rev. A **92**, 042304 (2015).

[34] T. Taminiau *et al.*, *Detection and control of individual nuclear spins using a weakly coupled electron spin,* Phys. Rev. Lett. **109**, 137602 (2012).

[35] M. Blok, N. Kalb, A. Reiserer, T. Taminiau and R. Hanson, *Towards quantum networks of single spins: analysis of a quantum memory with an optical interface in diamond,* Faraday Discuss. **184**, 173 (2015).

[36] J. Maze, J. Taylor and M. Lukin, *Electron spin decoherence of single nitrogen-vacancy defects in diamond,* Phys. Rev. B **78**, 094303 (2008).

[37] G. Balasubramanian *et al.*, *Ultralong spin coherence time in isotopically engineered diamond,* Nat. Mater. **8**, 383 (2009).

[38] J. M. Boss *et al.*, *One-and two-dimensional nuclear magnetic resonance spectroscopy with a diamond quantum sensor,* Phys. Rev. Lett. **116**, 197601 (2016).

[39] T. H. Taminiau, J. Cramer, T. van der Sar, V. V. Dobrovitski and R. Hanson, *Universal control and error correction in multi-qubit spin registers in diamond,* Nat. Nanotechnol. **9**, 171 (2014).

[40] A. Dréau, P. Spinicelli, J. Maze, J.-F. Roch and V. Jacques, *Single-shot readout of multiple nuclear spin qubits in diamond under ambient conditions,* Phys. Rev. Lett. **110**, 060502 (2013).

[41] G.-Q. Liu *et al.*, *Single-shot readout of a nuclear spin weakly coupled to a nitrogen-vacancy center at room temperature,* Phys. Rev. Lett. **118**, 150504 (2017).

[42] N. Kalb *et al.*, *Experimental creation of quantum zeno subspaces by repeated multi-spin projections in diamond,* Nat. Commun. **7**, 13111 (2016).

[43] M. Pfender *et al.*, *High-resolution spectroscopy of single nuclear spins via sequential weak measurements,* Nat. Commun. **10**, 1 (2019).

[44] K. Cujia, J. M. Boss, K. Herb, J. Zopes and C. L. Degen, *Tracking the precession of single nuclear spins by weak measurements,* Nature **571**, 230 (2019).

[45] M. Degen *et al.*, *Entanglement of dark electron-nuclear spin defects in diamond,* Nat. Commun. **12**, 1 (2021).

[46] G. Khutsishvili, *Spin diffusion and magnetic relaxation of nuclei,* Sov. Phys. JETP **15**, 909 (1962).

[47] R. Guichard, S. Balian, G. Wolfowicz, P. Mortemousque and T. Monteiro, *Decoherence of nuclear spins in the frozen core of an electron spin,* Phys. Rev. B **91**, 214303 (2015).

[48] C. Cabrillo, J. I. Cirac, P. Garcia-Fernandez and P. Zoller, *Creation of entangled states of distant atoms by interference,* Phys. Rev. A **59**, 1025 (1999).

[49] L. Robledo, H. Bernien, I. van Weperen and R. Hanson, *Control and coherence of the optical transition of single nitrogen vacancy centers in diamond,* Phys. Rev. Lett. **105**, 177403 (2010).

[50] P. Siyushev *et al.*, *Optically Controlled Switching of the Charge State of a Single Nitrogen-Vacancy Center in Diamond at Cryogenic Temperatures,* Phys. Rev. Lett. **110**, 167402 (2013).

[51] J. Choi *et al.*, *Robust dynamic hamiltonian engineering of many-body spin systems,* Phys. Rev. X **10**, 031002 (2020).

[52] M. Pfender *et al.*, *Nonvolatile nuclear spin memory enables sensor-unlimited nanoscale spectroscopy of small spin clusters,* Nat. Commun. **8**, 834 (2017).

[53] S. Baier *et al.*, *Orbital and spin dynamics of single neutrally-charged nitrogen-vacancy centers in diamond,* Phys. Rev. Lett. **125**, 193601 (2020).

[54] F. Heremans, G. Fuchs, C. Wang, R. Hanson and D. Awschalom, *Generation and transport of photoexcited electrons in single-crystal diamond,* Appl. Phys. Lett. **94**, 152102 (2009).

[55] M. A. Nielsen, *A simple formula for the average gate fidelity of a quantum dynamical operation,* Phys. Lett. A **303**, 249 (2002).

[56] J. Hadden *et al.*, *Strongly enhanced photon collection from diamond defect centers under microfabricated integrated solid immersion lenses,* Appl. Phys. Lett. **97**, 241901 (2010).

[57] T. Yeung, D. Le Sage, L. M. Pham, P. Stanwix and R. L. Walsworth, *Anti-reflection coating for nitrogen-vacancy optical measurements in diamond,* Appl. Phys. Lett. **100**, 251111 (2012).

[58] J. Cramer *et al.*, *Repeated quantum error correction on a continuously encoded qubit by real-time feedback,* Nat. Commun. **7**, 1 (2016).

[59] W. Pfaff *et al.*, *Unconditional quantum teleportation between distant solid-state quantum bits,* Science **345**, 532 (2014).

[60] J. R. Johansson, P. D. Nation and F. Nori, *Qutip: An open-source python framework for the dynamics of open quantum systems,* Comput. Phys. Commun. **183**, 1760 (2012).

[61] M. S. Barson, E. Krausz, N. B. Manson and M. W. Doherty, *The fine structure of the neutral nitrogen-vacancy center in diamond,* Nanophotonics **8**, 1985 (2019).

[62] M. A. Nielsen and I. Chuang, *Quantum computation and quantum information,* (2002).

[63] K. Fujii and K. Yamamoto, *Entanglement purification with double selection,* Phys. Rev. A **80**, 042308 (2009).

5

A TEN-QUBIT SOLID-STATE SPIN REGISTER

C. E. Bradley*, J. Randall*, M. H. Abobeih, R. C. Berrevoets, M. J. Degen, M. A. Bakker, M. Markham, D. J. Twitchen, T. H. Taminiau

Spins associated to single defects in solids provide promising qubits for quantum information processing and quantum networks. Recent experiments have demonstrated long coherence times, high-fidelity operations and long-range entanglement. However, control has so far been limited to a few qubits, with entangled states of three spins demonstrated. Realizing larger multi-qubit registers is challenging due to the need for quantum gates that avoid crosstalk and protect the coherence of the complete register. In this paper, we present novel decoherence-protected gates that combine dynamical decoupling of an electron spin with selective phase-controlled driving of nuclear spins. We use these gates to realise a 10-qubit quantum register consisting of the electron spin of a nitrogen-vacancy centre and 9 nuclear spins in diamond. We show that the register is fully connected by generating entanglement between all 45 possible qubit pairs, and realise genuine multipartite entangled states with up to 7 qubits. Finally, we investigate the register as a multi-qubit memory. We demonstrate the protection of an arbitrary single-qubit state for over 75 seconds - the longest reported for a single solid-state qubit - and show that two-qubit entanglement can be preserved for over 10 seconds. Our results enable the control of large quantum registers with long coherence times and therefore open the door to advanced quantum algorithms and quantum networks with solid-state spin qubits.

The results of this chapter have been published in Phys. Rev. X **9**, 031045 (2019).
*Equally contributing authors.

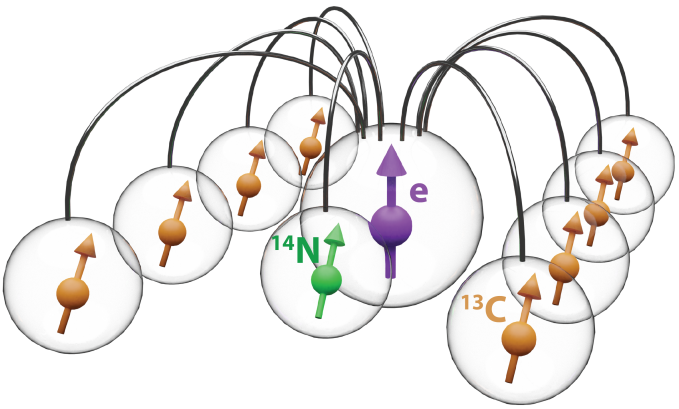

Figure 5.1: Illustration of the 10-qubit register developed in this work. The electron spin of a single NV centre in diamond acts as a central qubit and is connected by two-qubit gates to the intrinsic ^{14}N nuclear spin, and a further 8 ^{13}C nuclear spins surrounding the NV centre.

5.1. INTRODUCTION

Electron and nuclear spins associated with single defects in solids provide a promising platform for quantum networks and quantum computations[1,2]. In these hybrid registers, different types of spins fulfill different roles. Electron spins offer fast control[3–13] and high fidelity readout[7,14,15], and can be used to control and connect nuclear spins[15–21]. Furthermore, electron-electron couplings enable on-chip connectivity between defects[19,22,23], whilst coupling to photons[12,24–28] allows for the realization of long-range entanglement links[29–31]. Nuclear spins provide additional qubits with long coherence times that can be used to store and process quantum states[16,17,21,24,32–35].

Recent experiments have demonstrated various schemes for high-fidelity two-qubit gates[34,36–41], as well as basic quantum algorithms[36,42] and error correction codes[16,17]. However, to date, these systems have been restricted to few-qubit registers: the largest reported entangled state contains 3 qubits[16,17,43]. Larger quantum registers are desired for investigating advanced algorithms and quantum networks[44–46]. Such multi-qubit registers are challenging to realise due to the required gates that selectively control the qubits and at the same time decouple unwanted interactions in order to protect coherence in the complete register.

In this work, we develop a novel gate scheme based upon selective phase-controlled driving of nuclear spins interleaved with decoupling sequences on an electron spin. These gates enable high-fidelity control of hitherto inaccessible nuclear spin qubits. We combine these gates with previously developed control techniques[14,16,47] to realise a 10-qubit register composed of a diamond nitrogen-vacancy (NV) centre, its ^{14}N nuclear spin and 8 ^{13}C spins (Fig. 5.1). We show that the register is fully connected by preparing entangled states for all possible pairs of qubits. Furthermore, by also decoupling nuclear-nuclear interactions through echo sequences, we generate N-qubit Greenberger-Horne-Zeilinger (GHZ) states, and witness genuine multipartite entangle-

ment for up to 7 spins. Finally, we investigate the coherence properties of the register. We measure coherence times up to 63(2) seconds and show that an arbitrary single qubit state can be protected for over 75 seconds. Furthermore, we demonstrate that two-qubit entanglement can be preserved for over 10 seconds.

5.2. TWO-QUBIT GATES: THEORY

We consider an NV centre in diamond and surrounding ^{13}C nuclear spins. To realise a multi-qubit register, we design single-qubit gates and electron-nuclear two-qubit gates to control the NV ^{14}N spin and several individual ^{13}C spins. Key challenges in these hybrid systems of multiple coupled spins are to maintain coherence on the electron spin qubit and to avoid unwanted crosstalk. In particular, the electron spin continuously couples to all ^{13}C spins through the hyperfine interaction, and the dynamics of the electron spin and nuclear spins typically occur on very different timescales[36]. To address these issues, a variety of decoherence-protected gates, in which decoupling sequences on the electron spin are combined with nuclear spin control, have been investigated[36,37,39,40,48–52]. Here we develop and demonstrate a novel electron-nuclear two-qubit gate based upon phase-controlled radio-frequency (RF) driving of nuclear spins, interleaved with dynamical decoupling (DD) of the electron spin. We will refer to this scheme as a DDRF gate. Our scheme enables the control of additional ^{13}C spins while offering improved flexibility in dynamical decoupling to optimise the electron spin coherence and avoid unwanted crosstalk.

To design a selective two-qubit gate, we utilise the hyperfine interaction which couples each nuclear spin to the electron spin. As this interaction depends on the relative position of the spin to the NV, different nuclear spins can be distinguished by their precession frequencies[48–50]. In the interaction picture with respect to the electron energy splitting, and neglecting non-secular terms, the Hamiltonian describing the electron and a single ^{13}C nuclear spin is given by[48–50]

$$H = \omega_L I_z + A_\parallel S_z I_z + A_\perp S_z I_x, \tag{5.1}$$

where $\omega_L = \gamma B_z$ is the nuclear Larmor frequency set by the external magnetic field B_z along the NV axis, γ is the ^{13}C gyromagnetic ratio, S_α and I_α are the spin-1 and spin-1/2 operators of the electron and nuclear spins respectively, and $A_\parallel$ and $A_\perp$ are the parallel and perpendicular hyperfine components.

To control the nuclear spin, we apply RF pulses of Rabi frequency Ω, phase ϕ and frequency ω. To target a specific nuclear spin, we set $\omega = \omega_1$, where $\omega_1 = \sqrt{(\omega_L - A_\parallel)^2 + A_\perp^2}$ is the nuclear spin precession frequency when the electron is in the $m_s = -1$ spin projection. In the following we assume $(\omega_L - \omega_1) \gg \Omega$, such that driving of the nuclear spin is negligible while the electron is in the $m_s = 0$ spin projection, and set $A_\perp = 0$ for simplicity (see Sec. 5.8.3 for the general case). Considering only the $m_s = \{0, -1\}$ subspace, with the addition of RF driving and in a rotating frame at the RF frequency, the Hamiltonian of Eq. 5.1 becomes (see Sec. 5.8.3 and Ref.[36])

$$\begin{aligned} H = &|0\rangle\langle 0| \otimes (\omega_L - \omega_1) I_z \\ &+ |1\rangle\langle 1| \otimes \Omega(\cos(\phi) I_x + \sin(\phi) I_y), \end{aligned} \tag{5.2}$$

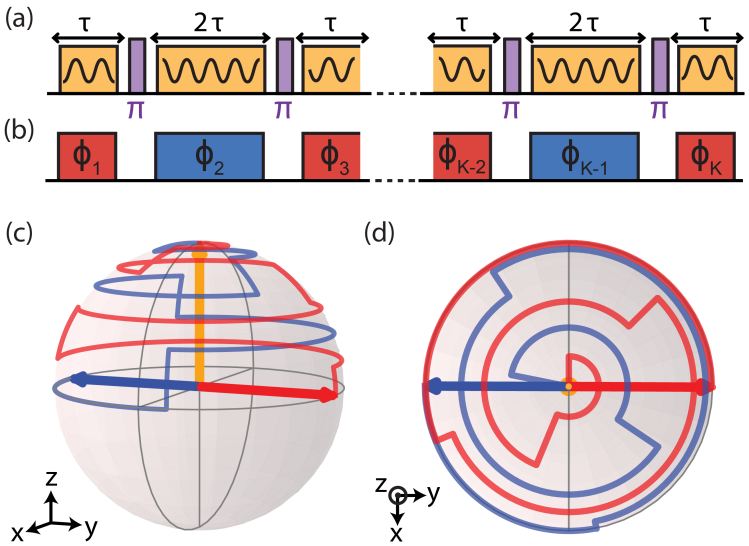

Figure 5.2: (a) Illustration of the pulse sequence employed to realise a DDRF gate. Dynamical decoupling pulses on the electron spin (purple) are interleaved with RF pulses (yellow) which selectively drive a single nuclear spin. (b) Illustration showing that the initial state of the electron spin determines which RF pulses are resonant with the nuclear spin. If the electron spin starts in $|1\rangle$ ($m_s = -1$), the odd RF pulses (red) are resonant. For initial electron state $|0\rangle$ ($m_s = 0$), the even (blue) RF pulses are resonant. The phase of each RF pulse is adapted to create the desired nuclear spin evolution, accounting for periods of free precession according to Eq. 5.3. (c) Nuclear spin trajectory on the Bloch sphere for a conditional rotation with $N = 8$ electron decoupling pulses. Starting from the initial nuclear state $|\uparrow\rangle$ (yellow), the red (blue) path shows the nuclear spin evolution for the case where the electron starts in the state $|1\rangle$ ($|0\rangle$). The final state vectors are anti-parallel along the equator: therefore, the gate is a maximally entangling two-qubit gate. (d) Top-down view of (c).

where $|0\rangle$ ($|1\rangle$) indicates the electron $m_s = 0$ ($m_s = -1$) spin projection. In this picture, for the electron in state $|0\rangle$, the nuclear spin undergoes precession around the $\hat{z}$-axis at frequency $(\omega_L - \omega_1) = A_\parallel$. Conversely, while the electron is in the state $|1\rangle$, the nuclear spin is driven around a rotation axis in the $\hat{x}$-$\hat{y}$ plane defined by the phase of the RF field ϕ.

To simultaneously decouple the electron spin from the environment, we interleave the RF pulses in a sequence of the form $(\tau$ - π - 2τ - π - $\tau)^{N/2}$, where π is a π-pulse on the electron spin, 2τ is the interpulse delay, and N is the total number of electron decoupling pulses (Fig. 5.2(a)) [48–50]. We consider the evolution of the nuclear spin during this sequence separately for the two initial electron eigenstates: $|0\rangle$ and $|1\rangle$ [48–50]. We label each successive RF pulse by integer $k = 1, ..., K$, where $K = N + 1$ is the total number of RF pulses. If the inital electron spin state is $|0\rangle$, only the even k RF pulses will be resonant and drive the nuclear spin (Fig. 5.2(b)). Conversely, for initial state $|1\rangle$, the odd k pulses are resonant. The desired nuclear spin evolution can now be created by setting the phases ϕ_k of the RF pulses.

We construct both an unconditional rotation (single-qubit gate) and a conditional rotation (two-qubit gate). To ensure that the sequential RF rotations build up construc-

tively, the phases of each RF pulse should be set to account for the periods of nuclear spin precession between them, which build up in integer multiples of $\phi_\tau = (\omega_L - \omega_1)\tau$. For the case where the electron starts in the state $|0\rangle$ (even k), the required sequence of phases is $\phi_\tau, 3\phi_\tau, 5\phi_\tau, \ldots$, while for the case where the electron starts in the state $|1\rangle$ (odd k) we require the sequence $0, 2\phi_\tau, 4\phi_\tau, \ldots$. The required phases are therefore given by (see Sec. 5.8.3)

$$\phi'_k = \begin{cases} (k-1)\phi_\tau + \pi & k \text{ odd} \\ (k-1)\phi_\tau & k \text{ even,} \end{cases} \tag{5.3}$$

where the (optional) π phase shift for the odd k sequence converts the unconditional rotation into a conditional rotation. By adding a further phase φ to all pulses, we can also set the rotation axis of the gate. The RF pulse phases are thus summarised by $\phi_k = \varphi + \phi'_k$.

With this choice of phases, the total evolution of the two-qubit system is given by $V = V_z \cdot V_{\text{CROT}}$. Here, V_z is an unconditional rotation of the nuclear spin around z (Sec. 5.8.3) and V_{CROT} is a conditional rotation of the nuclear spin depending on the electron state, given by

$$\begin{aligned} V_{\text{CROT}} = &|0\rangle\langle 0| \otimes R_\varphi(N\Omega\tau) \\ &+ |1\rangle\langle 1| \otimes R_\varphi(-N\Omega\tau), \end{aligned} \tag{5.4}$$

where $R_\varphi(\theta) = e^{-i\theta(\cos(\varphi)I_x + \sin(\varphi)I_y)/\hbar}$. V_{CROT} describes a controlled rotation of the nuclear spin with tuneable rotation angle (set by N, Ω and τ) and rotation axis (set by φ). Setting $N\Omega\tau = \pi/2$, a maximally entangling two-qubit operation is achieved, equivalent to a controlled-not (CNOT) gate up to local rotations. Example dynamics for a nuclear spin evolving under such a sequence are shown in Figs. 5.2(c) and (d).

Our design has several advantages. First, the gate allows nuclear spins with small or negligible $A_\perp$ to be controlled, thereby increasing the number of accessible nuclear spin qubits. Second, because the targeted dynamics are achieved by setting the RF phases and amplitudes, the interpulse delay τ of the decoupling sequence can be freely optimised to protect the electron coherence. This is in contrast to the gates described in van der Sar *et al.*[36], for which τ is restricted to a specific resonance condition for each spin, making multi-qubit control challenging. Third, because our method does not rely on an average frequency shift over the two electron spin states[37], our gates can also be used for selective control of nuclear spins coupled to spin-1/2 defects (such as the negatively-charged group-IV color centres[7,9,13,20,28,53,54]), and via a contact hyperfine coupling, such as for donor spins in silicon[34] and SiMOS quantum dots[21]. Finally, because control is achieved through the RF field, a multitude of avenues for future investigation are opened up, such as parallelizing gates by frequency multiplexing and using shaped and composite pulses to mitigate dephasing and crosstalk[38,55,56].

5.3. TWO-QUBIT GATES: EXPERIMENT

Our experiments are performed at 3.7 K using a single NV centre in diamond with natural abundance of carbon isotopes (1.1% ^{13}C). Further details of the sample and experimental setup can be found in Sec. 5.8.1. As a starting point, we use the DDRF gate to identify and characterise ^{13}C nuclear spin qubits surrounding the NV centre. If the electron spin

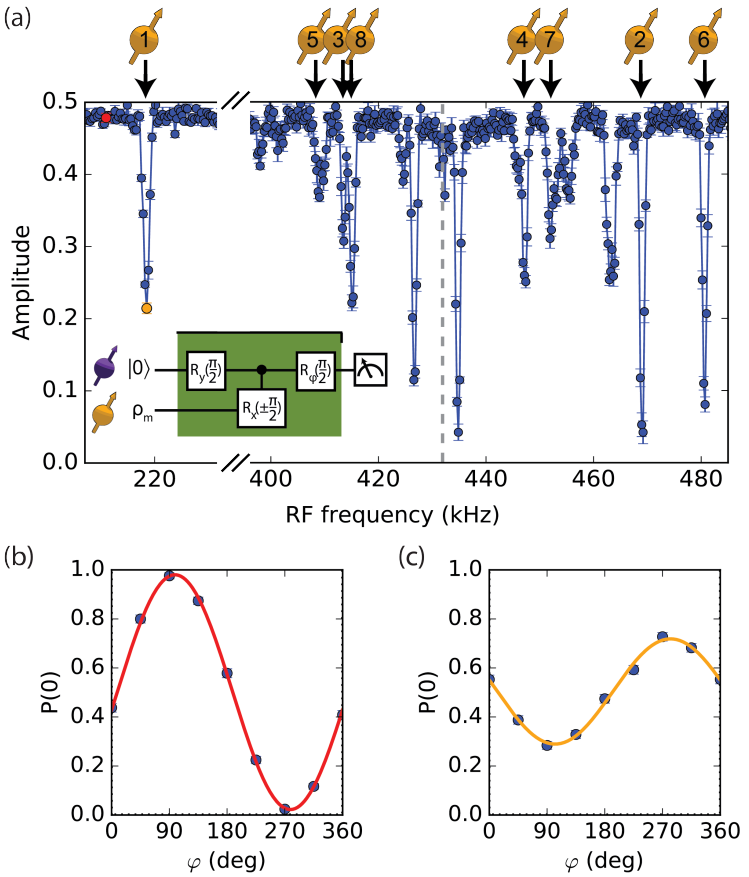

Figure 5.3: (a) Nuclear spin spectroscopy. After preparing the electron in a superposition state, the DDRF gate (controlled $\pm\pi/2$ rotation, see Eq. 5.4) is applied for different RF frequencies ω. The electron spin is then measured along a basis in the equatorial plane defined by angle φ (see inset). Each data point in (a) corresponds to the fitted amplitude A of the function $f(\varphi) = a + A\cos(\varphi + \varphi_0)$, where φ is swept from 0 to 360 deg and φ_0 accounts for deterministic phase shifts induced on the electron by the RF field. By fitting the amplitude, we distinguish such deterministic phase shifts from loss of coherence due to entangling interactions. The signals due to interaction with the 8 ^{13}C spins used in this work are labelled. The dashed gray line indicates the ^{13}C Larmor frequency ω_L. A detailed analysis of the spectrum is given in Sec. 5.8.4. (b,c) Example phase sweeps for two data points highlighted in red (b) and orange (c) in (a). Solid lines are fits to $f(\varphi)$. The DDRF gate parameters are $N = 48$ and $\tau = 8\tau_L$, where $\tau_L = 2\pi/\omega_L$ ($\approx 2.3\mu$s).

is prepared in a superposition state and the RF frequency is resonant with a nuclear spin in the environment, the entangling interaction (Eq. 5.4) decoheres the electron spin. Therefore, varying the RF frequency (ω) performs spectroscopy of the nuclear spin environment. Fig. 5.3 shows that multiple dips in the electron coherence can be observed, indicating selective interactions with several individual nuclear spins. Importantly, like other RF-based approaches[39,52], the DDRF sequence is sensitive to nuclear spins with small or negligible $A_\perp$. Besides extending the number of qubits that can be controlled with a single NV centre, this also enables the detection of additional spins when using the NV as a quantum sensor, which we exploit in parallel work to realise 3D imaging of large spin clusters (see Ch. 6)[57].

To verify the control offered by the DDRF two-qubit gate, we first demonstrate high fidelity ancilla-based initialization and readout by preparation and tomography of a maximally entangled electron-nuclear state. To test the gate, we select a ^{13}C spin (spin C1, Fig. 5.3) with a strong parallel hyperfine component of $A_\parallel/2\pi = 213.154(1)$ kHz, but a weak perpendicular hyperfine component $A_\perp/2\pi = 3.0(4)$ kHz. We exploit the freedom in choosing the interpulse delay by setting τ to an integer multiple of the ^{13}C Larmor period, $\tau_L = 2\pi/\omega_L$, so that unwanted interactions between the electron spin and other ^{13}C spins in the environment are effectively decoupled[47,58]. The choice of Rabi frequency Ω is a trade-off between obtaining faster gate speeds, maintaining frequency selectivity and minimising additional noise from the electronic hardware (see Sec. 5.8.1).

The sequence to perform the state preparation and tomography experiment is shown in Fig. 5.4(a)[16,37]. We first initialise the electron spin in the state $|0\rangle$ by resonant optical excitation[14]. We then swap the state of the electron spin onto the ^{13}C spin and reset the electron spin. Next, we prepare the electron in a superposition state before performing the DDRF controlled-rotation gate, ideally preparing the electron-nuclear Bell state $|\psi_{\text{Bell}}\rangle = (|0+\rangle + |1-\rangle)/\sqrt{2}$, where $|\pm\rangle = (|\downarrow\rangle \pm |\uparrow\rangle)/\sqrt{2}$.

To perform quantum state tomography on the two-qubit state, we first measure the electron spin along a chosen axis by appropriate basis rotations followed by Z-basis optical readout[14]. To mitigate potential dephasing of the nuclear spin induced by the electron spin measurement, we make the electron spin measurement non-destructive by using a short, weak laser pulse and conditioning progression of the sequence on the outcome $|0\rangle$, i.e. the detection of a photon[16,42] (see Sec. 5.8.5). Following appropriate basis rotations, we then use the electron spin to measure the nuclear spin in the X-basis[16]. In this measurement the electron is read out in a single-shot with average fidelity 0.945(2)[14]. We independently characterise the nuclear spin readout, which is then used to correct for readout infidelities in subsequent measurements (Sec. 5.8.5). In order to reconstruct the full electron-nuclear state, we perform the sequence with and without an additional electron π-pulse before the first readout (see Sec. 5.8.5).

The reconstructed density matrix from quantum state tomography is shown in Fig. 5.4(b). The prepared state ρ exhibits a fidelity, $\mathcal{F}_{\text{Bell}} = \langle\psi_{\text{Bell}}|\,\rho\,|\psi_{\text{Bell}}\rangle = 0.972(8)$ with the target Bell state. Based upon a simple depolarizing noise model, we estimate the two-qubit gate fidelity to be $\mathcal{F}_{\text{gate}} = 0.991(9)$ (Sec. 5.8.5). Additional characterization measurements in combination with numerical simulations indicate that the remaining infidelity can be mostly attributed to electron spin dephasing due to noise from the electronic hardware (Sec. 5.8.4).

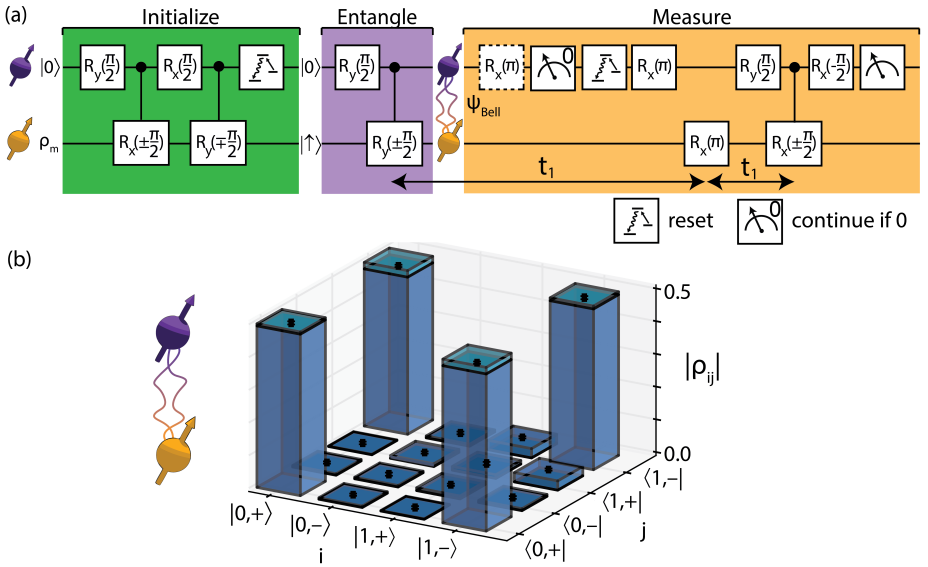

Figure 5.4: (a) Experimental sequence to prepare an electron-nuclear Bell state and determine the expectation value of the two-qubit operator ZX. A series of single and two-qubit gates are used to initialise the nuclear spin [16,37]. A subsequent $\pi/2$ rotation and two-qubit gate generate the Bell state $|\psi_{\text{Bell}}\rangle = (|0+\rangle + |1-\rangle)/\sqrt{2}$. A measurement of the electron spin in the Z-basis is followed by an X-basis measurement of the nuclear spin through the electron spin. These measurements are separated by a nuclear spin echo, which is implemented to mitigate dephasing of the nuclear spin. The entire sequence is applied with and without an additional electron π-pulse (dashed box) before the first electron readout, in order to reconstruct the electron state while ensuring that the measurement does not disturb the nuclear spin state [16,42]. (b) Density matrix of the electron-nuclear state after applying the sequence shown in (a) to qubit C1, reconstructed with state tomography. We correct for infidelities in the readout sequence, characterised in separate measurements (Sec. 5.8.5). The DDRF gate parameters are $N = 8$, $\tau = 17\tau_L \approx 39.4\,\mu$s, $\Omega/2\pi = 1.09(3)\,$kHz, and the total gate duration is $629\,\mu$s, compared with the nuclear spin $T_2^* = 12.0(6)\,$ms. We use error function pulse envelopes with a $7.5\,\mu$s rise / fall time for each RF pulse to mitigate pulse distortions induced by the RF electronics (see Sec. 5.8.1). The fidelity with the target Bell state is measured to be $\mathcal{F}_{\text{Bell}} = 0.972(8)$. Lighter blue shading indicates the density matrix for the ideal state $|\psi_{\text{Bell}}\rangle$.

5.4. A 10-QUBIT SOLID-STATE SPIN REGISTER

We now show how the combination of our DDRF gate with previously developed gates and control techniques [16,37] enables high-fidelity control of a 10-qubit hybrid spin register associated to a single NV-centre. Our register is composed of the electron and ^{14}N spins of the NV-centre, along with 8 ^{13}C nuclear spins (Fig. 5.1). Our quantum register is connected via the central electron spin. To demonstrate this, we first show that all nuclear spins can be entangled with the electron spin by following the protocol shown in Fig. 5.4(a). For the case of the nitrogen spin, initialization is performed by a measurement-based scheme which heralds the preparation in a particular eigenstate. Compared to previous work [59], we realise an improved initialization fidelity ($\mathcal{F}_{\text{init}} = 0.997(11)$) by pre-preparing the electron in the $m_s = -1$ state instead of a

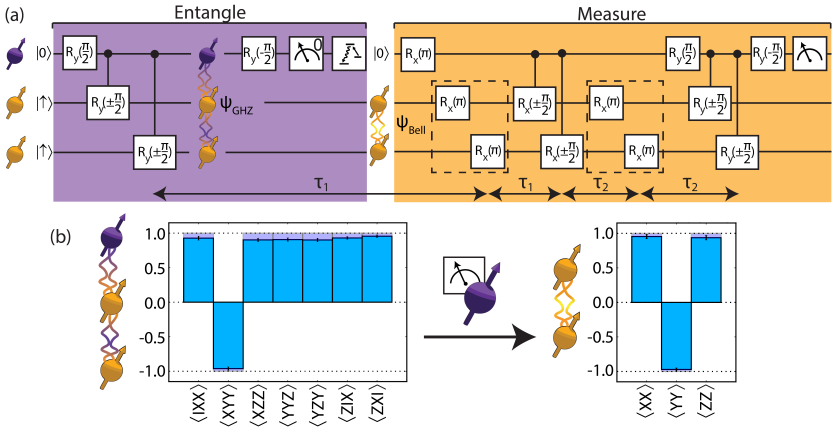

Figure 5.5: (a) Experimental sequence for the preparation of a nuclear-nuclear Bell state and measurement of the two-qubit operator ZZ. After preparation of the electron-nuclear-nuclear GHZ state $|\mathrm{GHZ}_3\rangle = (|0++\rangle + |1--\rangle)/\sqrt{2}$, an X-basis measurement on the ancilla (electron spin) projects the nuclear spins into the Bell state $|\Phi^+\rangle = (|++\rangle + |--\rangle)/\sqrt{2}$. Measurement of the two-qubit correlations between the nuclear spins is then performed through the electron spin. Spin echoes (dashed boxes) built into the measurement sequence protect the nuclear spins from dephasing errors. (b) Measured expectation values (non-zero terms of the ideal state only) for the electron-nuclear-nuclear state $|\mathrm{GHZ}_3\rangle$, and for the nuclear-nuclear state $|\Phi^+\rangle$. Blue (purple) bars show the experimental (ideal) expectation values for each operator. The nuclear-nuclear correlations are well preserved after a nondestructive measurement of the electron spin in the X-basis.

mixed state of $m_s = -1$ and $+1$, and by repeating the measurement-based initialization sequence twice (see Sec. 5.8.5). After initialization, we work in the $m_I = \{0,-1\}$ subspace, and perform operations analogous to those for the ^{13}C nuclear spins, including the two-qubit gates using the DDRF scheme. Genuine entanglement is probed by measuring the non-zero matrix elements of the target state, and confirmed by negativity of the entanglement witness $\mathcal{W}_{\mathrm{Bell}} = \mathbb{1} - 2|\psi_{\mathrm{Bell}}\rangle\langle\psi_{\mathrm{Bell}}|$[60].

Next, we show that the register is fully connected by preparing entangled states for all possible pairs of spins. To prepare nuclear-nuclear entanglement, we implement a probabilistic measurement-based scheme[61], as shown in Fig. 5.5(a). We first prepare a three-qubit GHZ state comprising the electron and two nuclear spins, $|\mathrm{GHZ}_3\rangle = (|0++\rangle + |1--\rangle)/\sqrt{2}$, before performing a non-destructive X-basis measurement on the electron spin. The measurement ideally prepares the Bell state $|\Phi^+\rangle = (|++\rangle + |--\rangle)/\sqrt{2}$ on the targeted pair of nuclear spins. Finally, we measure the necessary expectation values in order to reconstruct the non-zero matrix elements of this state and confirm bipartite entanglement (Fig. 5.5(b)).

The measured Bell state fidelities, ranging from 0.63(3) to 0.97(1), are shown in Fig. 5.6. We attribute the variations in the measured values to differences in the two-qubit gate fidelities for each spin. In particular, the lower values measured for ^{13}C spins C7 and C8 are due to short coherence times in combination with long two-qubit gate durations, necessitated by close spectral proximity to other spins (see Sec. 5.8.4). All data is measured using a single set of gate parameters, and using a single hardware configuration, rather than separately optimizing for each pair of qubits.

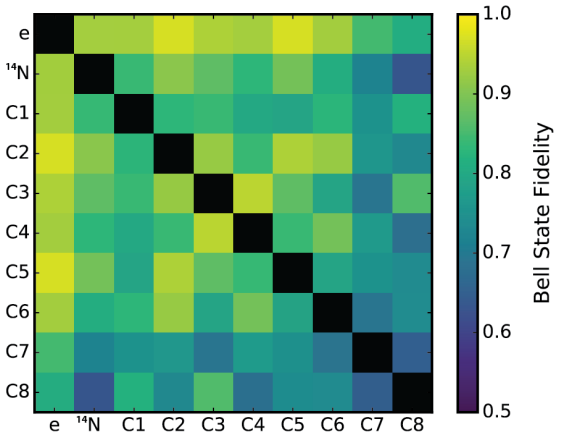

Figure 5.6: Measured Bell state fidelities for all pairs of qubits in the 10-qubit register. Genuine entanglement is confirmed in all cases, as witnessed by a fidelity exceeding 0.5 with the target state. Qubits C1, C7, C8 and ^{14}N are controlled using DDRF gates (Sec. 5.2). Qubits C2, C3, C4, C5, and C6 are controlled using the methods described in Taminiau *et al.*[37], as their hyperfine interaction parameters enable high-fidelity control using previously optimised gates.

5.5. GENERATION OF N-QUBIT GHZ STATES

Quantum information processing tasks such as computations and error correction will require the execution of complex algorithms comprising a large number of qubits. An important requirement for a quantum processor is thus the ability to perform operations on many of its constituents within a single algorithm. We test this capability by generating N-qubit GHZ type states, defined as

$$|\mathrm{GHZ}_N\rangle = \frac{1}{\sqrt{2}}\left(|0\rangle \otimes |+\rangle^{\otimes(N-1)} + |1\rangle \otimes |-\rangle^{\otimes(N-1)}\right). \tag{5.5}$$

To generate such states, we follow the sequence shown in Fig. 5.7(a). First, $N-1$ nuclear spins are initialised in the state $|\uparrow\rangle$. Next, we prepare the electron spin in a superposition state, and perform sequential controlled rotation gates between the electron and nuclear spins.

Characterizing the full quantum state for a system of this size is an expensive task due to the dimensionality of the associated Hilbert space. However, we can determine if the state exhibits genuine multipartite entanglement of all N qubits using an entanglement witness with a reduced subset of measurement bases[60]. For a GHZ state with system size N, there exist 2^N operators from which the non-zero elements of the density matrix can be reconstructed by linear inversion, and from which a fidelity with the target state can be calculated. Negativity of the entanglement witness $\mathcal{W}_{\mathrm{GHZ}} = \mathbb{1}/2 - |\mathrm{GHZ}_N\rangle\langle\mathrm{GHZ}_N|$ heralds genuine multipartite entanglement[60]. We determine the required expectation values of products of Pauli operators on the register via the electron spin. In these experiments, the readout sequence is modified slightly. Prior to the readout of the electron spin

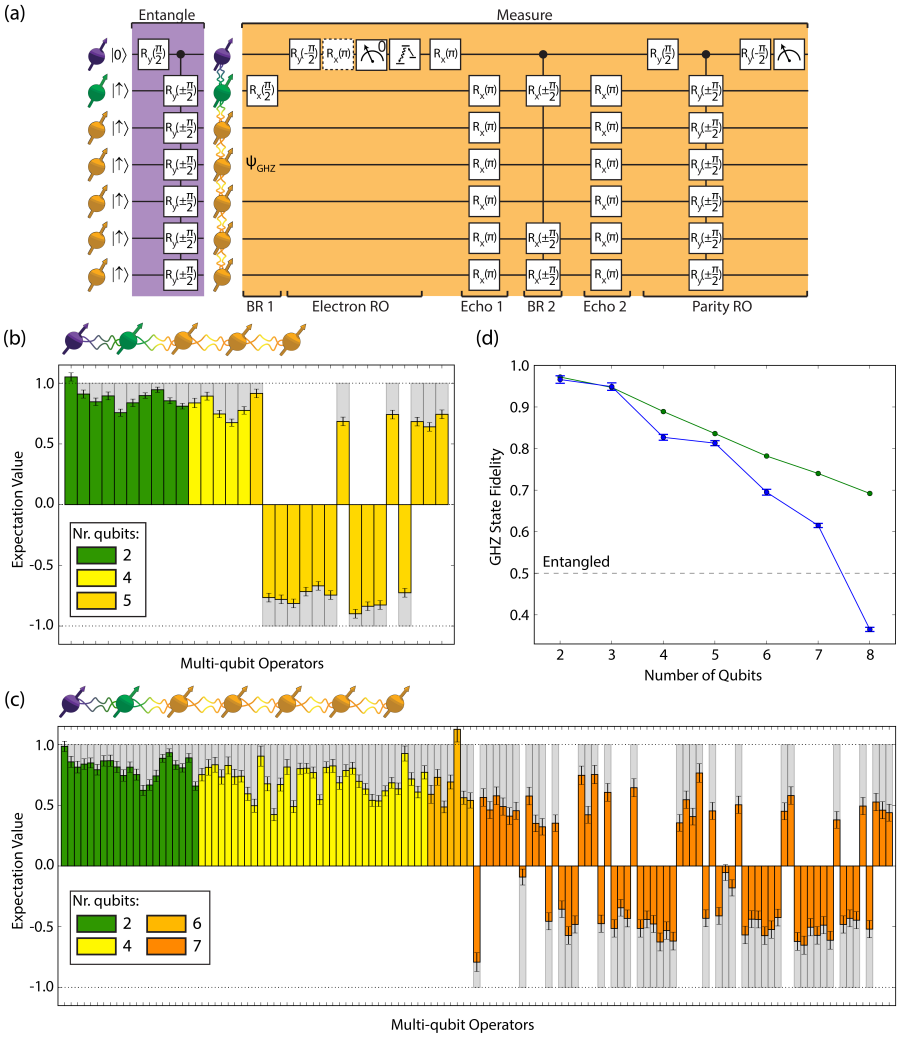

Figure 5.7: (a) Experimental sequence to prepare a 7-qubit GHZ state $|\mathrm{GHZ}_7\rangle$ (purple) and determine the expectation value of the 7-qubit operator $XYYYYZZ$ (orange). The measurement sequence is broken down into basis rotations (BR 1,2), an electron readout (RO), nuclear spin echoes (Echo 1,2), and a multi-qubit readout of the nuclear spins. All operations are applied sequentially (in the same way as shown in Fig. 5.5), but some are shown in parallel for clarity. (b-c) Bar plots showing the measured expectation values (non-zero terms of the ideal state only) after preparing the 5-spin (b) and 7-spin (c) GHZ states. The colors indicate the number of qubits involved, i.e. the number of (non-identity) operators in the expectation value (inset). Gray bars show the ideal expectation values. See Sec. 5.8.5 for the operator corresponding to each bar. The fidelity with the target state is 0.804(6) (b) and 0.589(5) (c), confirming genuine multipartite entanglement in both cases. (d) Plot of GHZ state fidelity against the number of constituent qubits. A value above 0.5 confirms genuine N-qubit entanglement. The blue points are the measured data, while the green points are theoretical predictions assuming a simple depolarizing noise model whose parameters are extracted from single- and two-qubit experiments. Numerical values are given in Sec. 5.8.5.

state, we rotate the nitrogen spin such that the desired measurement basis is mapped to the Z-basis. This ensures that the population in the measurement basis is protected from dephasing during the optical readout of the electron spin, which is caused by the large electron-nitrogen hyperfine coupling in the excited state (see Sec. 5.8.5 and Ref. [62]).

As the number of qubits is increased, a new challenge arises: the total sequence time becomes comparable to, or even exceeds the natural dephasing times (T_2^*) of the nuclear spins. In order to preserve the nuclear spin coherence, we insert spin (Hahn) echo pulses (RF π-pulses) into the sequence to refocus each spin at the point of the next operation performed upon it. In Sec. 5.8.5, we derive a general solution that can be used to algorithmically construct echo sequences that avoid any overlap in gates and that minimise idle time with the electron spin in a superposition state.

In Figs. 5.7(b,c), we show measurements for $N = 5$ and $N = 7$ qubits. In Fig. 5.7(d), we present the measured fidelities with the target GHZ states for 2 to 8 qubits, along with theoretical values as predicted by a depolarizing-noise model based on the individual two-qubit gate fidelities (Sec. 5.8.5). The growing discrepancy between the measured and predicted values for larger N suggests residual crosstalk between the qubits, which is not taken into account in the model. For registers comprising up to 7 spins we observe negativity of the witness $\mathcal{W}_{\mathrm{GHZ}}$, revealing genuine N-qubit entanglement of up to 7 qubits with high statistical significance.

5.6. A LONG LIVED QUANTUM MEMORY

The nuclear spin qubits surrounding the NV centre are promising candidates for quantum memories with long coherence times[32,63]. Here we investigate the coherence properties of the register under dynamical decoupling and show that an arbitrary single-qubit state can be protected for over 75 seconds. Furthermore, we show that two-qubit entanglement can be preserved beyond 10 seconds.

We first investigate the coherence of individual nuclear spin qubits under dynamical decoupling. After initializing the nuclear spin in the state $|+\rangle$, we prepare the electron in the state $|1\rangle$ (electron $T_1 = 3.6(3) \times 10^3$ s[47]). This has two effects. Firstly, it allows us to perform selective RF π-pulses on the target nuclear spin. Secondly, the magnetic field gradient imposed by the electron-nuclear hyperfine interaction induces a frozen core, which suppresses flip-flop interactions between nuclear spins[64,65] and thereby reduces the noise the spins are exposed to.

The observed spin-echo coherence times $T_2^{\alpha=1}$, with α the number of RF pulses, vary between 0.26(3) s to 0.77(4) s for the 8 ^{13}C spins. For the ^{14}N spin we find 2.3(2) s, consistent with the smaller gyromagnetic ratio by factor 3.4. The range of coherence times observed for the ^{13}C spins is likely caused by differences in the microscopic environment of each spin. In particular, ^{13}C spins close to the NV centre are in the heart of the frozen core, and, generally tend to couple predominantly to the part of the spin environment for which the dynamics are also suppressed most strongly. Spins farther from the NV tend to couple more strongly to the spin environment outside the frozen core. This explanation is consistent with the observation that the spin with the longest $T_2^{\alpha=1}$ of 0.77(4) s is located closest (C1, $r = 0.53(5)$ nm[57]) to the vacancy lattice site, while the shortest $T_2^{\alpha=1}$ of 0.26(3) s is found for a spin at a larger distance (C8, $r = 1.04(4)$ nm[57]). As expected,

increasing the number of decoupling pulses leads to an increase in the measured coherence times. For $\alpha = 256$ pulses, the decay time of C5 reaches $T_2^{\alpha=256} = 12.9(4)$ s, while for the ^{14}N spin, we measure $T_2^{\alpha=256} = 63(2)$ s (see Sec. 5.8.2). For the other ^{13}C spins for which we measure $T_2^{\alpha=256}$, we find a range of values from 4(1) to 25(4) seconds (Sec. 5.8.2).

To confirm that arbitrary quantum states can be protected, we prepare the six cardinal states and measure the average state fidelity under dynamical decoupling. The measured decay curves for spin C5 and the ^{14}N spin are shown in Fig. 5.8, where α is varied from 1 to 256. With 256 pulses, we measure a state fidelity exceeding the classical memory bound of $\frac{2}{3}$ at a time of 16.8 s for C5, and at a time of 75.3 s for the ^{14}N spin.

The coherence times demonstrated here are the longest reported for individual qubits in the solid state and exceed values for isolated nuclear spin qubits in isotopically purified materials[24,32,33]. More importantly, however, in our register we realise these long coherence times while maintaining access to 10 coupled spin qubits.

We exploit the multi-qubit nature of the register to investigate the protection of entangled states of two ^{13}C spin qubits. After preparing the state $|\Phi^+\rangle = (|{+}{+}\rangle + |{-}{-}\rangle)/\sqrt{2}$ following the sequence shown in Fig. 5.5(a), we again prepare the electron in the state $|1\rangle$. We then measure the Bell state fidelity as a function of total evolution time for $\alpha = 1$ to $\alpha = 256$ pulses. Note that since $|\Phi^+\rangle$ is an eigenstate of ZZ, its evolution is not affected by the coupling between the two qubits, which is predominantly dipolar and of the form CI_zI_z, with $C = 1.32(4)$ Hz[57]. The measured fidelities are plotted in Fig. 5.8(c). For $\alpha = 256$ decoupling pulses, we confirm the preservation of entanglement for > 10 s, as quantified by a fidelity exceeding 0.5 with the desired Bell state.

With the capability to protect multi-qubit quantum states, it becomes important to consider additional effects that may affect their coherence, such as the presence of correlated noise. As a first experimental step towards understanding such effects, we use entangled states of nuclear spins to explore spatial correlations within the noise environment. We perform experiments on two pairs of ^{13}C spins. We prepare two Bell states for each pair, one exhibiting even ZZ parity, which, written in the Z-basis, is given by $|\Phi^+\rangle = (|{\downarrow}{\downarrow}\rangle + |{\uparrow}{\uparrow}\rangle)/\sqrt{2}$, and another exhibiting odd ZZ parity, $|\Psi^-\rangle = (|{\downarrow}{\uparrow}\rangle - |{\uparrow}{\downarrow}\rangle)/\sqrt{2}$. The difference in the coherence times of these two states gives an indication of the amount of correlation in the noise experienced by the two spins[66]. In the case of perfectly correlated noise, one would expect the state $|\Phi^+\rangle$ to decay at four times the single qubit decay rate (superdecoherence), while the state $|\Psi^-\rangle$ would form a decoherence-free subspace[67,68]. In contrast, for completely uncorrelated noise, the coherence times for the two states would be identical.

We measure the coherence times for the two Bell states, varying the total evolution time for the case of a single spin-echo pulse ($\alpha = 1$) with the electron spin prepared in the state $|1\rangle$. In Fig. 5.8(d), we plot the normalised coherence signal for both Bell states and for both pairs of qubits. A statistically significant difference between the decay curves for the two Bell states is found for both pairs, where the odd-parity state $|\Psi^-\rangle$ decays more slowly than the even-parity state $|\Phi^+\rangle$, indicating partly correlated noise in the system. We can relate the size of the effect to the distance between the spins in the pairs, which has been characterised in separate work[57]. This reveals that the pair with a smaller separation (C1 and C6, distance 0.96(3) nm) shows more correlation than the

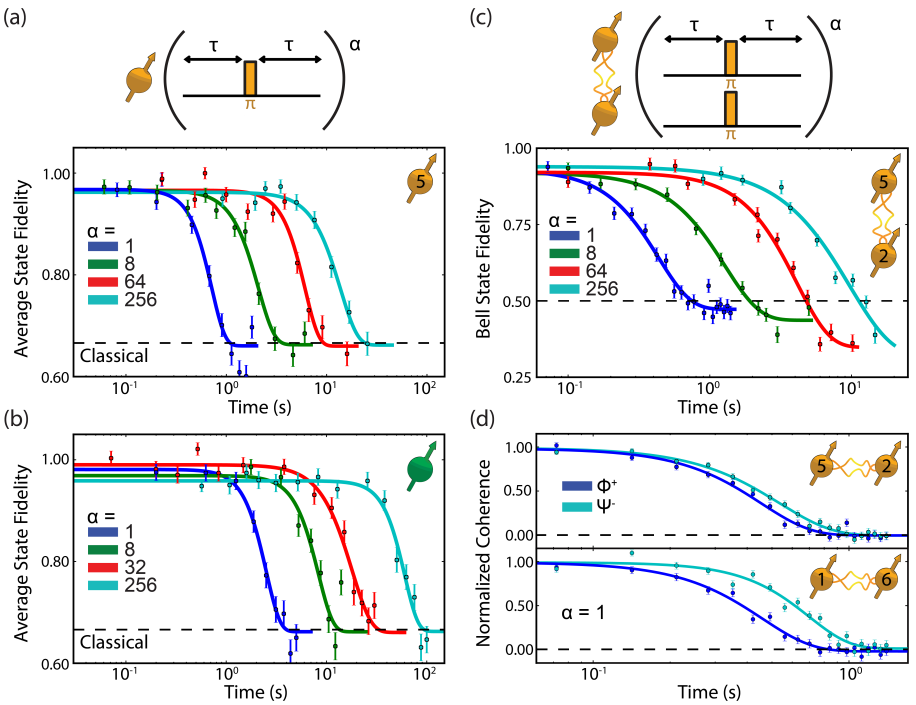

Figure 5.8: (a) Dynamical decoupling for spin C5. With $\alpha = 256$ pulses, the average state fidelity of the six cardinal states is measured to be 0.73(2) after 16.8 s, above the limit of $\frac{2}{3}$ for a classical memory with a confidence of 99.7% (upper-tailed Z test). Solid lines are fit to the function $f(t) = A + Be^{-(t/T)^n}$. The offset A is fixed using the average fidelity of the input states $|\uparrow\rangle$ and $|\downarrow\rangle$, which show no decay on these timescales. B, T and n are fit parameters which account for the decay of the fidelity due to interactions with the nuclear spin bath, external noise and pulse errors. (b) Dynamical decoupling of the ^{14}N spin. For $\alpha = 256$ pulses, the average state fidelity at 75.3 s is 0.73(3), which is above the bound for a classical memory with 99.4% confidence. (c) Dynamical decoupling of a pair of ^{13}C spins prepared in the Bell state $|\Phi^+\rangle$. Solid lines are fits to $f(t)$, but with A as a free parameter to account for the observed decrease in the ZZ correlations at large pulse numbers, likely due to pulse errors. With 256 decoupling pulses, genuine two-qubit entanglement is witnessed at times up to 10.2 s, where we observe a fidelity of 0.57(2) with the target Bell state (99.9% confidence of entanglement). In addition, interpolation of the fit yields 11.3(8) s as the point where the fidelity crosses 0.5 (Sec. 5.8.2). (d) Normalised coherence $(\langle XX\rangle \pm \langle YY\rangle)/2\mathcal{N}$, where $\mathcal{N}$ is a normalization factor, for two pairs of ^{13}C spins prepared in both the even and odd parity Bell states $|\Phi^+\rangle = (|\downarrow\downarrow\rangle + |\uparrow\uparrow\rangle)/\sqrt{2}$ and $|\Psi^-\rangle = (|\downarrow\uparrow\rangle - |\downarrow\uparrow\rangle)/\sqrt{2}$. Solid lines are fits to $f(t)$ with $A = 0$ and $B = 1$. For pair 1, the fitted decay times, T, are 0.45(2) s and 0.54(1) s for the states $|\Phi^+\rangle$ and $|\Psi^-\rangle$ respectively. For pair 2, the equivalent values are 0.46(2) s and 0.70(3) s.

pair with a larger separation (C5 and C2, 1.38(7) nm). This observation is consistent with the idea that spatially close spins tend to couple to the same nuclear spin environment, and therefore experience correlated noise, although large deviations from this rule are expected to be possible for specific cases[66]. Characterizing such correlated noise provides new opportunities to investigate the physics of decoherence in spin baths[66], and to develop and test quantum error correction schemes that are tailored for specific correlated noise[69,70].

5.7. CONCLUSION

In conclusion, we have developed a novel electron-nuclear two-qubit gate and applied these gates to realise a 10-qubit solid-state spin register that can protect an arbitrary single-qubit state for over one minute. The techniques developed in this work can be readily implemented for multi-qubit control in a variety of other donor and defect platforms, including spin-1/2[7,9,13,20,28,53,54] and contact hyperfine[21,34] systems, for which many previous gate designs are challenging to apply[37,48–50]. Further improvements in selectivity and fidelity of the gates are anticipated to be possible by (optimal) shaping of the RF pulses[38,55,56] and by reducing electronic noise. Additionally, the use of direct RF driving opens the possibility to perform gates in parallel on multiple qubits. Combined with already demonstrated long-range optical entanglement[29–31], our multi-qubit register paves the way for the realization of rudimentary few-node quantum networks comprising tens of qubits. This will enable the investigation of basic error correction codes and algorithms over quantum networks[44–46]. Finally, looking beyond quantum information, the gate sequences developed here also enable new quantum sensing methods[57].

5.8. SUPPLEMENTARY MATERIALS

5.8.1. EXPERIMENTAL DETAILS

SAMPLE

All experiments are performed on a high-purity, chemical-vapour-deposition homoepitaxially grown diamond (type IIa) with natural abundance of carbon isotopes (1.1% ^{13}C). The diamond was grown and cleaved (along the ⟨111⟩ crystal axis) by Element Six. We work with a naturally occurring NV centre which was selected based on the absence of strongly coupled (>500 kHz hyperfine coupling) ^{13}C spins, but without any other criteria on the spin environment. Microwave and RF fields are applied via a lithographically defined gold stripline. A solid-immersion lens enhances photoluminescence collection efficiency[14,71], and an aluminium-oxide layer is grown by atomic-layer-deposition to serve as an anti-reflection coating[61,72].

CONFOCAL MICROSCOPE AND NV OPERATIONS

The sample is held in a home-built confocal microscope based upon a closed cycle cryostat (Montana Cryostation, 3.7 K). We measure long NV electron spin relaxation and spin coherence times ($T_1 > 1$ h, $T_2^{DD} > 1$ s)[47], and we achieve fast spin operations (Rabi frequency: 14 MHz) and readout/initialization (~ 10 µs[14]). We perform spin-selective optical readout of the NV-centre to measure the spin state in a single shot, with fi-

delities of 0.905(2) for the bright state ($m_s = 0, := |0\rangle$) and 0.986(2) for the dark state ($m_s = -1, := |1\rangle$). The E_x and E_y optical transitions are split by 4.0 GHz due to lateral strain. All measurements are corrected for the finite readout fidelity in order to provide a best estimate for the actual state.

MAGNETIC FIELD STABILIZATION

An external magnetic field is applied along the NV-axis, with magnitude ~ 403 G. A PI loop (Team-Wavelength WEC3293) is used to stabilise the temperature of the permanent neodymium magnet, and thus the field. The temperature stability is measured to be 1.13 mK across a 24 hour period (one standard deviation), corresponding to a magnetic field stability of ~ 450 μG, or a 0.5 Hz frequency shift for the ^{13}C spins, which is negligible compared to the intrinsic linewidth ($1/\sqrt{2}\pi T_2^*$) of ~ 20 Hz. The field alignment is calibrated to within 0.1 degrees using a thermal echo sequence[57].

MICROWAVE AND RF SETUP

Microwave amplifier (AR 25S1G6) noise is suppressed by a fast microwave switch (TriQuint TGS2355-SM) with a suppression ratio of 40 dB. Video leakage noise generated by the switch is filtered with a high pass filter. To obtain effective MW pulses independent of the ^{14}N nuclear spin state, all microwave operations are performed using Hermite envelopes[55,73]. During dynamical decoupling, pulse errors are mitigated by implementation of the XY8 scheme[74]. In the initial two-qubit DDRF gate experiments (Fig. 5.4), we use an RF amplifier (Analog Devices ADA4870). To reduce ringing of the RF signal due to sub-period switching in the presence of an AC-coupling from a high-pass filter (3rd order Butterworth, 52 kHz, home-built), we use error function pulse shapes, with envelope function

$$f(t) = 1 - \frac{1}{2}\,\mathrm{erf}\left(\frac{2(\Delta t - t + t_0)}{\Delta t}\right) - \frac{1}{2}\,\mathrm{erf}\left(\frac{2(\Delta t + t - t_{\mathrm{pulse}})}{\Delta t}\right), \tag{5.6}$$

where Δt is the risetime, t_0 is the start time of the pulse, t_{pulse} is the pulse length and $\mathrm{erf}(x)$ is the error function. We also use error function pulses for the RF spin echo pulses (see Sec. 5.8.5). In the multi-qubit experiments, the RF signal is generated directly by an AWG (Tektronix 5014C, 4.5V pk-pk) to avoid heating of the chip and to allow shorter RF pulses without ringing from filters in the RF electronics. In all cases, we ensure that the RF pulses are comprised of an integer number of periods of the RF waveform, i.e. we ensure that $\omega t_{\mathrm{pulse}} = 2\pi n$ for integer n, where t_{pulse} is the RF pulse length. This ensures that any phase picked up on the electron spin due to the RF pulse is cancelled. We set n to maximise the length of t_{pulse} while ensuring that $t_{\mathrm{pulse}} < \tau$ for the first and last RF pulse in the DDRF sequence. For the remainder of the pulses, we use the value $2n$.

OPTICAL SETUP

Laser pulses are generated by direct current modulation (515 nm laser for charge state control, Cobolt MLD, on/off ratio of >135 dB) or by acoustic optical modulators (637 nm lasers for spin pumping and single-shot readout, Toptica DL Pro and New Focus TLB-6704-P). By placing two modulators in series (Gooch and Housego Fibre Q), an on/off ratio of >100 dB is obtained for the 637 nm lasers[47]. The laser frequencies are stabilised to within 2 MHz using a wavemeter (HF-ANGSTROM WS/U-10U).

5.8.2. 10 QUBIT REGISTER CHARACTERIZATION

QUBIT FREQUENCIES

	$\omega_0/2\pi$ [Hz]	$\omega_{-1}/2\pi$ [Hz]	$\omega_{+1}/2\pi$ [Hz]	$A_\parallel/2\pi$ [kHz]	$A_\perp/2\pi$ [kHz]
C1	431961(1)	218828(1)	645123(1)	213.154(1)	3.0(4)
C2	431956(1)	469020(1)	396542(1)	-36.308(1)	26.62(4)
C3	431958(1)	413477(1)	454427(1)	20.569(1)	41.51(3)
C4	431951(1)	447234(1)	424752(3)	-11.346(2)	59.21(3)
C5	431962(1)	408317(1)	457035(1)	24.399(1)	24.81(4)
C6	431962(1)	480625(1)	383480(40)	-48.58(2)	9(2)
C7	431956(1)	451802(1)	412175(5)	-19.815(3)	5.3(5)
C8	431973(1)	414407(1)	449687(2)	17.643(1)	8.6(2)
^{14}N	5069110(1)	2884865(1)	7263440(1)	2189.288(1)	-

Table 5.1: **Precession frequencies and hyperfine couplings for the nuclear spins.** ω_0, ω_{-1}, and ω_{+1} are the measured nuclear precession frequencies for the $m_s = 0, -1$ and $+1$ electron spin projections respectively, obtained from least-squares fits of Ramsey signals. $A_\parallel$ and $A_\perp$ are the hyperfine interaction components parallel and perpendicular to the applied magnetic field, obtained using the approximate relations in Eq. 5.7. For the ^{14}N spin the frequencies given are for the $m_I = 0 \leftrightarrow m_I = -1$ transition, and the parallel hyperfine component is taken as $(\omega_{+1} - \omega_{-1})/2$. Note that we use the definition $\omega_1 = \omega_{-1}$ in the rest of the chapter.

In Table 5.1, we give the measured precession frequencies for each nuclear spin, determined from Ramsey spectroscopy with the electron stored in the $m_s = 0, -1$ and $+1$ spin projections. For the ^{13}C spins, under both the secular approximation and the assumption of a perfectly aligned field, the hyperfine parameters can then be obtained from the relations

$$\begin{aligned} A_\parallel &= \frac{\omega_{+1}^2 - \omega_{-1}^2}{4\omega_0} \\ A_\perp &= \sqrt{\frac{\omega_{+1}^2 + \omega_{-1}^2 - 2\omega_0^2 - 2A_\parallel^2}{2}}. \end{aligned} \tag{5.7}$$

Note that due to the high accuracy of the Ramsey measurements, small deviations from Eqs. 5.7 (due to non-secular Hamiltonian terms and magnetic field misalignment) are likely to be larger than the uncertainties in the parameters extracted by propagating the measurement errors. Therefore, the quoted values are approximate.

COHERENCE MEASUREMENTS

Table 5.2 contains the measured coherence properties of each spin. T_2^* times are measured with the electron in the $m_s = -1$ and $m_s = 0$ spin projections, while T_2 measurements are performed with a single spin echo pulse for the $m_s = -1$ electron spin projection. A significantly lower T_2 time is observed for the $m_s = 0$ spin projection (~15-90 ms). This effect is attributed to the frozen core created by the NV centre, whereby the hyperfine interaction suppresses magnetic field noise due to flip-flop interactions[64]. A similar effect is observed for the longitudinal relaxation times of the ^{13}C spins. Due to the times required to acquire data, we do not perform full T_1 characterizations for all nuclear

spins with $m_s = -1$. However, a verification measurement is performed for a single nuclear spin, with the electron spin prepared in the $m_s = -1$ spin projection. We measure the decay from the $|\uparrow\rangle$ state for time periods up to 6 minutes, as shown in Fig. 5.9. On these timescales, only a small decay is observed. Dynamical decoupling measurements are performed with $\alpha = 256$ pulses with the electron again in the $m_s = -1$ projection. Example data is given for C5 and the ^{14}N spin in Fig. 5.10. For spins C6 and C8, the best signal was achieved with all pulses performed around the $\hat{x}$-axis. For the other spins, XY8 sequences were used[74]. For C8, we were unable to measure the coherence time for 256 pulses due to strong pulse errors caused by spectral overlap with other spins. Optimised pulse sequences for such situations will be investigated further in the future.

	T_2^* ($m_s = -1$) [ms]	T_2^* ($m_s = 0$) [ms]	T_2 ($m_s = -1$) [s]	$T_2^{\alpha=256}$ ($m_s = -1$) [s]
C1	12.0(6)	10.0(3)	0.77(4)	25(4)
C2	9.2(8)	9.1(5)	0.53(6)	6.8(8) [$\alpha = 256$]
				10.6(7) [$\alpha = 400$]
C3	11.9(5)	12.3(3)	0.68(3)	7.4(8)
C4	5.7(2)	5.3(4)	0.53(6)	4.1(4)
C5	15.6(8)	17.2(4)	0.62(3)	12.9(4)
C6	3.7(2)	3.6(2)	0.59(2)	13(2)
C7	4.1(6)	4.6(7)	0.52(3)	4(1)
C8	7.6(4)	7.6(3)	0.26(3)	1.2(2) [$\alpha = 8$]
^{14}N	23.2(7)	25.1(7)	2.3(2)	63(2)

Table 5.2: **Coherence times for the nuclear spins.** T_2^* is obtained from a least-squares fit of Ramsey signals, with evolution for the $m_s = -1$ and $m_s = 0$ electron spin projections. T_2 is obtained from a least-squares fit of a spin echo experiment, with free evolution measured for the $m_s = -1$ electron spin projection. $T_2^{\alpha=256}$ is obtained from a least-squares fit of a dynamical decoupling experiment with $\alpha = 256$ pulses, with the electron spin in the $m_s = -1$ spin projection.

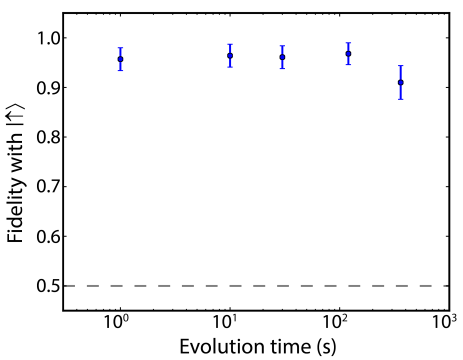

Figure 5.9: Longitudinal relaxation (T_1) measurement for nuclear spin C5. We prepare the nuclear spin in the $|\uparrow\rangle$ eigenstate, and the electron spin in the $m_s = -1$ projection. On timescales up to 6 minutes, only a minor decay is observed.

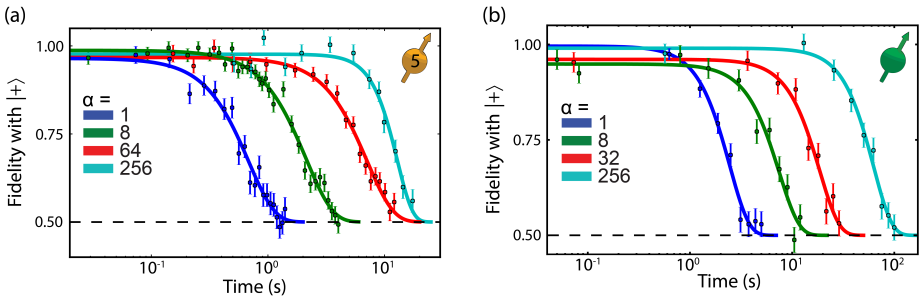

Figure 5.10: Dynamical decoupling of a single ^{13}C spin (C5) with α = 1, 8, 64 and 256 pulses (a) and the ^{14}N spin with α = 1, 8, 32 and 256 pulses (b). Each nuclear spin is initialised and read-out in the X-basis. We fit the data to the function $f(t) = A + Be^{-(t/T)^n}$ (solid lines), where $A = 0.5$, and B, T and n are fit parameters which account for the decay of the fidelity due to interactions with the nuclear spin bath, external noise and pulse errors. With 256 decoupling pulses, the fitted coherence times are $T_2^{\alpha=256}$ = 12.9(4) s (C5, (a)) and $T_2^{\alpha=256}$ = 63(2) s (14N, (b)).

5

ANALYSIS OF ENTANGLEMENT PRESERVATION

For the preservation of entanglement between a pair of nuclear spins, as presented in Fig. 5.8(c), we use a Bell state fidelity above 0.5 as an entanglement witness. To determine how long entanglement can be protected, we use two approaches. First, using the measured data points and their statistical uncertainties, we can perform an upper-tailed Z test to obtain a confidence interval that the state fidelity is above 0.5. For 10.2 s, the measured fidelity of 0.57(2) corresponds to a confidence interval of 99.9%.

A second approach is to modify the fit function used in Fig. 5.8:

$$f(t) = A + Be^{-(t/T)^n} \tag{5.8}$$

to instead incorporate a crossing value, t_c, at which the function crosses the threshold, denoted by c:

$$f(t) = c + B(e^{-(t/T)^n} - e^{-(t_c/T)^n}). \tag{5.9}$$

As before, B, T and n are free fit parameters. This approach is based upon interpolation of the data and therefore uses additional assumptions, but gives an estimate for the time at which the threshold is crossed. For the cases of $\alpha = 256$ in Figure 5.8(c), we find a crossing value of t_c = 11.3(8) s.

GATE PARAMETERS

The electron-nuclear gate parameters for each spin are given in Table 5.3. Spins C1, C7, C8 and ^{14}N are all controlled using the DDRF gate scheme, while the remaining spins are controlled using previously developed dynamical decoupling based gates[37]. Two parameter regimes are given for the electron-nuclear gate on spin C1. To produce the results shown in Fig. 5.4(b), we used a RF amplifier to increase the nuclear spin Rabi frequency. However, operating with this power caused issues during experiments involving

	N	τ (μs)	Gate duration (μs)	RF π-pulse duration (μs)
C1*	8	39.356	629	469
C1	48	16.204	1556	1330
C2	44	7.218	635	1096
C3	22	11.250	495	929
C4	20	16.480	659	734
C5	32	6.540	419	1606
C6	90	4.932	888	1173
C7	64	18.522	2371	1024
C8	48	23.152	2222	1592
^{14}N	12	16.204	389	278

Table 5.3: **Gate parameters for the nuclear spins.** N and τ parameterise a dynamical decoupling gate with N electron π-pulses, separated by 2τ (see Fig. 5.2(a)). Two sets of parameters are given for C1; the starred entry corresponds to the case with use of an RF amplifier (see text for details).

multiple nuclear spins. This is due to two effects; firstly, a loss of readout photons was observed due to heating of the sample. For the final readout, this could be mitigated by a wait duration of ~ 1 ms, as the longitudinal relaxation time of the electron spin is long (> 1 hour). Secondly, the use of an amplifier required additional high-pass filters due to the presence of low-frequency noise (see Sec. 5.8.1). The AC-coupling induced by these filters led to ringing effects over significant timescales (~ 10 – 100 μs) which can induce unwanted phases on the electron spin. We expect that these issues can be mitigated in future experiments by using a free-space RF antenna to prevent heating of the sample and an improved RF delivery system to reduce ringing. For spins C7 and C8, longer gate durations are used to avoid crosstalk with additional spectrally close nuclear spins (~ 1 kHz) [57].

5.8.3. TWO QUBIT GATES: THEORY

In this section we derive equations for the evolution of the NV-^{13}C system under the dynamical decoupling with RF (DDRF) gate sequence (Fig. 5.2). Here, we consider the case of a single ^{13}C nuclear spin interacting with the electron spin of an NV centre through the hyperfine interaction, under the presence of a radio frequency driving field. We first consider an approximate idealised case for which the evolution operator can be calculated analytically. We then consider the generalised case, where time-independent simulation of the system is enabled by the application of a piecewise treatment which accounts for the shift of nuclear spin quantization axis due to a change of the electron spin state. We set $\hbar = 1$ for all following derivations.

HAMILTONIAN

In the interaction picture with respect to the electron energy splitting and neglecting non-secular terms, the Hamiltonian of the NV-^{13}C system is given by

$$H = \omega_L I_z + A_\parallel S_z I_z + A_\perp S_z I_x + 2\Omega \cos\big(\omega t + \phi\big) I_x \tag{5.10}$$

where the final term describes the interaction of the nuclear spin with a radio frequency (RF) driving field polarised along x with frequency ω, phase ϕ and Rabi frequency Ω. Here, S_α and I_α are the spin-1 and spin-1/2 operators of the electron and nuclear spins respectively. $\omega_L = \gamma B_z$ is the nuclear spin Larmor frequency, where γ is the gyromagnetic ratio of the ^{13}C spin and B_z is the external magnetic field strength along the NV axis. $A_\parallel$ ($A_\perp$) is the component of the electron-nuclear hyperfine interaction parallel (perpendicular) to the NV axis.

BASIC DERIVATION

Here we derive the dynamics under a simple approximate model that gives the idealised evolution of the DDRF gate. Setting $A_\perp = 0$ and restricting to the $m_s = \{0, -1\}$ subspace of the electron spin, we can write Eq. 5.10 as

$$H = |0\rangle\langle 0| \otimes \omega_L I_z + |1\rangle\langle 1| \otimes \omega_1 I_z + 2\Omega\cos\big(\omega t + \phi\big) I_x, \tag{5.11}$$

where $|0\rangle$ ($|1\rangle$) indicates the electron $m_s = 0$ ($m_s = -1$) spin projection and $\omega_1 = \omega_L - A_\parallel$ is the nuclear spin precession frequency when the electron is in the state $|1\rangle$. We can now move to the rotating frame at frequency ω and make the rotating wave approximation (RWA), giving

$$\begin{aligned} H' &= R_0(t)(H - \omega I_z)R_0(t)^\dagger \\ &= |0\rangle\langle 0| \otimes (\omega_L - \omega) I_z + |1\rangle\langle 1| \otimes (\omega_1 - \omega) I_z + \Omega(\cos\big(\phi\big) I_x + \sin\big(\phi\big) I_y), \end{aligned} \tag{5.12}$$

where $R_0(t) = e^{i\omega t I_z}$. Setting the RF frequency resonant with the nuclear spin when the electron is in the state $|1\rangle$ ($\omega = \omega_1$) and neglecting driving of the nuclear spin when the electron is in the state $|0\rangle$ (i.e. assuming $\Omega \ll (\omega_L - \omega_1)$), we find[36]

$$H' = |0\rangle\langle 0| \otimes (\omega_L - \omega_1) I_z + |1\rangle\langle 1| \otimes \Omega(\cos\big(\phi\big) I_x + \sin\big(\phi\big) I_y). \tag{5.13}$$

This is equal to the Hamiltonian given in Eq. 5.2. Writing equation 5.13 in the form $H' = |0\rangle\langle 0| \otimes H_0 + |1\rangle\langle 1| \otimes H_1$, we can consider the evolution of the nuclear spin for the two electron eigenstates separately, giving the unitary operators

$$\begin{aligned} U_0(t) &= e^{-iH_0 t} = \begin{pmatrix} e^{-i(\omega_L - \omega_1)t/2} & 0 \\ 0 & e^{i(\omega_L - \omega_1)t/2} \end{pmatrix}, \\ U_1(t, \phi) &= e^{-iH_1 t} = \begin{pmatrix} \cos(\Omega t/2) & -(i\cos\big(\phi\big) + \sin\big(\phi\big))\sin(\Omega t/2) \\ -(i\cos\big(\phi\big) - \sin\big(\phi\big))\sin(\Omega t/2) & \cos(\Omega t/2) \end{pmatrix}. \end{aligned} \tag{5.14}$$

We now construct evolution operators for the dynamical decoupling sequence $(\tau - \pi - 2\tau - \pi - \tau)^{N/2}$. For simplicity, decoupling (π) pulses on the electron are treated to be perfect and instantaneous. We can consider separately the cases in which the electron starts in either $|0\rangle$ or $|1\rangle$, giving the total evolution operators V_0 and V_1 respectively, defined as

$$\begin{aligned} V_0 &= U_0(\tau) \cdot U_1(2\tau, \phi_{K-1}) \cdot U_0(2\tau) \cdots U_0(2\tau) \cdot U_1(2\tau, \phi_2) \cdot U_0(\tau) \\ V_1 &= U_1(\tau, \phi_K) \cdot U_0(2\tau) \cdot U_1(2\tau, \phi_{K-2}) \cdots U_1(2\tau, \phi_3) \cdot U_0(2\tau) \cdot U_1(\tau, \phi_1), \end{aligned} \tag{5.15}$$

where ϕ_k are the phases of each RF pulse, $k = 1,...,K$ and $K = N+1$. The total evolution of the two-spin system is then given by

$$V = |0\rangle\langle 0| V_0 + |1\rangle\langle 1| V_1. \tag{5.16}$$

As can be seen from Eq. 5.15, the even k RF pulses only affect the dynamics of V_0, while the odd k pulses only affect the dynamics of V_1. Therefore, we can design the sequences individually in order to achieve the desired conditional rotation of the nuclear spin. In order to ensure the rotations due to each RF pulse add up constructively, the phases ϕ_k should be adapted to account for the periods of free precession, which build up in integer multiples of $\phi_\tau = (\omega_L - \omega_1)\tau$. For the case of V_0, the required phases should be updated according to the sequence $\phi_\tau, 3\phi_\tau, 5\phi_\tau, \ldots$, while for the case of V_1 the sequence is $0, 2\phi_\tau, 4\phi_\tau, \ldots$. This would yield an unconditional rotation of the nuclear spin. To achieve a conditional rotation, we can additionally add a relative π phase shift to each phase in the V_1 sequence (odd k). Furthermore, we can add a phase φ to all RF pulses which can be used to set the rotation axis for the full gate. Combining these elements, the required RF pulse phases for a conditional rotation (two-qubit gate) are summarised as $\phi_k = \varphi + \phi'_k$, where

$$\phi'_k = \begin{cases} (k-1)\phi_\tau + \pi & k \text{ odd} \\ (k-1)\phi_\tau & k \text{ even,} \end{cases} \tag{5.17}$$

which is equal to Eq. 5.3. We can then substitute the phases defined by Eq. 5.17 into the sequence given in Eq. 5.15, which gives

$$\begin{aligned} V_0 &= \begin{pmatrix} e^{-iN(\omega_L-\omega_1)\tau/2}\cos(N\Omega\tau/2) & -ie^{-iN(\omega_L-\omega_1)\tau/2}e^{-i\varphi}\sin(N\Omega\tau/2) \\ -ie^{iN(\omega_L-\omega_1)\tau/2}e^{i\varphi}\sin(N\Omega\tau/2) & e^{iN(\omega_L-\omega_1)\tau/2}\cos(N\Omega\tau/2) \end{pmatrix} \\ &= R_z(N(\omega_L-\omega_1)\tau)\cdot R_\varphi(N\Omega\tau), \\ V_1 &= \begin{pmatrix} e^{-iN(\omega_L-\omega_1)\tau/2}\cos(N\Omega\tau/2) & ie^{-iN(\omega_L-\omega_1)\tau/2}e^{-i\varphi}\sin(N\Omega\tau/2) \\ ie^{iN(\omega_L-\omega_1)\tau/2}e^{i\varphi}\sin(N\Omega\tau/2) & e^{iN(\omega_L-\omega_1)\tau/2}\cos(N\Omega\tau/2) \end{pmatrix} \\ &= R_z(N(\omega_L-\omega_1)\tau)\cdot R_\varphi(-N\Omega\tau), \end{aligned} \tag{5.18}$$

where $R_z(\theta) = e^{-i\theta I_z}$ and $R_\varphi(\theta) = e^{-i\theta(\cos(\varphi)I_x + \sin(\varphi)I_y)}$. From Eq. 5.16, the total evolution operator is therefore described by $V = V_z \cdot V_{\text{CROT}}$, where V_z is an unconditional rotation of the nuclear spin around z, given by

$$V_z = \mathbb{1} \otimes R_z(N(\omega_L - \omega_1)\tau), \tag{5.19}$$

and V_{CROT} is a controlled rotation of the nuclear spin with tuneable rotation angle (set by N, Ω and τ) and rotation axis (set by φ), given by

$$V_{\text{CROT}} = |0\rangle\langle 0| \otimes R_\varphi(N\Omega\tau) + |1\rangle\langle 1| \otimes R_\varphi(-N\Omega\tau), \tag{5.20}$$

which is equal to Eq. 5.4. Setting $N\Omega\tau = \pi/2$, a maximally entangling two-qubit operation is achieved. With $\varphi = 0$, this operation is related to a controlled-not (CNOT) gate by the local rotations:

$$V_{\text{CROT}} = (R_z(\pi/2) \otimes \mathbb{1}) \cdot (\mathbb{1} \otimes R_x(\pi/2)) \cdot \text{CNOT} \tag{5.21}$$

where

$$\text{CNOT} = |0\rangle\langle 0| \otimes \mathbb{1} + |1\rangle\langle 1| \otimes X. \tag{5.22}$$

GENERALISED CASE

We now consider the dynamics under the more general case where $A_\perp \neq 0$, and where we do not neglect driving of the nuclear spin when the electron is in the state $|0\rangle$ (i.e. we do not assume that $\Omega \ll (\omega_L - \omega_1)$). In this case, when the electron is in the state $|1\rangle$, the nuclear spin precesses at frequency $\omega_1 = \sqrt{A_\perp^2 + (\omega_L - A_\parallel)^2}$, with quantization axis $A_\perp \hat{x} + (\omega_L - A_\parallel)\hat{z}$ at an angle β from $\hat{z}$, defined by $\cos(\beta) = (\omega_L - A_\parallel)/\omega_1$. As the nuclear spin quantization axis is now dependent on the electron spin state, we rewrite Eq. 5.10 as

$$\begin{aligned} H &= |0\rangle\langle 0| H_0 + |1\rangle\langle 1| H_1 \\ H_0 &= \omega_L I_z + 2\Omega\cos(\omega t + \phi) I_x \\ H_1 &= \omega_1 \widetilde{I}_z + 2\widetilde{\Omega}_x \cos(\omega t + \phi)\widetilde{I}_x + 2\widetilde{\Omega}_z \cos(\omega t + \phi)\widetilde{I}_z, \end{aligned} \tag{5.23}$$

where $\widetilde{I}_z = R_y(\beta) I_z R_y(\beta)^\dagger = \cos(\beta) I_z + \sin(\beta) I_x$, $\widetilde{I}_x = R_y(\beta) I_x R_y(\beta)^\dagger = \cos(\beta) I_x - \sin(\beta) I_z$, $\widetilde{\Omega}_x = \Omega\cos(\beta)$, $\widetilde{\Omega}_z = \Omega\sin(\beta)$ and $R_y(\theta) = e^{-i\theta I_y}$. We can define two different rotating frames depending on the electron spin state; $R_0(t) = e^{-i\omega t I_z}$ and $R_1(t) = e^{-i\omega t \widetilde{I}_z}$. After making the RWA, the interaction picture Hamiltonian terms become

$$\begin{aligned} H_0' &= R_0(t)(H_0 - \omega I_z) R_0(t)^\dagger \\ &= (\omega_L - \omega) I_z + \Omega(\cos(\phi) I_x + \sin(\phi) I_y), \\ H_1' &= R_1(t)(H_1 - \omega \widetilde{I}_z) R_1(t)^\dagger \\ &= (\omega_1 - \omega)\widetilde{I}_z + \widetilde{\Omega}_x(\cos(\phi)\widetilde{I}_x + \sin(\phi)\widetilde{I}_y) \\ &= (\omega_1 - \omega)(\cos(\beta) I_z + \sin(\beta) I_x) + \Omega\cos(\beta)(\cos(\phi)(\cos(\beta) I_x - \sin(\beta) I_z) + \sin(\phi) I_y). \end{aligned} \tag{5.24}$$

The Hamiltonian contains additional terms compared to the idealised case with $A_\perp = 0$ (Eq. 5.13). We would therefore like to analyze the effect of these terms on the gate dynamics. Since we have used a different rotating frame for the two electron states, the evolution through the dynamical decoupling sequence should be calculated in a piecewise manner, where we change rotating frame between each electron spin flip. The generalised evolution operators for the two initial electron states from Eq. 5.15 are then given by

$$\begin{aligned} V_0 &= U_0(\tau)\cdot R_0(N'\tau)\cdot R_1(N'\tau)^\dagger \cdot U_1(2\tau,\phi_{K-1})\cdot R_1((N'-2)\tau)\cdot R_0((N'-2)\tau)^\dagger \cdot U_0(2\tau)\cdots \\ &\quad \cdots U_0(2\tau)\cdot R_0(3\tau)\cdot R_1(3\tau)^\dagger \cdot U_1(2\tau,\phi_2)\cdot R_1(\tau)\cdot R_0(\tau)^\dagger \cdot U_0(\tau) \\ V_1 &= U_1(\tau,\phi_K)\cdot R_1(N'\tau)\cdot R_0(N'\tau)^\dagger \cdot U_0(2\tau)\cdot R_0((N'-2)\tau)\cdot R_1((N'-2)\tau)^\dagger \cdot U_1(2\tau,\phi_{K-2})\cdots \\ &\quad \cdots U_1(2\tau,\phi_3)\cdot R_1(3\tau)\cdot R_0(3\tau)^\dagger \cdot U_0(2\tau)\cdot R_0(\tau)\cdot R_1(\tau)^\dagger \cdot U_1(\tau,\phi_1), \end{aligned} \tag{5.25}$$

where $N' = 2N - 1$.

We calculate the evolution numerically following the treatment derived above, making use of the QuTip Python package [75]. To understand the effect of the additional terms from a non-zero $A_\perp$, we consider a test spin with a parallel hyperfine component $A_\parallel/2\pi$

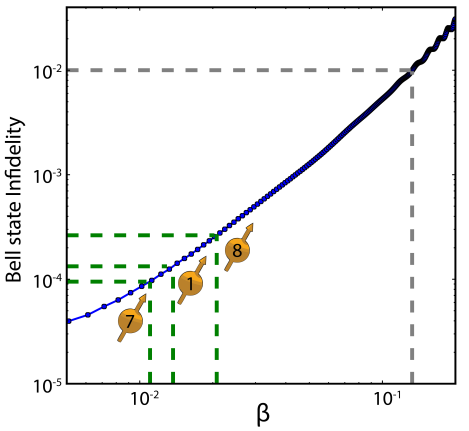

Figure 5.11: Theoretical infidelity of a Bell state generated by the DDRF gate as a function of the angle β between the nuclear spin quantization axes for the electron spin projections $m_s = 0$, $m_s = -1$. The dashed green lines indicate the values of β for the 3 ^{13}C spins for which we use DDRF gates. The dashed gray line indicates the β required for a gate infidelity of 1%.

= 50 kHz. As a measure of fidelity we apply the DDRF gate to create a Bell state (starting from an ideal initialised state) and take the fidelity with the ideal Bell state. In Fig. 5.11, we plot the simulated Bell state infidelity against the relative strength of the perpendicular hyperfine component $A_\perp$, quantified in terms of β. For reference, we mark the values of β for the 3 ^{13}C spins for which we use DDRF gates in the experiments described in Sec. 5.4. In all cases, the simulated infidelity from this component is $< 3\times10^{-4}$. We also mark the value of β for which the infidelity reaches 1% (~ 0.13). This corresponds to $A_\perp/2\pi \sim 60$ kHz for the ^{13}C Larmor frequency of $\omega_L/2\pi \sim 432$ kHz in our experiments, approximately equal to the largest $A_\perp$ observed in our register. It is important to note that this effect can be heavily suppressed by moving to larger magnetic fields. For example, at a field strength of 2000 G, a β value of 0.13 at 403 G would be reduced to 0.03, with a corresponding contribution to the infidelity less than 5×10^{-4}. Alternatively, one could also consider modifications to the gate design which account for the effect of non-zero $A_\perp$.

5.8.4. TWO-QUBIT GATES: EXPERIMENT

DDRF SPECTROSCOPY

A common approach to characterise the nuclear spin environment of an NV centre is to perform dynamical decoupling spectroscopy, where the spacing between a sequence of π-pulses on the electron spin is varied [48–50]. The DDRF interaction presented in this work can be used in a similar way, with the additional benefit that spins with small perpendicular hyperfine components can also be detected. The sequence for the spectroscopy experiment is shown in the inset of Fig. 5.12. First a $\pi/2$ pulse rotates the electron spin to $|+\rangle$, after which the DDRF interaction is applied with fixed N and τ. Finally a second $\pi/2$ pulse is applied with varying phase φ. By fitting the resulting oscillation, we

can distinguish between deterministic electron phase shifts caused by the RF field and loss of electron coherence due to interaction with the nuclear spin environment (see Fig. 5.3(b,c)). We can repeat this procedure while varying the frequency of the RF pulse, which will result in a dip in the amplitude if the RF frequency is resonant with one or more nuclear spins.

An example spectrum is shown in Fig. 5.12 (for the NV centre considered in the main text). We also show a theory curve from a numerical simulation of the sequence based on the identified nuclear spins. In addition to the 8 ^{13}C spins used in this work, an additional 19 ^{13}C spins in the local environment of this NV centre were identified in parallel work[57]. Therefore, we plot the expected signal due to all 27 known spins. The Rabi frequencies of each spin are observed to vary (see Table 5.3), which has not been investigated fully, but could be caused by frequency dependencies of the RF transmission as well as by the non-secular interaction terms in the electron-nuclear hyperfine coupling Hamiltonian[57,58,76,77]. Since the parameters associated with these non-secular terms were not measured, we do not take them into account directly in the model, but rather input the measured Rabi frequencies for each spin individually.

As described in Sec. 5.8.3, the DDRF interaction realises an entangling operation with a nuclear spin if the RF frequency matches the precession frequency when the electron is in the $m_s = -1$ spin projection, i.e. when $\omega = \omega_1$. This is due to the constructive buildup of small rotations from each RF pulse within the dynamical decoupling sequence, which is ensured by setting the phase of each pulse according to Eq. 5.17. However, constructive buildup is also possible at other RF frequencies if the condition $\phi'_k(\omega) - \phi'_k(\omega_1) = 0 \bmod 2\pi$ is satisfied, where $\phi'_k(\omega)$ is the generalised version of Eq. 5.17 where $\omega_1 \to \omega$. Solving for ω, we find resonance conditions

$$\omega_m = \omega_1 + \frac{2\pi m}{\tau}, \tag{5.26}$$

for integer m. Examples of such off-resonant interactions are indicated by the arrows in Fig. 5.12(b). The strengths of the off-resonant interactions are set by the Rabi frequency in combination with the detuning of the RF field from both ω_1 and ω_L. For the parameters used in Fig. 5.12, the off-resonant interactions are separated by integer multiples of $2\pi \times 54$ kHz. The two highlighted peaks therefore correspond to $m = 4$; $\omega_m/2\pi = 434.828$ kHz for C1 and $m = -1$; $\omega_m/2\pi = 426.625$ kHz for C6. Additional unconditional rotations of the nuclear spins can also occur when $\omega_p = \omega_1 + (2p+1)\pi/\tau$ for integer p, for which $\phi'_k(\omega_p) = (k-1)\phi_\tau + \pi$ for all k. These rotations do not entangle the electron and nuclear spins and therefore do not show up in the spectroscopy measurements, but can cause additional unwanted crosstalk. In order to avoid such unwanted crosstalk in the 10-qubit register, we ensure that any conditional or unconditional off-resonant interactions do not overlap with the resonances of any targeted spins.

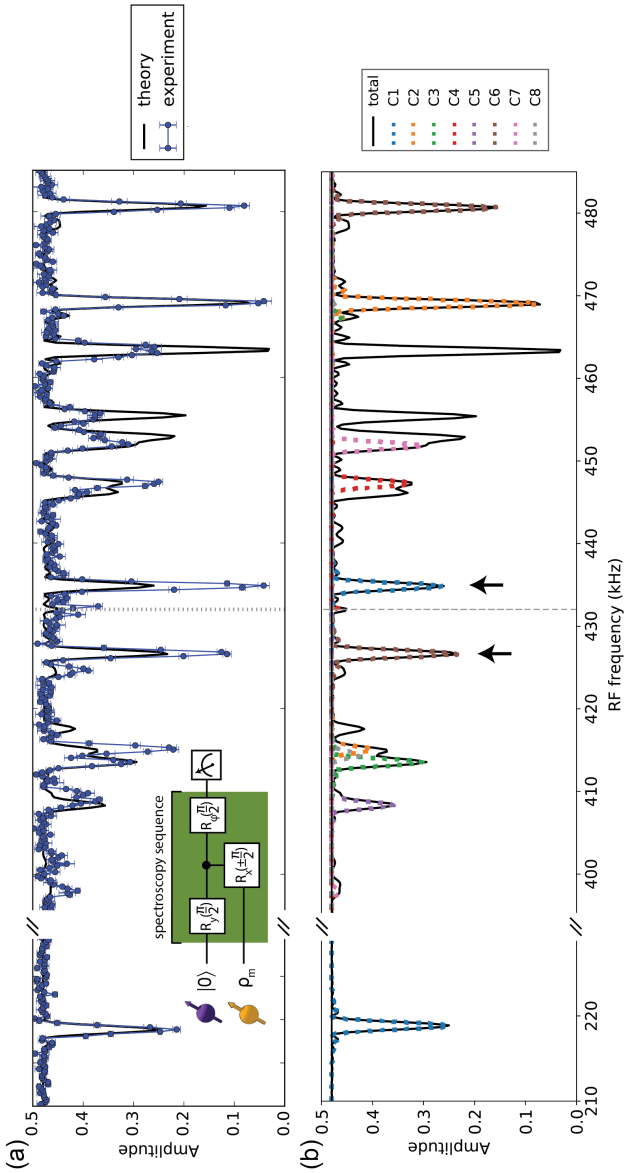

Figure 5.12: Spectroscopy of the nuclear spin environment using the DDRF interaction. (a) Measured spectrum (blue points) using the sequence described in the text and illustrated in the inset. Each data point corresponds to the fitted amplitude A of the function $f(\varphi) = a + A\cos(\varphi + \varphi_0)$, where φ is swept from 0 to 360 deg and φ_0 accounts for deterministic phase shifts induced on the electron by the RF field. By fitting the amplitude, we distinguish these phase shifts from loss of coherence due to entangling operations. The black line is the result of a numerical simulation incorporating all 27 known spins surrounding the NV centre [57]. (b) Individual numerical simulations for each of the 8 ^{13}C spins used in this work. The black arrows indicate two prominent dips that are caused by off-resonant interactions with ^{13}C spins from the DDRF interaction (see text), corresponding to $m = 4$ for C1 (blue dashed line) and $m = -1$ for C6 (brown dashed line).

Spin	$\mathcal{F}_{\text{Bell}}$ (measured)	$\mathcal{F}_{\text{Bell}}$ (simulated)
C1*	0.972(8)	0.998
C1	0.93(1)	0.990
C7	0.85(2)	0.797
C8	0.81(2)	0.892
^{14}N	0.93(1)	0.99996

Table 5.4: **Measured and simulated electron-nuclear spin Bell state fidelities for the nuclear spins controlled by DDRF gates.** For C1, the spectrally closest spin is C5. For C7, there are three spins within 5 kHz; C4 and two unused spins with hyperfine components $\{A_\parallel/2\pi, A_\perp/2\pi\} = \{-20.7, 12\}$ kHz and $\{-23.2, 13\}$ kHz[57]. For C8, there are two spins within 5 kHz; C3 and one unused spin with hyperfine components $\{A_\parallel/2\pi, A_\perp/2\pi\} = \{14.5, 10\}$ kHz. *Measured with use of RF amplifier, see Sec. 5.8.1.

SOURCES OF INFIDELITY FOR THE DDRF GATE

As shown in Sec. 5.8.3, the perpendicular component of the electron-nuclear hyperfine interaction contributes $< 10^{-3}$ to the infidelity of the DDRF gate for the spins used in this work. We now consider two additional sources of infidelity in our numerical model: crosstalk between spins and nuclear spin dephasing. To model crosstalk, we consider a system composed of the NV electron spin, the target nuclear spin, and any additional nuclear spins within a 5 kHz spectral range of the target spin that were identified in Abobeih *et al.*[57]. If there are no spins within 5 kHz, we include only the nearest spin. To account for nuclear spin dephasing, we use Monte Carlo methods. At the start of each simulation, we randomly draw a detuning of the angular frequency from a Gaussian distribution with $\sigma = (\sqrt{2}/T_2^*)$ and shift the nuclear spin frequencies ω_L and ω_1 accordingly. All simulations are performed with 500 samples. The gate parameters, T_2^* values, and hyperfine couplings used to simulate each spin are the same as those measured experimentally (Tables 5.1, 5.2 and 5.3). We assume a magnetic field of 403.55 G, aligned along the NV axis. We calculate the Bell state fidelity from a simulated experiment following the sequence shown in Fig. 5.4(a). In the simulation, the electron is initialised in the state $|0\rangle$, while the nuclear spins are initially in a mixed state. We then apply the 'initialise' and 'entangle' blocks of the sequence shown in Fig. 5.4(a) to the target nuclear spin, where each two-qubit gate is simulated using the unitary operator as described in Eq. 5.25. We simulate the Bell state fidelities for both gate regimes on the nuclear spin C1, along with the gates used for spins C7, C8, and ^{14}N. For simplicity, the ^{14}N spin is treated analogously to the ^{13}C spins, with appropriately modified Larmor frequency and hyperfine interaction strength. Additionally, we assume perfect initialization for the ^{14}N spin. In the simulations, we allow for optimization of the Rabi frequency Ω and of the nuclear spin readout basis (the azimuthal angle) to maximise the fidelity, following the calibration procedure used in the experiments. In Table 5.4 we compare the simulated and measured values. For the spins C1 and ^{14}N, the simulated Bell state fidelities are quite high compared to the measured values, indicating that nuclear spin dephasing and crosstalk are not the dominant infidelity mechanisms in these cases. Conversely, for C7 and C8, the simulation predicts a large contribution from these two effects.

For the case shown in Fig. 5.4(b) (C1* in Table 5.4), we independently measure the loss of coherence of the electron spin during the DDRF gate by applying the same dy-

namical decoupling sequence without any RF pulses. We perform the experiment shown in the inset of Fig. 5.3(a) with $\varphi = 90$ deg, after which the electron spin should ideally end up in the state $|0\rangle$. We perform this experiment for two cases: one where the RF source is connected and one where it is disconnected. We interleave these two cases in blocks of 20000 repetitions (10 blocks in total) to ensure that any measured difference is not due to drifts in the experimental setup. For the case where the RF source is disconnected, we measure $P(0) = 0.999(2)$ and for the case where it is connected, we measure $P(0) = 0.992(2)$. This indicates that loss of coherence on the electron spin during the DDRF gate due to noise from the RF source is a significant source of infidelity in this case. Careful design of a low noise RF delivery system could therefore lead to significant improvements in the gate fidelities.

5.8.5. MULTI-QUBIT ENTANGLEMENT EXPERIMENTS

QUBIT INITIALIZATION

Spin	$\mathcal{F}_{\text{init}}$
e	0.998(2)
C1*	0.983(1)
C1	0.965(5)
C2	0.985(5)
C3	0.970(5)
C4	0.965(5)
C5	0.980(5)
C6	0.985(5)
C7	0.86(1)
C8	0.83(1)
^{14}N	0.997(11)

Table 5.5: **Measured initialization fidelities for the spin register.**

Initialization is performed at the start of all experiments. Initialization fidelities for all spins are given in Table 5.5. The electron spin can be prepared in the $m_s = 0$ spin projection with high fidelity (0.998(2)) by resonant optical excitation [14].

The ^{13}C nuclear spins are sequentially initialised by a partial swap sequence which maps the $|0\rangle$ state of the electron spin onto the target nuclear spin [37]. We assume symmetric state preparation and measurement errors (see below). The spread of values is due to the different two-qubit gate fidelity for each nuclear spin [16].

The ^{14}N spin is initialised by a measurement-based initialization (MBI) at the start of the sequence [14]. Unlike previous implementations of this scheme, where the electron spin was prepared in a mixture of the $m_s = \pm 1$ projections, we initialise into the $m_s = 0$ state, after which a microwave π-pulse prepares the electron in the $m_s = -1$ spin projection with high probability (>99%). In this way, we immediately double the success rate of the procedure. We also perform the MBI sequence twice, thereby suppressing ^{14}N initialization errors due to imperfect readout. Fig. 5.13 shows an example electron spin resonance experiment following nitrogen initialization in $m_I = -1$. The transition is split

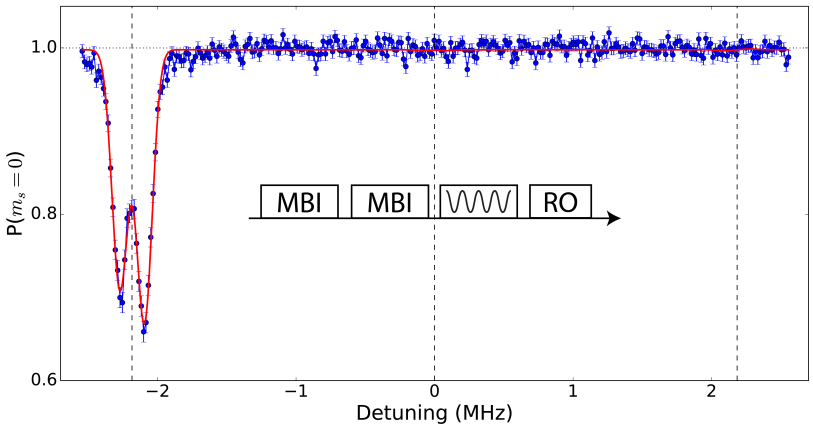

Figure 5.13: Electron spin resonance experiment from which the ^{14}N spin initialization may be inferred. We repeat a measurement based initialization sequence twice in order to suppress initialization errors from erroneous photon detection events. We then perform a highly selective microwave pulse (duration: 10µs), followed by optical readout of the NV electron spin. We sweep the frequency of the microwave pulse; the detuning shown is relative to the $m_s = 0 \leftrightarrow m_s = -1$ transition frequency (1.74667(1) GHz). We fit six Lorentzian lines, accounting for a stronger coupled ^{13}C nuclear spin (C1) along with the ^{14}N splitting.

into six lines due to hyperfine coupling to the ^{14}N (~ 2.18 MHz) and a ^{13}C spin (C1; ~ 213 kHz). We fit six Lorentzian lines to determine the relative height of the dips, which correspond to the populations in each of the nitrogen spin states. The fitted amplitudes reveal populations of $p_{-1} = 0.997(11)$, $p_0 = 0.003(6)$, and $p_{+1} = 0.000(6)$. We thus improve on the initialization fidelity for this nuclear spin by an order of magnitude relative to previous work (previously measured ~ 0.96 for this NV[59]). After initialization of the spin-1 ^{14}N, we work in a two-level subspace $m_I = \{-1, 0\}$, and perform the remainder of the operations analogously to the ^{13}C spins, including two-qubit gates using the DDRF scheme.

MEASUREMENT OF ELECTRON-NUCLEAR ENTANGLED STATES

To characterise electron-nuclear entangled states, we generalise the method described in Kalb *et al.*[42] to multiple spins and arbitrary electron states. We first measure the electron spin in a chosen basis, before measuring the relevant multi-qubit expectation values for the nuclear spins. The latter step is performed by multi-qubit measurements using the electron as an ancilla. In order to minimise dephasing on the nuclear spins during the first electron measurement, we only continue and perform the nuclear spin measurements in the case that we receive a photon detection event within the first 60µs (10µs for the experiment shown in Fig. 5.4, 5µs for the electron-nitrogen experiment in Fig. 5.6), and dynamically stop the measurement on receipt of the photon. This has multiple advantages. First, we simultaneously minimise unwanted spin-flips after heralding the electron state, and dephasing of the nuclear spins due to the optical cycling process. Second, we enhance the projectivity of our measurement. Compared to single-shot readout (average fidelity 0.945(2)), the electron spin state fidelity after a projective read-

out of maximum duration 60μs is found to be 0.992(1). If limited to 10μs, this fidelity rises to 0.996(1). The shorter duration was selected for the data in Fig. 5.4 in order to measure the performance of the DDRF two-qubit gate with minimal disturbance from additional effects such as measurement-induced dephasing, at a cost of a reduction in the experimental repetition rate. After 10μs, the probability of detecting a photon given that the electron was in the spin state $|0\rangle$ is 28(2)%, compared with 88(2)% after 60μs. For the electron-nitrogen experiment in Fig. 5.6, an even shorter duration is required as significant dephasing arises due to the large electron-nitrogen hyperfine coupling in the excited state. The corresponding detection probability after 5μs is 6%.

To appropriately measure the entanglement correlations for both the $M_i = +1$ and $M_i = -1$ electron spin measurement outcomes, we perform the sequence twice. Here M_i is the outcome of an electron measurement in the $i = \{X, Y, Z\}$ basis. In the first sequence (sequence A), we measure the electron after the appropriate basis rotation, while in the second sequence (sequence B), we perform an additional π-pulse prior to the electron readout (see Fig. 5.4(a)). The electron measurement probabilities $p(M_i = \pm 1)$ are then reconstructed from the probability of photon detection across each pair of measurements, using the relations

$$\begin{aligned} p(M_i = +1) &= \frac{p_i^A(n>0)}{p_i^A(n>0) + p_i^B(n>0)}, \\ p(M_i = -1) &= \frac{p_i^B(n>0)}{p_i^A(n>0) + p_i^B(n>0)}, \end{aligned} \tag{5.27}$$

where $p_i^A(n>0)$ is the probability to detect >0 photons during the measurement in sequence A (no π-pulse) and $p_i^B(n>0)$ is the probability to detect >0 photons during the measurement in sequence B (with π-pulse). We can then calculate the electron-nuclear expectation values as

$$\begin{aligned} \langle I_e \otimes O_n \rangle &= p(M_Z = +1)\langle O_n \rangle_{M_Z=+1} + p(M_Z = -1)\langle O_n \rangle_{M_Z=-1}, \\ \langle X_e \otimes O_n \rangle &= p(M_X = +1)\langle O_n \rangle_{M_X=+1} - p(M_X = -1)\langle O_n \rangle_{M_X=-1}, \\ \langle Y_e \otimes O_n \rangle &= p(M_Y = +1)\langle O_n \rangle_{M_Y=+1} - p(M_Y = -1)\langle O_n \rangle_{M_Y=-1}, \\ \langle Z_e \otimes O_n \rangle &= p(M_Z = +1)\langle O_n \rangle_{M_Z=+1} - p(M_Z = -1)\langle O_n \rangle_{M_Z=-1}, \end{aligned} \tag{5.28}$$

where O_n is the nuclear spin Pauli operator and $\langle O_n \rangle_{M_i=\pm 1}$ is the expectation value of O_n given that the electron measurement gave the outcome $+1$ (sequence A) or -1 (sequence B). While this measurement procedure minimises dephasing for the ^{13}C spins, the large excited state hyperfine coupling between the electron and the ^{14}N can lead to significant dephasing within a few optical cycles[62]. Consequently, for the multi-qubit experiments shown in Fig. 5.7, we protect the nitrogen spin state by performing a basis rotation that maps the desired measurement basis to the Z-basis prior to the electron measurement.

NUCLEAR SPIN READOUT CORRECTION

In order to provide best estimates for the state fidelities, we correct the results for infidelities in the readout sequence. We base the correction on methods developed in a previous work[16]. We first calculate a single qubit readout fidelity for each nuclear spin

based on a symmetric initialization and readout scheme. That is, we prepare a nuclear spin into the eigenstate $|\uparrow\rangle$, and measure in the Z-basis. Assuming the process is symmetric, for each nuclear spin we can write

$$\langle Z_j \rangle = C_{\mathrm{Qj}}^2, \tag{5.29}$$

where $\langle Z_j \rangle$ is the measured expectation value in the Z-basis for spin j, and C_{Qj} is the error associated with the initialization and readout processes. For the nitrogen spin, we use an independently measured value of 0.997(11) for the initialization fidelity (see Fig. 5.13), and can directly extract the correction factor through the relationship

$$\langle Z_{^{14}\mathrm{N}} \rangle = C_{^{14}\mathrm{N,init}} C_{^{14}\mathrm{N,RO}}. \tag{5.30}$$

To correct a multi-qubit readout, we now prepare the corresponding multi-qubit state, for example: $|\uparrow\uparrow\uparrow\rangle$. Measurement of the expectation value $\langle Z_1 Z_2 Z_3 \rangle$ allows one to calculate an appropriate readout correction, following the relation

$$\langle Z_1 Z_2 Z_3 \rangle = C_{\mathrm{Q1,init}} C_{\mathrm{Q2,init}} C_{\mathrm{Q3,init}} C_{\mathrm{Q1,Q2,Q3}}, \tag{5.31}$$

where $C_{\mathrm{Q1,Q2,Q3}}$ accounts for the error associated with the 3-qubit readout (for example, due to decoherence of the electron spin and crosstalk to other nuclear spins).

To calculate the factor $C_{\mathrm{Q1,Q2,Q3}}$, we require the initialization fidelities, $C_{\mathrm{Q1,init}}, C_{\mathrm{Q2,init}}, C_{\mathrm{Q3,init}}$, which may now differ from the values measured in the single qubit experiments (C_{Qj}) due to crosstalk during the multi-qubit initialization procedure. To characterise these values, we also measure the expectation values $\langle Z_1 I_2 I_3 \rangle$, $\langle I_1 Z_2 I_3 \rangle$ and $\langle I_1 I_2 Z_3 \rangle$. Taking the previously measured single qubit readout fidelities, and following the relations

$$\begin{aligned} \langle Z_1 I_2 I_3 \rangle &= C_{\mathrm{Q1,init}} C_{\mathrm{Q1}} \\ \langle I_1 Z_2 I_3 \rangle &= C_{\mathrm{Q2,init}} C_{\mathrm{Q2}} \\ \langle I_1 I_2 Z_3 \rangle &= C_{\mathrm{Q3,init}} C_{\mathrm{Q3}}, \end{aligned} \tag{5.32}$$

we retrieve the initialization fidelities, and thus arrive at a value for $C_{\mathrm{Q1,Q2,Q3}}$. Similar analysis enables characterization of multi-qubit readout for all combinations of spins used in the entanglement experiments.

SPIN ECHOES

In order to protect nuclear spin coherences across the multi-qubit entanglement and measurement sequences, composed of up to 14 two-qubit gates and 7 single-qubit gates on nuclear spins, we integrate RF spin echo pulses into the measurement sequence. These pulses are inserted in two positions; after the entanglement step, and after the basis rotations required for measurement of the appropriate multi-qubit Pauli operators. In this way, we extend typical nuclear spin coherence times of order 10 ms to 0.2 - 0.8 s (see Table 5.2). The exact sequencing of the echo pulses, along with the required single and two-qubit gates, is tailored to the specific measurement basis.

The timings for the echo pulses are calculated from the point of the final microwave pulse of the entanglement sequence. We identify the nuclear spins to be read out, the

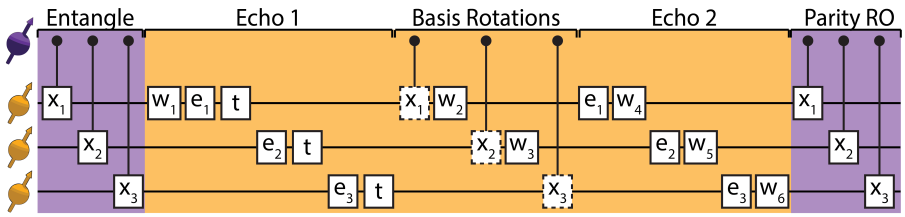

Figure 5.14: Example of a nuclear spin measurement sequence interspersed with spin echo pulses for the case of 3 nuclear spins. Purple (orange) boxes correspond to periods in which the electron spin state is in superposition (the $m_s = -1$ spin projection). Boxes x_1, x_2, x_3 correspond to gate operations on nuclear spins 1, 2, and 3 respectively, with their individual durations. Dashed boxes indicate that - in the case a basis rotation is not required on a given spin - idling is performed for an equal duration to the operation time. Similarly, boxes e_1, e_2, and e_3 correspond to spin echo pulses on those spins, also with unique lengths. Boxes $w_1 - w_6$ are unique wait durations which must be derived from a set of simultaneous equations (Eqs. 5.33 and 5.34). Electron pulses, repumping operations and optical readout are omitted for simplicity and can be considered part of the wait boxes. t is a spacing parameter for the first round of echoes, which can be increased in the case that a solution is not found for those equations due to the relative lengths of the gate and echo durations for each nuclear spin.

time since the last operation acting upon them, and their respective gate and echo durations. A specific challenge for our sequence is to time the refocussing points of the second round of echoes such that no additional waiting time is added during the readout. In this way, we minimise the duration for which the electron spin state is in superposition and thus sensitive to dephasing noise. Instead, the electron spin is in the $m_s = -1$ projection during idling times, and only suffers depolarization due to longitudinal relaxation (T_1 timescales >1 hour). We identify a general solution, for which an example for 3 nuclear spins is given in Fig. 5.14.

Considering Fig. 5.14, we wish to balance the times between successive operations on a given nuclear spin and the spin echo pulse which separates them. For example, to balance the delays such that the echo pulse e_1 refocusses the nuclear spin between the first and second x_1 operations, we must solve the equation (see Fig. 5.14 for timing definitions)

$$x_2 + x_3 + w_1 = 3t + e_2 + e_3 \tag{5.33}$$

For the remainder of the echoes, we must simultaneously solve the following relations alongside Eq. 5.33:

$$\begin{aligned} x_3 + w_1 + e_1 &= t + e_3 + x_1 + w_2 \\ w_1 + e_1 + e_2 + t &= x_1 + w_2 + x_2 + w_3 \\ w_2 + x_2 + w_3 + x_3 &= w_4 + e_2 + w_5 + e_3 + w_6 \\ w_3 + x_3 + e_1 + w_4 &= w_5 + e_3 + w_6 + x_1 \\ e_1 + w_4 + e_2 + w_5 &= w_6 + x_1 + x_2 \end{aligned} \tag{5.34}$$

The identification of a solution ensures that all nuclear spins are refocussed at the point of each operation acting upon them. The example given here is readily scaled for an

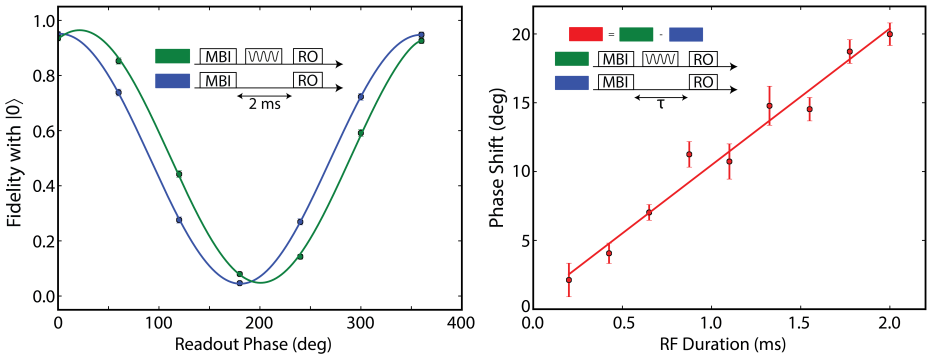

Figure 5.15: Characterization of the AC-Stark effect. Experiments are performed on the two ^{13}C spins C3 and C5, detuned by 5160(2) Hz. (a) Measurement of the phase shift induced on spin C3 by a 2 ms RF pulse applied on spin C5. We first initialise spin C3 in the X-basis. We then either apply the RF pulse (green) or allow the qubit to idle for the same duration (blue). Finally, we sweep the phase of the nuclear spin readout (in the $\hat{x}$-$\hat{y}$ plane). We fit both curves to the function $f(\phi) = 0.5 + A\cos(\phi + \phi_0)$, and extract the phase shift $\delta\phi_0$. (b) Plot of the fitted phase shifts $\delta\phi_0$, against the duration of the applied RF pulse, t_{pulse}. From a linear fit $f(t_{\text{pulse}}) = a + At_{\text{pulse}}$, we extract a value of 28(2) Hz for the AC-Stark shift, in agreement with the predicted value of 28(1) Hz.

increasing number of nuclear spins. In experiment, we calculate the specific delays for each measurement basis by translating this sequence structure into a matrix equation which is algorithmically generated and solved using the Sympy Python package[78]. The output of this algorithm is directly fed into the control software to program the experimental sequences.

Echo pulses are implemented by RF driving at the unique precession frequency of each nuclear spin (in the $m_s = -1$ electron spin state). An error-function envelope with a rise time of 7.5µs is used to mitigate ringing of the RF signal due to sharp switching (see Sec. 5.8.1). π-pulse durations for the echo pulses are given in Table 5.3. To estimate the fidelity of the echo pulses, we numerically simulate the effect of a 1 ms, square-envelope RF pulse with Rabi frequency $\Omega/2\pi = 500$ Hz following the numerical model described in Sec. 5.8.3. The RF pulse is set to be resonant with a test spin whose hyperfine interaction components are chosen to be $A_\parallel/2\pi = 50$ kHz and $A_\perp/2\pi = 20$ kHz and dephasing time $T_2^* = 10$ ms. Assuming perfect electron spin initialization in the $m_s = -1$ projection, and perfect nuclear spin initialization in each of the 6 cardinal states, we find the average fidelity with the ideal states to be 0.998.

We note that the measured Rabi frequencies associated with each spin are not equal, an effect which we attribute to frequency dependencies of the RF transmission, along with the non-secular interaction terms in the electron-nuclear hyperfine coupling Hamiltonian[50,57,58,77]. For nuclear spins which are initialised and read out using standard dynamical decoupling sequences, we calibrate the phase of the RF pulse to match the azimuthal angle of the hyperfine interaction for that spin[79–81].

We also account for the AC-Stark shift imposed on the other spins by the echo pulses. As an example, consider two nuclear spins A and B. We prepare spin A in the X-basis,

apply the echo pulse on spin B, and then measure the phase of spin A. We then repeat this sequence, but do not apply any RF power. The difference in the measured phases of spin A reveals the shift due to the AC-Stark effect. The AC-Stark shift is approximately given by

$$\Delta\omega_{-1} = \frac{1}{2}\frac{\Omega^2}{\omega - \omega_{-1}}, \tag{5.35}$$

where Ω is the Rabi frequency, ω is the RF frequency, and ω_{-1} is the $m_s = -1$ nuclear spin precession frequency. Fig. 5.15 shows a measurement of this frequency shift for spins C3 and C5, which have close spectral proximity (detuning of 5160(2) Hz). We measure a Rabi frequency of 538(12) Hz for spin C3. By sweeping the duration of the RF pulse on spin C5, we can extract a phase shift of 9.9(6) degrees/ms of applied RF, corresponding to a frequency shift of 28(2) Hz. A calculation using Eq. 5.35 for the known RF frequency and Rabi frequency predicts a value of 28(1) Hz, in agreement with the measurement. We perform a similar calibration for all spins in the register.

5

BELL STATE MEASUREMENTS

In Table 5.6, we present the numerical values for the Bell state matrix presented in Fig. 5.6. The data utilises a single set of gate parameters, rather than separately optimizing the parameters to avoid crosstalk between each pair of qubits.

	e	^{14}N	C1	C2	C3	C4	C5	C6	C7	C8
e	-	0.93(1)	0.93(1)	0.97(1)	0.94(1)	0.93(1)	0.97(1)	0.93(1)	0.85(1)	0.81(2)
^{14}N	0.93(1)	-	0.84(3)	0.91(2)	0.87(2)	0.83(2)	0.89(2)	0.81(3)	0.72(4)	0.63(3)
C1	0.93(1)	0.84(3)	-	0.83(2)	0.84(2)	0.80(2)	0.79(2)	0.83(2)	0.75(4)	0.82(5)
C2	0.97(1)	0.91(2)	0.83(2)	-	0.92(2)	0.84(2)	0.94(2)	0.92(2)	0.76(3)	0.73(3)
C3	0.94(1)	0.87(2)	0.84(2)	0.92(2)	-	0.95(3)	0.87(2)	0.79(2)	0.69(3)	0.86(7)
C4	0.93(1)	0.83(2)	0.80(2)	0.84(2)	0.95(3)	-	0.84(2)	0.89(2)	0.77(4)	0.68(4)
C5	0.97(1)	0.89(2)	0.79(2)	0.94(2)	0.87(2)	0.84(2)	-	0.79(2)	0.75(3)	0.74(6)
C6	0.93(1)	0.81(3)	0.83(2)	0.92(2)	0.79(2)	0.89(2)	0.79(2)	-	0.69(3)	0.74(5)
C7	0.85(2)	0.72(4)	0.75(4)	0.76(3)	0.69(3)	0.77(4)	0.75(3)	0.69(3)	-	0.65(6)
C8	0.81(2)	0.63(3)	0.82(5)	0.73(3)	0.86(7)	0.68(4)	0.74(6)	0.74(5)	0.65(6)	-

Table 5.6: **Bell state fidelities for all pairs of spins.** Data as presented in Fig. 5.6. The target state is $(|0+\rangle + |1-\rangle)/\sqrt{2}$ for electron-nuclear Bell states, and $(|++\rangle+|--\rangle)/\sqrt{2}$ for the nuclear-nuclear Bell states. The fidelities are calculated from the expectation values of the Pauli operators with non-zero expectation values for those states, extracted from measurements. That is, $\mathcal{F} = (1 + \langle XZ\rangle + \langle YY\rangle + \langle ZX\rangle)/4$ for the electron-nuclear Bell states, and $\mathcal{F} = (1 + \langle XX\rangle - \langle YY\rangle + \langle ZZ\rangle)/4$ for nuclear-nuclear Bell states. Statistical errors (one standard deviation) are given in parentheses.

THEORETICAL PREDICTIONS FOR MULTI-QUBIT STATE FIDELITIES

We use a simple depolarizing noise model to estimate the gate fidelities and predict the scaling of the GHZ state fidelity $\mathcal{F}_{\text{GHZ}} = \langle \text{GHZ}_N | \rho | \text{GHZ}_N \rangle$ with the number of qubits added, where $|\text{GHZ}_N\rangle = (|0\rangle \otimes |+\rangle^{\otimes(N-1)} + |1\rangle \otimes |-\rangle^{\otimes(N-1)})/\sqrt{2}$ is the state ideally created by the application of the entanglement sequence (Fig. 5.7(a)) to the initial state $|0\rangle \otimes |\uparrow\rangle^{\otimes(N-1)}$. We use two measured quantities: the initialization fidelity $\mathcal{F}_{\text{init},j} = \langle \uparrow_j | \rho_{\text{init},j} | \uparrow_j \rangle = (1 + C_{Qj,\text{init}})/2$ of each nuclear spin j (Table 5.5), and the Bell state fidelity $\mathcal{F}_{\text{Bell},j}$ after an entangling sequence between the electron and nuclear spin

j (Table 5.7). For the entanglement sequence, we assume perfect single-qubit rotations on the electron spin, while each two-qubit gate is modelled by a noisy operation[82]

$$\mathscr{E}_j(\rho) = (1-p_j)U_j\rho U_j^\dagger + \frac{p_j}{16}\sum_{\alpha,\beta}\alpha_e\beta_j\rho\alpha_e\beta_j, \tag{5.36}$$

where $\alpha,\beta \in \{I,X,Y,Z\}$ are single qubit Pauli operators, p_j is the error probability and U_j is the ideal unitary operation given by

$$U_j = |0\rangle\langle 0|_e \otimes R_y(\pi/2)_j + |1\rangle\langle 1|_e \otimes R_y(-\pi/2)_j. \tag{5.37}$$

Applying the two-qubit entanglement sequence (Fig. 5.4(a)) using Eq. 5.36 for the two-qubit gate, we can find an analytical solution for the error probability in terms of the measured initialization and Bell state fidelities, given by

$$p_j = 1 - \frac{1-4\mathscr{F}_{\text{Bell},j}}{1-4\mathscr{F}_{\text{init},e}\mathscr{F}_{\text{init},j}}. \tag{5.38}$$

The two-qubit gate fidelity can then be estimated from the error probability using the relation[82]

$$\begin{aligned}\mathscr{F}_{\text{gate},j} &= \min_{|\psi_j\rangle}\left[\langle\psi_j|U_j^\dagger\mathscr{E}_j(|\psi_j\rangle\langle\psi_j|)U_j|\psi_j\rangle\right] \\ &= 1-\frac{3p_j}{4},\end{aligned} \tag{5.39}$$

where the minimization is over all possible pure electron-nuclear two-qubit states $|\psi_j\rangle$. Calculated values of $\mathscr{F}_{\text{gate},j}$ are shown in Table 5.7. We can then use $\mathscr{F}_{\text{init},j}$ and p_j to predict F_{GHZ} for a larger number of qubits by applying the multi-qubit entanglement sequence shown in Fig. 5.7(a) to the initial state

$$\begin{aligned}\rho_{\text{init}} = &\left(\mathscr{F}_{\text{init},e}|0\rangle\langle 0|_e + (1-\mathscr{F}_{\text{init},e})|1\rangle\langle 1|_e\right) \\ &\bigotimes_{j=1}^{N-1}\left(\mathscr{F}_{\text{init},j}|\uparrow\rangle\langle\uparrow|_j + (1-\mathscr{F}_{\text{init},j})|\downarrow\rangle\langle\downarrow|_j\right).\end{aligned} \tag{5.40}$$

The resulting values are shown in Table 5.8 and Fig. 5.7(d). Note that this model does not capture the effects of correlated noise and crosstalk between spins, which provides a possible explanation for the deviation of the measured fidelities from the theoretically predicted values as the number of qubits is increased.

ADDITIONAL DATA FOR THE N-QUBIT GHZ STATE EXPERIMENTS

Figs. 5.7(b,c) show two example bar plots of the non-zero expectation values for 5 and 7 qubit GHZ states. Fig. 5.16 shows the bar plots for 2-8 qubit GHZ states, from which the fidelities shown in Table 5.8 and plotted in Fig. 5.7(d) are calculated. Fig. 5.17 shows the bar plots of the non-zero expectation values after initializing 1-7 nuclear spin qubits, which are used for correct to readout errors as described above.

Spin	$\mathcal{F}_{\text{Bell}}$ (measured)	$\mathcal{F}_{\text{gate}}$ (extracted)
C1*	0.972(8)	0.991(9)
C1	0.93(1)	0.97(1)
C2	0.97(1)	0.99(1)
C3	0.94(1)	0.97(1)
C4	0.93(1)	0.97(1)
C5	0.97(1)	0.99(1)
C6	0.93(1)	0.95(1)
C7	0.85(2)	0.99(3)*
C8	0.81(2)	0.98(3)*
^{14}N	0.93(1)	0.94(1)†

Table 5.7: **Measured Bell state fidelities between the electron and each nuclear spin, as well as the extracted two-qubit electron-nuclear gate fidelities.** The extracted two-qubit gate fidelities are calculated with Eq. 5.39, using initialization fidelities taken from Table 5.5. *The measured initialization and Bell state fidelities are similar for these spins, suggesting significant effects that are not taken into account in this model. †The optical projective measurement on the electron spin is expected to have a greater effect on the nitrogen spin due to the strong hyperfine coupling when the electron is in the excited state. This is not taken into account in the model, and therefore the gate fidelity is expected to be higher than calculated here.

Number of qubits	Spin added	$\mathcal{F}_{\text{init}}$ [predicted]	$\mathcal{F}_{\text{init}}$ [measured]	$\mathcal{F}_{\text{GHZ}}$ [predicted]	$\mathcal{F}_{\text{GHZ}}$ [measured]	$\mathcal{W}_{\text{GHZ}}$ violation (σ)
2	C5	0.978	0.970(11)	0.972	0.966(9)	51
3	C2	0.963	0.968(10)	0.947	0.949(9)	49
4	C6	0.949	0.917(8)	0.889	0.827(7)	46
5	^{14}N	0.946	0.905(7)	0.836	0.813(6)	52
6	C1	0.913	0.885(8)	0.782	0.695(7)	27
7	C3	0.886	0.862(6)	0.740	0.615(5)	23
8	C4	0.855	0.682(6)	0.692	0.365(5)	-

Table 5.8: **Predicted and measured initialization and GHZ state fidelities for different numbers of qubits.** Predicted fidelities for the initial states are calculated as the fidelity of ρ_{init} (Eq. 5.40) with the ideal initial state $|0\rangle \otimes |\uparrow\rangle^{\otimes(N-1)}$, while the measured values are calculated from measurements of the non-zero expectation values for this state (see Fig. 5.17). Predicted fidelities for the GHZ states are calculated by applying the entanglement sequence shown in Fig. 5.7(a) to the initial state ρ_{init}, where each two-qubit gate is modelled as the noisy operation given in Eq. 5.36. Also tabulated are the experimental violations (in statistical standard deviations) of the witness $\mathcal{W}_{\text{GHZ}} = \mathbb{1} - 2|\text{GHZ}_N\rangle\langle\text{GHZ}_N|$.

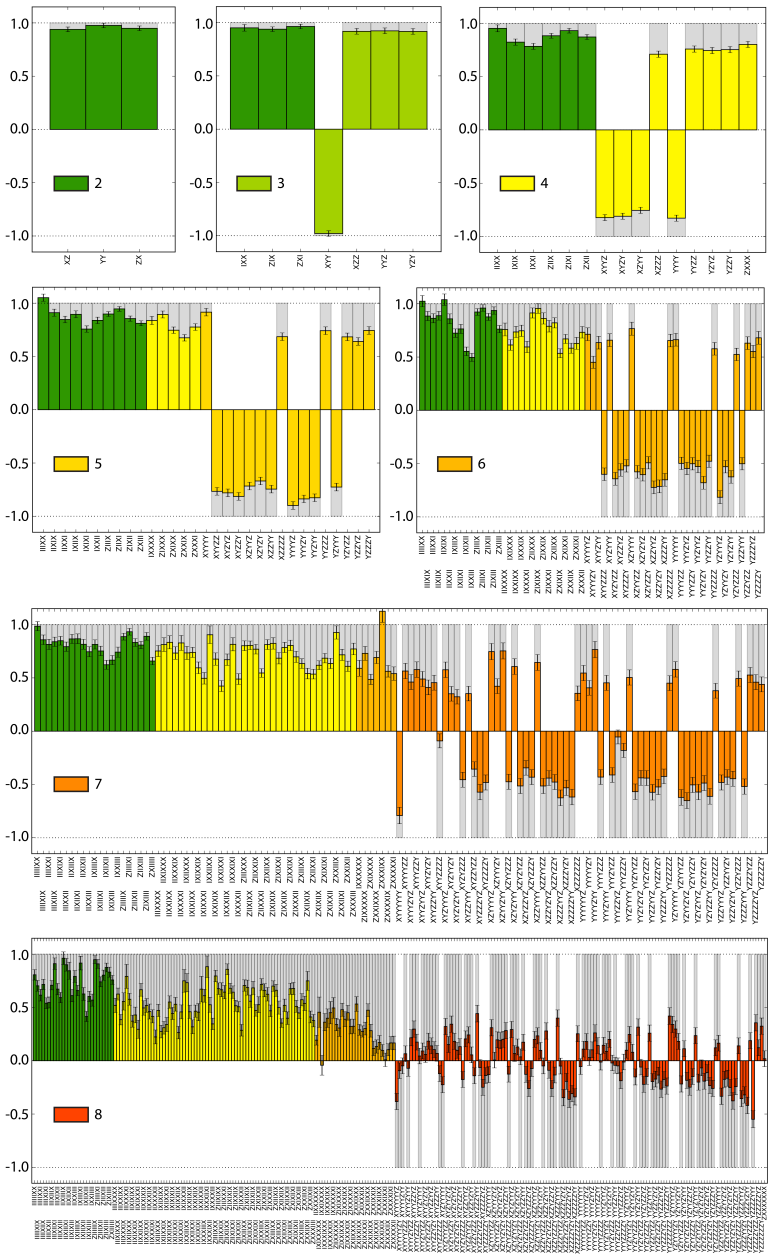

Figure 5.16: Bar plots showing the non-zero expectation values for 2-8 qubit GHZ states, used to calculate the GHZ state fidelity plotted in Fig. 5.7(d). The colors indicate the number of qubits involved, i.e. the number of (non-identity) operators in the expectation value (inset). Gray bars show the ideal expectation values.

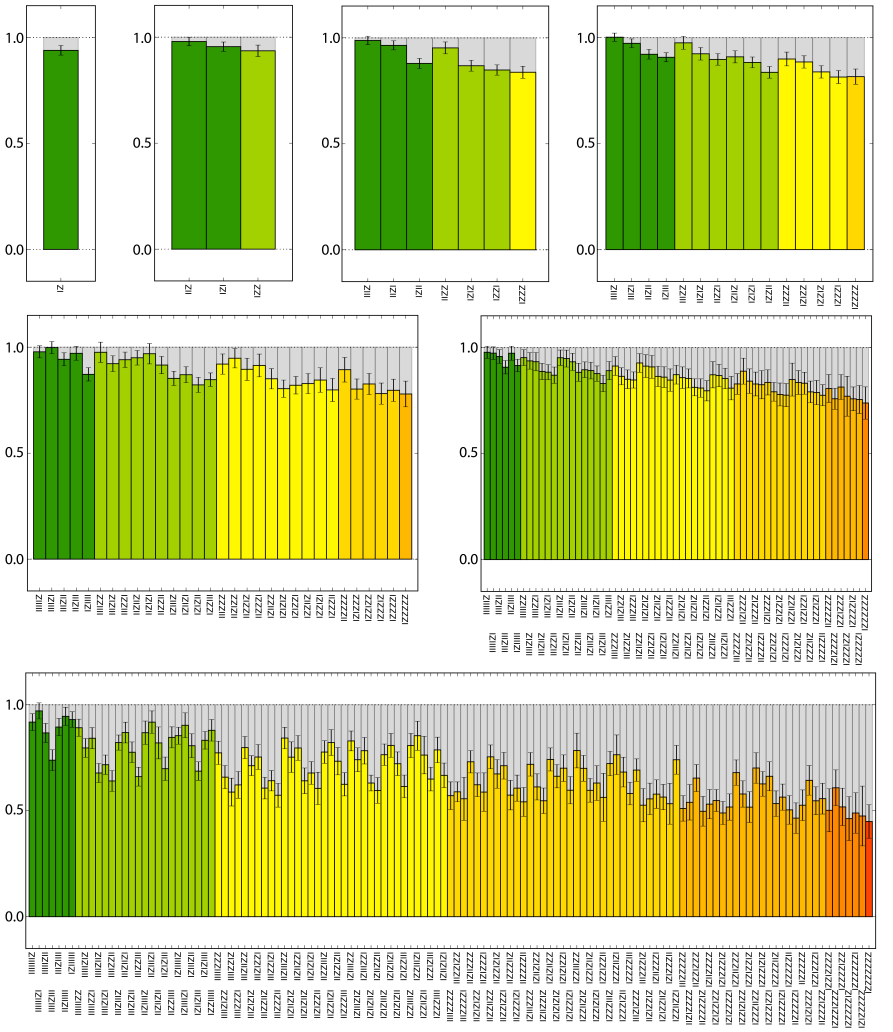

Figure 5.17: Bar plots showing the non-zero expectation values for 1-7 nuclear spin qubits after initializing in the state $|0\rangle \otimes |\uparrow\rangle^{\otimes(N-1)}$. These measurements are used to correct for readout errors (see Sec. 5.8.5). The colors indicate the number of qubits involved, i.e. the number of (non-identity) operators in the expectation value, shown in the insets of Fig. 5.16. Gray bars show the ideal expectation values.

REFERENCES

[1] D. D. Awschalom, R. Hanson, J. Wrachtrup and B. B. Zhou, *Quantum technologies with optically interfaced solid-state spins,* Nat. Photonics **12**, 516 (2018).

[2] F. A. Zwanenburg *et al.*, *Silicon quantum electronics,* Rev. Mod. Phys. **85**, 961 (2013).

[3] G. De Lange, Z. Wang, D. Riste, V. Dobrovitski and R. Hanson, *Universal dynamical decoupling of a single solid-state spin from a spin bath,* Science **330**, 60 (2010).

[4] G. Fuchs, V. Dobrovitski, D. Toyli, F. Heremans and D. Awschalom, *Gigahertz dynamics of a strongly driven single quantum spin,* Science **326**, 1520 (2009).

[5] D. J. Christle *et al.*, *Isolated electron spins in silicon carbide with millisecond coherence times,* Nat. Mater. **14**, 160 (2015).

[6] H. Seo *et al.*, *Quantum decoherence dynamics of divacancy spins in silicon carbide,* Nat. Commun. **7**, 12935 (2016).

[7] D. D. Sukachev *et al.*, *Silicon-vacancy spin qubit in diamond: a quantum memory exceeding 10 ms with single-shot state readout,* Phys. Rev. Lett. **119**, 223602 (2017).

[8] T. Iwasaki *et al.*, *Germanium-vacancy single color centers in diamond,* Sci. Rep. **5**, 12882 (2015).

[9] P. Siyushev *et al.*, *Optical and microwave control of germanium-vacancy center spins in diamond,* Phys. Rev. B **96**, 081201 (2017).

[10] J. N. Becker *et al.*, *All-optical control of the silicon-vacancy spin in diamond at millikelvin temperatures,* Phys. Rev. Lett. **120**, 053603 (2018).

[11] B. Pingault *et al.*, *Coherent control of the silicon-vacancy spin in diamond,* Nat. Commun. **8**, 15579 (2017).

[12] M. E. Trusheim *et al.*, *Transform-limited photons from a coherent tin-vacancy spin in diamond,* Phys. Rev. Lett **124**, 023602 (2020).

[13] A. E. Rugar, C. Dory, S. Sun and J. Vučković, *Characterization of optical and spin properties of single tin-vacancy centers in diamond nanopillars,* Phys. Rev. B **99**, 205417 (2019).

[14] L. Robledo *et al.*, *High-fidelity projective read-out of a solid-state spin quantum register,* Nature **477**, 574 (2011).

[15] J. J. Pla *et al.*, *High-fidelity readout and control of a nuclear spin qubit in silicon,* Nature **496**, 334 (2013).

[16] J. Cramer *et al.*, *Repeated quantum error correction on a continuously encoded qubit by real-time feedback,* Nat. Commun. **7**, 1 (2016).

[17] G. Waldherr *et al.*, *Quantum error correction in a solid-state hybrid spin register,* Nature **506**, 204 (2014).

[18] G. Wolfowicz *et al., 29si nuclear spins as a resource for donor spin qubits in silicon,* New J. Phys. **18**, 023021 (2016).

[19] G. Tosi *et al., Silicon quantum processor with robust long-distance qubit couplings,* Nat. Commun. **8**, 450 (2017).

[20] M. H. Metsch *et al., Initialization and readout of nuclear spins via a negatively charged silicon-vacancy center in diamond,* Phys. Rev. Lett. **122**, 190503 (2019).

[21] B. Hensen *et al., A silicon quantum-dot-coupled nuclear spin qubit,* Nat. Nanotechnol. **15**, 13 (2020).

[22] F. Dolde *et al., Room-temperature entanglement between single defect spins in diamond,* Nat. Phys. **9**, 139 (2013).

[23] T. Yamamoto *et al., Strongly coupled diamond spin qubits by molecular nitrogen implantation,* Phys. Rev. B **88**, 201201 (2013).

[24] S. Yang *et al., High-fidelity transfer and storage of photon states in a single nuclear spin,* Nat. Photonics **10**, 507 (2016).

[25] E. Togan *et al., Quantum entanglement between an optical photon and a solid-state spin qubit,* Nature **466**, 730 (2010).

[26] D. J. Christle *et al., Isolated spin qubits in sic with a high-fidelity infrared spin-to-photon interface,* Phys. Rev. X **7**, 021046 (2017).

[27] A. Sipahigil *et al., An integrated diamond nanophotonics platform for quantum-optical networks,* Science **354**, 847 (2016).

[28] R. E. Evans *et al., Photon-mediated interactions between quantum emitters in a diamond nanocavity,* Science **362**, 662 (2018).

[29] H. Bernien *et al., Heralded entanglement between solid-state qubits separated by three metres,* Nature **497**, 86 (2013).

[30] B. Hensen *et al., Loophole-free bell inequality violation using electron spins separated by 1.3 kilometres,* Nature **526**, 682 (2015).

[31] P. C. Humphreys *et al., Deterministic delivery of remote entanglement on a quantum network,* Nature **558**, 268 (2018).

[32] P. C. Maurer *et al., Room-Temperature Quantum Bit Memory Exceeding One Second,* Science **336**, 1283 (2012).

[33] J. T. Muhonen *et al., Storing quantum information for 30 seconds in a nanoelectronic device,* Nat. Nanotechnol. **9**, 986 (2014).

[34] J. P. Dehollain *et al., Bell's inequality violation with spins in silicon,* Nat. Nanotechnol. **11**, 242 (2016).

[35] S. Freer *et al., A single-atom quantum memory in silicon,* Quantum Sci. Technol. **2**, 015009 (2017).

[36] T. Van der Sar *et al., Decoherence-protected quantum gates for a hybrid solid-state spin register,* Nature **484**, 82 (2012).

[37] T. H. Taminiau, J. Cramer, T. van der Sar, V. V. Dobrovitski and R. Hanson, *Universal control and error correction in multi-qubit spin registers in diamond,* Nat. Nanotechnol. **9**, 171 (2014).

[38] X. Rong *et al., Experimental fault-tolerant universal quantum gates with solid-state spins under ambient conditions,* Nat. Commun. **6**, 8748 (2015).

[39] S. Zaiser *et al., Enhancing quantum sensing sensitivity by a quantum memory,* Nat. Commun. **7**, 12279 (2016).

[40] T. K. Unden, D. Louzon, M. Zwolak, W. H. Zurek and F. Jelezko, *Revealing the emergence of classicality using nitrogen-vacancy centers,* Phys. Rev. Lett. **123**, 140402 (2019).

[41] Y.-Y. Huang *et al., Experimental realization of robust geometric quantum gates with solid-state spins,* Phys. Rev. Lett. **122**, 010503 (2019).

[42] N. Kalb *et al., Entanglement distillation between solid-state quantum network nodes,* Science **356**, 928 (2017).

[43] S. B. van Dam, J. Cramer, T. H. Taminiau and R. Hanson, *Multipartite entanglement generation and contextuality tests using nondestructive three-qubit parity measurements,* Phys. Rev. Lett. **123**, 050401 (2019).

[44] B. M. Terhal, *Quantum error correction for quantum memories,* Rev. Mod. Phys. **87**, 307 (2015).

[45] N. H. Nickerson, Y. Li and S. C. Benjamin, *Topological quantum computing with a very noisy network and local error rates approaching one percent,* Nat. Commun. **4**, 1756 (2013).

[46] N. H. Nickerson, J. F. Fitzsimons and S. C. Benjamin, *Freely scalable quantum technologies using cells of 5-to-50 qubits with very lossy and noisy photonic links,* Phys. Rev. X **4**, 041041 (2014).

[47] M. H. Abobeih *et al., One-second coherence for a single electron spin coupled to a multi-qubit nuclear-spin environment,* Nat. Commun. **9**, 1 (2018).

[48] S. Kolkowitz, Q. P. Unterreithmeier, S. D. Bennett and M. D. Lukin, *Sensing distant nuclear spins with a single electron spin,* Phys. Rev. Lett. **109**, 137601 (2012).

[49] T. Taminiau *et al., Detection and control of individual nuclear spins using a weakly coupled electron spin,* Phys. Rev. Lett. **109**, 137602 (2012).

[50] N. Zhao *et al., Sensing single remote nuclear spins,* Nat. Nanotechnol. **7**, 657 (2012).

[51] Z.-Y. Wang, J. Casanova and M. B. Plenio, *Delayed entanglement echo for individual control of a large number of nuclear spins,* Nat. Commun. **8**, 14660 (2017).

[52] M. Pfender *et al.*, *Nonvolatile nuclear spin memory enables sensor-unlimited nanoscale spectroscopy of small spin clusters,* Nat. Commun. **8**, 834 (2017).

[53] T. Müller *et al.*, *Optical signatures of silicon-vacancy spins in diamond,* Nat. Commun. **5**, 3328 (2014).

[54] G. Thiering and A. Gali, *Ab initio magneto-optical spectrum of group-iv vacancy color centers in diamond,* Phys. Rev. X **8**, 021063 (2018).

[55] L. M. Vandersypen and I. L. Chuang, *Nmr techniques for quantum control and computation,* Rev. Mod. Phys. **76**, 1037 (2005).

[56] F. Dolde *et al.*, *High-fidelity spin entanglement using optimal control,* Nat. Commun. **5**, 3371 (2014).

[57] M. Abobeih *et al.*, *Atomic-scale imaging of a 27-nuclear-spin cluster using a quantum sensor,* Nature **576**, 411 (2019).

[58] L. Childress *et al.*, *Coherent dynamics of coupled electron and nuclear spin qubits in diamond,* Science **314**, 281 (2006).

[59] N. Kalb *et al.*, *Experimental creation of quantum zeno subspaces by repeated multi-spin projections in diamond,* Nat. Commun. **7**, 13111 (2016).

[60] O. Gühne and G. Tóth, *Entanglement detection,* Phys. Rep. **474**, 1 (2009).

[61] W. Pfaff *et al.*, *Demonstration of entanglement-by-measurement of solid-state qubits,* Nat. Phys. **9**, 29 (2013).

[62] M. Blok *et al.*, *Manipulating a qubit through the backaction of sequential partial measurements and real-time feedback,* Nat. Phys. **10**, 189 (2014).

[63] N. Kalb, P. C. Humphreys, J. Slim and R. Hanson, *Dephasing mechanisms of diamond-based nuclear-spin memories for quantum networks,* Phys. Rev. A **97**, 062330 (2018).

[64] G. Khutsishvili, *Spin diffusion and magnetic relaxation of nuclei,* Sov. Phys. JETP **15**, 909 (1962).

[65] R. Guichard, S. Balian, G. Wolfowicz, P. Mortemousque and T. Monteiro, *Decoherence of nuclear spins in the frozen core of an electron spin,* Phys. Rev. B **91**, 214303 (2015).

[66] D. Kwiatkowski and Ł. Cywiński, *Decoherence of two entangled spin qubits coupled to an interacting sparse nuclear spin bath: Application to nitrogen vacancy centers,* Phys. Rev. B **98**, 155202 (2018).

[67] D. A. Lidar, I. L. Chuang and K. B. Whaley, *Decoherence-free subspaces for quantum computation,* Phys. Rev. Lett. **81**, 2594 (1998).

[68] A. Reiserer *et al.*, *Robust quantum-network memory using decoherence-protected subspaces of nuclear spins,* Phys. Rev. X **6**, 021040 (2016).

[69] T. Monz *et al.*, *14-qubit entanglement: Creation and coherence,* Phys. Rev. Lett. **106**, 130506 (2011).

[70] D. Layden, M. Chen and P. Cappellaro, *Efficient quantum error correction of dephasing induced by a common fluctuator,* Phys. Rev. Lett. **124**, 020504 (2020).

[71] J. Hadden *et al.*, *Strongly enhanced photon collection from diamond defect centers under microfabricated integrated solid immersion lenses,* Appl. Phys. Lett. **97**, 241901 (2010).

[72] T. Yeung, D. Le Sage, L. M. Pham, P. Stanwix and R. L. Walsworth, *Anti-reflection coating for nitrogen-vacancy optical measurements in diamond,* Appl. Phys. Lett. **100**, 251111 (2012).

[73] W. S. Warren, *Effects of arbitrary laser or nmr pulse shapes on population inversion and coherence,* J. Chem. Phys. **81**, 5437 (1984).

[74] T. Gullion, D. B. Baker and M. S. Conradi, *New, compensated carr-purcell sequences,* J. Magn. Reson. **89**, 479 (1990).

[75] J. R. Johansson, P. D. Nation and F. Nori, *Qutip 2: A python framework for the dynamics of open quantum systems,* Comput. Phys. Commun. **184**, 1234 (2013).

[76] N. Zhao, J.-L. Hu, S.-W. Ho, J. T. Wan and R. Liu, *Atomic-scale magnetometry of distant nuclear spin clusters via nitrogen-vacancy spin in diamond,* Nat. Nanotechnol. **6**, 242 (2011).

[77] S. Sangtawesin *et al.*, *Hyperfine-enhanced gyromagnetic ratio of a nuclear spin in diamond,* New J. Phys. **18**, 083016 (2016).

[78] A. Meurer *et al.*, *Sympy: symbolic computing in python,* PeerJ Comput. Sci. **3**, e103 (2017).

[79] J. Zopes, K. Herb, K. Cujia and C. Degen, *Three-dimensional nuclear spin positioning using coherent radio-frequency control,* Phys. Rev. Lett. **121**, 170801 (2018).

[80] K. Sasaki, K. M. Itoh and E. Abe, *Determination of the position of a single nuclear spin from free nuclear precessions detected by a solid-state quantum sensor,* Phys. Rev. B **98**, 121405 (2018).

[81] A. Laraoui, D. Pagliero and C. A. Meriles, *Imaging nuclear spins weakly coupled to a probe paramagnetic center,* Phys. Rev. B **91**, 205410 (2015).

[82] M. A. Nielsen and I. Chuang, *Quantum computation and quantum information,* (2002).

6

ATOMIC-SCALE MAGNETIC RESONANCE IMAGING USING A QUANTUM SENSOR

M. H. Abobeih, J. Randall, C. E. Bradley, H. P. Bartling, M. A. Bakker, M. J. Degen, M. Markham, D. J. Twitchen, T. H. Taminiau

Nuclear magnetic resonance (NMR) is a powerful method for determining the structure of molecules and proteins[2]. Whereas conventional NMR requires averaging over large ensembles, recent progress with single-spin quantum sensors[3–10] has created the prospect of magnetic imaging of individual molecules[11–14]. As an initial step towards this goal, isolated nuclear spins and spin pairs have been mapped[15–22]. However, large clusters of interacting spins—such as those found in molecules—result in highly complex spectra. Imaging these complex systems is an outstanding challenge because it requires high spectral resolution and efficient spatial reconstruction with sub-angstrom precision. Here we realise such atomic-scale imaging using a single nitrogen-vacancy (NV) centre as a quantum sensor, and demonstrate it on a model system of 27 coupled ^{13}C nuclear spins in a diamond. We present a multidimensional spectroscopy method that isolates individual nuclear-nuclear spin interactions with high spectral resolution (< 80 mHz) and high accuracy (2 mHz). We show that these interactions encode the composition and interconnectivity of the cluster, and develop methods to extract the 3D structure of the cluster with sub-angstrom resolution. Our results demonstrate a key capability towards magnetic imaging of individual molecules and other complex spin systems[10–14].

The results of this chapter have been published in Nature **576**, 7787 (2019).
For length considerations of the thesis, the supplementary materials are not included here, but can be found online [1].

6.1. INTRODUCTION

The nitrogen-vacancy (NV) centre in diamond has emerged as a powerful quantum sensor[3–14,23,24]. The NV electron spin provides long coherence times[6,7,21] and high-contrast optical readout[6,25,26], enabling high sensitivity over a large range of temperatures[6,7,21,26,27]. Pioneering experiments with near-surface NV centres have demonstrated spectroscopy of small ensembles of nuclear spins in nano-scale volumes[3,4,6–9], and electron-spin labelled proteins[5]. Furthermore, single nuclear spin sensitivity has been demonstrated and isolated individual nuclear spins and spin pairs have been mapped[15–22]. Together, these results have established the NV centre as a promising platform for magnetic imaging of complex spin systems and single molecules[11–14].

In this work, we realise a key ability towards that goal: the 3D imaging of large nuclear-spin structures with atomic resolution. The main idea of our method is to obtain structural information by accessing the couplings between individual nuclear spins. Three key elements are: (1) realising high spectral resolution so that small couplings can be accessed, (2) isolating such couplings from complex spectra, and (3) transforming the revealed connectivity into the 3D spatial structure with sub-angstrom precision.

The basic elements of our experiment are illustrated in Fig. 6.1a. We consider a cluster of ^{13}C nuclear spins in the vicinity of a single NV centre in diamond at 4 Kelvin. This cluster provides a model system for the magnetic imaging of single molecules and spin structures external to the diamond. Each ^{13}C spin precesses at a shifted frequency due to the hyperfine interaction with the electron spin, resembling a chemical shift in traditional NMR[2,28]. These shifts enable different nuclear spins in the cluster to be distinguished.

6.2. MULTIDIMENSIONAL SPECTROSCOPY

We use the NV electron spin as a sensor to probe the nuclear-nuclear interactions (Fig. 6.1b). Inspired by NMR spectroscopy[2,28], we develop sequences that employ spin-echo double-resonance (SEDOR) techniques to isolate and measure individual couplings with high spectral resolution. First, we polarise a nuclear “probe" spin (frequency $RF1$) using recently developed quantum sensing sequences that can detect spins in any direction from the NV, enabling access to a large number of spins (see Sec. 6.7.3)[29]. Second, we let this probe spin evolve for a time t and apply N echo pulses that decouple it from the other spins and environmental noise. Simultaneously, pulses on a “target" spin in the cluster (frequency $RF2$) re-couple it to the probe spin, selecting the interaction between these two spins. Finally, a second sensing sequence detects the resulting polarisation of the probe spin through a high-contrast readout of the electron spin (see Sec. 6.7.5), which enables fast data collection. This double-resonance sequence provides a high spectral resolution through a long nuclear phase accumulation time. Importantly, the resolution is not limited by the relatively short coherence time of the electron spin sensor (see Sec. 6.7.5)[25,30].

It is instructive to first consider the case without echo pulses ($N = 0$). In such a Ramsey-type measurement[25–27,30,31], all couplings act simultaneously. This results in complex spectra that indicate the presence of multiple spins and many nuclear-nuclear

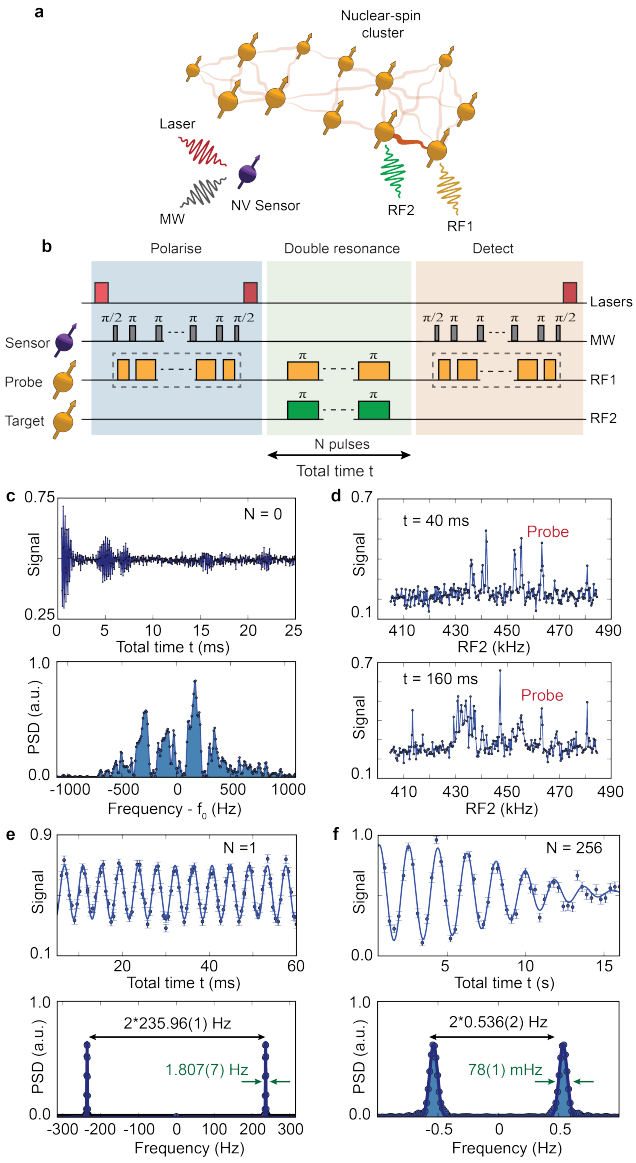

Figure 6.1: **Basic concepts of the experiment. a,** We consider an individual cluster of ^{13}C nuclear spins near a single NV centre in diamond. To obtain the 3D structure of the cluster we use the NV electron spin as a quantum sensor to measure nuclear-nuclear spin couplings. **b,** Experimental sequence. The NV sensor is used to polarise and detect the "probe" spin(s) at frequency $RF1$ (see Sec. 6.7.3). A double-resonance sequence of N echo pulses is applied simultaneously on the probe spin(s) ($RF1$) and the "target" spin(s) ($RF2$), so that the coupling between these spins is selectively detected. See Fig. 6.5 for the detailed sequence. **c,** A Ramsey signal ($N = 0$) for a nuclear spin in the cluster (detuning $f_0 = 5$ kHz relative to $RF1 = 455.37$ kHz). Because all couplings are probed simultaneously, the power spectral density (PSD) yields a complex non-resolvable spectrum. See Fig. 6.6 for more examples. **d,** Double-resonance spectroscopy ($N = 1$). Sweeping the target frequency ($RF2$) reveals all spins that couple to the probe spin(s). For larger t, more peaks appear as weaker couplings become visible. $RF1 = 463.27$ kHz. **e,** Sweeping the evolution time t for a fixed $RF1$ and $RF2$ reveals the coupling strength between spins. This example reveals a 235.96(1) Hz coupling between two spins with a spectral resolution of 1.807(7) Hz FWHM. $RF1 = 463.27$ kHz and $RF2 = 455.37$ kHz. **f,** An example with $N = 256$ echo pulses showing an extended coherence time to 10.9(5) seconds, which enables selective measurements of sub-Hz couplings with high spectral resolution (78(1) mHz) and precision (2 mHz). $RF1 = 408.32$ kHz and $RF2 = 413.48$ kHz. All graphs: see Sec. 6.7.6 for fit functions. Error bars are one standard deviation, a.u. indicates arbitrary units.

spin interactions in the cluster (Fig. 6.1c). However, this 1D measurement gives no direct information on the connectivity between spins. Additionally, the underlying structure of individual spins and couplings is obscured by the many frequencies (2^j for coupling to j spins) and the low spectral resolution of >30 Hz FWHM (set by the dipolar-broadened linewidth of the nuclear spins and inversely proportional to the dephasing time T_2^*).

In contrast, our double-resonance sequence enables couplings between specific spins to be isolated and measured with high resolution. We first scan the target frequency $RF2$ for a fixed probe frequency $RF1$ (Fig. 6.1d). This reveals the spectral positions of nuclear spins coupled to the probe spin. We then sweep the evolution time t and Fourier transform the signal to quantify the coupling strengths (Fig. 6.1e). For a single pulse ($N = 1$), the nuclear spin coherence time is $T_2 = 0.58(2)$ s, yielding a spectral resolution of 1.807(7) Hz and a centre frequency accuracy of 10 mHz. The spectral resolution is set by the coherence of the sample spins and can be further enhanced by applying more echo pulses. For $N = 256$, a resolution of 78(1) mHz and an accuracy of 2 mHz are obtained, making it possible to detect sub-Hertz interactions (Fig. 6.1f). The obtained resolution is an improvement by a factor $\sim 10^3$ over Ramsey-type spectroscopy on the same type of sample (Fig. 6.1c) [19–22,25,27,30], and is an order of magnitude higher than in previous experiments on other spin samples [7–9,26,31,32].

To characterise the complete cluster, we perform 3D spectroscopy by varying the probe frequency $RF1$, the target frequency $RF2$, and the evolution time t. The combinations of $RF1$ and $RF2$ reveal the spectral positions of the spins in the cluster. The coupling between spins is retrieved from the Fourier transform along the time dimension t. This yields a 3D data set that in principle encodes the composition and connectivity of the spin cluster (Fig. 6.2).

6.3. RESOLVING SPECTRALLY OVERLAPPING SPINS

In general, multiple spins can have (near-)identical precession frequencies. This has two consequences. First, the echo pulses will invert these spins simultaneously, so that multiple couplings are probed at the same time. Figure 6.3a shows an example with one probe spin and three target spins. This example illustrates that, while the resulting spectra are more complex, the high spectral resolution of our method enables retrieval of the underlying nuclear-nuclear couplings even when several spins overlap spectrally.

Second, to determine the number of spins in the cluster, and to assign the measured couplings to them, we need to resolve the ambiguity introduced by the fact that multiple spins can overlap spectrally. For example, the observation of a coupling between frequencies $\{RF1, RF2\} = \{A, C\}$ and a coupling between frequencies $\{B, C\}$ is by itself not enough to determine if there are one or two spins with frequency C. Our method resolves such ambiguities by extracting an over-determined data set with many couplings that together constrain the problem. This enables individual spins to be uniquely identified from their connections to the rest of the cluster (see Fig. 6.3b for an example).

6.4. CORRECTIONS FOR ELECTRON MEDIATED INTERACTIONS

Transforming the 3D spectra into a spatial structure requires a precise relation between the measured couplings and the relative positions of the spins. A complication is that

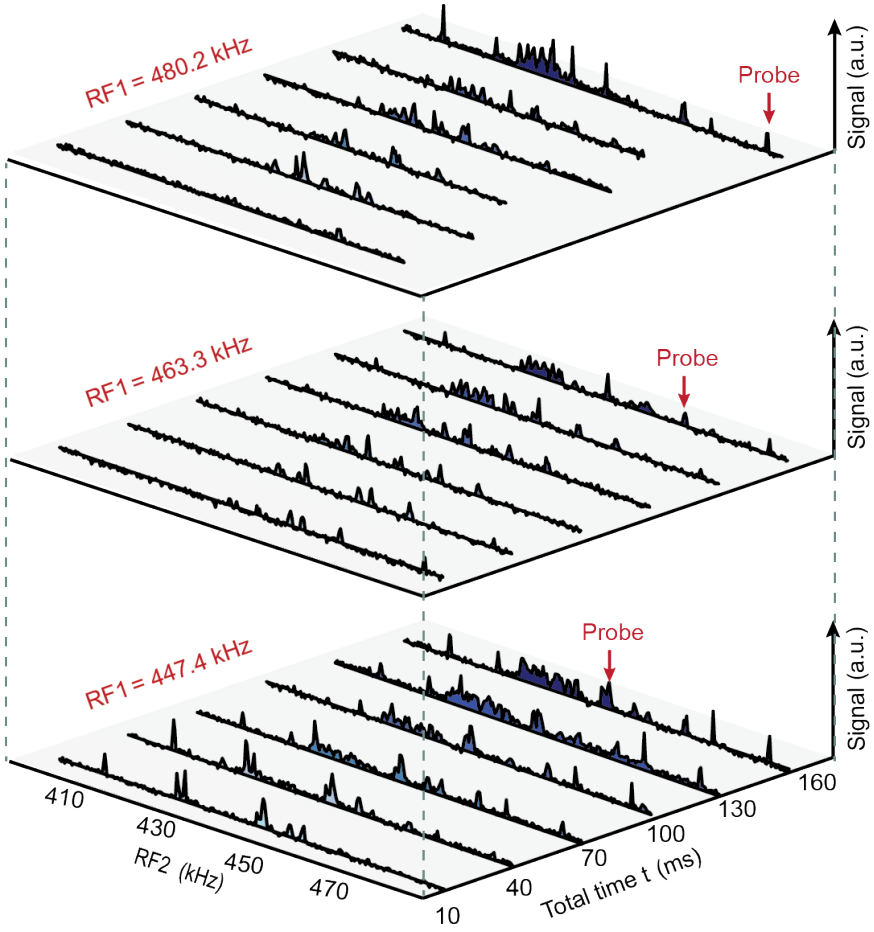

Figure 6.2: **Three-dimensional spectroscopy.** By varying the probe frequency $RF1$, the target frequency $RF2$, and the evolution time t, we obtain a three-dimensional data set that encodes the composition of the spins in the cluster and their couplings. The observation of a signal at $\{RF1, RF2\}$ indicates the presence of one or more spins at both frequencies and a coupling between them. The Fourier transform along the time dimension t reveals the spin-spin coupling strengths. Examples for three different $RF1$ values are shown.

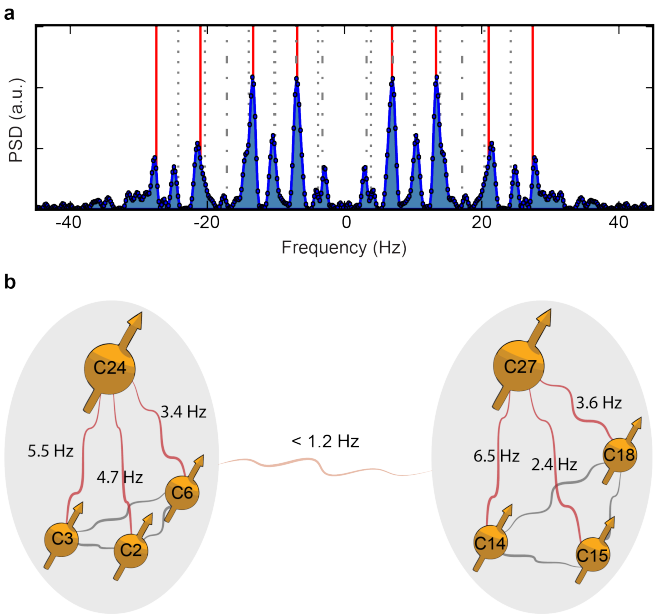

Figure 6.3: **Spectrally overlapping spins. a,** Retrieving couplings when multiple spins are re-coupled simultaneously. Example in which the echo pulses invert three target spins (quadruple resonance). The PSD reveals a complex, yet resolvable, spectrum. Red lines indicate the 8 frequencies $f = \pm f_1 \pm f_2 \pm f_3$, where $f_1 = 17.17(2)$ Hz, $f_2 = 7.05(3)$ Hz and $f_3 = 3.21(4)$ Hz are the extracted couplings of the probe spin to three target spins. Grey dashed lines mark additional frequency components that appear due to failures to invert one or two of the target spins [1]. **b,** Overcoming ambiguity in identifying spins and assigning couplings. Example from the data. Spins C2, C3, C6, C14, C15 and C18 all yield a coupling signal to the same RF2 frequency. Because the couplings between these 6 spins reveal that they are part of two spatially separated sub-clusters, it follows that the signals at RF2 must originate from two distinct spins (C24 and C27).

the presence of electronic spins can modify the nuclear couplings[33], causing the measured value to deviate from a basic dipole-dipole coupling. We use perturbation theory to derive a set of many-body corrections that depend on the electron-nuclear and nuclear-nuclear couplings, and the magnetic field direction (see Sec. 6.7.7). For the type of cluster considered here, the corrections could be significant. However, the signs of the leading terms depend on the electron spin state. By averaging the measured couplings for the $m_s = +1$ and $m_s = -1$ states, the deviations are strongly reduced. Together with a novel method to align the magnetic field to within 0.07 degrees (see Sec. 6.7.2), this enables us to approximate the nuclear-nuclear couplings as dipolar.

6.5. ATOMIC-SCALE IMAGING OF THE CLUSTER

Finally, we determine the structure of the spin cluster. Figure 6.4a summarises all extracted couplings. We identify $M = 27$ nuclear spins and retrieve a total of 171 pairwise couplings, out of the total of $M(M-1)/2 = 351$ couplings. The structure of the cluster is completely described by $3M - 4 = 77$ spatial coordinates (see Sec. 6.7.8), so that the problem is over-determined. However, due to the large number of parameters and local minima, a direct least-squares minimisation[11] is challenging. Instead, we sequentially build the structure by progressively adding spins, while keeping track of all possible structures that match the measured couplings within a certain tolerance.

We use two different methods. The first method constrains the spin coordinates to the diamond lattice. The second method discretises space in a general cubic lattice, with voxel spacing down to 5×10^{-3} nm ($\sim 1/70$th of the lattice constant, see Sec. 6.7.8). While this second method is more computationally intensive, it uses minimum a priori knowledge and can be applied on arbitrary spin systems. We run these analyses in parallel with the measurements, so that sets of the most promising spin assignments and structures are regularly created. These yield predictions for which unmeasured couplings (combinations of $RF1$ and $RF2$) are required to decide between different assignments and structures, which we use to guide the experiments and reduce the total measurement time (see Sec. 6.7.8).

Figure 6.4b shows the structure obtained for the 27 spins using the diamond-lattice. The blue connections show the strongest couplings (> 3 Hz) and visualise the interconnectivity of the cluster. The cubic-lattice method yields a nearly identical structure (see Sec. 6.7.8); the average distance between the spin positions for the two solutions is 0.58 Å, a fraction of the bond length of ~ 1.54 Å. As a final step, we use these structures as inputs for least-squares minimisation, where the x, y, z coordinates are allowed to relax to any value. The solution obtained lies close to the initial guess with an average distance of 0.46 Å. The uncertainties for the spatial coordinates (δx, δy, δz) are below a diamond bond length for all 27 spins (Fig. 6.4c,d), indicating atomic-scale imaging of the complete 27-spin cluster.

Additionally, we determine the position of the NV sensor relative to the cluster. Although not required to reconstruct the cluster, this provides a control experiment. We measure the coupling of the ^{14}N nuclear spin to 12 of the ^{13}C spins (Fig. 6.8). This unambiguously determines the location of both the ^{14}N atom and the vacancy (fit uncertainties < 0.3 Å). We can now compare the electron-^{13}C hyperfine couplings to previous den-

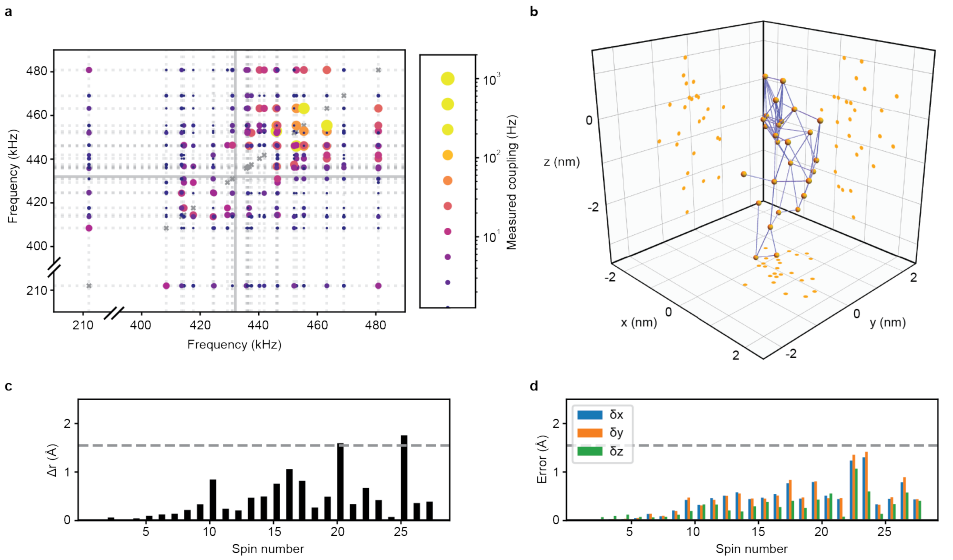

Figure 6.4: **Atomic-scale imaging of the 27-nuclear-spin cluster. a,** 2D plot summarising all couplings between the 27 spins identified from the 3D spectroscopy (Fig. 6.2). Includes identification of spins with overlapping frequencies. The size and colour of each point indicates the strength of the measured coupling averaged over the electron $m_s = +1$ and $m_s = -1$ states. Dashed grey lines indicate the nuclear spin frequencies ($m_s = -1$ state). Solid grey lines indicate the bare ^{13}C Larmor frequency. Total measurement time: ~ 400 hours. Numerical values and uncertainties are given in the supplemental materials [1]. **b,** 3D structure of the nuclear spins obtained using the diamond-lattice method (see text). Blue lines indicate couplings greater than 3 Hz and illustrate the connectivity of the cluster. See Fig. 6.7 for zoom-ins of strongly coupled subclusters. **c,** Distance Δr between the obtained spin positions from the diamond-lattice method (see text) and from a least-squares optimisation. Deviations are generally below one diamond bond length (dashed line, ~ 1.54 Å). **d,** The uncertainties for the 77 spatial coordinates of the cluster from a least-squares optimisation are less than the bond length, indicating atomic-scale resolution. In depth comparisons between the structures and uncertainties obtained with the different methods are given in the supplementary materials [1].

sity functional theory (DFT) calculations for 5 of our spins[34]. All 5 couplings agree with the DFT calculations (Fig. 6.8), providing an independent corroboration of the extracted structure, as well as a direct test of the DFT calculations. Looking beyond quantum sensing, this precise microscopic characterisation of the NV environment provides new opportunities for improved control of quantum bits for quantum information[21,25,29,32,33], and for investigating many-body physics in coupled spin systems.

In our method, the NV sensor spin is exclusively used to create and detect polarisation (Fig. 6.1b). Therefore, the two main requirements for the sensor spin are (1) a high-contrast readout to keep measurement times manageable, and (2) that it does not limit the spectral resolution by disturbing the evolution of the nuclear spins through relaxation[26,31,32]. We satisfy these requirements by working at 4 Kelvin, so that the electron relaxation is negligible ($T_1 = 3.6(3) \times 10^3\,\mathrm{s}$[21]), and high-fidelity readout through resonant optical excitation is available (see Sec. 6.7.1). Recent experiments have demonstrated both these requirements up to room temperature[6,26,27,31,32]. The electron spin relaxation—milliseconds at room temperature—can be decoupled from the sample spins through laser illumination[31,32] or sequential weak measurements[26,27]. High-contrast readout has been demonstrated by using a nuclear spin as a memory that can be read out repeatedly[6,31]. Nuclear spins themselves are well-isolated from temperature[32]. Therefore, when combined with those methods, the ideas presented here could be extended to ambient conditions.

6.6. CONCLUSION

In conclusion, we have developed and demonstrated 3D atomic-scale imaging of large clusters of nuclear spins using a single-spin quantum sensor. Our approach is compatible with room temperature operation[26,27,31,32] and could be extended to larger structures, as the number of required measurements scales linearly with the number of spins. Future improvements in the data acquisition and the computation of 3D structures can further reduce time requirements. In particular, recent methods to polarise and measure nuclear spins are expected to improve sensitivity[26,27], especially for samples with weak couplings to the NV sensor. Optimised sampling of the measurements and adaptive algorithms based on a real-time structure analysis can further reduce the total number of required measurements. Therefore, when combined with recent progress in nanoscale NMR with near-surface NV centres[3–9], our results provide a path towards the magnetic imaging of individual molecules and complex spin structures external to diamond[11–14].

6.7. METHODS

6.7.1. SAMPLE AND NV CENTRE SENSOR

We use a naturally occurring NV centre in a homoepitaxially chemical-vapor-deposition (CVD) grown diamond with a 1.1% natural abundance of ^{13}C and a $\langle 111 \rangle$ crystal orientation (Element Six). The NV is placed in a solid-immersion lens to enhance photon collection efficiency[35]. The NV centre has been selected for the absence of ^{13}C spins with

hyperfine couplings > 500 kHz. The NV electron spin coherence times are $T_2^* = 4.9(2)\,\mu$s and $T_2 = 1.182(5)$ ms. We work at 4 Kelvin, so that the electron relaxation is negligible ($T_1 = 3.6(3) \times 10^3$ s[21]), and use high-fidelity readout through resonant optical excitation (average $F = 94.5\%$)[35].

The nuclear-spin dephasing times observed range from $T_2^* = 3$ ms to 17 ms, corresponding to a inhomogeneous linewidth of $\sim 30 - 150$ Hz. Due to the frequency differences between nuclear spins in $m_s = \pm 1$ (Table 6.1), spin diffusion is strongly suppressed and the longitudinal relaxation of the nuclear spins is $T_1 > 6$ minutes[29].

6.7.2. MAGNETIC FIELD ALIGNMENT

A magnetic field of ~ 403 G is applied using a room-temperature permanent magnet which is installed on a XYZ translation stage to control the strength and the direction of the magnetic field. Our methods are based on echoes and are therefore robust against slow fluctuations in the magnetic field strength. Although magnetic field drift has no significant effect on the measured nuclear-nuclear couplings, we stabilise the magnetic field to < 3 mG using temperature stabilisation of the magnet and an automatic recalibration procedure (every few hours).

We align the magnetic field along the NV axis to avoid electron-mediated shifts that cause the measured couplings to deviate from nuclear-nuclear dipolar coupling (see supplemental materials[1]). We use a "thermal" echo sequence—previously introduced to measure temperature[36] (see Fig. 6.9). In this sequence, the electron evolves half of the time in a superposition of the states $m_s = 0$ and $m_s = -1$, and half of the time in a superposition of $m_s = 0$ and $m_s = +1$. Since the energies of the states $m_s = \pm 1$ are shifted by equal and opposite amounts by Hamiltonian terms proportional to S_z, the effects of such terms are cancelled. However, Hamiltonian terms that shift the energies of $m_s = \pm 1$ in the same way, such as the magnetic field perpendicular to z, do not cancel. Therefore, the sequence decouples the main source of noise (the magnetic field fluctuations along z from the surrounding spin bath), while remaining sensitive to shifts caused by a non-zero magnetic field in the x, y directions. This sequence extends the sensing time from $T_2^* \approx 5\,\mu$s to $T_2 \approx 1$ ms, resulting in an uncertainty in the alignment of 0.07 degrees (Fig. 6.9).

6.7.3. QUANTUM SENSING SEQUENCES

We employ two different sensing sequences (see the polarise and detect blocks in Fig. 6.1b). Sequence A consists of dynamical decoupling sequences of N' equally spaced π-pulses on the electron spin of the form $(\tau_r - \pi - \tau_r)^{N'}$ [37–39]. This sequence is only sensitive to nuclear spins with a significant electron-nuclear hyperfine component perpendicular to the applied magnetic field[37]. The inter-pulse spacing $2\tau_r$ determines the spin frequency that is being probed.

Sequence B is a recently developed method, described in detail in Bradley *et al.*[29], that interleaves the dynamical decoupling sequence with RF pulses. This method enables the detection of spins with a weak or negligible perpendicular hyperfine component[29,31]. For this sequence, the frequency of the RF pulse sets the targeted spin frequency, while τ_r can be freely chosen[29]. Importantly, the amplitudes and phases of the

RF pulses are set so that they together build up to the desired evolution[29]. The added RF field imprints a deterministic phase on the electron spin sensor[29], which we compensate by calibrating the phase of the electron $\pi/2$-pulses.

6.7.4. ELECTRON-NUCLEAR SPECTROSCOPY

As a starting point, we use the electron spin as a sensor to roughly characterise some of the nuclear spins in the cluster. We perform spectroscopy by sweeping the interpulse delay τ_r in sequence A (see for example Abobeih *et al.*[21]) and the RF frequency for sequence B[29]. This identifies the frequency range at which spins are present in the cluster and provides the parameters to polarise and detect several spins[25]. Note that the resolution of this spectroscopy technique is limited by the electron spin T_2 and the nuclear spin T_2^*.

6.7.5. NUCLEAR-NUCLEAR DOUBLE-RESONANCE SPECTROSCOPY

The sequence for the double-resonance experiments is shown in Fig. 6.1b and Fig. 6.5. To polarise and detect the probe spin, we either use sequence A (without the RF1 pulses in the dashed box) or sequence B (with the RF1 pulses), depending on whether the perpendicular hyperfine coupling to the electron spin is significant or not. For sequence A, we set the interpulse delay as $\tau_r = (2k-1)\pi/(\omega_0 + RF1)$, with k an integer and ω_0 the ^{13}C Larmor frequency for the electron $m_s = 0$ state, and calibrate the number of pulses N' to maximise the signal[37]. For sequence B we calibrate the RF power to maximise the signal.

We create nuclear polarisation by projective measurements[25]. First the electron is prepared in a superposition state through resonant excitation[35] and a $\pi/2$ pulse. Second, the sensing sequence correlates the phase of the electron with the nuclear spin state. Finally, the electron is read out so that the nuclear spin is projected into a polarised state[25]. To enhance the signal-to-noise ratio and to ensure that the electron measurement does not disturb the nuclear spin evolution, we only perform the double-resonance sequence if a photon was detected during the electron readout[25]. The resulting signal contrast for different spins varies from 20% to 96%.

Because the correlation data is read out and stored in the electronics, the ultimate limit for the spectral resolution of our method - i.e. when applied on hypothetical signals with infinitesimal spectral width - is set by the precision of the 10 MHz reference clock used for the timing of the waveform generator[8,40,41]. For the double-resonance sequence, the phases of the RF1 echo pulses are calibrated so that their phase difference is 0 or $\pi/2$ with respect to the polarisation axis, which is determined by the direction of the hyperfine interaction[19,20,42]. For the target spins, the phase of the RF2 pulse does not affect the signal and is arbitrarily set.

To mitigate pulse errors we alternate the phases of the pulses following the XY8 scheme[43], both for the electron and nuclear spins. For the electron spin, we use Hermite pulse envelopes[44] with Rabi frequency ~ 14 MHz to obtain effective microwave pulses without initialisation of the intrinsic ^{14}N nuclear spin. The nuclear-spin Rabi frequencies are in the range $0.3 - 0.7$ kHz.

6.7.6. DATA ANALYSIS

We extract the spin-spin couplings f and their uncertainties from fitting the time-domain double-resonance signals (e.g. Fig. 6.1e-f, top) to $S = a + A \cdot e^{-(t/T_2)^n} \cos(2\pi f t + \phi)$, where T_2 is the coherence time (also a fit parameter). The PSD is obtained from a Fourier transform of the time domain signal with zero filling[2] and the D.C. component filtered out (e.g. Fig. 6.1e-f, bottom). The spectral resolution (FWHM) is obtained from a Gaussian fit of the PSD. Alternatively we can define the spectral resolution (FWHM) directly from the time domain signal as $\frac{2\sqrt{ln2}}{\pi T_2}$. This yields a spectral resolution of 0.91(3) Hz for Fig. 6.1e. For the spin in Fig. 6.1f, using $N = 1$ yields a spectral resolution of 0.8(1) Hz and using $N = 256$ yields 49(2) mHz. Note that no saturation of the improvement of spectral resolution with the number of pulses is yet observed. Therefore, with more pulses (and longer measurement times) higher spectral resolutions and more precise measurements are feasible.

6.7.7. ELECTRON-MEDIATED INTERACTIONS

We calculate corrections to the nuclear-nuclear couplings due to the presence of the electron spin using perturbation theory up to second order. The effect of other nuclear spins on nuclear-nuclear couplings was found by numerical simulations to be negligible (∼ mHz). In contrast to previous results for strong electron-nuclear couplings[33,45], here many-body interactions due to the non-secular nuclear-nuclear couplings must be taken into account. The resulting frequency in a double-resonance experiment is of the form (see supplemental materials[1])

$$f_{\mathrm{DR}}(m_s = \pm 1) \approx \frac{1}{4\pi} |C + \\ + \Delta\lambda_1(m_s) + \Delta\lambda_2(m_s) + \Delta\lambda_3(m_s)|, \tag{6.1}$$

where C is the parallel (zz) component of the dipole-dipole interaction between the nuclear spins and $\Delta\lambda_i$ are correction terms due to the presence of the electron spin[1].

The dominant correction for our parameter regime is $\Delta\lambda_2$, which depends on both the electron-nuclear and nuclear-nuclear interactions. We make a Taylor expansion up to first order in $A_{zz}^{(j)}/\gamma_c B_z$, where $A_{zz}^{(j)}$ is the parallel electron-nuclear hyperfine coupling for spin j, γ_c is the nuclear gyromagnetic ratio and B_z is the component of the magnetic field along the NV axis. This yields an expression of the form $\Delta\lambda_2(m_s) \approx m_s \Delta\lambda_2^{(0)} + \Delta\lambda_2^{(1)}$, where the leading, zeroth-order, correction $m_s \Delta\lambda_2^{(0)}$ is given by

$$\Delta\lambda_2^{(0)} = \frac{(A_{zx}^{(1)} + A_{zx}^{(2)})C_{zx} + (A_{zy}^{(1)} + A_{zy}^{(2)})C_{zy}}{\gamma_c B_z}, \tag{6.2}$$

where $A_{zx}^{(j)}$ (C_{zx}) and $A_{zy}^{(j)}$ (C_{zy}) are the perpendicular electron-nuclear (nuclear-nuclear) coupling components. We cancel this term by averaging the double-resonance frequencies measured for the $m_s = \pm 1$ electron spin projections.

The remaining electron-mediated corrections depend on the angles of the electron-nuclear hyperfine interactions. Because these angles are unknown, we estimate the maximum possible shift for each spin-spin interaction by maximising over all angles. For our

cluster (Fig. 6.4), most of these maximum possible shifts are small (their average value is ~ 0.03 Hz). In rare cases, the maximum possible correction runs up to 0.6 Hz [1], but as the locations of the involved spins are already precisely fixed through strong (> 20 Hz) interactions with several other spins, this would have a negligible effect on the obtained structure. Therefore, we can base the structural analysis on dipole-dipole interactions.

6.7.8. 3D STRUCTURE ANALYSIS

The 3D structure of the nuclear spins is obtained using the dipole-dipole coupling formula, which relates the zz couplings C_{ij} to the spatial x, y, z coordinates of spins i and j as

$$C_{ij} = \frac{\alpha_{ij}}{\Delta r_{ij}^3}\left(\frac{3(z_j - z_i)^2}{\Delta r_{ij}^2} - 1\right), \tag{6.3}$$

where $\Delta r_{ij} = \sqrt{(x_j - x_i)^2 + (y_j - y_i)^2 + (z_j - z_i)^2}$, $\alpha_{ij} = \mu_0 \gamma_i \gamma_j \hbar / 4\pi$, μ_0 is the permeability of free space, γ_i is the gyromagnetic ratio of nuclear spin i and $\hbar$ is the reduced Planck constant.

The goal is to minimise the sum of squares $\xi = \sum_{i<j} |\Delta f_{ij}|^2$, where $\Delta f_{ij} = f_{ij} - |C_{ij}|/4\pi$ are the residuals and f_{ij} are the measured coupling frequencies. For $M = 27$ spins, there are $3M - 4 = 77$ free coordinates and $M(M-1)/2 = 351$ pairwise couplings, of which 171 were determined in this work. ξ can in principle be minimised using standard fitting methods, however tests with randomly generated spin clusters indicate that the initial guess for the coordinates should be within ~ 0.5 Å in order for the fit to converge to the correct solution. For 27 spins, this corresponds to an intractable $\sim 10^{100}$ possible initial guesses. Instead we sequentially build the structure by adding spins one-by-one.

For the diamond lattice positioning method, we first use the strongest measured coupling to any spin that is already positioned to reduce the position of a new spin to a number of possible lattice coordinates. For each possible coordinate, we then check if the predicted couplings to all other spins satisfy $\Delta f_{ij} < \mathcal{T}$, where $\mathcal{T} = 1.1$ Hz is a tolerance that is chosen to ensure that all promising configurations are included while maintaining reasonable computation time. Configurations are discarded if they do not satisfy this requirement for one or more of the pairwise couplings. If more than $X_{\text{cutoff}} = 5000$ possible configurations are identified, only the best X_{cutoff} solutions are kept, according to their ξ values.

For the cubic lattice positioning method, the same procedure is followed, with the key difference being that the lattice is adaptively generated depending on the strongest coupling to an already positioned spin in the cluster (see supplemental materials [1]). This ensures that in each case the lattice spacing is fine enough to appropriately sample the volume associated with the dipole-dipole coupling between the nuclear spins.

6.7.9. ROBUSTNESS OF THE ANALYSIS

The method is robust to failure. The problem is generally highly over-determined, so that discarding the correct configuration due to X_{cutoff} will lead to no solution at all, rather than an erroneous solution. Given enough computational resources, a correct solution is

always expected to be found. As a test, we used the cubic lattice reconstruction method on 17 randomly generated 30-spin clusters spins with added noise and no erroneous structures were returned[1].

6.7.10. COMPARISON TO 1D RAMSEY SPECTROSCOPY

Fig. 6.6 compares the 1D Ramsey signal with reconstructed spectra from our 3D spectroscopy. This comparison illustrates the effective improvement in resolution, and the ability to resolve dense spectra, of our method. Note that, apart from the spectral resolution, the signals should not be compared directly, because the Ramsey experiment is difficult to interpret quantitatively. First, the Ramsey signals likely contain contributions from multiple spins, both due to spectral overlap and higher-order contributions[37–39]. Second, any inadvertent polarisation of other spins in the cluster or the environment modifies the spectrum. These effects are difficult to separate from actual nuclear-nuclear couplings, and the fact that the spectra are asymmetric indicates that they play a significant role. Our 3D spectroscopy method resolves these issues.

6.7.11. FINDING THE POSITION OF THE NV CENTRE

Because the NV electron wavefunction is not known a-priori, we cannot use the electron-nuclear couplings to find the NV position. In particular, density functional theory (DFT) calculations[34] indicate that, for electron-nuclear couplings in the range observed here, assuming a point-dipole model for the electron spin can lead to large discrepancies, and is therefore not justified.

Our approach is to measure the couplings between the ^{13}C spins and the NV nitrogen nuclear spin, for which the point-dipole approximation is accurate. The nitrogen-^{13}C couplings can be measured using a similar double-resonance procedure as for measuring ^{13}C-^{13}C couplings. We use the nitrogen spin as the probe spin: this gives better spectral resolution, due to its longer coherence time ($T_2 = 2.3(2)\,\mathrm{s}$[29]). We initialise the nitrogen spin in $m_I = 0$ using measurement-based initialisation[35] and manipulate the spin state using RF pulses. Fig. 6.8b shows the measured couplings between the nitrogen and ^{13}C spins.

Using the couplings, the nitrogen spin is added to the ^{13}C nuclear spin cluster using the diamond lattice positioning method, where $\gamma_j \to \gamma_n = 2\pi \times 0.3077\,\mathrm{kHz/G}$, the nitrogen gyromagnetic ratio, in equation 6.3. Determining the nitrogen lattice site also allows the vacancy site to be determined due to the known N-V distance and the alignment with the magnetic field along z, thereby giving the location and the orientation of the NV centre with respect to the ^{13}C nuclear spin cluster. The resulting 3D plot showing the best solution is shown in Fig. 6.8a. The nitrogen spin coordinate is the same for all 5000 configurations identified. Fig. 6.8c gives the results of a least-squares fit.

6.7.12. COMPARISON TO DFT

Now that we independently determined the position of the ^{13}C spins relative to the NV centre, we can compare the hyperfine couplings to DFT calculations, without any prior assumptions. In Nizovtsev *et al.*[34], hyperfine couplings are calculated for 510 lattice sites surrounding the NV centre. Fig. 6.8d shows the lattice positions given in Nizovtsev *et al.*

along with the coordinates of the ^{13}C spins found in this work. The ^{13}C spin coordinates are transformed so that the nitrogen spin is at the origin, and mirrored such that $z \rightarrow -z$, in order to be in the correct coordinate frame. Additionally a scaling factor of 1.02 was applied, which was found by comparing the 510 lattice sites from Nizovtsev *et al.* with the same sites in our work. 5 of the 27 spins identified in this work were calculated in Nizovtsev *et al.* The remaining spins cannot yet be compared with DFT calculations. Fig. 6.8e shows the measured electron-^{13}C hyperfine couplings (see Table 6.1), as well as those predicted in Nizovtsev *et al.*, for the 5 spins. For the DFT results, we take the average of the predicted couplings for the possible C_{3v} symmetric lattice sites. Additionally, we take the negative of the predicted $A_{\parallel}$ for all spins (a global minus sign is possible due to the unknown orientation of the magnetic field along z).

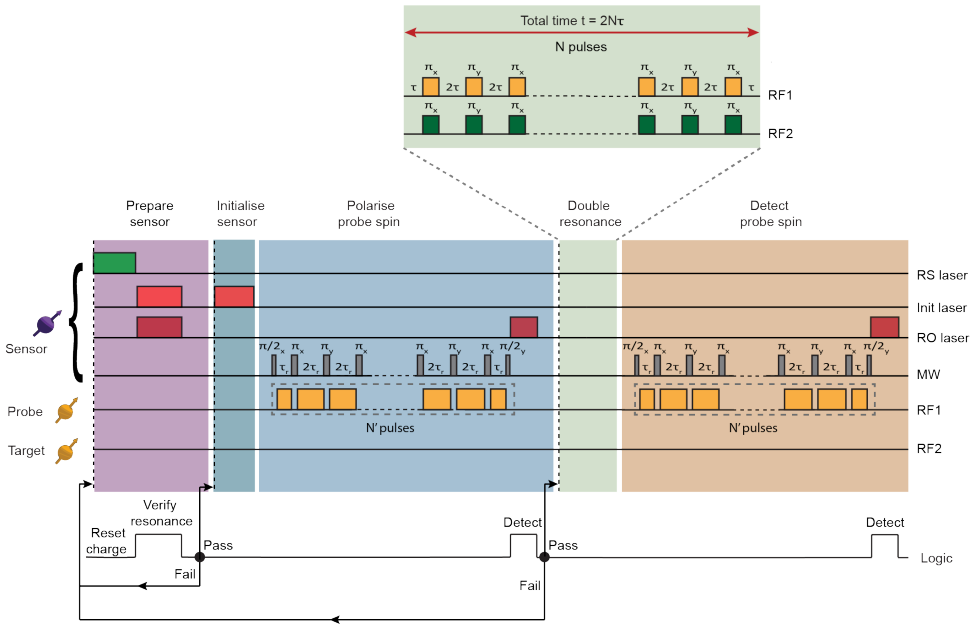

Figure 6.5: **Experimental sequence.** The pulse sequence consists of five parts: sensor preparation, sensor initialisation, polarisation of the probe spin, double resonance, and detection of the probe spin. Sensor preparation: The NV centre is prepared by excitation with two 637 nm lasers for 150 μs and counting the detected photons (RO laser resonant with the E_x transition and Init laser with the $E^{'}$ transition)[25,35]. If the number of photons exceeds a certain threshold, the NV is in the negative charge state and resonant with both lasers, and we proceed to the next step. If not, we apply a 515 nm laser (charge reset (RS) laser, 1 ms) and repeat the process[25,35]. Sensor initialisation: The NV electron spin is initialised into the $m_s = 0$ state through spin pumping (Init laser, 100 μs)[35]. Polarising probe spin: First, the NV sensor is brought into a superposition state using a $\pi/2$ pulse. Then, a dynamical decoupling sequence of N' equally spaced π-pulses on the electron spin of the form $(\tau_r - \pi - \tau_r)^{N'}$ is applied. This sequence correlates the state of the nuclear spin(s) with the phase of the electron spin. We use two different sequences (see Sec. 6.7.3). For sequence B, the MW π-pulses are interleaved with radio-frequency pulses ($RF1$) that resonantly drive the probe spin(s) (dashed box), see Bradley *et al.* for details[29]. A second $\pi/2$ pulse maps the electron phase to population and the electron spin is read out (RO laser). Double resonance: N echo pulses are applied simultaneously on the probe spin(s) ($RF1$) and the target spin(s) ($RF2$), so that the coupling between these spins is isolated. To mitigate pulse errors we alternate the phases of the pulses following the XY8 scheme[43]. Detecting probe spin: The detection sequence is the same as the polarisation sequence except for the final RO laser pulse which is applied for 10 μs and with higher power.

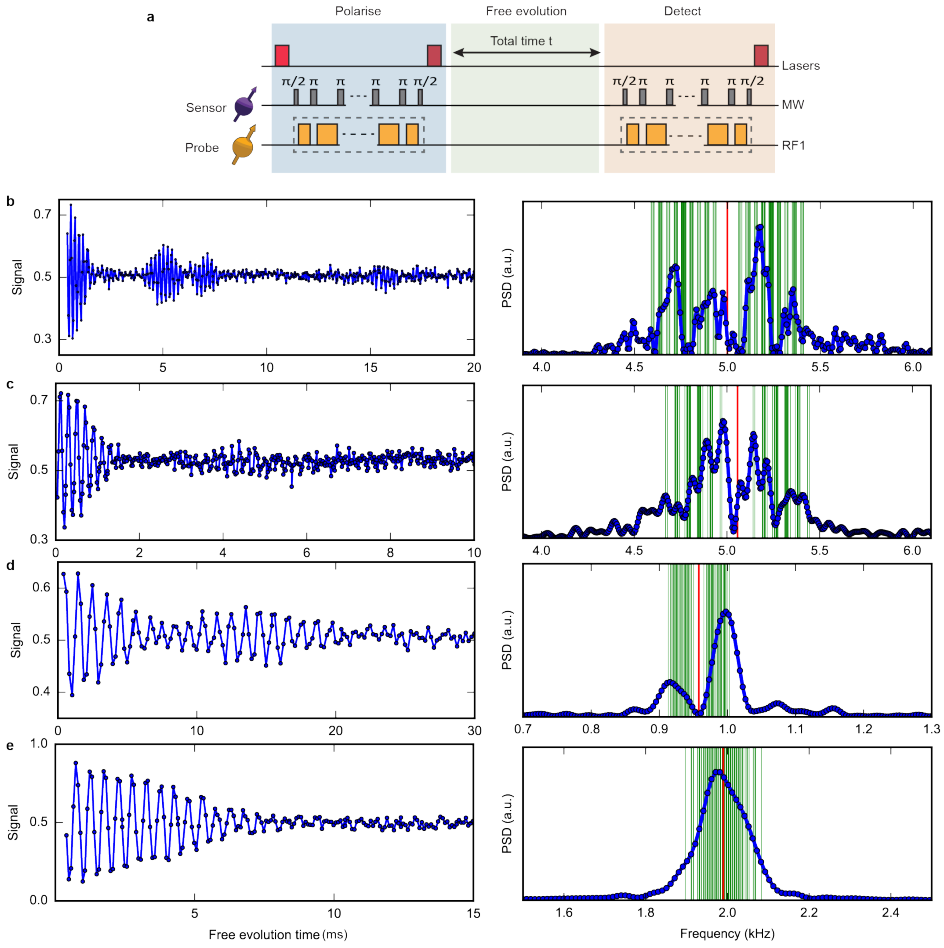

Figure 6.6: **Ramsey experiments and reconstructed underlying spectra.** **a**, Schematic of the pulse sequence used to perform the Ramsey experiment (equivalent to correlation spectroscopy). See Sec. 6.7.10 and Fig. 6.5 for details. **b**, Ramsey signal for C2 and the corresponding power spectral density (5 kHz detuning). The red line represents the central frequency f_0. Green lines are the 2^7 frequencies based on the 7 strongest coupling strengths extracted from our high resolution double-resonance spectroscopy[1]. These frequencies are given by $f_0 \pm f_1 \pm f_2 \pm f_3 \pm f_4 \pm f_5 \pm f_6 \pm f_7$, where f_1 to f_7 are the 7 largest measured coupling strengths for C2. **c**, The same experiment for C3 (~ 5 kHz detuning), **d**, for C15 (~ 1 kHz detuning) and **e**, for C5 (~ 2 kHz detuning).

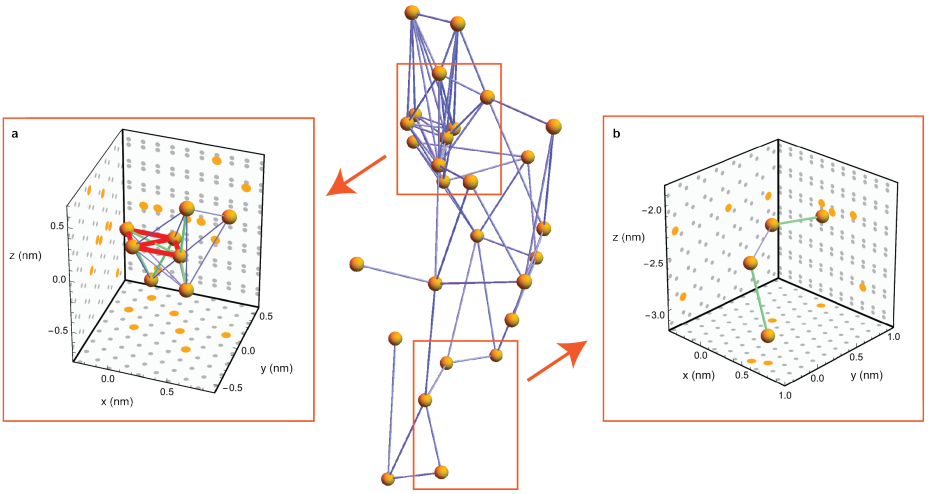

Figure 6.7: **Strongly coupled subclusters.** 3D plots showing the structure of two strongly coupled subclusters (orange panels) within the larger cluster (shown in the centre). The positions of the subclusters within the larger cluster are marked by the orange boxes and arrows. Ramsey measurements performed on spins within these subclusters show clear beating signals within their T_2^* dephasing time (see for example Fig. 6.6). Panel a) shows an 8 spin subcluster, while panel b) shows a 4 spin subcluster. Couplings above 3 Hz are marked blue, above 20 Hz green and above 50 Hz red. Grey points show the 2D projections of the diamond lattice coordinates.

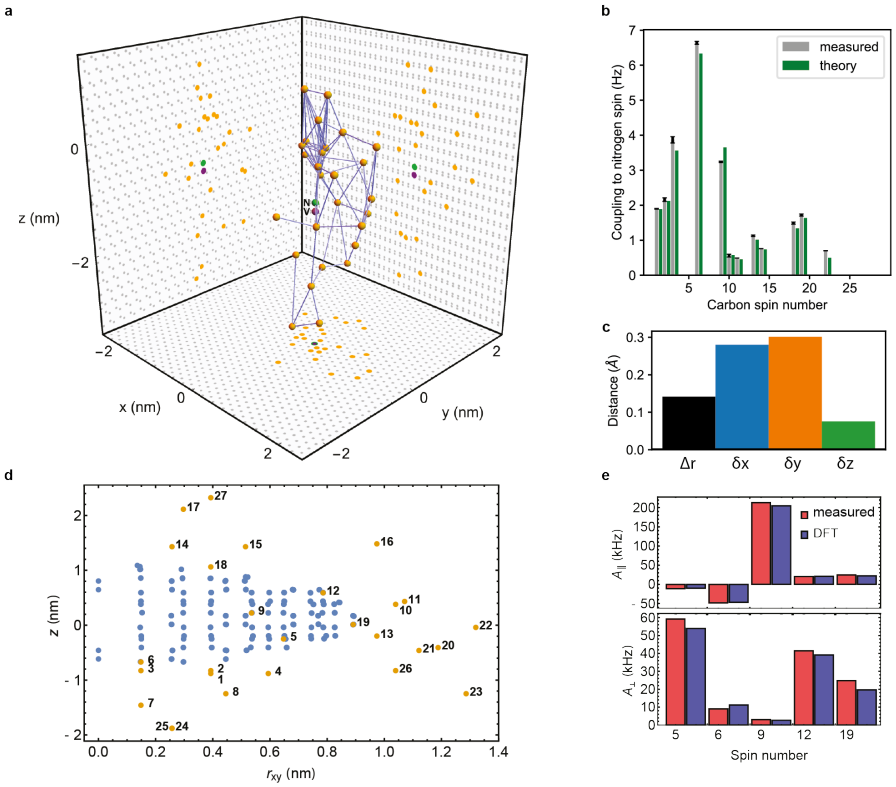

Figure 6.8: **Finding the position of the NV centre. a,** 3D plot showing the 27 nuclear spin cluster as shown in Fig. 6.4, with the position of the nitrogen spin (green) and vacancy (purple) lattice sites calculated from the measured nitrogen-^{13}C couplings. The grey dots show the 2D projections of the diamond lattice coordinates. **b,** Bar plot showing the measured couplings f_{iN} between ^{13}C spin i and the nitrogen spin (grey), as well as the theoretically calculated couplings $|C_{iN}|/4\pi$ (green). Error bars are one standard deviation. See supplemental materials for the numerical values [1]. **c,** Bar plots of Δr for the fitted position for the nitrogen spin (black), as well as fit errors δx (blue), δy (orange) and δz (green), where the ^{13}C spins are fixed at the diamond lattice solution. **d,** Plot of z vs. $r_{xy} = \sqrt{x^2 + y^2}$ for all lattice positions used in the DFT calculation from Nizovtsev *et al.*[34] (blue) and for the appropriately transformed ^{13}C coordinates found in this work (orange). Spins 5, 6, 9, 12 and 19 match a DFT lattice position, while the rest of the spins identified are outside of the 510 lattice sites simulated. **e,** Measured electron-^{13}C parallel (top) and perpendicular (bottom) hyperfine couplings for the 5 spins that are within the DFT calculation volume (red, taken from Table 6.1), compared with the DFT results from Nizovtsev *et al.* (blue).

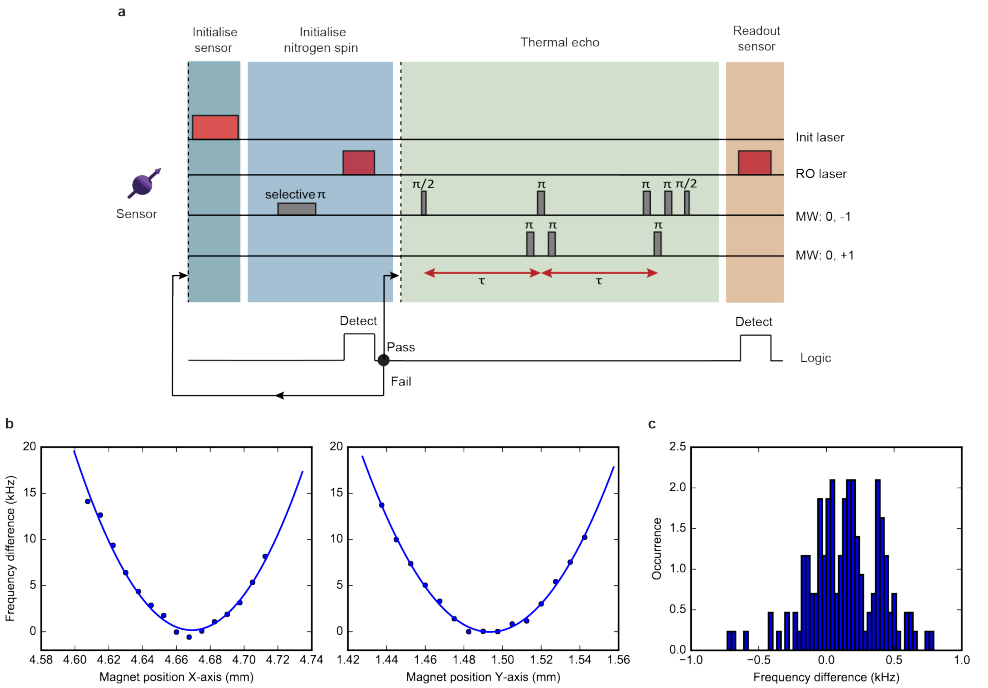

Figure 6.9: **Aligning the magnetic field using a thermal echo sequence. a,** Pulse sequence for the thermal echo measurement[36]. The electron spin is prepared in a superposition of the states $m_s = 0$ and $m_s = -1$ in the first half of the sequence, and then swapped to a superposition of $m_s = 0$ and $m_s = +1$ for the second half, using a sequence of three closely spaced π pulses. By sweeping τ, the average frequency $f_{\mathrm{TE}} = (f_{+1} + f_{-1})/2$ is obtained, which is minimised when $B_\perp = 0$. $f_{\pm 1}$ are the $m_s = 0 \leftrightarrow m_s = \pm 1$ transition frequencies. The NV nitrogen spin is initialised in $m_I = 0$[35]. **b,** Magnetic field alignment by scanning the magnet position in two orthogonal directions. The obtained thermal echo frequencies are fitted to a parabolic function to find the optimum position (i.e. minimal f_{TE}). The plots show the frequency difference $f_{\mathrm{TE}} - 2.877652\,\mathrm{GHz}$. **c,** Placing the magnet at the optimum position and repeating the measurement 200 times (over a 10-hour period). The obtained average frequency difference is 0.13 kHz, with a standard deviation of 0.27 kHz, which is consistent with the statistical measurement error. Therefore, the total uncertainty for the magnet alignment is ~ 0.4 kHz which corresponds to a perpendicular field of 0.5 Gauss or a misalignment angle of 0.07 degrees.

6.8. PROPERTIES OF THE NUCLEAR SPIN CLUSTER

This section summarises the properties of the nuclear spin cluster that we retrieved from the 3D spectroscopy. This knowledge will be utilised in Ch. 7 to develop a nuclear-spin-based quantum simulator.

Table 6.1 gives the precession frequencies of the 27 spins that compose the cluster. Table 6.2 summarises the retrieved couplings between these spins when the electron is in the $m_s = -1$ state.

Additionally, Table 6.1 gives estimates for the hyperfine couplings of the nuclear spins to the electron spin. These electron-nuclear couplings play no role in retrieving the structure of the cluster as our imaging method solely relies on the internal nuclear-nuclear couplings. Instead, these couplings are used to estimate realistic bounds on electron-mediated interactions [1] and to provide an independent comparison to DFT calculations (see Sec. 6.7.12).

The hyperfine couplings are estimated as follows. Under the secular approximation and assuming a perfectly aligned magnetic field, the nuclear spin precession frequencies ω_{m_s} for electron spin state m_s are given by [37]

$$\begin{aligned} \omega_0 &= \omega_L, \\ \omega_{\pm 1} &= \sqrt{(\omega_L \pm A_\parallel)^2 + A_\perp^2}, \end{aligned} \tag{6.4}$$

where $\omega_L = \gamma_c B_z$ is the Larmor frequency, γ_c is the ^{13}C gyromagnetic ratio and B_z is the $\hat{z}$ component of the externally applied magnetic field. Rearranging equations 6.4, we obtain expressions for the electron-^{13}C hyperfine parameters, given by

$$\begin{aligned} A_\parallel &= \frac{\omega_{+1}^2 - \omega_{-1}^2}{4\omega_0}, \\ A_\perp &= \sqrt{\frac{\omega_{+1}^2 + \omega_{-1}^2 - 2\omega_0^2 - 2A_\parallel^2}{2}}. \end{aligned} \tag{6.5}$$

For spins C5, C6, C9, C10, C12, C14, C18 and C19, we measure the $m_s = 0$ precession frequency ω_0, while for the rest of the spins we use the average of these measured values ($= 2\pi \cdot 431.960$ kHz). We observe a standard deviation of 6 Hz in the measured values of ω_0, which can be attributed to non-secular terms in the Hamiltonian in conjunction with a slightly misaligned magnetic field (< 0.1 deg, see Fig. 6.9). For spins C24 to C27, equations 6.5 give imaginary values for $A_\perp$, which we attribute to shifts in ω_0 that are not captured in this approximate model. For these spins we set $A_\perp = 0$ in the table.

	$\omega_{-1}/2\pi$ (kHz)	$\omega_{+1}/2\pi$ (kHz)	$A_\parallel/2\pi$ (kHz)	$A_\perp/2\pi$(kHz)	τ_r (μs)	N'	Sequence
C1	452.83(2)	411.40(2)	-20.72(1)	12(1)	7.435	64	A
C2	455.37(2)	408.956(9)	-23.22(1)	13(1)	8.92	62	A
C3	463.27(2)	400.79(2)	-31.25(1)	8(2)	18.522	48	B
C4	446.23(4)	418.10(1)	-14.07(2)	13(1)	-	-	-
C5	447.234(1)	424.752(3)	-11.346(2)	59.21(3)	16.480	20	A
C6	480.625(1)	383.48(4)	-48.58(2)	9(2)	4.932	90	A
C7	440.288(6)	423.65(2)	-8.32(1)	3(5)	-	-	-
C8	441.77(1)	422.20(4)	-9.79(2)	5(4)	-	-	-
C9	218.828(1)	645.123(1)	213.154(1)	3.0(4)	16.204	48	B
C10	414.407(1)	449.687(2)	17.643(1)	8.6(2)	23.152	48	B
C11	417.523(4)	446.612(3)	14.548(3)	10(1)	10.812	58	A
C12	413.477(1)	454.427(1)	20.569(1)	41.51(3)	11.25	22	A
C13	424.449(1)	440.490(1)	8.029(1)	21.0(4)	10.682	36	A
C14	451.802(1)	412.175(5)	-19.815(3)	5.3(5)	18.522	64	B
C15	446.010(5)	418.093(3)	-13.961(3)	9(1)	8.444	72	A
C16	436.67(5)	427.35(3)	-4.66(3)	7(4)	-	-	-
C17	437.61(1)	426.38(2)	-5.62(1)	5(2)	-	-	-
C18	469.020(1)	396.542(1)	-36.308(1)	26.62(4)	7.218	44	A
C19	408.317(1)	457.035(1)	24.399(1)	24.81(4)	6.540	32	A
C20	429.403(4)	434.782(6)	2.690(4)	11(1)	-	-	-
C21	430.937(3)	433.36(1)	1.212(5)	13(1)	-	-	-
C22	424.289(3)	439.655(7)	7.683(4)	4(3)	-	-	-
C23	435.143(7)	428.789(5)	-3.177(5)	2(4)	-	-	-
C24	436.183(3)	427.732(7)	-4.225(4)	0(6)	-	-	-
C25	435.827(5)	428.079(9)	-3.873(5)	0(4)	-	-	-
C26	435.547(2)	428.31(1)	-3.618(5)	0(2)	-	-	-
C27	435.990(3)	427.910(9)	-4.039(5)	0(3)	-	-	-

Table 6.1: **The 27 nuclear spins.** Retrieved ^{13}C spin precession frequencies ω_{-1}, ω_{+1} for the $m_s = -1$ and $m_s = +1$ electron spin projections respectively. Obtained by least-squares fitting the frequency scan signal in double resonance experiments to a Gaussian function [1] or from fits of Ramsey signals to sinusoidal functions with Gaussian decays. $A_\parallel$ and $A_\perp$ are estimates for the parallel and perpendicular components of the electron-^{13}C hyperfine interaction respectively, obtained from the measured frequencies ω_{-1}, ω_{+1} and ω_0 (see Eqs. 6.5). τ_r and N' are the half pulse delay and the total number of pulses used in the polarisation and detection sequences (Fig. 6.5). The sequence column identifies whether sequence A or B was used to polarise/detect the spin. The spins marked with "-" were detected as target spins (no initialisation or direct detection with the electron spin required). The dephasing time, T_2^*, for the spins in the cluster varies from 3 ms to 17 ms. The measured coherence time (T_2) using a single refocusing pulse is typically ~0.5 s, corresponding to a FWHM spectral resolution of ~1 Hz in the double resonance experiments.

	C1	C2	C3	C4	C5	C6	C7	C8	C9	C10	C11	C12	C13	C14	C15	C16	C17	C18	C19	C20	C21	C22	C23	C24	C25	C26	C27	N
C1	-	61.88(9)	61.49(6)	236.0(2)	7.05(3)	12.66(6)	4.81(1)	2.9(2)	1.07(7)	<1	-	<1	<1	<1	-	-	-	1.0(1)	<1	-	2.3(2)	-	-	7.8(2)	2.2(2)	-	-	1.95(1)
C2	61.88(9)	-	235.95(1)	61.40(8)	17.17(2)	19.1(1)	5.61(6)	1.6(1)	1.11(6)	2.1(1)	1.4(1)	0.97(9)	<1	<1	<1	-	-	1.07(7)	<1	-	3.14(7)	-	-	4.6(1)	4.1(2)	<1	-	2.25(5)
C3	61.49(6)	235.95(1)	-	24.9(1)	3.21(4)	28.99(7)	20.2(4)	13.1(1)	2.53(7)	<1	<1	1.37(7)	<1	<1	-	-	-	1.01(7)	<1	-	2.3(1)	-	-	5.5(1)	5.0(3)	3.1(2)	-	3.87(9)
C4	236.0(2)	61.40(8)	24.9(1)	-	19.0(1)	7.0(1)	-	-	-	-	-	<1	<1	<1	<1	-	-	-	-	-	-	-	-	-	-	-	-	-
C5	7.05(3)	17.17(2)	3.21(4)	19.0(1)	-	2.5(9)	1.1(2)	0.9(2)	0.96(4)	7.75(3)	<1	<1	-	-	1.9(1)	-	-	2.33(5)	0.6(2)	7.1(1)	9.90(7)	-	-	-	-	-	-	-
C6	12.66(6)	19.1(1)	28.99(7)	7.0(1)	2.5(9)	-	16.50(9)	12.64(5)	6.48(2)	<1	<1	2.01(5)	<1	0.8(2)	-	-	-	1.28(6)	<1	1.1(3)	1.96(9)	-	0.8(2)	3.4(1)	5.6(2)	4.89(9)	-	6.69(4)
C7	4.8(1)	5.61(6)	20.2(4)	-	1.1(2)	16.50(9)	-	-	1.45(7)	<1	-	0.4(2)	<1	<1	-	-	-	<1	-	-	-	-	-	-	-	-	-	-
C8	2.9(2)	1.6(1)	13.1(1)	-	0.9(2)	12.64(5)	-	-	1.53(5)	<1	-	1.15(9)	3.11(8)	<1	<1	-	-	<1	-	-	-	-	-	-	-	-	-	-
C9	1.07(7)	1.11(6)	2.53(7)	-	0.96(4)	6.48(2)	1.45(7)	1.53(5)	-	1.12(7)	1.26(3)	1.56(4)	1.8(2)	3.77(3)	-	<1	1.1(1)	1.39(1)	8.45(2)	-	-	3.70(7)	0.7(1)	-	3.5(1)	0.89(4)	3.25(2)	
C10	<1	2.1(1)	<1	-	7.75(3)	<1	<1	<1	1.12(7)	-	14.51(7)	1.2(1)	<1	<1	3.7(5)	5.0(1)	-	<1	<1	6.9(2)	3.8(2)	-	-	-	-	-	-	0.56(3)
C11	-	1.4(1)	<1	-	<1	<1	-	-	1.26(3)	14.51(7)	-	3.35(3)	<1	<1	2.1(3)	4.7(1)	-	0.5(3)	<1	9.5(2)	-	-	-	-	<1	-	-	0.49(2)
C12	<1	0.97(9)	1.37(7)	<1	<1	2.01(5)	0.4(2)	1.15(9)	1.56(4)	1.2(1)	3.35(3)	-	12.17(6)	1.46(9)	-	<1	1.26(6)	1.1(2)	0.536(2)	-	-	1.7(2)	1.1(1)	-	-	-	-	-
C13	<1	<1	<1	<1	-	<1	<1	3.11(8)	1.8(2)	<1	<1	12.17(6)	-	<1	<1	<1	<1	-	1.3(2)	-	-	7.3(1)	3.5(1)	-	-	-	-	1.2(1)
C14	<1	<1	<1	<1	-	0.8(2)	<1	<1	3.77(3)	<1	<1	1.46(9)	<1	-	8.89(7)	2.1(2)	21.7(3)	1.39(6)	1.6(1)	-	-	-	-	-	-	6.3(2)	0.76(3)	
C15	-	<1	-	<1	1.9(1)	-	-	<1	-	3.7(5)	2.1(3)	-	<1	8.89(7)	-	24.6(3)	-	<1	<1	-	-	-	-	-	-	2.2(6)	-	
C16	-	-	-	-	-	-	-	-	<1	5.0(1)	4.7(1)	<1	<1	2.1(2)	24.6(3)	-	-	1.5(1)	<1	-	-	-	-	-	-	-	-	
C17	-	-	-	-	-	-	-	-	1.1(1)	-	-	1.26(8)	<1	21.7(3)	-	-	-	2.42(5)	0.9(1)	-	-	-	-	-	-	-	-	
C18	1.0(1)	1.07(7)	1.01(7)	-	2.33(5)	1.28(6)	<1	<1	1.39(1)	<1	0.5(3)	1.1(2)	-	1.39(6)	<1	1.5(1)	2.42(5)	-	1.32(4)	-	1.50(7)	-	-	-	-	3.60(6)	1.49(4)	
C19	<1	<1	<1	-	0.6(2)	<1	-	-	8.45(2)	<1	<1	0.536(2)	1.3(2)	1.6(1)	<1	<1	0.9(1)	1.32(4)	-	1.7(3)	-	1.4(1)	-	-	0.4(3)	0.65(5)	1.72(3)	
C20	-	-	-	-	7.1(1)	1.1(3)	-	-	-	6.9(2)	9.5(2)	-	-	-	-	-	-	-	1.7(3)	-	-	-	-	-	-	-	-	
C21	2.3(2)	3.14(7)	2.3(1)	-	9.90(7)	1.96(9)	-	-	-	3.8(2)	-	-	-	-	-	-	-	1.59(7)	-	-	-	-	-	-	-	-	-	
C22	-	-	-	-	-	-	-	-	3.70(7)	-	-	1.7(2)	7.3(1)	-	-	-	-	-	1.4(1)	-	-	-	-	-	-	-	0.70(7)	
C23	-	-	-	-	-	0.8(2)	-	-	0.7(1)	-	-	1.1(1)	3.5(1)	-	-	-	-	-	-	-	-	-	-	-	-	-	-	
C24	7.8(2)	4.6(1)	5.5(1)	-	-	3.4(1)	-	-	-	-	-	-	-	-	-	-	-	-	-	-	-	-	-	-	-	-	-	
C25	2.2(2)	4.1(2)	5.0(3)	-	-	5.6(2)	-	-	-	-	<1	-	-	-	-	-	-	-	-	-	-	-	-	-	-	-	-	
C26	-	<1	3.1(2)	-	-	4.89(9)	-	-	3.5(1)	-	-	-	-	-	-	-	-	-	0.4(3)	-	-	-	-	-	-	-	-	
C27	-	-	-	-	-	-	-	-	0.89(4)	-	-	-	-	6.3(2)	2.2(6)	-	-	3.60(6)	0.65(5)	-	-	-	-	-	-	-	-	
N	1.95(1)	2.25(5)	3.87(9)	-	-	6.69(4)	-	-	3.25(2)	0.56(3)	0.49(2)	-	1.2(1)	0.76(3)	-	-	-	1.49(4)	1.72(3)	-	-	0.70(7)	-	-	-	-	-	-

Table 6.2: All measured coupling frequencies in Hz for the $m_s = -1$ electron spin projection. To account for the cases where pulse errors cannot be neglected, the coupling frequencies are extracted by fitting the time-domain double resonance signals to $S = a + A \cdot e^{-(t/T_2)^n} \cos(2\pi f t + \phi) + B \cdot e^{-(t/T_2)^n}$, where T_2 is the coherence time and n, A and B are fit parameters that account for the signal decay shape, contrast and pulse errors. For the couplings marked as < 1 Hz in the tables, no oscillation was observed within the decay time. All couplings in the table are measured using $N = 1$ ($T_2 \sim 0.5$ s) except for C19 - C12 ($N = 256$) and C9 - C18 ($N = 32$).

REFERENCES

[1] See Supplemental Materials at https://www.nature.com/articles/s41586-019-1834-7, which contains experimental details and parameters, derivation of the electron-mediated couplings, and further description of the fitting methods. This part of the paper is not reproduced in this thesis due to length considerations. .

[2] G. S. Rule and T. K. Hitchens, *Fundamentals of protein NMR spectroscopy*, Vol. 5 (Springer Science & Business Media, 2006).

[3] H. Mamin *et al.*, *Nanoscale nuclear magnetic resonance with a nitrogen-vacancy spin sensor,* Science **339**, 557 (2013).

[4] T. Staudacher *et al.*, *Nuclear magnetic resonance spectroscopy on a (5-nanometer)^3 sample volume,* Science **339**, 561 (2013).

[5] F. Shi *et al.*, *Single-protein spin resonance spectroscopy under ambient conditions,* Science **347**, 1135 (2015).

[6] I. Lovchinsky *et al.*, *Nuclear magnetic resonance detection and spectroscopy of single proteins using quantum logic,* Science **351**, 836 (2016).

[7] N. Aslam *et al.*, *Nanoscale nuclear magnetic resonance with chemical resolution,* Science **357**, 67 (2017).

[8] D. R. Glenn *et al.*, *High-resolution magnetic resonance spectroscopy using a solid-state spin sensor,* Nature **555**, 351 (2018).

[9] J. Smits *et al.*, *Two-dimensional nuclear magnetic resonance spectroscopy with a microfluidic diamond quantum sensor,* Sci. Adv. **5**, eaaw7895 (2019).

[10] I. Lovchinsky *et al.*, *Magnetic resonance spectroscopy of an atomically thin material using a single-spin qubit,* Science **355**, 503 (2017).

[11] A. Ajoy, U. Bissbort, M. D. Lukin, R. L. Walsworth and P. Cappellaro, *Atomic-scale nuclear spin imaging using quantum-assisted sensors in diamond,* Phys. Rev. X **5**, 011001 (2015).

[12] M. Kost, J. Cai and M. B. Plenio, *Resolving single molecule structures with nitrogen-vacancy centers in diamond,* Sci. Rep. **5**, 11007 (2015).

[13] V. Perunicic, C. Hill, L. Hall and L. Hollenberg, *A quantum spin-probe molecular microscope,* Nat. Commun. **7**, 12667 (2016).

[14] Z.-Y. Wang, J. F. Haase, J. Casanova and M. B. Plenio, *Positioning nuclear spins in interacting clusters for quantum technologies and bioimaging,* Phys. Rev. B **93**, 174104 (2016).

[15] A. Sushkov *et al.*, *Magnetic resonance detection of individual proton spins using quantum reporters,* Phys. Rev. Lett. **113**, 197601 (2014).

[16] C. Müller *et al., Nuclear magnetic resonance spectroscopy with single spin sensitivity,* Nat. Commun. **5**, 4703 (2014).

[17] F. Shi *et al., Sensing and atomic-scale structure analysis of single nuclear-spin clusters in diamond,* Nat. Phys. **10**, 21 (2014).

[18] J. Zopes *et al., Three-dimensional localization spectroscopy of individual nuclear spins with sub-angstrom resolution,* Nat. Commun. **9**, 4678 (2018).

[19] J. Zopes, K. Herb, K. Cujia and C. Degen, *Three-dimensional nuclear spin positioning using coherent radio-frequency control,* Phys. Rev. Lett. **121**, 170801 (2018).

[20] K. Sasaki, K. M. Itoh and E. Abe, *Determination of the position of a single nuclear spin from free nuclear precessions detected by a solid-state quantum sensor,* Phys. Rev. B **98**, 121405 (2018).

[21] M. H. Abobeih *et al., One-second coherence for a single electron spin coupled to a multi-qubit nuclear-spin environment,* Nat. Commun. **9**, 1 (2018).

[22] X. Kong *et al., Artificial intelligence enhanced two-dimensional nanoscale nuclear magnetic resonance spectroscopy,* NPJ Quantum Inf. **6**, 1 (2020).

[23] E. L. Rosenfeld, L. M. Pham, M. D. Lukin and R. L. Walsworth, *Sensing coherent dynamics of electronic spin clusters in solids,* Phys. Rev. Lett. **120**, 243604 (2018).

[24] H. S. Knowles, D. M. Kara and M. Atatüre, *Demonstration of a coherent electronic spin cluster in diamond,* Phys. Rev. Lett. **117**, 100802 (2016).

[25] J. Cramer *et al., Repeated quantum error correction on a continuously encoded qubit by real-time feedback,* Nat. Commun. **7**, 1 (2016).

[26] M. Pfender *et al., High-resolution spectroscopy of single nuclear spins via sequential weak measurements,* Nat. Commun. **10**, 1 (2019).

[27] K. Cujia, J. M. Boss, K. Herb, J. Zopes and C. L. Degen, *Tracking the precession of single nuclear spins by weak measurements,* Nature **571**, 230 (2019).

[28] C. Slichter, *Principles of Magnetic Resonance* (Springer, 1996).

[29] C. E. Bradley *et al., A ten-qubit solid-state spin register with quantum memory up to one minute,* Phys. Rev. X **9**, 031045 (2019).

[30] A. Laraoui *et al., High-resolution correlation spectroscopy of* ^{13}C *spins near a nitrogen-vacancy centre in diamond,* Nat. Commun. **4**, 1651 (2013).

[31] M. Pfender *et al., Nonvolatile nuclear spin memory enables sensor-unlimited nanoscale spectroscopy of small spin clusters,* Nat. Commun. **8**, 834 (2017).

[32] P. C. Maurer *et al., Room-Temperature Quantum Bit Memory Exceeding One Second,* Science **336**, 1283 (2012).

[33] M. G. Dutt *et al.*, *Quantum register based on individual electronic and nuclear spin qubits in diamond,* Science **316**, 1312 (2007).

[34] A. P. Nizovtsev *et al.*, *Non-flipping 13c spins near an nv center in diamond: hyperfine and spatial characteristics by density functional theory simulation of the c510 [nv] h252 cluster,* New J. Phys. **20**, 023022 (2018).

[35] L. Robledo *et al.*, *High-fidelity projective read-out of a solid-state spin quantum register,* Nature **477**, 574 (2011).

[36] D. M. Toyli, C. F. de las Casas, D. J. Christle, V. V. Dobrovitski and D. D. Awschalom, *Fluorescence thermometry enhanced by the quantum coherence of single spins in diamond,* Proc. Natl. Acad. Sci. **110**, 8417 (2013).

[37] T. Taminiau *et al.*, *Detection and control of individual nuclear spins using a weakly coupled electron spin,* Phys. Rev. Lett. **109**, 137602 (2012).

[38] S. Kolkowitz, Q. P. Unterreithmeier, S. D. Bennett and M. D. Lukin, *Sensing distant nuclear spins with a single electron spin,* Phys. Rev. Lett. **109**, 137601 (2012).

[39] N. Zhao *et al.*, *Sensing single remote nuclear spins,* Nat. Nanotechnol. **7**, 657 (2012).

[40] J. M. Boss, K. Cujia, J. Zopes and C. L. Degen, *Quantum sensing with arbitrary frequency resolution,* Science **356**, 837 (2017).

[41] S. Schmitt *et al.*, *Submillihertz magnetic spectroscopy performed with a nanoscale quantum sensor,* Science **356**, 832 (2017).

[42] A. Laraoui, D. Pagliero and C. A. Meriles, *Imaging nuclear spins weakly coupled to a probe paramagnetic center,* Phys. Rev. B **91**, 205410 (2015).

[43] T. Gullion, D. B. Baker and M. S. Conradi, *New, compensated carr-purcell sequences,* J. Magn. Reson. **89**, 479 (1990).

[44] W. S. Warren, *Effects of arbitrary laser or nmr pulse shapes on population inversion and coherence,* J. Chem. Phys. **81**, 5437 (1984).

[45] N. Zhao, J.-L. Hu, S.-W. Ho, J. T. Wan and R. Liu, *Atomic-scale magnetometry of distant nuclear spin clusters via nitrogen-vacancy spin in diamond,* Nat. Nanotechnol. **6**, 242 (2011).

7

A MANY-BODY-LOCALIZED TIME CRYSTAL IN A SPIN-BASED QUANTUM SIMULATOR

J. Randall*, C. E. Bradley*, F. V. van der Gronden, A. Galicia, M. H. Abobeih, M. Markham, D. J. Twitchen, F Machado, N. Y. Yao, T. H. Taminiau

The discrete time crystal (DTC) is a recently discovered phase of matter that spontaneously breaks time-translation symmetry. Disorder-induced many-body-localization is required to stabilise a DTC to arbitrary times, yet an experimental investigation of this localized regime has proven elusive. Here, we observe the hallmark signatures of a many-body-localized DTC using a novel quantum simulation platform based on individually controllable ^{13}C nuclear spins in diamond. We demonstrate the characteristic long-lived spatiotemporal order and confirm that it is robust for generic initial states. Our results are consistent with the realisation of an out-of-equilibrium Floquet phase of matter and establish a programmable quantum simulator based on solid-state spins for exploring many-body physics.

The results of this chapter are undergoing peer review.
*Equally contributing authors.

7.1. INTRODUCTION

A time crystal spontaneously breaks time-translation symmetry[1]. While time crystals cannot exist for time-independent Hamiltonians[2], it is predicted that periodically driven 'Floquet' quantum many-body systems can break discrete time-translation symmetry[3–7]. Such a discrete time crystal (DTC) spontaneously locks onto a period that is a multiple of that of the drive and is stable against perturbations. It represents a novel phase of matter that only exists out of equilibrium and exhibits long-range spatial and temporal order. Stabilising the DTC phase to arbitrary times requires disorder-induced many-body-localization (MBL), which prevents heating from the periodic drive and induces a breakdown of ergodicity[3–9].

Pioneering experiments have revealed signatures of time-crystalline order in a range of systems including trapped ions[10,11], spin ensembles[12–15], ultracold atoms[16,17] and superconducting qubits[18]. However, none of these experiments satisfy the theoretical requirements for MBL under periodic driving[6,19]. The observed responses have instead been attributed to a variety of fascinating critical and prethermal mechanisms that lead to slow, but finite, thermalisation[6,7,11,19–22]. Experimentally investigating the DTC phase, stabilised by MBL, has remained an outstanding challenge[6,19].

Here, we present an observation of the hallmark signatures of the many-body-localized DTC phase. We develop a quantum simulator based on individually controllable and detectable ^{13}C nuclear spins in diamond, which can be used to realise a range of many-body Hamiltonians with tunable parameters and dimensionalities. We show that this simulator can be programmed to satisfy all requirements for a DTC, including stabilising MBL under periodic driving. We implement a periodic Floquet sequence in a one-dimensional (1D) chain of $L = 9$ spins, and observe the characteristic long-lived DTC response with twice the driving period. By combining the ability to prepare arbitrary initial states with site-resolved measurements, we confirm the DTC response for a variety of initial states up to $N = 800$ Floquet cycles. This robustness for generic initial states provides a key signature to distinguish the many-body-localized DTC phase from prethermal mechanisms, which only show a long-lived response for selected states[6,11,19].

7.2. A QUANTUM SIMULATOR BASED ON SINGLE ^{13}C SPINS

Our experiments are performed on a system of ^{13}C nuclear spins in diamond close to a nitrogen-vacancy (NV) centre at 4 K (Fig. 7.1A). The nuclear spins are well-isolated qubits with coherence times up to tens of seconds[25]. They are coupled via dipole-dipole interactions and are accessed through the optically addressable NV electronic spin[23,25]. With the electronic spin in the $m_s = -1$ state, the electron-nuclear hyperfine interaction induces a frequency shift h_j for each nuclear spin, which — combined with an applied magnetic field B_z in the z-direction — reduces the dipolar interactions to Ising form (Sec. 7.5.2). We additionally apply a radio-frequency (rf) driving field to implement nuclear-spin rotations. The nuclear-spin Hamiltonian is then given by $H = H_{\text{int}} + H_{\text{rf}}$, where H_{int}

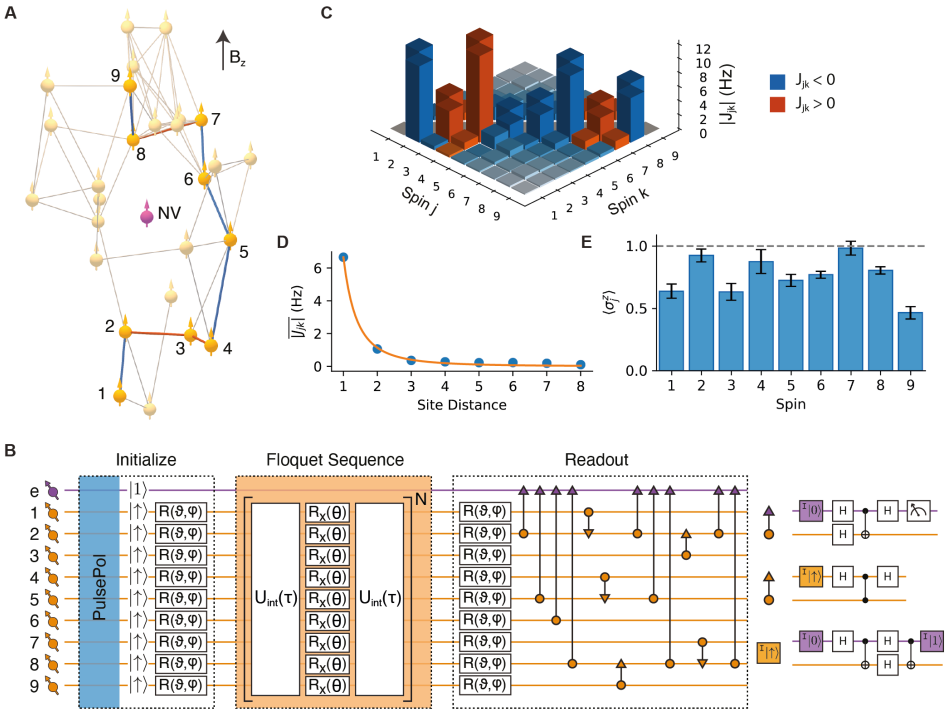

Figure 7.1: **Programmable spin-based quantum simulator.** (**A**) We program an effective 1D chain of 9 spins in an interacting cluster of 27 ^{13}C nuclear spins (orange) close to a single NV centre. Connections indicate nuclear-nuclear couplings $|J_{jk}| > 1.5\,\text{Hz}$, and blue (red) lines represent negative (positive) nearest-neighbor couplings within the chain[23]. Magnetic field: $B_z \sim 403\,\text{G}$. (**B**) Experimental sequence: The spins are initialised by applying the PulsePol sequence[24], followed by rotations of the form $R(\vartheta,\varphi) = \exp\left[-i\frac{\vartheta}{2}(\sin(\varphi)\sigma^x + \cos(\varphi)\sigma^y)\right]$. After evolution under the Floquet sequence $U_F = [U_{\text{int}}(\tau)\cdot U_x(\theta)\cdot U_{\text{int}}(\tau)]^N$, the spins are sequentially read out through the NV electronic spin using electron-nuclear and nuclear-nuclear two-qubit gates (see text). Colored boxes with 'I' denote re-initialisation into the given state. (**C**) Coupling matrix for the 9-spin chain. (**D**) Average coupling magnitude as a function of site distance across the chain. Orange line: least-squares fit to a power-law function $J_0/|j-k|^\alpha$, giving $J_0 = 6.7(1)\,\text{Hz}$ and $\alpha = 2.5(1)$. (**E**) Measured expectation values $\langle\sigma_j^z\rangle$ after initialising the state $|\uparrow\uparrow\uparrow\uparrow\uparrow\uparrow\uparrow\uparrow\uparrow\rangle$. The data is corrected for measurement errors (Sec. 7.5.5).

and H_{rf} describe the interaction and rf driving terms respectively:

$$\begin{aligned} H_{\text{int}} &= \sum_j (B + h_j)\sigma_j^z + \sum_{j<k} J_{jk}\sigma_j^z\sigma_k^z \\ H_{\text{rf}} &= \sum_j \Omega(t)\sigma_j^x. \end{aligned} \tag{7.1}$$

Here σ_j^β, $\beta = x, y, z$ are the Pauli matrices for spin j, $B = \gamma_c B_z/2$ is the magnetic field splitting, γ_c is the ^{13}C gyromagnetic ratio, J_{jk} is the zz component of the dipole-dipole interaction between spins j and k, $\Omega(t)$ is the applied time-dependent rf field and we set $\hbar = 1$. The system has previously been characterised in detail (Sec. 7.5.3)[23]; for 27 ^{13}C spins the hyperfine shifts h_j, the spatial coordinates, and the 351 interaction terms J_{jk} are known.

To investigate the DTC phase, we apply a periodic Floquet sequence consisting of free evolution $U_{\text{int}}(\tau) = \exp(-iH_{\text{int}}\tau)$, interleaved with global spin rotations $U_x(\theta) = \exp\left(-i\theta\sum_j^L \sigma_j^x/2\right)$. To realise the global rotations, we develop multi-frequency rf pulses that simultaneously rotate a chosen subset of spins (H_{rf} in Eq. 7.1) (see Sections 7.5.1 and 7.5.2). We symmetrise the Floquet sequence such that $U_F = [U_{\text{int}}(\tau)\cdot U_x(\theta)\cdot U_{\text{int}}(\tau)]^N$, where N is the number of Floquet cycles (Fig. 7.1B). For $\theta \sim \pi$, this decouples the targeted spins from their environment, while preserving the internal interactions (see Sections 7.5.3 and 7.5.7).

To stabilise MBL under periodic driving, the Hamiltonian must satisfy two requirements[5,6,19]. First, the spin-spin interactions J_{jk} must be sufficiently short-ranged. For power-law interactions that fall off as $1/r^\alpha$, it is believed that MBL requires $\alpha > 2d$, where d is the dimension of the system[† 19,27,28]. For dipole-dipole interactions, $\alpha = 3$. Because the nuclear spins are randomly positioned in $d = 3$ dimensions, the short-ranged requirement is not naturally met. To resolve this, we program an effective 1D spin chain using a subset of 9 spins (Figs. 7.1A,C, see Sec. 7.5.3). As a function of site distance across the chain, a fit to the averaged couplings falls of as $1/|j-k|^{2.5(1)}$ (Fig. 7.1D), confirming that the finite-sized chain maps onto an approximately 1D system whose interactions fall off sufficiently fast to be compatible with MBL. Second, since the periodic rotations in U_F approximately cancel the on-site disorder terms h_j, the system must exhibit Ising-even disorder to stabilise MBL in the Floquet setting[5,6,19]. This corresponds to disorder in the couplings J_{jk}, which is naturally satisfied here (Fig. 7.1C).

To reveal the signature spatiotemporal order of the DTC phase, one must prepare a variety of initial states and perform site-resolved measurements[19]. We use a combination of new and existing methods to realise the required initialisation, single-spin control, and individual single-shot measurement for all spins in the chain (Fig. 7.1B).

First, we initialise the spins through a recently introduced dynamical-nuclear-polarisation sequence called PulsePol[24]. This sequence polarises nuclear spins in the vicinity of the NV centre and prepares the 1D chain in the state $|\uparrow\uparrow\uparrow\uparrow\uparrow\uparrow\uparrow\uparrow\uparrow\rangle$. We analyze and optimise the polarisation transfer in Sec. 7.5.6. Subsequently, each spin can be independently rotated to an arbitrary state by selective rf pulses (Sec. 7.5.1).

[†] We note that avalanche instabilities can also destabilise MBL in power-law interacting systems, and understanding the role of such processes is an important outstanding question[26].

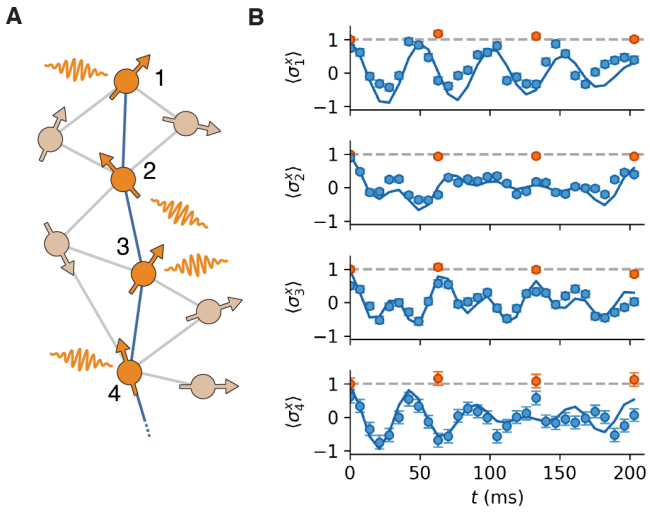

Figure 7.2: **Isolating spin chains.** (**A**) We test the programming of interacting spin chains for the first 4 spins of the 9-spin chain (Figs. 7.1A,C,D). For $\theta \sim \pi$, the Floquet sequence U_F decouples the spin chain from its environment, but preserves the internal interactions. (**B**) Measured expectation values $\langle\sigma_j^x\rangle$ after initialising the state $|{+}{+}{+}{+}\rangle$ and applying U_F with $\theta = \pi$. Here $t = 2\tau N$ is varied by fixing $\tau = 3.5$ ms and varying N. The blue (orange) points show the evolution with (without) spin-spin interactions (Sec. 7.5.2). Blue lines: numerical simulations of only the 4-spin system (Sec. 7.5.2). Measurements in this figure and hereafter are corrected for state preparation and measurement errors.

Second, after Floquet evolution, we read out the spins by sequentially mapping their $\langle\sigma_j^z\rangle$ expectation values to the NV electronic spin (Sec. 7.5.5), and measuring the electronic-spin state via resonant optical excitation[25]. Spins j=2,5,6,8 can be directly accessed using previously developed electron-nuclear two-qubit gates[25]. To access the other spins (j=1,3,4,7,9), which couple weakly to the NV, we develop a protocol based on nuclear-nuclear two-qubit gates through spin-echo double resonance (Sec. 7.5.5). We use these gates to map the spin states to other, directly accessible, spins in the chain. Fig. 7.1E shows the measured $\langle\sigma_j^z\rangle$ expectation values after preparing the state $|{\uparrow}{\uparrow}{\uparrow}{\uparrow}{\uparrow}{\uparrow}{\uparrow}{\uparrow}{\uparrow}\rangle$.

We verify that we can isolate the dynamics of a subset of spins by studying the first 4 spins of the 9-spin chain (Fig. 7.2A). We prepare the superposition state $|{+}{+}{+}{+}\rangle$, where $|+\rangle = (|\uparrow\rangle + |\downarrow\rangle)/\sqrt{2}$, and apply U_F with $\theta = \pi$. We first verify that the state is preserved when each spin is individually decoupled to remove interactions (Fig. 7.2B, see Sec. 7.5.3). In contrast, with internal interactions, the four spins entangle and undergo complex dynamics. The measured evolution matches a numerical simulation containing only the 4 spins, indicating that the system is strongly interacting and protected from external decoherence.

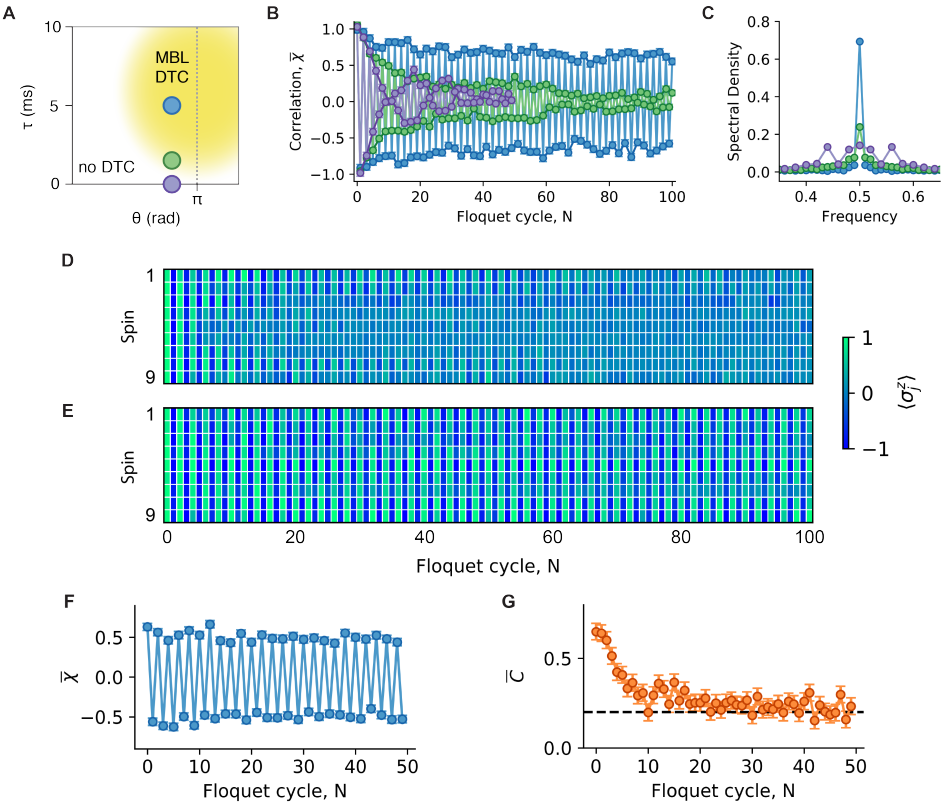

Figure 7.3: **Discrete time crystal in the 9-spin chain.** (**A**) Sketch of the phase diagram as a function of τ and θ when applying U_F (Fig. 7.1B) [6]. The yellow region indicates the many-body-localized DTC phase. The colored points mark three combinations of $\{\theta,\tau\}$ that illustrate the DTC phase transition. Additional data for other values are given in Sec. 7.5.4. (**B**) Averaged two-point correlation $\overline{\chi}$ as a function of the number of Floquet cycles N, for $\theta = 0.95\pi$ and initial state $|\uparrow\uparrow\uparrow\uparrow\uparrow\uparrow\uparrow\uparrow\uparrow\rangle$. Without interactions (purple), $\overline{\chi}$ decays quickly. With small interactions ($\tau = 1.55$ ms, green), the system is on the edge of the transition to the DTC phase. With strong interactions ($\tau = 5$ ms, blue), the subharmonic response is stable and persists over all 100 Floquet cycles. (**C**) The corresponding Fourier transforms show a sharp peak at $f = 0.5$ emerging as the system enters the DTC phase. (**D** and **E**) Individual spin expectation values $\langle\sigma^z\rangle$ for interaction times $\tau = 1.55$ ms (D) and $\tau = 5$ ms (E). (**F** and **G**) Averaged two-point correlation $\overline{\chi}$ (F) and coherence $\overline{C}$ (G) after preparing the superposition state $[\cos(\pi/8)|\uparrow\rangle + \sin(\pi/8)|\downarrow\rangle]^{\otimes 9}$ and applying U_F with $\tau = 5$ ms. The subharmonic response in $\overline{\chi}$ is preserved, while $\overline{C}$ quickly decays due to interaction-induced local dephasing. The dashed line in (G) indicates a reference value for $\overline{C}$ measured after preparing the state $|\uparrow\rangle^{\otimes 9}$ (Sec. 7.5.4).

7.3. EXPLORING THE DTC PHASE

With this capability confirmed, we turn to the 9-spin chain and the DTC phase. The expectation for the DTC phase is a long-lived period-doubled response that is stabilised against perturbations of U_F through many-body interactions. To illustrate this, we set $\theta = 0.95\pi$, a perturbation from the ideal value of π, and tune the system through the DTC phase transition by changing τ, which effectively sets the interaction strength (see Figs. 7.3A-C).

We first investigate the state $|\uparrow\uparrow\uparrow\uparrow\uparrow\uparrow\uparrow\uparrow\uparrow\rangle$ and consider the averaged two-point correlation function $\overline{\chi} = \frac{1}{L}\sum_{j=1}^{L}\langle\sigma_j^z(N)\rangle\langle\sigma_j^z(0)\rangle$, where $\langle\sigma_j^z(N)\rangle$ is the expectation value at Floquet cycle N for spin j. Without interactions, the deliberate under-rotations ($\theta < \pi$), in combination with naturally present noise in the applied control fields, lead to a rapid decay (Figs. 7.3B,C). By introducing moderate interactions ($\tau = 1.55$ ms), the system is on the edge of the phase transition, and the interactions begin to stabilise the subharmonic response (Figs. 7.3B,C,D). Finally, for strong interactions ($\tau = 5$ ms), the subharmonic response is stabilised despite the perturbations of θ (Figs. 7.3B,C,E). The individual spin measurements confirm that the spins are synchronised and the signature long-lived spatiotemporal response is observed (Fig. 7.3E).

To rule out trivial non-interacting explanations, we prepare the superposition state $[\cos(\pi/8)|\uparrow\rangle + \sin(\pi/8)|\downarrow\rangle]^{\otimes 9}$ and perform full single-qubit tomography for each spin for different values of N[3]. The two-point correlation $\overline{\chi}$, shows a persistent subharmonic response similar to the initial state $|\uparrow\uparrow\uparrow\uparrow\uparrow\uparrow\uparrow\uparrow\uparrow\rangle$ (Fig. 7.3F). In contrast, the coherence $\overline{C} = \frac{1}{L}\sum_{j=1}^{L}\sqrt{\langle\sigma_j^x\rangle^2 + \langle\sigma_j^y\rangle^2}$ shows a quick decay on a timescale of approximately 10 Floquet cycles, indicating rapid local dephasing due to internal many-body interactions that generate entanglement across the system (Fig. 7.3G).

While the results shown in Fig. 7.3 are consistent with a DTC, these measurements alone do not distinguish the many-body-localized DTC phase from prethermal responses[6,11,19]. In particular, the hallmark of the MBL DTC phase is robust spatiotemporal order for generic initial states. Conversely, prethermal responses only exhibit long-lived oscillations for a particular range of initial states[6,19].

We study a range of generic initial states of the form $\bigotimes_j^L |m_j\rangle$, $m_j \in \{\uparrow,\downarrow\}$, starting with the Néel state $|\uparrow\downarrow\uparrow\downarrow\uparrow\downarrow\uparrow\downarrow\uparrow\rangle$ (Fig. 7.4A). Like the polarised state, the Néel state shows a stable, period-doubled response (Figs. 7.4B,C). Fig. 7.4D shows the decay of the DTC response for the Néel state, the polarised state, and a further 9 randomly chosen initial states. To illustrate that a variety of states with different properties are considered, we evaluate their energy density $\mathscr{E} = \langle H_{\text{eff}}\rangle / J_0 L$ (Fig. 7.4E), where J_0 is the average nearest-neighbor coupling strength (Fig. 7.1D) and H_{eff} is the leading order term in the Floquet-Magnus expansion of U_F (Sec. 7.5.2). The selected initial states cover a range of energy densities. The response shows no significant dependence on the initial state up to $N = 800$, consistent with a DTC stabilised by MBL.

To highlight the importance of disorder, we perform a numerical investigation with and without disorder (Sec. 7.5.8). For the parameters of the disordered 9-spin chain without decoherence, we find a stable period-doubled response up to $N \sim 10^6$ for all initial states. For a hypothetical 9-spin chain without disorder, but with the same average couplings, there is no MBL and the time-crystalline response is state-dependent and

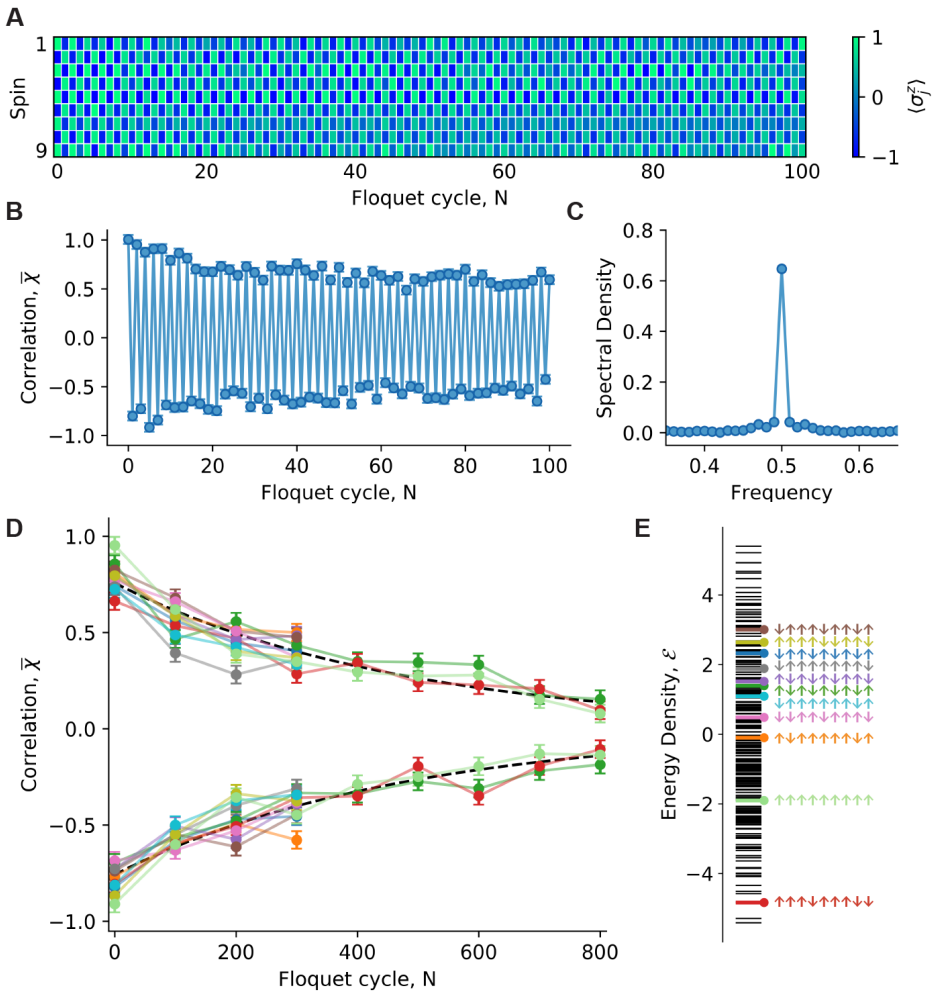

Figure 7.4: **Observation of the DTC response for generic initial states.** (**A**) Individual spin expectation values $\langle\sigma^z\rangle$ as a function of N after initialising the spins in the Néel state $|\uparrow\downarrow\uparrow\downarrow\uparrow\downarrow\uparrow\downarrow\uparrow\rangle$ and applying U_F for $\theta = 0.95\pi$ and $\tau = 5\,\text{ms}$. (**B**) Averaged two-point correlation function $\overline{\chi}$, corresponding to the data in (A). The DTC response persists to similar high N as for the polarised state (Fig. 7.3B). (**C**) Fourier transform of the data in (B), showing the period-doubled response. (**D**) Average correlation for even (upper curve) and odd (lower curve) N for 9 randomly chosen initial states, plus the polarised state and the Néel state (indicated in (E)) with $\theta = 0.95\pi$ and $\tau = 5\,\text{ms}$. Each data point is the average over even/odd integers in the range N to $N+10$. Three of the states are measured up to $N = 800$, the others to $N = 300$. The dashed black line is a fit of $|\overline{\chi}|$, averaged over the three states measured to $N = 800$, using a phenomenological function $f(N) = Ae^{-N/N_{1/e}}$, giving $A = 0.76(1)$ and $N_{1/e} = 472(17)$. (**E**) Calculated energy density $\mathscr{E}$ for all possible states of the form $\otimes_j^L \left|m_j\right\rangle$, $m_j \in \{\uparrow,\downarrow\}$ (black lines). The initial states measured in (D) are indicated by the corresponding colors.

fully decays within 300 Floquet cycles for some states. These simulations show that robust spatiotemporal order associated with the many-body-localized DTC phase can be distinguished from disorder-free prethermal responses within the experimentally accessible timescales.

While the DTC phase in an ideal isolated system is predicted to persist to arbitrary times, environmental decoherence inevitably causes decay in any experimental implementation. We observe a 1/e decay value of $N_{1/e} = 472(17)$ — corresponding to a time ~ 4.7 s — highlighting that our platform is highly isolated. However, understanding how the DTC response is affected by different decoherence mechanisms is an outstanding challenge. While the dominant decoherence mechanism for the spins is dephasing with a timescale on the order of seconds[25], the DTC phase is expected to be particularly robust to its effects[19]. This suggests that the observed decay arises from a more subtle interplay between the Floquet sequence and the environment, which might be suppressed using future optimised decoupling sequences. Crucially, the numerical calculations without decoherence show that the finite size of the spin chain does not limit the observed DTC response.

7.4. CONCLUSION

In conclusion, we present an observation of the hallmark signatures of the many-body-localized DTC phase. Unlike previous experiments, our quantum simulator operates in a regime consistent with MBL and the DTC response is observed to be stable for generic initial states. This result highlights the importance of both many-body interactions and disorder for stabilising time-crystalline order. The developed methods provide new opportunities to investigate Floquet phases of matter, including topologically protected phases[6], and time-crystalline order in a variety of settings complementary to MBL, such as open systems where the interplay between dissipation and interactions leads to distinct DTC phenomena[29–31].

From a broader perspective, this work introduces a programmable quantum simulator based on solid-state spins. By connecting different subsets of spins, larger one-dimensional chains and two- and three-dimensional systems can be realised. The combination of excellent coherence, individual control and site-selective measurement enables the programming of a wide variety of many-body Hamiltonians. Future scalability beyond tens of spins might be achieved by exploiting spins external to the diamond[32,33], by linking multiple electronic-spin defects through dipolar coupling[34], by photonic remote entanglement[35], or by combinations of these methods.

7.5. SUPPLEMENTARY MATERIALS

7.5.1. EXPERIMENTAL SETUP

SAMPLE AND NV CENTRE

The experiments are performed on a naturally occurring NV centre using a home-built confocal microscope based on a 3.7 K cryostat (Montana Cryostation). The diamond was homoepitaxially grown using chemical vapor deposition and cleaved along the ⟨111⟩ axis (Element Six). There is a natural abundance (1.1%) of ^{13}C. The NV centre was selected on

the absence of strongly coupled ^{13}C spins (> 500 kHz hyperfine coupling), but without any other criteria on the spin environment. An external magnetic field of $B_z = 403.553$ G is applied along the NV-axis (the z-axis) using a permanent neodymium magnet, which is temperature stabilised using a feedback loop[25]. The field is aligned to within 0.1 degrees using a thermal echo sequence[23]. The NV electron spin has a dephasing time of $T_2^* = 4.9(2)\,\mu$s and a spin echo time of $T_2 = 1.182(5)$ ms, which can be extended to $T_2^{\mathrm{DD}} > 1$ s using dynamical decoupling[36]. The electron relaxation ($T_1 > 1$ h) at this temperature is negligible[36]. We measure the NV electron spin state in a single shot using spin-selective optical readout[37]. The readout fidelities are 0.905(2) (0.986(2)) for the $m_s = 0$ ($m_s = -1$) state with an average fidelity of $F = 0.946(1)$. All measurements are corrected for readout in order to provide a best estimate for the actual state.

MICROWAVE PULSES

We apply microwave pulses to drive the NV electron spin transition $m_s = 0 \leftrightarrow m_s = -1$ at 1.746666(3) GHz using single-sideband modulation. IQ signals are generated at 250 MHz using an AWG (Tektronix 5014C) and upconverted using a vector RF source (Rohde & Schwarz SGS100A). The output of this source is then amplified (AR 25S1G6). Microwave amplifier noise is suppressed by 40 dB using a fast microwave switch (TriQuint TGS2355-SM). Video leakage noise generated by the switch is filtered with a high pass filter. For the PulsePol sequence used for initialisation of the simulator (Sec. 7.5.6), square pulse envelopes are used with duration 30 ns (15 ns) for a π ($\pi/2$) pulse. During dynamical decoupling gates for nuclear-spin readout (Sec. 7.5.5), Hermite pulse envelopes[38,39] are used to obtain high-fidelity rotations of the electron spin independent of the ^{14}N nuclear spin state, with peak Rabi frequencies of 35 MHz (23 MHz) for a π ($\pi/2$) pulse. Pulse errors during dynamical decoupling are mitigated using the XY8 scheme[40].

RADIO-FREQUENCY PULSES

We apply radio-frequency (RF) pulses in the frequency range 400 − 500 kHz (see Table 7.1) to directly and selectively drive the ^{13}C spins. To prepare initial states of the form $|m_j\rangle^{\otimes N}$, $m_j \in \{\uparrow, \downarrow\}$, and for the rotations used in the nuclear-nuclear readout method (Sec. 7.5.5), we use single-frequency pulses with an error-function envelope[25]. For the x-rotations in the Floquet sequence, and the global basis rotations used to initialise the states $|{+}{+}{+}{+}\rangle$ (Fig. 7.2B) and $[\cos(\pi/8)|\uparrow\rangle + \sin(\pi/8)|\downarrow\rangle]^{\otimes L}$ (Figs. 7.3F,G), and to read out $\langle\sigma_j^x\rangle$ / $\langle\sigma_j^y\rangle$, we use multi-frequency pulses. This allows us to rotate all 9 spins in the 1D chain simultaneously and independently of other spins in the environment, which is crucial for realising the Floquet sequence in these experiments. To reduce crosstalk between spins, we use a $\sin^2$ pulse envelope for the multi-frequency pulses. The waveform for a pulse containing L frequency components is therefore given by

$$V(t) = \sin^2\left(\frac{\pi t}{t_p}\right)\sum_j^L V_j \cos\left(2\pi f_j (t - \frac{t_p}{2}) + \phi_j\right), \tag{7.2}$$

where t_p is the pulse length, V_j, f_j and ϕ_j are the amplitude, frequency and phase of frequency component j, respectively, and t runs from 0 to t_p.

In order to generate the multi-frequency pulses with sufficient power, we amplify the signal from an AWG (Tektronix 5014C) using an RF amplifier (Analog Devices ADA4870,

gain +12 dB), and apply filtering to reduce additional noise on the signal (3rd-order Butterworth high-pass filter, 52 kHz, and 7th-order linear-phase low-pass filter, 850 kHz, both home-built). Additionally, we stagger the phases ϕ_j of each pulse to ensure that the frequency components do not constructively interfere at the centre of the $\sin^2$ pulse envelope.

Applying multiple frequency components to the nuclear spins simultaneously can cause AC Stark shifts if two spins are close in frequency. To minimise coherent pulse errors from such shifts, we iteratively calibrate the pulse parameters for each spin (frequency and amplitude). The resulting calibrated frequency components for each spin are given in Table 7.1.

7.5.2. DERIVATION OF H AND U_F

INTERACTION HAMILTONIAN

The Hamiltonian of the ground-state NV electron spin coupled to a bath of interacting ^{13}C nuclear spins is given by

$$H = \Delta_{\mathrm{ZFS}}(S^z)^2 + \gamma_e B_z S^z + \sum_j \gamma_c \vec{B}\cdot\vec{I}_j + \sum_j \vec{S}\cdot\mathbf{A}_j\cdot\vec{I}_j + \sum_{j<k}\vec{I}_j\cdot\mathbf{C}_{jk}\cdot\vec{I}_k, \tag{7.3}$$

where Δ_{ZFS} is the zero-field splitting, γ_e (γ_c) is the electron (^{13}C nuclear) gyromagnetic ratio, B_z is the externally applied global magnetic field along the z-axis, $\mathbf{A}_j$ is the electron-^{13}C hyperfine tensor for nuclear spin j and $\mathbf{C}_{jk}$ is the ^{13}C-^{13}C dipole-dipole coupling tensor between nuclear spins j and k. Here $\vec{S} = (S^x, S^y, S^z)$ and $\vec{I}_j = (I_j^x, I_j^y, I_j^z)$ are the spin vectors for the electron and nuclear spins, respectively, where S^α are the spin-1 matrices representing the electron spin ground state levels $m_s = \{0, \pm 1\}$ and $I_j^\alpha = \sigma_j^\alpha/2$, where σ_j^α are the Pauli spin matrices. In the experiments described throughout the text, the electron spin is prepared in the $m_s = -1$ eigenstate for the duration of the quantum simulation part of the sequence (U_F in Fig. 7.1B). We therefore only need to consider the nuclear spin Hamiltonian for the $m_s = -1$ state, given by

$$H_{-1} = \sum_j \left[(\gamma_c B_z - A_j^\parallel) I_j^z - A_j^\perp(\cos\left(\varphi_j^\perp\right) I_j^x + \sin\left(\varphi_j^\perp\right) I_j^y)\right] + \sum_{j<k}\vec{I}_j\cdot\mathbf{C}_{jk}\cdot\vec{I}_k, \tag{7.4}$$

where $A_j^\parallel = A_j^{zz}$ is the parallel hyperfine component, $A_j^\perp = \sqrt{(A_j^{zx})^2 + (A_j^{zy})^2}$ is the perpendicular hyperfine magnitude and $\varphi_j^\perp$ is the perpendicular hyperfine azimuthal angle. Other hyperfine interaction terms have been neglected in the secular approximation. This Hamiltonian is used for the numerical simulations presented in Fig. 7.2. The hyperfine and nuclear-nuclear interactions for the 9 spins are given in Tables 7.1 and 7.2, while the azimuthal angles $\varphi_\perp^j$ are approximated from the known spatial angles relative to the position of the vacancy lattice site[†] (Table 7.1).

In our experiments we apply a strong magnetic field of $B_z \sim 403$ G. In this case, we can further simplify H_{-1} by using the fact that $(\gamma_c B_z - A_j^\parallel) \gg A_j^\perp$ and $|A_j^\parallel - A_k^\parallel| \gg C_{jk}^{zz}$ for

[†]Note that these angles are only equal under the approximation that the electron is a point dipole located at the vacancy, and therefore the actual hyperfine azimuthal angles may differ due to the finite size and shape of the electron wavefunction.

all j,k. This allows us to neglect non-secular terms and therefore obtain the interaction Hamiltonian H_{int} presented in Eq. 7.1, given by

$$H_{-1} \approx H_{\text{int}} = \sum_j (B + h_j)\sigma_j^z + \sum_{j<k} J_{jk}\sigma_j^z\sigma_k^z, \tag{7.5}$$

where $B + h_j = \frac{1}{2}\sqrt{(\gamma_c B_z - A_j^{\parallel})^2 + (A_j^{\perp})^2}$ and $J_{jk} = C_{jk}^{zz}/4$. For $B + h_j$ we have here included the contribution from $A_j^{\perp}$ to the precession frequency[41]. This Hamiltonian is used for the numerical simulations presented in Sections 7.5.7 and 7.5.8.

SPIN ROTATIONS

As described in Sec. 7.5.1, the spin rotations in the Floquet sequence are implemented using multi-frequency rf pulses. With a general time-dependent voltage $V(t)$, the nuclear-spin Hamiltonian has an additional term

$$H_{\text{rf}}(t) = \sum_j \Omega(t)\sigma_j^x, \tag{7.6}$$

where $\Omega(t) = \gamma_c \beta V(t)$ with β being a conversion factor from applied voltage to magnetic field at the NV centre. We assume that the field is polarised in the x-direction*. Together with Eq. 7.5, this term gives Eq. 7.1, $H(t) = H_{\text{int}} + H_{\text{rf}}(t)$.

We apply multi-frequency pulses of the form given in Eq. 7.2. For the simulations presented in Fig. 7.2, the unitary evolution during the pulses is calculated by numerically integrating the time-dependent Hamiltonian $H_{-1} + H_{\text{rf}}(t)$, with $V(t)$ given by Eq. 7.2, using the QuTiP Python package[42]. To arrive at the Floquet operator U_F, we can simplify $H(t)$ under the approximation that the spin-spin interactions can be neglected during the pulse, which is valid in the regime $\Omega_j \gg J_{jk}$, where $\Omega_j = \gamma_c \beta V_j$. In this case, after transforming to the interaction picture with respect to $H_0 = \sum_j (B + h_j)\sigma_j^z$ and setting each frequency component in $V(t)$ (Eq. 7.2) equal to one of the spin precession frequencies ($2\pi f_j = 2(B + h_j)$), the Hamiltonian becomes

$$\begin{aligned} H'(t) &= e^{iH_0 t} H(t) e^{-iH_0 t} - H_0 \\ &= \sin^2\left(\frac{\pi t}{t_p}\right) \sum_j^L \frac{\Omega_j}{2} \left(\cos\left(\phi_j'\right)\sigma_j^x + \sin\left(\phi_j'\right)\sigma_j^y\right), \end{aligned} \tag{7.7}$$

where $\phi_j' = \phi_j - (B + h_j)t_p$ and we have neglected off-resonant terms. Since $[H'(t_1), H'(t_2)] = 0$, we can use the fact that

$$\int_0^{t_p} \sin^2\left(\frac{\pi t}{t_p}\right) dt = \frac{t_p}{2}, \tag{7.8}$$

*In reality the polarisation is not known, however field components in the z-direction will cancel in the rotating wave approximation as long as they oscillate sufficiently fast, and therefore the only effect would be a reduction in the experimentally determined parameter β for all spins. Field components in the y-direction will add a global phase shift, which can be neglected without loss of generality for the experiments described in this work.

to calculate the unitary operator at $t = t_p$ in the rotating frame, given by

$$\begin{aligned} U'(t_p) &= \exp\left(-i\int_0^{t_p} H'(t)\,dt\right) \\ &= \exp\left(i\frac{t_p}{2}H_0\right)\cdot\exp\left(-i\frac{t_p}{2}\sum_j^L \frac{\Omega_j}{2}\left(\cos(\phi_j)\sigma_j^x + \sin(\phi_j)\sigma_j^y\right)\right)\cdot\exp\left(-i\frac{t_p}{2}H_0\right), \end{aligned} \tag{7.9}$$

where in the second line we have used the identity

$$e^{-i\theta(\cos(\phi_0+\phi_1)\sigma^x+\sin(\phi_0+\phi_1)\sigma^y)} = e^{-i\phi_1\sigma^z/2}e^{-i\theta(\cos(\phi_0)\sigma^x+\sin(\phi_0)\sigma^y)}e^{i\phi_1\sigma^z/2}. \tag{7.10}$$

Finally, we can revert to the lab frame, giving

$$\begin{aligned} U(t_p) &= e^{-iH_0t_p}U'(t_p) \\ &= \exp\left(-i\frac{t_p}{2}H_0\right)\cdot\exp\left(-i\sum_j^L \frac{\theta_j}{2}\left(\cos(\phi_j)\sigma_j^x + \sin(\phi_j)\sigma_j^y\right)\right)\cdot\exp\left(-i\frac{t_p}{2}H_0\right). \end{aligned} \tag{7.11}$$

The effect of the multi-frequency pulse under these approximations is therefore equivalent to instantaneous rotations of each spin by an angle $\theta_j = \Omega_j t_p/2$ around an axis at angle ϕ_j in the $x-y$ plane, between two periods of free precession under the Hamiltonian H_0 for time $t_p/2$.

For short pulse times and setting $\phi_j = 0$ and $\theta_j = \theta$, we can approximate that $U(t_p) \approx U_x(\theta) = \exp\left(-i\theta\sum_j^L \sigma_j^x/2\right)$. Combining with $U_{\rm int}(\tau) = \exp(-iH_{\rm int}\tau)$, we therefore arrive at the ideal Floquet sequence $U_F = [U_{\rm int}(\tau)\cdot U_x(\theta)\cdot U_{\rm int}(\tau)]^N$.

EFFECTIVE HAMILTONIAN

For $\theta = \pi - \epsilon$, the Floquet sequence unitary operator over two periods is given by

$$\begin{aligned} e^{-i2\tau H_{\rm eff}} = U_F^2 &= U_{\rm int}(\tau)\cdot U_x(\pi-\epsilon)\cdot U_{\rm int}(2\tau)\cdot U_x(\pi-\epsilon)\cdot U_{\rm int}(\tau) \\ &= U_0(\tau)\cdot U_{zz}(\tau)\cdot U_x(-\epsilon)\cdot X\cdot U_0(2\tau)\cdot U_{zz}(2\tau)\cdot X\cdot U_x(-\epsilon)\cdot U_0(\tau)\cdot U_{zz}(\tau) \\ &= U_0(\tau)\cdot U_{zz}(\tau)\cdot U_x(-\epsilon)\cdot U_0(-2\tau)\cdot U_{zz}(2\tau)\cdot U_x(-\epsilon)\cdot U_0(\tau)\cdot U_{zz}(\tau), \end{aligned} \tag{7.12}$$

where $X = (\sigma_j^x)^{\otimes L}$ is a global x-rotation of the spins and we have split $U_{\rm int}(\tau)$ into single-spin terms $U_0(\tau) = \exp\left(-i\tau\sum_j(B+h_j)\sigma_j^z\right)$ and pairwise interactions $U_{zz}(\tau) = \exp\left(-i\tau\sum_{j<k}J_{jk}\sigma_j^z\sigma_k^z\right)$. To leading order in ϵ (valid for $\epsilon \ll \pi$), the effective Hamiltonian is given by the time-average of the exponents in Eq. 7.12[6,21], given by

$$\begin{aligned} H_{\rm eff} &\approx \frac{1}{4\tau}\left[4\tau\sum_{j<k}J_{jk}\sigma_j^z\sigma_k^z - \epsilon\sum_j\sigma_j^x\right] \\ &= \sum_{j<k}J_{jk}\sigma_j^z\sigma_k^z - \frac{\epsilon}{4\tau}\sum_j\sigma_j^x. \end{aligned} \tag{7.13}$$

This effective Hamiltonian is used to calculate the energy density $\mathscr{E} = \langle H_{\rm eff}\rangle/J_0L$ for different initial product states in the diagram in Fig. 7.4E. The wide range of energy densities serves to illustrate the variety of initial states considered, despite $H_{\rm eff}$ not being a conserved quantity of the dynamics.

Spin	$A_\parallel$ (kHz)	$A_\perp$ (kHz)	$f_{-1,j}$ (Hz)
1	-5.62(1)	5(2)	437665(12)
2	-19.815(3)	5.3(5)	451816(5)
3	-13.961(3)	9(1)	445960(6)
4	-4.66(3)	7(4)	436606(8)
5	17.643(1)	8.6(2)	414367(3)
6	-11.346(2)	59.21(3)	447450(11)
7	-14.07(2)	13(1)	446627(7)
8	-48.58(2)	9(2)	480667(7)
9	-9.79(2)	5(4)	441763(17)

Table 7.1: Measured parameters for the 9 ^{13}C nuclear spins used in this work. $A_\parallel$ ($A_\perp$): Parallel (perpendicular) hyperfine couplings. $f_{-1,j}$: Calibrated frequency components for each spin for the 9-frequency pulse (Eq. 7.2).

U_F WITHOUT INTERACTIONS

In Figs. 7.2B and 7.3B,C, we apply the Floquet sequence with the interactions turned off. This is achieved by individually applying the sequence to each spin in turn. For $\theta \sim \pi$, this decouples each targeted spin from the others and is therefore equivalent to evolving under U_F with $J_{jk} = 0$ for all j, k.

7.5.3. PROGRAMMING THE 1D CHAIN

IDENTIFYING THE CHAIN

As discussed in Sec. 7.2, many-body-localization (MBL) is only stabilised if the spin-spin interactions J_{jk} are sufficiently short-ranged. We have a system of nuclear spins randomly positioned in 3 dimensional space, that interact through dipolar interactions which exhibit a power-law scaling $1/r^3$. This power-law exponent, $\alpha = 3$, is thus equal to the system dimensionality, $d = 3$, whereas MBL is compatible with $\alpha > 2d$ [19,28].

To resolve this challenge, we use a decoupling sequence to isolate a subset of spins which have a smaller effective dimensionality. In previous work, we characterised 27 individual ^{13}C spins surrounding this NV centre [23]: their coupling matrix of 351 mutual interaction strengths are known. In principle, complex decoupling sequences can be used to realise any type of effective coupling matrix. Here, we consider a sequence that decouples 9 spins from the other spins, and look for a combination of spins that naturally forms an effective 1D chain. We thus perform a numerical search for a suitable effective 1D system (a spin chain) using those known parameters.

Starting from each of the 27 spins, we consider links to any other spin in the system, and accept all cases where the nearest-neighbor coupling exceeds $|J_{jk}| = 2.5$ Hz. We then try to add a third spin, which must again exhibit a nearest-neighbor coupling > 2.5 Hz to either end of the chain, but additionally must not have any non-nearest-neighbor coupling > 2 Hz. We iteratively add further spins which satisfy these requirements to identify a suitable spin chain. For the 9-spin chain we selected, we fit an average power-law exponent of $\alpha = 2.5(1)$ (Fig. 7.1D).

Spin	x (nm)	y (nm)	z (nm)
1	0.000	0.000	0.000
2	-0.126	-0.073	0.669
3	-0.504	0.582	0.669
4	-0.378	1.092	0.618
5	-0.631	1.092	1.699
6	-0.631	0.655	2.317
7	-0.757	0.437	2.934
8	-0.126	0.073	2.729
9	0.126	0.364	3.295

	1	2	3	4	5	6	7	8	9
1	-	-10.8(2)	-0.52	0.28	-0.19	-0.20	-0.12	-0.19	-0.10
2	-10.8(2)	-	4.44(4)	1.0(1)	-0.08	-0.39	-0.23	-0.4(1)	-0.19
3	-0.52	4.44(4)	-	12.3(2)	-1.8(2)	-0.95(5)	-0.31	-0.33	-0.17
4	0.28	1.0(1)	12.3(2)	-	-2.5(5)	-0.60	-0.22	-0.20	-0.14
5	-0.19	-0.08	-1.8(2)	-2.5(5)	-	-3.88(2)	-0.90	-0.18	-0.30
6	-0.20	-0.39	-0.95(5)	-0.60	-3.88(2)	-	-9.48(5)	1.2(4)	-0.4(1)
7	-0.12	-0.23	-0.31	-0.22	-0.90	-9.48(5)	-	3.5(5)	1.25
8	-0.19	-0.4(1)	-0.33	-0.20	-0.18	1.2(4)	3.5(5)	-	-6.32(2)
9	-0.10	-0.19	-0.17	-0.14	-0.30	-0.4(1)	1.25	-6.32(2)	-

Table 7.2: Coordinates (left, relative to Spin 1) and spin-spin interactions J_{jk} (right, in Hz) for the 9 spins, taken from Abobeih et al.[23]. Interactions given with uncertainties were directly measured for the electron state $m_s = -1$, while values without uncertainties are calculated from the coordinates using Eq. 7.14.

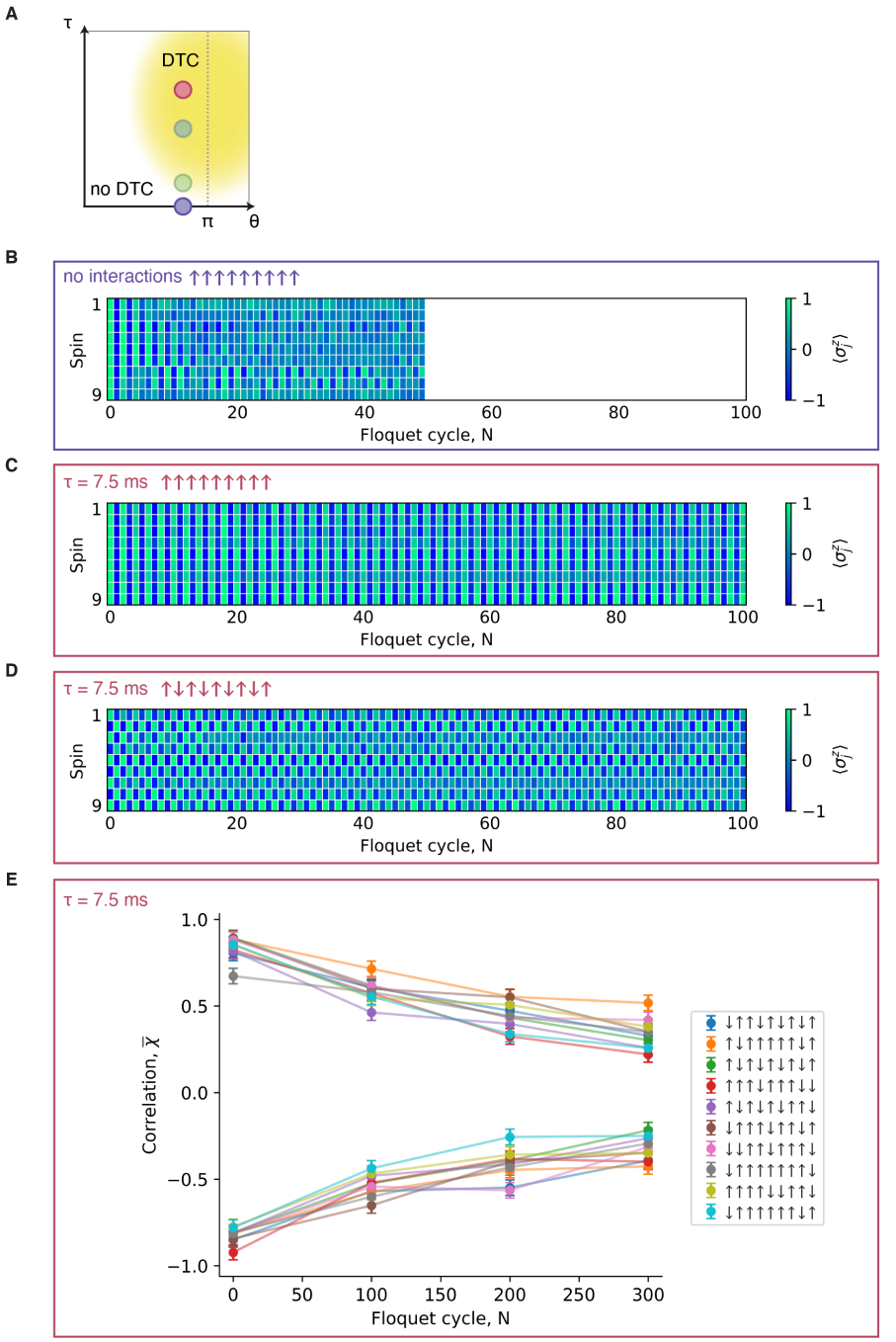

Figure 7.5: **Additional DTC data.** Additional data showing individual spin magnetisations for different parameters $\{\tau, \theta\}$. (**A**) Phase diagram as shown in Fig. 7.3A, with an additional point shown (red, $\tau = 7.5$ ms). (**B**) Individual spin results underlying the averaged plot shown in Figs. 7.3B, C for the case of no interactions (Sec. 7.5.2). (**C-E**) Additional datasets for $\tau = 7.5$ ms (red point in (A)) for an initial polarised state (C), Néel state (D) and 10 of the initial states measured in Fig. 7.4D (E).

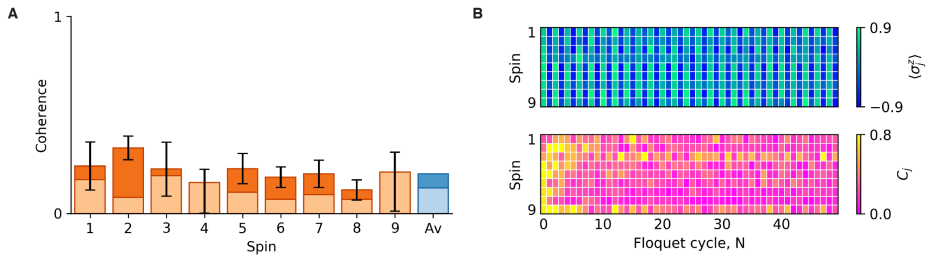

Figure 7.6: **Individual spin data for Figs. 3F,G** (**A**) Measured coherence for each spin after preparing the state $|\uparrow\uparrow\uparrow\uparrow\uparrow\uparrow\uparrow\uparrow\uparrow\uparrow\rangle$ (dark colored bars). The light shaded bars indicate the contribution from shot noise in the underlying measurements of $\langle\sigma_j^x\rangle$ and $\langle\sigma_j^y\rangle$. The residual measured coherence is likely due to pulse errors in the $\pi/2$ basis rotations. The blue bar shows the average of the orange bars over all spins. The dark blue bar is used to indicate a baseline in Fig. 7.3G. (**B**) Individual spin magnetisations (top) and coherences (bottom) after preparing the superposition state $[\cos(\pi/8)|\uparrow\rangle + \sin(\pi/8)|\downarrow\rangle]^{\otimes 9}$.

1D CHAIN SPIN PARAMETERS

Table 7.1 gives the parameters for the 9 ^{13}C spins used in this work. The first two columns give the electron-nuclear hyperfine couplings $A_\parallel$ and $A_\perp$ (Abobeih et al.[23]), which are extracted from the measured precession frequencies for different NV electron m_s states. The final column gives the calibrated frequency components used for the 9-frequency pulse (Eq. 7.2), which includes small frequency shifts due to couplings to other polarised spins and Stark shifts from off-resonant frequency components.

Table 7.2 gives the coordinates and spin-spin interactions J_{jk} for the 9 spins (Abobeih et al.[23]). Interactions with uncertainties given in parentheses are measured values for the NV electron state $m_s = -1$. Interactions shown without uncertainties were not directly measured, but can be calculated from the known spin coordinates[23] using the dipole-dipole formula, given by[43]

$$J_{jk} = \frac{C_{jk}^{zz}}{4} = \frac{C_0}{4\Delta r_{jk}^3}\left(1 - \frac{3(z_j - z_k)^2}{\Delta r_{jk}^2}\right), \tag{7.14}$$

where $\Delta r_{jk} = \sqrt{(x_j - x_k)^2 + (y_j - y_k)^2 + (z_j - z_k)^2}$, $C_0 = \mu_0 \gamma_c^2 \hbar / 4\pi$, μ_0 is the permeability of free space, and $\hbar$ is the reduced Planck constant.

7.5.4. ADDITIONAL DATA

Fig. 7.5 shows individual spin magnetisation data underlying Figs. 7.3B,C, as well as additional datasets for $\tau = 7.5$ ms. Fig. 7.6 shows the underlying data for Figs. 7.3F,G.

7.5.5. READOUT OF THE FULL NUCLEAR-SPIN CHAIN

One of the key requirements for the experiments presented in this work is the ability to read out all individual spins within an interacting system. We develop a readout scheme in which some of the nuclear spins are directly read out through the NV electron spin,

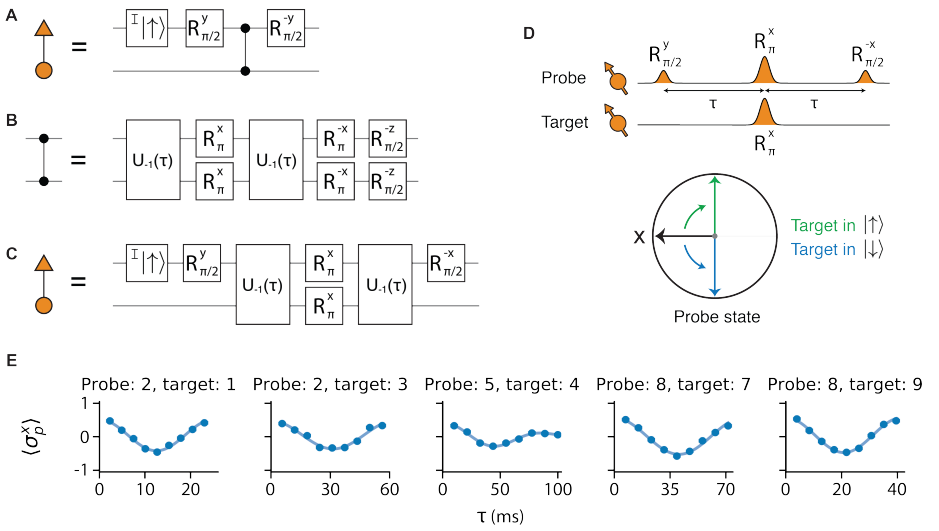

Figure 7.7: **Nuclear-nuclear readout.** (**A**) Quantum circuit for readout via nuclear-nuclear two-qubit gates. R_θ^β denotes a rotation by an angle θ around an axis $\beta = x, y, z$. (**B**) Compilation of the ideal controlled-phase gate using the native nuclear-nuclear interactions. $U_{-1}(\tau)$ denotes free evolution for a period, $\tau_{\mathrm{RO}} = \pi/8J_{tp}$, during which time the electron is in the $m_s = -1$ state. (**C**) Compilation of (A) using the native interactions. (**D**) Evolution of the probe spin at the optimal read-out point ($\tau_{RO} = \pi/8J_{tp}$). Orthogonal states of the target spin are mapped into orthogonal states of the probe spin. (**E**) Characterisation curves for all probe-target spin combinations used in this work. The solid lines are a fit to Eq. 7.25, with resulting fit parameters given in Table 7.3.

while other, not directly accessible, nuclear spins are first mapped to other nuclear spins that are accessible.

In previous work utilising ^{13}C spins in diamond[25,41], single-spin readout was achieved via dynamical decoupling sequences utilising individual electron-nuclear hyperfine interactions. However, these approaches require that the interactions are simultaneously strong (enabling fast, high fidelity gates), and spectrally heterogeneous (avoiding unwanted entanglement with non-targeted spins). This requirement is not generically met when considering larger nuclear spin systems, where some spins are only weakly coupled to the NV centre. To overcome this challenge, we developed a new technique to read out nuclear spins that are more weakly coupled to the NV centre electron spin, leveraging our knowledge of the spatial environment of the spin system and of the nuclear-nuclear couplings[23]. In particular, we isolate individual nuclear-nuclear interactions which can be used to map the state of a weaker coupled 'target' nuclear spin to a stronger coupled 'probe' nuclear spin. The stronger hyperfine interaction between the probe spin and the NV centre then enables readout using previously established techniques[25].

NUCLEAR-NUCLEAR READOUT

The desired quantum circuit to map the state from one nuclear spin to another is shown in Fig. 7.1B. Both the Hadamard and controlled-phase gates are not native to our system and must be compiled from native operations. Fig. 7.7A shows the compilation of the circuit replacing the Hadamard gates by native single qubit rotations. In Fig. 7.7B we show the compilation of the controlled-phase gate. The central feature is the 'interaction' block, where we interleave two periods of free evolution with concurrent spin-echo pulses applied to the target and probe spins (spin-echo double-resonance, SEDOR), with the electron spin in the state $m_s = -1$. These echo pulses serve to decouple the target and probe from all other spins while preserving their mutual interaction[23]. Under this condition, we can neglect the presence of other nuclear spins. From Eq. 7.5, we have

$$H_{-1} \approx H_{\text{int}} = (B + h_t)\sigma_t^z + (B + h_p)\sigma_p^z + J_{tp}\sigma_t^z\sigma_p^z, \tag{7.15}$$

with the parameters defined after Eq. 7.5. The subscripts t and p denote the target and probe spins, respectively. The unitary evolution during the interaction block is given by

$$U_{\text{SEDOR}}(\tau) = U_{\text{int}}(\tau) \cdot R_p^x(\pi) \cdot R_t^x(\pi) \cdot U_{\text{int}}(\tau). \tag{7.16}$$

Here, $U_{\text{int}}(\tau) = \exp(-iH_{\text{int}}\tau)$ and $R_j^{\phi}(\theta) = e^{-i\theta(\cos(\phi)\sigma_j^x + \sin(\phi)\sigma_j^y)/2}$ is a rotation of spin j by an angle θ around an axis ϕ. In the case that $\tau = \tau_{\text{RO}} \equiv \pi/(8J_{tp})$, this block realises a maximally-entangling operation.

In Fig. 7.7C we show the compiled readout circuit as implemented in the experiment. Note that this sequence incurs an additional π-rotation to the target spin which we do not rectify, as the state is discarded after the measurement. The unitary evolution describing the full sequence is given by

$$U_{\text{RO}} = R_p^x(-\pi/2) \cdot U_{\text{SEDOR}}(\tau_{\text{RO}}) \cdot R_p^y(\pi/2). \tag{7.17}$$

We first initialise the probe spin in the state $|\uparrow\rangle$, while the target spin is in an unknown state which is to be read out in the σ^z-basis. The initial state of the system is therefore given by

$$\rho_i = \begin{pmatrix} 1 & 0 \\ 0 & 0 \end{pmatrix} \otimes \begin{pmatrix} a & b \\ c & d \end{pmatrix}, \tag{7.18}$$

where $\langle\sigma_t^z\rangle_i = a - d$ is the expectation value we would like to read out. After applying the nuclear-nuclear readout sequence (Eq. 7.17), and tracing over the target spin, we find the final state and associated σ^z-basis spin projection of the probe spin as desired, given by

$$\rho_{p,f} = \text{Tr}_t(U_{\text{RO}}\rho_f U_{\text{RO}}^{\dagger}) = \begin{pmatrix} a & 0 \\ 0 & d \end{pmatrix}, \tag{7.19}$$

$$\langle\sigma_p^z\rangle_f = \text{Tr}(\rho_{p,f}\sigma_p^z) = a - d = \langle\sigma_t^z\rangle_i. \tag{7.20}$$

The state of the probe spin can then be read out via the electron spin using previously developed approaches[25,44]. Importantly, after this measurement, the probe spin can be reinitialised via a swap operation with the electron spin[25,44], and can then be further used to probe the state of additional target spins. Readout of other bases can be achieved via single-qubit rotations of the target spin prior to the nuclear-nuclear readout sequence.

QUANTIFYING NUCLEAR-NUCLEAR READOUT IN THE PRESENCE OF EXPERIMENTAL ERRORS

While the above analysis shows that the readout scheme effectively maps the state of a target spin onto a probe spin via their mutual coupling, the measured signal may be affected by a number of experimental imperfections. These imperfections typically lead to two effects. First, pulse errors on the target spin can cause the readout sequence to fail. Second, the measurement contrast can be reduced due to decoherence of the probe spin or imperfect mapping of the probe spin state to the electron spin. Here we show that we can use the signal obtained via an orthogonal measurement basis to characterise these imperfections and thereby extract the underlying $\langle\sigma_t^z\rangle_i$.

In Eq. 7.17, the final rotation $R_p^x(-\pi/2)$ maps $\langle\sigma_p^y\rangle$ to $\langle\sigma_p^z\rangle$. If we instead apply a rotation $R_p^y(-\pi/2)$, we can measure the expectation value $\langle\sigma_p^x\rangle$. We can calculate $\langle\sigma_p^\phi\rangle_f$ for $\phi \in \{x, y\}$ as a function of τ to get

$$\langle\sigma_p^x\rangle_f(\tau) = \cos\big(4J_{tp}\tau\big), \tag{7.21}$$

$$\langle\sigma_p^y\rangle_f(\tau) = \langle\sigma_t^z\rangle_i \sin\big(4J_{tp}\tau\big). \tag{7.22}$$

PULSE ERRORS ON THE TARGET SPIN

First, we consider the effect of pulse errors on the target spin. In particular, we denote a probability, ϵ, with which the pulse fails to invert the target. In such cases, the probe spin coherence is preserved by its own inversion pulse, but the target spin is decoupled, turning off the interaction. Thus we have $\langle\sigma_p^x\rangle = 1$ and $\langle\sigma_p^y\rangle = 0$. Taking a statistical average according to the failure rate, we arrive at the expectation values

$$\langle\sigma_p^x\rangle_f(\tau,\epsilon) = \epsilon + (1-\epsilon)\cos\big(4J_{tp}\tau\big), \tag{7.23}$$

$$\langle\sigma_p^y\rangle_f(\tau,\epsilon) = (1-\epsilon)\langle\sigma_t^z\rangle_i \sin\big(4J_{tp}\tau\big). \tag{7.24}$$

AMPLITUDE DAMPING

Second, we consider effects which result in a dampened signal. These include imperfect mapping from the probe spin to the electron spin, pulse errors on the probe spin (resulting in dephasing on a timescale $T_2^* \ll \tau_{\mathrm{RO}}$), and T_2-timescale dephasing of the probe spin. All of these effects can be encapsulated by a constant factor δ, alongside a time-dependent function $f(t) = \exp[-\tau/\tau_0]^n$. Here, τ_0 and n are the characteristic timescale and exponent for the decay of the signal. Applying these terms to Eqs. 7.23, 7.24, we find

$$\langle\sigma_p^x\rangle_f(\tau,\delta,\epsilon,n,\tau_0,\beta) = \delta\,\exp\big[-(\tau/\tau_0)^n\big]\,(\epsilon + (1-\epsilon)\cos\big(4\beta J_{tp}\tau\big)), \tag{7.25}$$

$$\langle\sigma_p^y\rangle_f(\tau,\delta,\epsilon,n,\tau_0,\beta) = \delta\,\exp\big[-(\tau/\tau_0)^n\big]\,(1-\epsilon)\langle\sigma_t^z\rangle_i \sin\big(4\beta J_{tp}\tau\big). \tag{7.26}$$

Here β is a multiplicative factor to account for small changes in coupling frequency due to unwanted couplings to other spins.

MITIGATING EXPERIMENTAL IMPERFECTIONS

Considering Eq. 7.25, we note that the $\langle\sigma_p^x\rangle_f$ readout signal is dependent on all of the discussed experimental imperfections, but critically does not depend on the initial target spin polarisation. Therefore, we can use this signal to characterise those parameters. Fig.

7.7E shows characterisation curves for all probe-target spin combinations used in this work. We fit the data using Eq. 7.25 and the resulting fit parameters are given in Table 7.3. Once β, δ, ϵ, τ_0, and n have been identified, these values can be used to obtain $\langle\sigma_t^z\rangle_i$ by performing the $\langle\sigma_p^y\rangle_f$ measurement at τ_{RO} and inverting Eq. 7.26 to give

$$\langle\sigma_t^z\rangle_i = \frac{\langle\sigma_p^y\rangle_f}{\delta\sin\left(4\beta J_{tp}\tau_{\mathrm{RO}}\right)\exp[-(\tau_{\mathrm{RO}}/\tau_0)^n]\,(1-\epsilon)}, \tag{7.27}$$

READOUT FOR THE 1D CHAIN

To read out the spins making up the 1D chain, we use a combination of previously developed electron-nuclear two-qubit gates[25] and our new nuclear-nuclear readout method. The circuits used for initialisation and readout via electron-nuclear two-qubit gates are shown in Fig. 7.1B. The compilation of these circuits using native gates is given in Bradley et al.[25]. The method used for readout for each spin, as well as the associated parameters, are given in Table 7.3. We read out the spins sequentially according to the sequence shown in Fig. 7.1B, where the electron spin and any required probe spins are reset before each readout sequence using optical spin pumping and dynamical decoupling based sequences, respectively[25]. Due to the close spectral proximity of spins 3 and 7, which can cause additional errors in the nuclear-nuclear readout sequence, we read out spin 7 in a separate run of the experiment, while the remaining 8 spins are read out sequentially in a single run.

To account for readout imperfections and thereby accurately estimate the expectation values, we correct the results for readout errors using separate characterisation measurements. For the spins that are read out directly via the electron spin, we follow the method described in Bradley et al.[25], while for spins that are read out using the nuclear-nuclear readout sequence, we use Eq. 7.27.

7.5.6. INITIALISING THE QUANTUM SIMULATOR: DYNAMIC NUCLEAR POLARISATION

This section describes the initialisation of the spin chain with the PulsePol sequence, a recently developed dynamic nuclear polarisation method[24]. We summarise the theoretical background, with a focus on the differences compared to previous studies. We then discuss the optimisation of the sequence. In contrast to previous studies, the individual control and measurement enables us to track the polarisation dynamics quantitatively and on the single spin level. This reveals that the polarisation dynamics themselves present an interesting, and not yet fully understood, many-body problem.

HAMILTONIAN

Dynamic nuclear polarisation (DNP) methods encompass a variety of techniques to realise hyperpolarisation of the nuclear spin bath via polarisation transfer from a central well-controlled electron spin[24,45,46]. While the intrinsic energy scales of the differing spin species forbid natural flip-flop interactions between them, the use of Hamiltonian engineering can overcome this barrier. If this process can be made to occur much faster than nuclear spin diffusion, and is combined with fast and high-fidelity electron spin reset, repeated application can lead to large-scale nuclear spin bath polarisation[47].

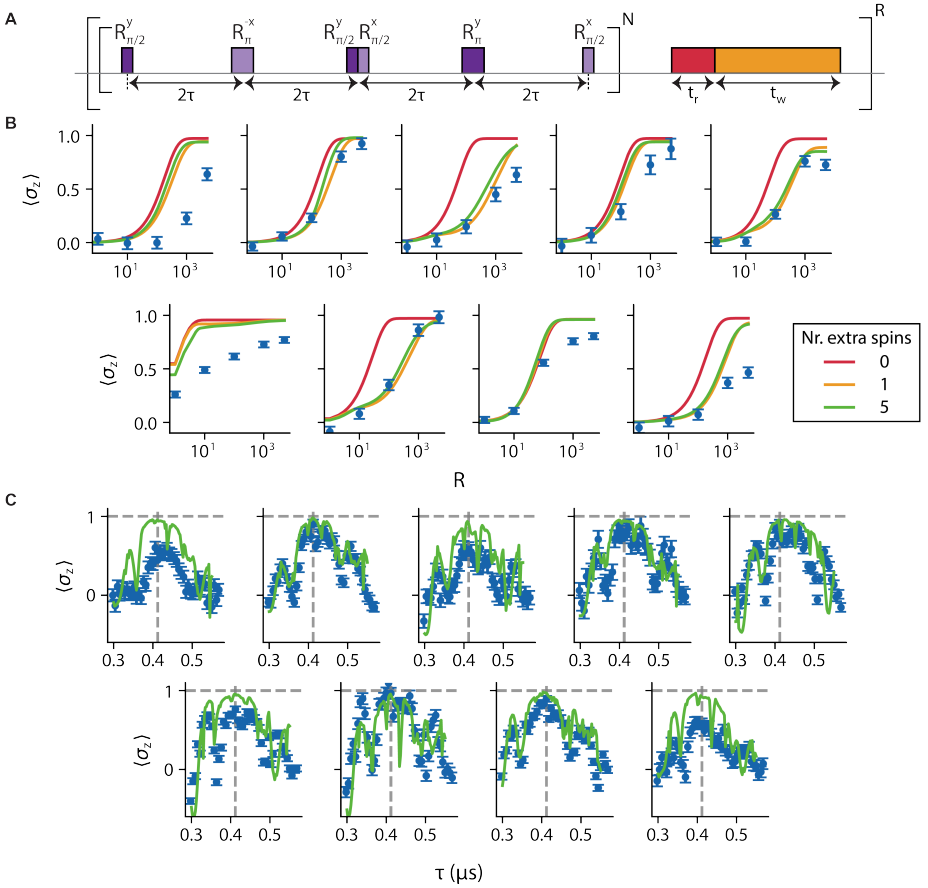

Figure 7.8: **PulsePol characterisation.** (**A**) Schematic representation of the PulsePol sequence. The purple pulses are microwave pulses that act on the electron spin. $t_r = 10\ \mu$s is the reset time (the total time for which the reset laser is applied) and $t_w = 14\ \mu$s is a waiting time that was included due to hardware restrictions. (**B**) Polarisation of each spin (1-9 from top left to bottom right) as a function of the number of repetitions R for $\tau = 0.412\ \mu$s and $N = 4$. The red, orange and green solid lines are simulations of the ^{13}C spin of interest, the ^{14}N spin, and an additional 0, 1 or 5 spins included in the environment respectively, which were chosen using the method described in the text. (**C**) Polarisation of each spin (1-9 from top left to bottom right) as a function of the parameter τ of PulsePol with $N = 4$ and $R = 5000$. Solid lines are the results of simulations including 5 environmental spins. The dashed vertical line represents the value of τ employed in the DTC experiments and the horizontal line at a polarisation value of 1 is included as a guide to the eye.

Spin	Gate Type	τ (μs)	N	C_Q
2	DDrf	37.04	32	0.65(3)
5	DDrf	37.04	32	0.64(3)
6	DD	16.48	20	0.91(1)
8	DD	4.932	90	0.88(2)

Spin	Probe	τ_{RO} (ms)	β	δ	ϵ	τ_0 (ms)	n
1	2	5.76	0.92(1)	0.52(2)	0.09(2)	-	-
3	2	14.06	0.90(1)	0.48(2)	0.12(2)	-	-
4	5	25.00	1.06(2)	0.43(3)	0.11(3)	65(4)	3(1)
7	8	17.86	0.88(1)	0.57(2)	0.04(2)	-	-
9	8	9.89	0.95(1)	0.57(2)	0.09(1)	-	-

Table 7.3: Readout parameters for the spins in the 1D chain. Left: Readout parameters for the spins that are directly read out using electron-nuclear gates. We use either the DD or DDrf sequence[25], with N pulses in a CPMG-type sequence with pulse spacing τ. Following Ref.[25], the parameter C_Q is measured by initialising the spin in $|\uparrow\rangle$ and reading out $\langle\sigma^z\rangle$, and subsequent measurements are readout corrected so that $\langle\sigma^z\rangle' = \langle\sigma^z\rangle/C_Q$. Right: Readout parameters for spins that are read out using the new nuclear-nuclear readout method (Sec. 7.5.5). The spin state is mapped to a probe spin using a SEDOR sequence with interaction time τ_{RO}. The last five columns give the fit parameters for a characterisation measurement using Eq. 7.25, from which we can estimate $\langle\sigma^z\rangle$ of the target spin using Eq. 7.27. Dashed lines indicate spins where no decay was observed on the timescale of the characterisation measurement, and therefore the exponential function in Eq. 7.25 was set to 1.

In this work, we employ the recently developed PulsePol sequence which is schematised in Fig. 7.8A[24]. For values of the characteristic timescale τ close to $\tau_0 \equiv (3\pi/8\gamma_c B_z)$ = 0.434 μs, the effective system Hamiltonian is given by

$$H_{\mathrm{eff}} = \sum_j \Delta\omega_j I_j^z - \sum_j \alpha A_j^{\perp}\left(S^+ I_j^- + S^- I_j^+\right), \tag{7.28}$$

where $\Delta\omega_j \approx [\gamma_c B_z - (A_j^{\parallel}/2) - (3\pi/8\tau)]$ and $\alpha = (2/\sqrt{12}\pi) \approx 0.184$. $I_j^{\pm}$ and $S^{\pm}$ are spin-1/2 ladder operators for the j-th nuclear spin and the electron spin respectively (the unoccupied m_s = +1 level is neglected), and the sum is over all the nuclear spins of the environment. Importantly, this Hamiltonian differs from that given in Schwartz et al.[24] by the term $\sum_j \Delta\omega_j I_j^z$. This term, arising at first order from the individual hyperfine couplings $A_j^{\parallel}$, introduces z-disorder between nuclear spins which plays a central role in the polarisation transfer process.

As described in Villazon et al.[48], Hamiltonians which do not exhibit z-disorder host dark states which prevent complete polarisation of the system, even after an infinite number of DNP cycles. The origin of this z-disorder in our Hamiltonian (in contrast to Ref.[24]) is due to the different choice of electron effective-spin-1/2 basis states. Using the $m_s = 0$ and m_s = -1 levels (rather than $m_s = \pm 1/2$), the bare system Hamiltonian from which the effective Hamiltonian is derived is

$$H = \sum_j \gamma_c B_z I_j^z - |-1\rangle\langle -1| \sum_j \left(A_j^{\perp} I_j^x + A_j^{\parallel} I_j^z\right), \tag{7.29}$$

where $|-1\rangle\langle -1|$ is the projector on the $m_s = -1$ state of the electron spin.

EXPERIMENTAL OPTIMISATION AND NUMERICAL SIMULATIONS

The polarisation dynamics under PulsePol are dependent on a number of parameters of the sequence: the characteristic timescale τ, the number of applications of the PulsePol primitive between electron resets, N, and the total number of polarisation cycles, R (see Fig. 7.8A). Based on preliminary simulations of the system, we identified $N = 4$ as a suitable working point. In Fig. 7.8B we show the measured polarisation of each nuclear spin in the 9 spin chain as a function of R, for $\tau = 0.412$ μs. We observe that the system polarisation continues to increase up to at least $R = 5000$ iterations of PulsePol, which is the value used throughout the presented experiments. In Fig. 7.8C we show the dependence of the polarisation on τ. For this choice of R, the maximal mean polarisation for the 9 spin chain, $\overline{\langle\sigma^z\rangle} = 0.75(2)$, is obtained at $\tau = 0.412$ μs, corresponding to an average single-qubit initialisation fidelity of $F_{\text{init}} = 0.88(1)$ (Fig. 7.1E). This value of τ is detuned from the centre of the expected resonance: at $\tau_0 \approx 0.436$ μs we find $\overline{\langle\sigma^z\rangle} = 0.64(2)$. The mechanism behind the reduced polarisation rate at the resonant value is not yet well understood, but may arise due to the simultaneous addressing of a larger number of spins in the environment, leading to slower polarisation for the targeted spins used in this work.

To explain the observed polarisation, we compare the results to numerical simulations for the same conditions, using the Hamiltonian of Eq. 7.29, and taking into account experimental imperfections. In particular, electron π ($\pi/2$) rotations are modelled by finite square pulses with a duration of 30 ns (15 ns). Furthermore, we account for the finite waiting time of ~24 μs spent in $m_s = 0$ between the electron reset — which is expected to occur in ~500 ns for the 30 nW optical power used here[49] — and the start of the next PulsePol cycle. We further include the nitrogen spin, which adds Hamiltonian terms:

$$H_N = Q(I_N^z)^2 + \gamma_N B_z I_N^z - |-1\rangle\langle -1| \otimes \left(A_N^{\parallel} I_N^z + A_N^{\perp} I_N^x\right), \tag{7.30}$$

where $Q/2\pi = -4.945$MHz is the quadrupole splitting, γ_N is the gyromagnetic ratio of the nitrogen, $A_N^{\parallel}$ ($A_N^{\perp}$) is the parallel (perpendicular) electron-nuclear hyperfine component and I_N^{α} are the spin-1 matrices for the nitrogen spin.

One challenge is that it is not possible to numerically simulate a large number of spins using exact diagonalisation. In the course of investigation through simulations, it became apparent that including particular subsets of the 27 known ^{13}C spins[23] could lead to vastly different polarisation dynamics. In the present approach, for each spin shown in Fig. 7.8, we first simulate the result when combined pairwise with each of the other known spins. We then select the 5 ^{13}C spins (alongside the target and the nitrogen spin) which have the largest impact, as quantified by

$$\xi_{jk} = \sum_{R=1}^{5000} \left|\text{PP}_1(j,\tau,N,R) - \text{PP}(j,k,\tau,N,R)\right|, \tag{7.31}$$

where τ, N and R are the PulsePol parameters, $\text{PP}_1(j,\tau,N,R)$ is the polarisation of the j-th ^{13}C spin after PulsePol without including any other spin in the simulation (red line in Fig. 7.8B)) and $\text{PP}(j,k,\tau,N,R)$ is the polarisation of the j-th ^{13}C spin when including also the k-th spin (orange line in Fig. 7.8B). ξ_{jk} is the integral of the absolute area between the red and orange solid lines in Fig. 7.8B. These sets of spins, shown in Table 7.4, are used

Spin	Env. 1	Env. 2	Env. 3	Env. 4	Env. 5
1	6	12	13	14	11
2	15	11	12	10	6
3	6	12	13	7	11
4	6	12	13	11	10
5	6	12	13	7	11
6	7	12	3	13	11
7	6	13	12	11	10
8	6	10	12	13	11
9	6	12	5	13	11

Spin	$A_\parallel$ (kHz)	$A_\perp$ (kHz)
10	213.154(1)	3.0(4)
11	-36.308(1)	26.62(4)
12	20.569(1)	41.51(3)
13	24.399(1)	24.81(4)
14	14.548(3)	10(1)
15	-20.72(1)	12(1)
16	-4.039(5)	0(3)

Table 7.4: Parameters for the simulations used in Fig. 7.8. Left: Five most relevant spins (Env. 1-5) for each simulated spin according to Eq. 7.31. Simulations which incorporated only one environmental spin use Env. 1. Right: Measured parameters for the Spins 10-16 that were employed in the simulations, taken from Abobeih et al.[23] (Spin 16 is used in simulations in Sec. 7.5.7). $A_\parallel$ ($A_\perp$) is the parallel (perpendicular) hyperfine coupling. The parameters for Spins 1-9 are given in Table 7.1.

for the simulations shown in Fig. 7.8. Typically, spins found to have the largest impact were those with similar $A^\parallel$ to the target, and those with generally large $A^\perp$. However, a more comprehensive study of these effects is needed to realise a general framework.

Despite the inclusion of all of these effects, there remains a discrepancy between the experimentally measured values and the simulation results. While there is reasonable qualitative agreement, the absolute achieved polarisation is lower in experiment than that reached in simulation (which is uniformly close to unity). This does not appear to be explained by spin diffusion: the inclusion of a depolarising channel between resets, $\Delta_\lambda(\rho) = \lambda\rho + (1-\lambda)\frac{\mathbf{I}}{\mathrm{Tr}\{\mathbf{I}\}}$, with $\lambda = \exp(-8\tau N/T_1)$, requires a relaxation timescale of 1-10 ms (dependent upon the investigated spin) to induce any noticeable effect. This is at least an order of magnitude shorter than the fastest known relaxation timescales within our system. A second possible cause is the inability to include the full set of known spins in simulation, along with a wider spin bath. The effects of a large number of additional spins are not yet well understood.

Importantly, to our knowledge, our experiment is the first in which DNP techniques have been combined with individual nuclear-spin read-out. Our methods therefore offer new opportunities to study polarisation transfer in complex spin systems, and to improve their efficacy.

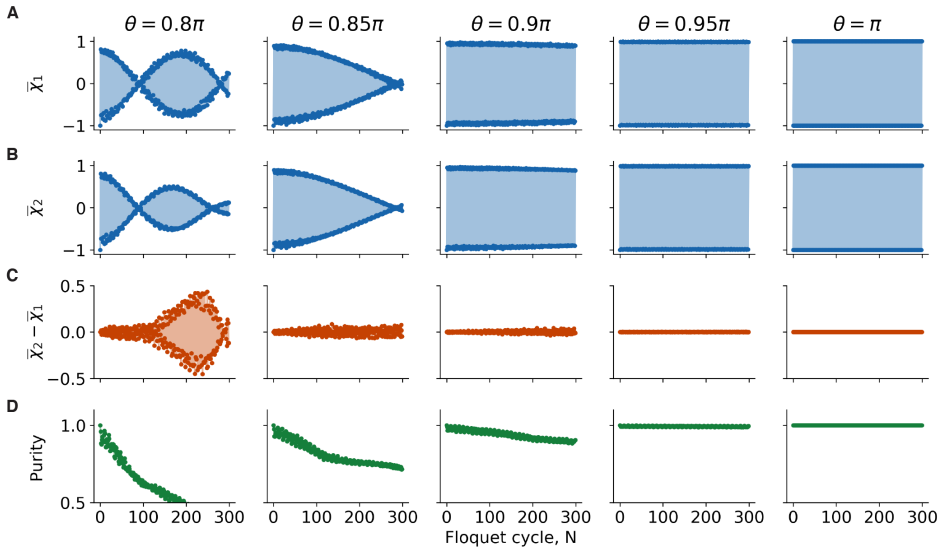

Figure 7.9: **Decoherence from the environment.** Numerical simulation of U_F (Sec. 7.5.2) showing the averaged two-point correlation $\overline{\chi}$ as a function of the number of Floquet cycles N for the first 4 spins of the 1D chain after initialising in the state $|\uparrow\uparrow\uparrow\uparrow\rangle$. Columns are for different rotation angles θ (indicated at the top) with $\tau = 5\,\text{ms}$ in all cases. (**A**) Result with only the 4 targeted spins included in the simulation. (**B**) Result with 4 additional spins from the environment included (not part of the spin chain, parameters given in Tables 7.4 and 7.5). These additional spins are initialised in the maximally mixed state. (**C**) Difference between the two cases. (**D**) Purity (= $\text{Tr}[\rho^2]$) of the four-spin reduced density matrix after taking the partial trace over the additional spins.

7.5.7. DECOHERENCE FROM THE ENVIRONMENT

In this work, we isolate a targeted subset of spins, enabling the realisation of an effective one-dimensional chain in a three-dimensional system. For rotation angles $\theta \sim \pi$, we can symmetrise the Floquet sequence to resemble a CPMG sequence in order to simultaneously provide the required decoupling, thereby simplifying the experiment. In Fig. 7.9, we investigate the effect of the spin environment on the dynamics for different rotation angles. We numerically simulate the Floquet sequence U_F (Sec. 7.5.2) up to $N = 300$ cycles for two cases. First, we include only the first 4 spins of the 1D chain to obtain the ideal dynamics in a perfect closed system. Second, we additionally include 4 spins that are not part of the chain, but couple strongly to the 4 targeted spins (see Table 7.5 for the parameters of the additional spins). It can be seen that the difference in average two-point correlation between the two cases increases as θ moves away from π. For the value of $\theta = 0.95\pi$ used in the experiments, the difference remains less than 0.1 over all Floquet cycles simulated. The additional spins can cause shifts in the individual on-site disorder strengths, which can change the measured signal even if the quantum state of the targeted spins remains completely pure. To distinguish these effects, in Fig. 7.9 we also plot the purity (= $\text{Tr}[\rho^2]$) of the four-spin reduced density matrix after tracing over

the additional spins. For $\theta = 0.95\pi$, there is a small loss in purity, although this is suppressed compared to larger values of $\pi - \theta$. In future experiments, the decoupling pulses and the rotations in the Floquet sequence could be separated so that the rotation angle for the decoupling is always equal to π, allowing lower values of θ to be investigated while ensuring good isolation from the spin bath. This would further improve the coherence of the effective 1D chain.

	10	11	14	16
1	-0.55(2)	-1.21(1)	-0.23	6.34
2	-1.885(8)	0.7(2)	-0.07	-3.15(5)
3	-1.05(8)	0.3	-0.36	-1.1(2)
4	-0.09	0.75(2)	-2.35(2)	0.05

Table 7.5: Interactions between the four targeted spins (1, 2, 3, 4) and the four additional spins included in the simulation (10, 11, 14, 16). Interactions with uncertainties given in parentheses are measured values for the NV electron state $m_s = -1$, while interactions shown without uncertainties are calculated from the spin coordinates according to Eq. 7.14. Hyperfine parameters for the additional spins are given in Table 7.4.

7.5.8. INITIAL STATE DEPENDENCE

In Sec. 7.3 we present the evolution of 11 initial bitstrings, of which 9 are randomly chosen, for up to N=300-800 Floquet periods. The long-lived subharmonic response observed for all states is consistent with the many-body-localised DTC phase and provides a mechanism to distinguish it from a prethermal response. Here, we present numerical simulations that show clear differences between our system Hamiltonian and a similar Hamiltonian without disorder[6,19]. These differences manifest themselves within the timescales accessed by our experiments.

We again simulate the Floquet sequence U_F (Sec. 7.5.2) for two scenarios, using $\theta = 0.95\pi$ and $\tau = 5$ ms. In the first scenario, we use the measured system parameters, with the h_j^z given by the values of $A_\parallel$ in Table 7.1, and the J_{jk} given by the values in Table 7.2. In the second scenario, we consider the absence of both onsite disorder (all $h_j^z = 0$) as well as the Ising-even disorder terms which can stabilise MBL[5,6,19]. That is, we homogenise the J_{jk} as given in Table 7.6. We set all the nearest-neighbour couplings equal to the mean magnitude measured across the chain: $J_0 = 6.67$ Hz, with the remainder of the couplings falling off as a function of distance with an exponent of $\alpha = 2.5$.

In Figs. 7.10E,F, we show the simulation results for up to $N = 10^8$ Floquet periods. Crucially, in the disorder-free case, we see strong variations between differing initial states within ~100-1000 periods. In the presence of disorder, these discrepancies are suppressed up to $\sim 10^6$ periods. The two scenarios can be distinguished within the experimentally accessed timescales (N = 300-800 periods, Figs. 7.10C,D). While we do observe some state-dependence at late times even in the disordered scenario, this is attributed to finite-size effects[3,6]. Extending to larger system sizes is expected to stabilise the DTC phase for all bitstrings at increasingly larger times.

	1	2	3	4	5	6	7	8	9
1	-	6.67	1.18	0.43	0.21	0.12	0.07	0.05	0.04
2	6.67	-	6.67	1.18	0.43	0.21	0.12	0.07	0.05
3	1.18	6.67	-	6.67	1.18	0.43	0.21	0.12	0.07
4	0.43	1.18	6.67	-	6.67	1.18	0.43	0.21	0.12
5	0.21	0.43	1.18	6.67	-	6.67	1.18	0.43	0.21
6	0.12	0.21	0.43	1.18	6.67	-	6.67	1.18	0.43
7	0.07	0.12	0.21	0.43	1.18	6.67	-	6.67	1.18
8	0.05	0.07	0.12	0.21	0.43	1.18	6.67	-	6.67
9	0.04	0.05	0.07	0.12	0.21	0.43	1.18	6.67	-

Table 7.6: Pairwise spin-spin interactions J_{jk} (Hz) for a theoretical homogeneous 9-spin 1D chain, as used for simulations which are free of disorder.

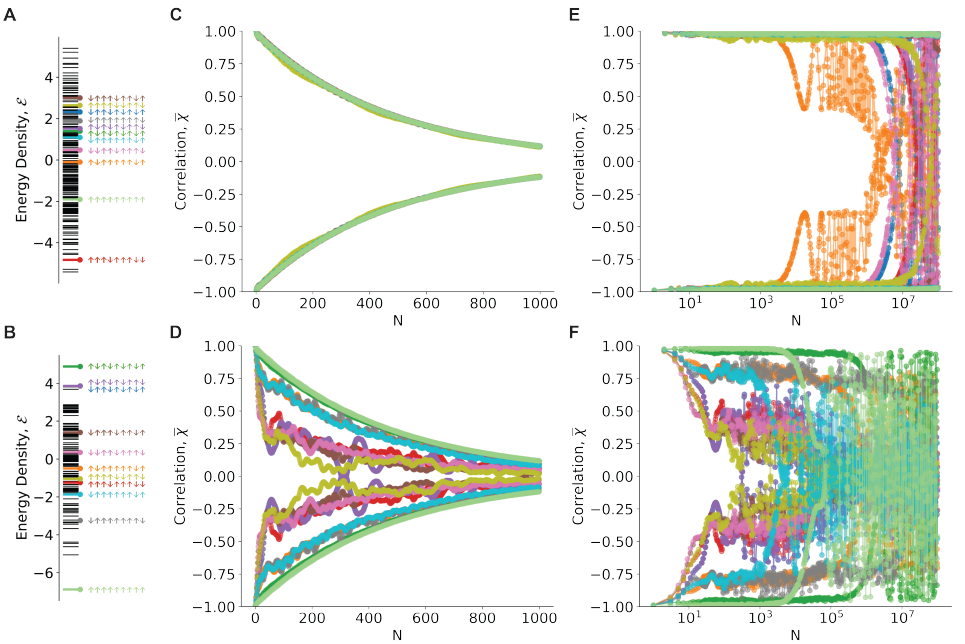

Figure 7.10: **Initial state dependence** (**A** and **B**) Calculated energy densities $\mathcal{E}$ for all possible states of the form $\bigotimes_j^L \left|m_j\right\rangle$, $m_j \in \{\uparrow, \downarrow\}$ (black lines), for the disordered experimental Hamiltonian (Table 7.2, A) and a theoretical disorder-free Hamiltonian (Table 7.6, B). The initial states measured in Fig. 7.4D are indicated by the corresponding colors. (**C** and **D**) Simulated values of the correlation function $\overline{\chi}$ for the 11 initial states used in the experiments, up to $N = 1000$ Floquet periods, with (C) and without (D) disorder. The simulated results are multiplied by the decay function $f(N) = Ae^{-N/N_{1/e}}$, with $N_{1/e} = 472(17)$ extracted from a fit to the experimental data (Fig. 7.4D). Clear behavioural differences can be observed within the experimentally accessed timescales. (**E** and **F**) Simulated values of the correlation function $\overline{\chi}$ up to $N = 10^8$ Floquet periods, with (E) and without (F) disorder.

REFERENCES

[1] F. Wilczek, *Quantum time crystals,* Phys. Rev. Lett. **109**, 160401 (2012).

[2] H. Watanabe and M. Oshikawa, *Absence of quantum time crystals,* Phys. Rev. Lett. **114**, 251603 (2015).

[3] D. V. Else, B. Bauer and C. Nayak, *Floquet time crystals,* Phys. Rev. Lett. **117**, 090402 (2016).

[4] V. Khemani, A. Lazarides, R. Moessner and S. L. Sondhi, *Phase structure of driven quantum systems,* Phys. Rev. Lett. **116**, 250401 (2016).

[5] N. Y. Yao, A. C. Potter, I.-D. Potirniche and A. Vishwanath, *Discrete time crystals: Rigidity, criticality, and realizations,* Phys. Rev. Lett. **118**, 030401 (2017).

[6] V. Khemani, R. Moessner and S. L. Sondhi, *A brief history of time crystals,* arXiv:1910.10745 (2019).

[7] D. V. Else, C. Monroe, C. Nayak and N. Y. Yao, *Discrete time crystals,* Annu. Rev. Condens. Matter Phys. **11**, 467 (2020).

[8] D. A. Abanin, E. Altman, I. Bloch and M. Serbyn, *Colloquium: Many-body localization, thermalization, and entanglement,* Rev. Mod. Phys. **91**, 021001 (2019).

[9] L. D'Alessio and M. Rigol, *Long-time behavior of isolated periodically driven interacting lattice systems,* Phys. Rev. X **4**, 041048 (2014).

[10] J. Zhang *et al.*, *Observation of a discrete time crystal,* Nature **543**, 217 (2017).

[11] A. Kyprianidis *et al.*, *Observation of a prethermal discrete time crystal,* Science **372**, 1192 (2021).

[12] S. Choi *et al.*, *Observation of discrete time-crystalline order in a disordered dipolar many-body system,* Nature **543**, 221 (2017).

[13] J. Rovny, R. L. Blum and S. E. Barrett, *Observation of discrete-time-crystal signatures in an ordered dipolar many-body system,* Phys. Rev. Lett. **120**, 180603 (2018).

[14] S. Pal, N. Nishad, T. S. Mahesh and G. J. Sreejith, *Temporal order in periodically driven spins in star-shaped clusters,* Phys. Rev. Lett. **120**, 180602 (2018).

[15] J. O'Sullivan *et al.*, *Signatures of discrete time crystalline order in dissipative spin ensembles,* New J. Phys. **22**, 085001 (2020).

[16] J. Smits, L. Liao, H. T. C. Stoof and P. van der Straten, *Observation of a space-time crystal in a superfluid quantum gas,* Phys. Rev. Lett. **121**, 185301 (2018).

[17] S. Autti, V. B. Eltsov and G. E. Volovik, *Observation of a time quasicrystal and its transition to a superfluid time crystal,* Phys. Rev. Lett. **120**, 215301 (2018).

[18] P. Frey and S. Rachel, *Simulating a discrete time crystal over 57 qubits on a quantum computer,* arXiv:2105.06632 (2021).

[19] M. Ippoliti, K. Kechedzhi, R. Moessner, S. L. Sondhi and V. Khemani, *Many-body physics in the nisq era: quantum programming a discrete time crystal,* arXiv:2007.11602 (2020).

[20] D. V. Else, B. Bauer and C. Nayak, *Prethermal phases of matter protected by time-translation symmetry,* Phys. Rev. X **7**, 011026 (2017).

[21] F. Machado, D. V. Else, G. D. Kahanamoku-Meyer, C. Nayak and N. Y. Yao, *Long-range prethermal phases of nonequilibrium matter,* Phys. Rev. X **10**, 011043 (2020).

[22] P. Peng, C. Yin, X. Huang, C. Ramanathan and P. Cappellaro, *Floquet prethermalization in dipolar spin chains,* Nat. Phys. **17**, 444 (2021).

[23] M. Abobeih *et al.*, *Atomic-scale imaging of a 27-nuclear-spin cluster using a quantum sensor,* Nature **576**, 411 (2019).

[24] I. Schwartz *et al.*, *Robust optical polarization of nuclear spin baths using hamiltonian engineering of nitrogen-vacancy center quantum dynamics,* Sci. Adv. **4**, eaat8978 (2018).

[25] C. E. Bradley *et al.*, *A ten-qubit solid-state spin register with quantum memory up to one minute,* Phys. Rev. X **9**, 031045 (2019).

[26] W. De Roeck and F. Huveneers, *Stability and instability towards delocalization in many-body localization systems,* Phys. Rev. B **95**, 155129 (2017).

[27] N. Y. Yao *et al.*, *Many-body localization in dipolar systems,* Phys. Rev. Lett. **113**, 243002 (2014).

[28] A. L. Burin, *Many-body delocalization in a strongly disordered system with long-range interactions: Finite-size scaling,* Phys. Rev. B **91**, 094202 (2015).

[29] Z. Gong, R. Hamazaki and M. Ueda, *Discrete time-crystalline order in cavity and circuit qed systems,* Phys. Rev. Lett. **120**, 040404 (2018).

[30] N. Y. Yao, C. Nayak, L. Balents and M. P. Zaletel, *Classical discrete time crystals,* Nat. Phys. **16**, 438 (2020).

[31] A. Lazarides, S. Roy, F. Piazza and R. Moessner, *Time crystallinity in dissipative floquet systems,* Phys. Rev. Res. **2**, 022002 (2020).

[32] J. Cai, A. Retzker, F. Jelezko and M. B. Plenio, *A large-scale quantum simulator on a diamond surface at room temperature,* Nat. Phys. **9**, 168 (2013).

[33] I. Lovchinsky *et al.*, *Magnetic resonance spectroscopy of an atomically thin material using a single-spin qubit,* Science **355**, 503 (2017).

[34] F. Dolde *et al.*, *Room-temperature entanglement between single defect spins in diamond,* Nat. Phys. **9**, 139 (2013).

[35] M. Pompili *et al.*, *Realization of a multinode quantum network of remote solid-state qubits,* Science **372**, 259 (2021).

[36] M. H. Abobeih *et al.*, *One-second coherence for a single electron spin coupled to a multi-qubit nuclear-spin environment,* Nat. Commun. **9**, 1 (2018).

[37] L. Robledo *et al.*, *High-fidelity projective read-out of a solid-state spin quantum register,* Nature **477**, 574 (2011).

[38] L. M. Vandersypen and I. L. Chuang, *Nmr techniques for quantum control and computation,* Rev. Mod. Phys. **76**, 1037 (2005).

[39] W. S. Warren, *Effects of arbitrary laser or nmr pulse shapes on population inversion and coherence,* J. Chem. Phys. **81**, 5437 (1984).

[40] T. Gullion, D. B. Baker and M. S. Conradi, *New, compensated carr-purcell sequences,* J. Magn. Reson. **89**, 479 (1990).

[41] T. Taminiau *et al.*, *Detection and control of individual nuclear spins using a weakly coupled electron spin,* Phys. Rev. Lett. **109**, 137602 (2012).

[42] J. R. Johansson, P. D. Nation and F. Nori, *Qutip 2: A python framework for the dynamics of open quantum systems,* Comput. Phys. Commun. **184**, 1234 (2013).

[43] C. Slichter, *Principles of Magnetic Resonance* (Springer, 1996).

[44] T. H. Taminiau, J. Cramer, T. van der Sar, V. V. Dobrovitski and R. Hanson, *Universal control and error correction in multi-qubit spin registers in diamond,* Nat. Nanotechnol. **9**, 171 (2014).

[45] P. London *et al.*, *Detecting and polarizing nuclear spins with double resonance on a single electron spin,* Phys. Rev. Lett. **111**, 067601 (2013).

[46] J. E. Lang *et al.*, *Quantum bath control with nuclear spin state selectivity via pulse-adjusted dynamical decoupling,* Phys. Rev. Lett. **123**, 210401 (2019).

[47] T. Unden *et al.*, *Coherent control of solid state nuclear spin nano-ensembles,* NPJ Quantum Inf. **4**, 1 (2018).

[48] T. Villazon, A. Chandran and P. W. Claeys, *Integrability and dark states in an anisotropic central spin model,* Phys. Rev. Res. **2**, 032052 (2020).

[49] A. Reiserer *et al.*, *Robust quantum-network memory using decoherence-protected subspaces of nuclear spins,* Phys. Rev. X **6**, 021040 (2016).

8

CONCLUSIONS AND OUTLOOK

In this chapter, I summarise the findings of this thesis. I then discuss open questions from this research, and near-term improvements which may enable the next generation of experiments. Finally, I provide an outlook towards large-scale quantum information processing using spin systems associated with optically-active solid-state defects.

8.1. SUMMARY

In this thesis, we developed novel techniques that allow for the control and understanding of both electronic and nuclear spin systems associated with single NV centres in diamond. Building upon these advances, we implemented protocols related to quantum networks (Ch. 4), quantum computation (Ch. 5), quantum sensing (Ch. 6), and quantum simulation (Ch. 7). Here I summarise the conclusions of each chapter:

- In **Chapter 3**, we used resonant excitation spectroscopy to reveal the fine structure of the NV^0 centre. With time-resolved fluorescence measurements, we characterised its orbital- and spin-dynamics for the first time. We developed novel heralding schemes, with which we demonstrated high-fidelity initialisation and single-shot read-out of the NV^0 spin-state. This work elucidates a number of key properties of the NV^0 centre, which will play an important role in large-scale NV-based quantum networks.

- In **Chapter 4**, we characterised a ^{13}C quantum-network memory in isotopically-engineered diamond. We demonstrated a two order-of-magnitude improvement in memory robustness upon the state-of-the-art, and further showed that the memory can be protected from NV centre ionisation. Finally, we numerically investigated the performance of such a memory for future quantum-network experiments, and found that key primitives for distributed quantum information processing are now within reach.

- In **Chapter 5**, we developed novel two-qubit gates, and employed them to realise a fully connected 10-qubit register with coherence times of up to one minute. Furthermore, we showed genuine multipartite entanglement of 7 spin qubits. Our findings demonstrate that this spin system is a promising platform for quantum information processing.

- In **Chapter 6**, we demonstrated atomic-scale magnetic resonance imaging of a cluster of 27 ^{13}C nuclear spins surrounding a single NV centre in diamond. This experiment provides detailed knowledge of the nuclear spin environment of a single electron spin, and serves as a proof-of-principle towards the goal of imaging single molecules or spin complexes outside the diamond.

- In **Chapter 7**, we built upon the knowledge obtained in Ch. 6 to develop a quantum simulator based on ^{13}C spins. We implemented the driven-Ising model in a chain of 9 spins. Using novel control techniques to initialise and measure this system, we synthesised and characterised the many-body-localised discrete-time-crystalline phase. This work gives insights into thermalisation in many-body quantum systems and establishes nuclear spins in diamond as a powerful quantum simulation platform.

In the remainder of this chapter, I will discuss both the near-term and longer-term outlook of this work. While there are many exciting avenues based on optically-active defects which are likely to develop in the coming years, for the long-term outlook I will focus on large-scale quantum information processing (QIP) architectures.

8.2. NEAR-TERM ADVANCES

In this section, I will address three distinct topics arising from this thesis for which near-term advances now appear feasible. First, I will discuss the challenge of ionisation in NV-based quantum networks, an issue which must be overcome in order to scale that approach further. Second, I will review avenues for improving two-qubit gate fidelities, which are perhaps the most immediate obstacle in developing a quantum information processing platform based upon nuclear spins in diamond. Finally, I will explore potential quantum simulations with tens of nuclear-spin qubits and a possible pathway towards a 50-qubit system of ^{13}C spins for this purpose.

8.2.1. OVERCOMING IONISATION IN NV-BASED QUANTUM NETWORKS

In Chs. 3 and 4, we first investigated the properties of the neutrally-charged nitrogen vacancy centre, and then showed that a sufficiently weakly-coupled ^{13}C could be made robust to a (deliberate) ionisation and recharging event. Such ionisation events are an important error-channel that will have to be overcome to realise large-scale quantum networks based on NV centres. While the results of Ch. 4 show promise, here I discuss some of the outstanding questions from these works.

First, there is a discrepancy between the measured NV^0 spin-T_1 time found in Ch. 3 (1.5 s) compared with that inferred in Ch. 4 (0.6 ms). This is likely explained by the differences between these works, in particular that Ch. 3 used high magnetic field (1850 G) and a much reduced nitrogen impurity concentration (<5 ppb), compared with 50 G and ~75 ppb in Ch. 4. However, confirmation of this requires further studies. This has some challenges: the techniques developed in Ch. 3 utilise spectral isolation of individual optical transitions, which becomes poor at low magnetic fields. Nevertheless, it may be that polarisation-addressing alone gives sufficient contrast. Alternatively, the T_1 time can be estimated from Ramsey measurements on sufficiently weakly-coupled nuclear spins which are not decohered by the ionisation and recharging processes (as in Ch. 4).

The NV^0 spin-T_1 time has an important consequence, namely that short T_1 ($A_\parallel \ll 1/T_1$) adds a dissipative decoupling effect which extends the nuclear spin coherence (Ch. 4), whereas long T_1 can enable single-shot read-out (Ch. 3), from which the post-ionisation spin state could be detected, and the acquired nuclear spin phases appropriately compensated. Thus, understanding the mechanisms which set this timescale could allow selection of the desired regime. Alternatively, the effective NV^0 spin-T_1 time might be reduced by driving its ground state spin transitions (in both orbitals) to realise a form of continuous dynamical decoupling[1,2]. A first step here is to actually observe these microwave transitions. Armed with high-fidelity spin initialisation and single-shot read-out, this appears to be relatively straightforward. However, a technical challenge is that the short orbital-T_1 necessitates fast driving, but current devices are not designed to operate in the 10-15 GHz frequency band where the transitions are expected to lie.

A more open question is how to ultimately overcome charge-state conversion in a large-scale quantum network. The more effectively the data qubits can be decoupled from ionisation processes of the communication qubit, the more freedom given here. One option is to continuously apply a recharging laser during all optical processes[3], but this may lead to unwanted spectral diffusion. Adding regular charge-state measure-

ments and feedback may be less intrusive, but comes at the cost of a time overhead. In the long-term, a defect hosting a completely stable charge-state would alleviate this concern.

8.2.2. IMPROVED CONTROL FIDELITIES FOR NUCLEAR-SPIN REGISTERS

In Ch. 5, we developed techniques for quantum information processing using a 10 qubit register associated with a single NV centre. This work significantly advanced our experimental capabilities, but it is clear that there is still much to improve. Within our platform, the building-blocks of any quantum circuit — state preparation[†], conditional logic and measurement — rely on electron-nuclear gates. This is a simultaneous hindrance and benefit: two-qubit gate errors impact all these processes, but improvements in those gates consequently advance them. In this section, I will discuss pathways for improving dynamical-decoupling-based two-qubit gates (DD and DDrf). All given metrics are as measured in natural-abundance (1.1% ^{13}C) devices[4,5].

At present, our two-qubit gates are limited by two main factors. The first is decoherence (of both spin species). For the electron spin, this occurs on a timescale of up to $T_2^{\mathrm{N=100}}$ ~30 ms for the $O(100)$ decoupling pulses used for such gates[4]. T_2 has been seen to be reduced by high-power RF electronics, due to low-frequency noise which is not easily filtered when using resonant drives at f ~400 kHz[5]. A carefully designed RF delivery system (including an AWG with lower 1/f noise) would aid this. Alternatively, higher magnetic fields would increase the ^{13}C frequencies, facilitating low-frequency filtering. The residual T_2 decoherence is thought to originate from distant ^{13}C pairs[4,6–8]. Ideally, tailored spin environments would remove the spin-bath while maintaining a spin register around the defect. Delta-doping may partially achieve this, but methods for precise 3D localisation are currently lacking[9–11].

For the nuclear spins, our gate schemes do not incorporate coherence-protection. As the duration of a (selective) nuclear spin-echo is comparable to the two-qubit gate duration itself, echoes cannot be incorporated analogously as for the electron spin. Resultingly, the nuclear spins undergo T_2^* dephasing due to ZZ interactions with other ^{13}C spins. Typical T_2^* times are in the region of 3-20 ms[5]. These dephasing timescales can be improved by polarising the local spin environment (Fig. 8.1(a))[12], and then choosing weakly-interacting spins for a given algorithm. Further improvement could be achieved by designing novel gate schemes which do incorporate nuclear spin decoupling[13].

The second limitation for our present gate schemes is crosstalk: unwanted driving of non-targeted spins. As each controllable nuclear spin is addressed via a unique precession frequency, selective spectral windows are desired which do not affect other spins. There is a trade-off between gate speed and coherence time: slower gates can have higher spectral selectivity, but the constituent qubits experience additional decoherence during this time. Of course, even in the absence of decoherence, arbitrarily slow gates would be impractical. A general strategy to address this challenge is to modify the control sequences to engineer spectral windows which minimise the time-bandwidth product and cancel unwanted harmonics. For DD gates, a number of schemes have been designed towards this goal, and further optimisation is likely[14–16]. Moreover, such

[†]Alternatively, dynamic nuclear polarisation (see Ch. 7) can be used for state initialisation, but its limitations are not yet well understood, and fidelities are yet to match the gate-based approach.

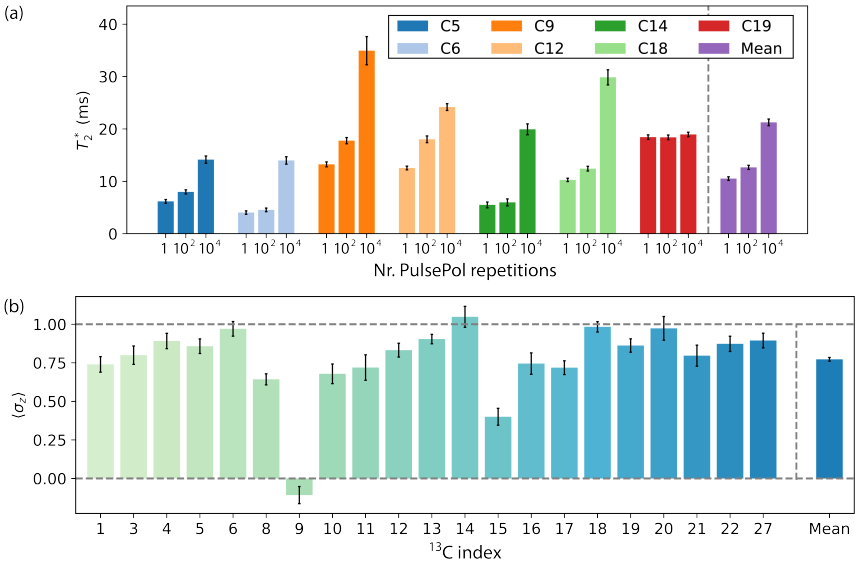

Figure 8.1: **Extending nuclear spin capabilities: Preliminary data (a)** ^{13}C T_2^* measurements after spin-bath polarisation. The mean T_2^* time increases from 10.5(3) ms to 21.2(6) ms after 10000 PulsePol repetitions (τ = 0.412 μs, N = 4, Ch. 7). C19 shows no improvement as it is limited by C9, which does not polarise for these PulsePol parameters (see below). **(b)** Initialisation and read-out of a 21 nuclear spin register using PulsePol and either DD/DDf-based read-out (Ch. 5) or NNRO (Ch. 7). The data is corrected for read-out errors. The mean single-qubit initialisation fidelity with $|\uparrow\rangle$ is 0.882(6) after 10000 PulsePol repetitions (N = 4, τ=0.412 μs). C9 does not polarise for these parameters due to its large $A_\parallel$ = 213 kHz. Carbon indices follow the labelling of Ch. 6. For further measurement details see the M.Sc. thesis of Asier Galicia [12]. Measurements performed by AG and CEB.

approaches can likely be applied to the DDrf gates developed in Ch. 5. A drawback of these techniques is that they typically incorporate a larger number of decoupling pulses and/or sub-nanosecond temporal resolution, imposing additional technical requirements [17].

A complementary approach is to leverage the precise knowledge of the system Hamiltonian (Ch. 6). Most simply, this means judiciously selecting gate parameters to minimise crosstalk to other known spins. More sophisticated approaches could use this Hamiltonian in novel gate designs built upon methods such as optimal control [18–20].

8.2.3. QUANTUM SIMULATIONS WITH TENS OF NUCLEAR SPIN QUBITS

In Chs. 6 and 7, we characterised a system of 27 ^{13}C nuclear spins, and then performed a quantum simulation of a many-body-localised discrete time crystal (MBL DTC) using a 1D chain of 9 of those spins. Here I will discuss immediate opportunities for this platform, and avenues to reach ~50 spins: a regime in which numerical simulations of quantum dynamics can approach intractability [21–24].

Considering the range of implementable Hamiltonians in this experiment, we may now be able to investigate a number of open questions. For example, some regimes of

the driven Ising model have yet to be experimentally accessed, such as the topologically-protected 0π-Paramagnet phase[25,26]. Considering discrete time crystals, MBL is thought to be the only mechanism which can stabilise a DTC to arbitrary times (Ch. 7). However, disordered systems in the critical regime[†] are speculated to exhibit some robustness, due to slow power-law thermalisation arising from rare resonant spin exchange[27,28]. This regime can be accessed by using the full $d = 3$ dimensionality of our system. Many aspects of the critical DTC remain unexplored, with previous experiments being performed on ensembles which were unable to address individual spins[29–31].

A range of further Hamiltonians may be engineered through Floquet engineering and/or isolating chosen subsets of spins[32–34]. For example, we may be able to shed new light on spin diffusion in disordered dipolar systems and the resulting emergent hydrodynamics[35–37]. In general, single-spin control allows for complex state preparation and the measurement of selected multi-qubit operators, which could be used to witness entanglement dynamics[38,39].

I now consider a path to extend the system size. This requires identifying further spins which are weakly coupled to the NV centre (and hence were not detected in Chs. 5 and 6). Such weak couplings currently preclude high-fidelity control via the electron spin, but nuclear-nuclear read-out (NNRO, Ch. 7) provides an alternative avenue for spin detection and read-out. Furthermore, the use of dynamic nuclear polarisation techniques (Ch. 7) allows for wide-scale initialization[12,40–43]. As a first step towards this goal, Fig. 8.1(b) shows the initialisation and read-out of a 21 spin system.

In principle, concatenating multiple rounds of NNRO enables iterative state mapping from a distant target using a chain of spins (repeater-like). A challenge is that — due to their weak coupling to the electron — those distant spins have increasingly degenerate resonance frequencies. Although the individual nature of spectrally degenerate spins can be confirmed by their nuclear-nuclear couplings (Ch. 6), degeneracy introduces challenges for selective control. However, with careful optimisation, an increase in the system size by at least a factor ~2 appears feasible. This would place the system in a fascinating regime where numerical simulation of the complete quantum state is essentially intractable for classical computers[21–24].

8.3. LARGE-SCALE QUANTUM INFORMATION PROCESSING WITH DEFECT-BASED QUANTUM NETWORKS

In the previous section I described near-term experiments which build upon the results of this thesis. Here I will consider the longer-term prospects for distributed quantum information processing (DQIP) using defect-based quantum networks.

In Sec. 8.2.3, I argued that a 50+ spin quantum simulator is feasible using a 'single NV-many ^{13}C' system (Chs. 5, 6, 7). However, it is unlikely that this approach will realise scalable, error-corrected computation. An inevitable bottleneck is that only the electron spin can be directly initialised and read-out, meaning that the system read-out duration increases with size (a major issue for error correction). An alternative approach — widely studied within the community and discussed within Ch. 4 — is to build a modular

[†]The critical regime is characterised by interactions that fall off as $1/r^d$ for a system of dimension d[26].

system (Fig. 8.2(a)), in which *each* module (or 'node') contains one or more communication qubit (here, the electron spin) alongside a number of data qubits (or 'quantum memories', ^{13}C nuclear spins). All nodes can run on a parallel clock cycle, such that adding further modules does not increase the cycle time. Spatially-separated nodes can be interfaced ('linked') through photonic entanglement, realising a quantum network for distributed computation[44–47].

DQIP can be broken down into two key aspects: the processing and storage of quantum states within each module, and the distribution of high-fidelity entanglement between nodes ('remote' entanglement). Alongside spins in diamonds, a number of experimental platforms have demonstrated key building blocks towards quantum networks[48–57]. Theoretical work has shown that universal fault-tolerant quantum computation is possible in such a network using a distributed surface code[44,45].

Quantum networks based on NV centres in diamond are currently among the most advanced. Recent work has demonstrated deterministic entanglement delivery[3] and entanglement distillation[58] within a two-node network, and entanglement swapping[59] and teleportation[60] in the first three-node network of its kind. However, further progress is needed to enable scalable DQIP with this platform. Two key challenges are that the optical interface is inefficient, and the data qubits are either fragile or have slow associated gate durations[61].

8.3.1. DISTRIBUTING ENTANGLEMENT BETWEEN NETWORK NODES

At present, generating remote entanglement is the slowest process in NV-based quantum networks. As outlined in Ch. 4, this process relies on the emission and subsequent detection of indistinguishable photons from each node. There are two key inefficiencies. First, the NV centre Debye-Waller factor is only 0.03, meaning that the vast majority of emitted photons are emitted incoherently in the phonon-sideband[62,63]. Second, collection efficiencies for solid-immersion lens devices are typically ~5%[64]. Therefore, the probability that an optical excitation of the NV centre results in the detection of a coherently emitted photon ('coherent collection efficiency', CCE) is only ~1/1000[3,59,64]. While low success probabilities for remote entanglement do not (directly[†]) impact the fidelity of a heralded link, decoherence of data qubits during this slow process is one of the major error channels in the system. Increasing the remote entangling rates would thus improve both the speed and performance of NV-based DQIP.

A promising route is to couple the NV centre to an optical cavity. This addresses both of the aforementioned inefficiencies: Purcell enhancement leads to a higher emission fraction in the ZPL, and the cavity preferentially emits in a well-defined spatial mode which can be efficiently collected[66,67]. There are challenges, however. Charge noise induces spectral diffusion of near-surface NV centres, obstructing integration in nanophotonic devices[68,69]. A widespread effort is focused on mitigating this surface noise[70–72], but at present, optically coherent NV centres have only been observed in bulk-like material[69]. Fortunately, Fabry-Pérot micro-cavities can accommodate this, using few-μm-thick diamond membranes[69,73–75]. In a recent breakthrough, this approach has shown Purcell enhancement of optically coherent NV centres[76], but performance-limiting sys-

[†]Indirectly, low success probabilities necessitate single-photon protocols to achieve practical entangling rates, at the cost of intrinsically reduced fidelities[3,65].

tem vibrations must be overcome. Feasible system improvements are anticipated to increase the CCE to ~1/10[75,76]. Combined with the results of Ch. 4, this would give a network number N_{network} ~1000, an exciting regime for high-fidelity DQIP.

Ultimately, however, nanophotonic cavities may be preferable to micro-cavities. Their compatibility with photonic integrated circuits provides a compelling route towards chip-scale devices hosting many emitters[77–79]. To follow this approach, surface-effects must be mitigated for NV centres, or alternative defects can be used which are amenable to such integration. Here, group-IV colour centres in diamond have emerged as promising candidates[61,80]. Alongside good intrinsic optical properties, they show no first-order sensitivity to electric fields due to inversion-symmetry[81–85]. Recent work has shown strong-coupling to photonic crystal cavities — with coherent cooperativities ~100 for the SiV^- centre[86,87] — and integration of single defects in 128 waveguides on a photonic chip (albeit without demonstrating interactions between them)[79]. The strong-coupling regime of cavity quantum electrodynamics offers new prospects using reflection-based spin-photon entangling schemes[86,88], which led to the demonstration of memory-enhanced quantum communication using the SiV^- centre[87].

To employ group-IV defects for DQIP, the next challenge is to obtain spin properties matching their exciting optical properties. Compared with the NV centre, the increased complexity of their ground-state spin structure[61,80,89] imposes complications such as dilution refrigerator operation or all-optical control[90–92]. Moreover, their spin-1/2 nature hinders DD-based two-qubit gates[5,86]. Thus, in the coming years, novel control techniques and device designs must be investigated. Alternatively, a wide variety of other defects are being investigated, and perhaps one will be discovered which brings the 'best of both worlds': combining the spin properties of the NV^- centre with the optical properties of the group-IV colour centres[93,94]. It should be mentioned that this might not be in diamond: recent work on defects in silicon carbide[95–97], and rare-earth ions in other solid-state crystals[98,99] show promise. Silicon carbide is a particularly interesting host material due to its use in the electronics industry, with well-developed techniques for wafer production, controlled doping and integrated circuit processing[100].

8.3.2. INTRA-NODE QUANTUM INFORMATION PROCESSING

In Sec 8.2.2, I discussed routes which may enable higher two-qubit gate fidelities within our platform. Here, I will focus on another major challenge for the network-based approach: robust data qubits.

While exceptional coherence properties have been demonstrated for nuclear-spin qubits[1,5,101–103], in a network setting, the stochastic nature of remote entanglement adds an extra challenge. With 'always-on' interactions, uncontrolled dynamics of the communication qubit induce data qubit dephasing. In Ch. 4, we utilised isotopic engineering to reduce the NV-^{13}C coupling, such that a ^{13}C data qubit was made more robust to those stochastic dynamics. However, further improvements to the robustness and operation speeds are likely possible.

First, the entanglement generation sequence can be optimised to minimise both the stochasticity and the effect this has on the data qubit. For example, recent work used high magnetic fields to reduce the duration per entangling attempt (limited by the ^{13}C Larmor period), decreasing the time for which the ^{13}C was sensitive to stochastic events

(alongside the absolute time per successful link)[59]. Increasing the speed and fidelity of NV reinitialisation would be similarly beneficial, and may be achieved by tuning of the excited state energy levels[104–106]. Finally, the fidelity of echo pulses can be improved by optimal control and active MW power stabilisation[18–20,107].

Second, alternate approaches can be taken to achieve reduced couplings between the communication and data qubits. In Ch. 4, we saw that reducing this coupling to $A_\parallel$ ~80 Hz through isotopic purification allows for ~10^5 entangling attempts before decoherence of an arbitrary quantum state encoded into the ^{13}C spin. This constitutes a major improvement on the prior state-of-the-art, paving the way for deterministic non-local two-qubit operations and parity measurements. There are caveats to isotopic purification, however. In particular, electron-nuclear gates are slow, as they are limited by the perpendicular hyperfine coupling, $A_\perp$, which is typically comparable to $A_\parallel$ (two-qubit gate duration of ~25 ms in Ch. 4). While those gate speeds can be tolerated in smaller demonstrations, they will ultimately limit achievable computation rates.

Ideally, weak-couplings would be combined with fast two-qubit logic. While this seems somewhat paradoxical in a system with always-on interactions, there are mechanisms which allow this. For example, decoherence-protected subspaces (DPS) suppress dephasing of an encoded qubit while maintaining the operation speeds of the constituent qubits[108]. Thus, few-kHz effective couplings could be achieved even in natural abundance ^{13}C devices[109]. The major challenge here is that each node must yield 3-5 well-controlled DPS for error-correction[44,45]. Using current methods for device fabrication and qubit control, this would be highly probabilistic.

A more radical approach is to use pairs of electron spins ('coupled defects')[110,111] (Fig. 8.2(b)). The first electron spin acts as the communication qubit, while the second spin — at a distance of ~10 nm — is a 'bus qubit' which hosts a register of nuclear spins. These data qubits would exhibit $O(100)$ Hz couplings to the optically-active qubit, but the electron spin couplings are a factor ~3000 larger (γ_e/γ_{13C}). Thus, the bus qubit could mediate fast operations between the communication qubit and the data qubits. A further benefit is that it could also be used to create a frozen core for the data qubits during remote entanglement generation[5,112,113].

The major challenges for this approach are the creation of optically coherent coupled defects, and the independent control of those defects. Independent MW control of a pair of NV centres might be achieved by either using different defect orientations[110], or creating large magnetic field gradients[114]. However, achieving sufficient isolation of the optical transitions appears challenging[115,116]. Furthermore, current implantation techniques — the most obvious path for creating coupled defects — do not routinely create NV centres with good optical properties[117].

An appealing approach is to use different electron spin species for each role. For example, a group-IV colour centre acting as a communication qubit, which is magnetically coupled to an NV bus qubit. The different addressing frequencies for each species would prevent crosstalk. Importantly, lifetime-limited linewidths have been observed for implanted group-IV colour centres[79,86,118], while the optical coherence requirements for the bus qubit are not as stringent. It may even be possible to use a bus qubit without an optical interface, such as a P1 centre[119].

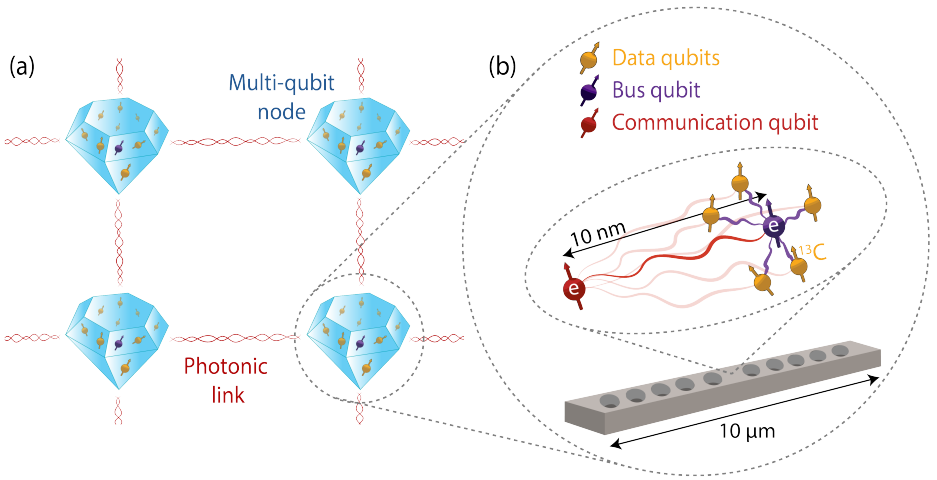

Figure 8.2: **DQIP using defect spins.** **(a)** Individual modules host a communication qubit which facilitates remote (inter-node) entanglement via photons, alongside data qubits to store and process quantum states. Fault-tolerant quantum computation is possible using a distributed surface code for quantum error correction, for which the four nodes shown here act as a unit cell [44,45,120]. **(b)** Envisioned quantum network node utilising coupled-defect spins in photonic crystal cavities. The communication qubit (red electron spin) is coupled to the cavity, providing an efficient optical interface. A bus qubit (purple electron spin) is magnetically coupled (purple lines) by at least tens-of-kHz to a register of proximal ^{13}C data qubits (yellow spins), enabling quantum control. Importantly, the two electron spins are also magnetically coupled by ~100 kHz (dark red line), such that the bus qubit can mediate entanglement between the communication qubit and the data qubits. However, the data qubits have sub-kHz couplings (faded red lines) to the communication qubit, such that they are robust to stochastic dynamics during remote entanglement generation. As the communication and bus qubits are of different species (e.g. group-IV and NV$^-$, respectively), they can be independently addressed, and the bus qubit is also unaffected by the remote entanglement sequence.

REFERENCES

[1] P. C. Maurer *et al., Room-Temperature Quantum Bit Memory Exceeding One Second,* Science **336**, 1283 (2012).

[2] S. Baier *et al., Orbital and spin dynamics of single neutrally-charged nitrogen-vacancy centers in diamond,* Phys. Rev. Lett. **125**, 193601 (2020).

[3] P. C. Humphreys *et al., Deterministic delivery of remote entanglement on a quantum network,* Nature **558**, 268 (2018).

[4] M. H. Abobeih *et al., One-second coherence for a single electron spin coupled to a multi-qubit nuclear-spin environment,* Nat. Commun. **9**, 1 (2018).

[5] C. E. Bradley *et al., A ten-qubit solid-state spin register with quantum memory up to one minute,* Phys. Rev. X **9**, 031045 (2019).

[6] N. Zhao, J.-L. Hu, S.-W. Ho, J. T. Wan and R. Liu, *Atomic-scale magnetometry of distant nuclear spin clusters via nitrogen-vacancy spin in diamond,* Nat. Nanotechnol. **6**, 242 (2011).

[7] F. Shi *et al., Sensing and atomic-scale structure analysis of single nuclear-spin clusters in diamond,* Nat. Phys. **10**, 21 (2014).

[8] H. Bartling *et al., Coherence and entanglement of inherently long-lived spin pairs in diamond,* arXiv:2103.07961 (2021).

[9] K. Ohno *et al., Engineering shallow spins in diamond with nitrogen delta-doping,* Appl. Phys. Lett. **101**, 082413 (2012).

[10] B. A. Myers *et al., Probing surface noise with depth-calibrated spins in diamond,* Phys. Rev. Lett. **113**, 027602 (2014).

[11] T. Unden *et al., Coherent control of solid state nuclear spin nano-ensembles,* NPJ Quantum Inf. **4**, 1 (2018).

[12] A. Galicia, *On the hyperpolarisation of 13c spins in diamond,* M.Sc. Thesis, TUDelft (2021).

[13] Z.-Y. Wang, J. Casanova and M. B. Plenio, *Delayed entanglement echo for individual control of a large number of nuclear spins,* Nat. Commun. **8**, 14660 (2017).

[14] J. Casanova, Z.-Y. Wang, J. Haase and M. Plenio, *Robust dynamical decoupling sequences for individual-nuclear-spin addressing,* Phy. Rev. A **92**, 042304 (2015).

[15] T. K. Unden, D. Louzon, M. Zwolak, W. H. Zurek and F. Jelezko, *Revealing the emergence of classicality using nitrogen-vacancy centers,* Phys. Rev. Lett. **123**, 140402 (2019).

[16] W. Dong, F. Calderon-Vargas and S. E. Economou, *Precise high-fidelity electron–nuclear spin entangling gates in nv centers via hybrid dynamical decoupling sequences,* New J. Phys. **22**, 073059 (2020).

[17] J. Zopes *et al.*, *High-resolution quantum sensing with shaped control pulses,* Phys. Rev. Lett. **119**, 260501 (2017).

[18] F. Dolde *et al.*, *High-fidelity spin entanglement using optimal control,* Nat. Commun. **5**, 3371 (2014).

[19] X. Rong *et al.*, *Experimental fault-tolerant universal quantum gates with solid-state spins under ambient conditions,* Nat. Commun. **6**, 8748 (2015).

[20] P. Rembold *et al.*, *Introduction to quantum optimal control for quantum sensing with nitrogen-vacancy centers in diamond,* AVS Quant. Sci. **2**, 024701 (2020).

[21] S. Aaronson and A. Arkhipov, *The computational complexity of linear optics,* in *Proceedings of the forty-third annual ACM symposium on Theory of computing* (2011) pp. 333–342.

[22] J. Preskill, *Quantum computing and the entanglement frontier,* arXiv:1203.5813 (2012).

[23] F. Arute *et al.*, *Quantum supremacy using a programmable superconducting processor,* Nature **574**, 505 (2019).

[24] H.-S. Zhong *et al.*, *Quantum computational advantage using photons,* Science **370**, 1460 (2020).

[25] C. W. von Keyserlingk and S. L. Sondhi, *Phase structure of one-dimensional interacting floquet systems. i. abelian symmetry-protected topological phases,* Phys. Rev. B **93**, 245145 (2016).

[26] V. Khemani, R. Moessner and S. L. Sondhi, *A brief history of time crystals,* arXiv:1910.10745 (2019).

[27] P. W. Anderson, *Absence of diffusion in certain random lattices,* Phys. Rev. **109**, 1492 (1958).

[28] W. W. Ho, S. Choi, M. D. Lukin and D. A. Abanin, *Critical time crystals in dipolar systems,* Phys. Rev. Lett. **119**, 010602 (2017).

[29] S. Choi *et al.*, *Observation of discrete time-crystalline order in a disordered dipolar many-body system,* Nature **543**, 221 (2017).

[30] G. Kucsko *et al.*, *Critical thermalization of a disordered dipolar spin system in diamond,* Phys. Rev. Lett. **121**, 023601 (2018).

[31] J. Choi *et al.*, *Probing quantum thermalization of a disordered dipolar spin ensemble with discrete time-crystalline order,* Phys. Rev. Lett. **122**, 043603 (2019).

[32] M. Bukov, L. D'Alessio and A. Polkovnikov, *Universal high-frequency behavior of periodically driven systems: from dynamical stabilization to floquet engineering,* Adv. Phys. **64**, 139 (2015).

[33] T. Kuwahara, T. Mori and K. Saito, *Floquet–magnus theory and generic transient dynamics in periodically driven many-body quantum systems,* Ann. Phys. **367**, 96 (2016).

[34] C. Monroe *et al., Programmable quantum simulations of spin systems with trapped ions,* Rev. Mod. Phys. **93**, 025001 (2021).

[35] C. Zu *et al., Emergent hydrodynamics in a strongly interacting dipolar spin ensemble,* arXiv:2104.07678 (2021).

[36] M. Joshi *et al., Observing emergent hydrodynamics in a long-range quantum magnet,* arXiv:2107.00033 (2021).

[37] D. Wei *et al., Quantum gas microscopy of kardar-parisi-zhang superdiffusion,* arXiv:2107.00038 (2021).

[38] A. Lukin *et al., Probing entanglement in a many-body–localized system,* Science **364**, 256 (2019).

[39] T. Brydges *et al., Probing rényi entanglement entropy via randomized measurements,* Science **364**, 260 (2019).

[40] I. Schwartz *et al., Robust optical polarization of nuclear spin baths using hamiltonian engineering of nitrogen-vacancy center quantum dynamics,* Sci. Adv. **4**, eaat8978 (2018).

[41] J. E. Lang *et al., Quantum bath control with nuclear spin state selectivity via pulse-adjusted dynamical decoupling,* Phys. Rev. Lett. **123**, 210401 (2019).

[42] J. Randall *et al., Observation of a many-body-localized discrete time crystal with a programmable spin-based quantum simulator,* arXiv:2107.00736 (2021).

[43] O. Whaites, J. Randall, T. Taminiau and T. Monteiro, *Adiabatic dynamical-decoupling based control of nuclear spin registers,* arXiv:2107.01931 (2021).

[44] N. H. Nickerson, Y. Li and S. C. Benjamin, *Topological quantum computing with a very noisy network and local error rates approaching one percent,* Nat. Commun. **4**, 1756 (2013).

[45] N. H. Nickerson, J. F. Fitzsimons and S. C. Benjamin, *Freely scalable quantum technologies using cells of 5-to-50 qubits with very lossy and noisy photonic links,* Phys. Rev. X **4**, 041041 (2014).

[46] C. Monroe *et al., Large-scale modular quantum-computer architecture with atomic memory and photonic interconnects,* Phys. Rev. A **89**, 022317 (2014).

[47] S. Wehner, D. Elkouss and R. Hanson, *Quantum internet: A vision for the road ahead,* Science **362** (2018).

[48] S. Ritter *et al., An elementary quantum network of single atoms in optical cavities,* Nature **484**, 195 (2012).

[49] D. Hucul *et al.*, *Modular entanglement of atomic qubits using photons and phonons,* Nat. Phys. **11**, 37 (2015).

[50] A. Delteil *et al.*, *Generation of heralded entanglement between distant hole spins,* Nat. Phys. **12**, 218 (2016).

[51] W. Rosenfeld *et al.*, *Event-ready bell test using entangled atoms simultaneously closing detection and locality loopholes,* Phys. Rev. Lett. **119**, 010402 (2017).

[52] R. Riedinger *et al.*, *Remote quantum entanglement between two micromechanical oscillators,* Nature **556**, 473 (2018).

[53] L. Stephenson *et al.*, *High-rate, high-fidelity entanglement of qubits across an elementary quantum network,* Phys. Rev. Lett. **124**, 110501 (2020).

[54] Y. Yu *et al.*, *Entanglement of two quantum memories via fibres over dozens of kilometres,* Nature **578**, 240 (2020).

[55] P. Magnard *et al.*, *Microwave quantum link between superconducting circuits housed in spatially separated cryogenic systems,* Phys. Rev. Lett. **125**, 260502 (2020).

[56] L. D. Burkhart *et al.*, *Error-detected state transfer and entanglement in a superconducting quantum network,* PRX Quantum **2**, 030321 (2021).

[57] Y. Zhong *et al.*, *Deterministic multi-qubit entanglement in a quantum network,* Nature **590**, 571 (2021).

[58] N. Kalb *et al.*, *Entanglement distillation between solid-state quantum network nodes,* Science **356**, 928 (2017).

[59] M. Pompili *et al.*, *Realization of a multinode quantum network of remote solid-state qubits,* Science **372**, 259 (2021).

[60] S. L. N. Hermans *et al.*, *Qubit teleportation between non-neighbouring nodes in a quantum network,* In preparation (2021).

[61] M. Ruf, N. H. Wan, H. Choi, D. Englund and R. Hanson, *Quantum networks based on color centers in diamond,* arXiv:2105.04341 (2021).

[62] G. Davies, *Vibronic spectra in diamond,* Journal of Physics C: Solid state physics **7**, 3797 (1974).

[63] A. Faraon, P. E. Barclay, C. Santori, K.-M. C. Fu and R. G. Beausoleil, *Resonant enhancement of the zero-phonon emission from a colour centre in a diamond cavity,* Nat. Photonics **5**, 301 (2011).

[64] H. Bernien *et al.*, *Heralded entanglement between solid-state qubits separated by three metres,* Nature **497**, 86 (2013).

[65] C. Cabrillo, J. I. Cirac, P. Garcia-Fernandez and P. Zoller, *Creation of entangled states of distant atoms by interference,* Phys. Rev. A **59**, 1025 (1999).

[66] A. Reiserer and G. Rempe, *Cavity-based quantum networks with single atoms and optical photons,* Rev. Mod. Phys. **87**, 1379 (2015).

[67] E. Janitz, M. K. Bhaskar and L. Childress, *Cavity quantum electrodynamics with color centers in diamond,* Optica **7**, 1232 (2020).

[68] M. W. Doherty *et al.*, *The nitrogen-vacancy colour centre in diamond,* Phys. Rep. **528**, 1 (2013).

[69] M. Ruf *et al.*, *Optically coherent nitrogen-vacancy centers in micrometer-thin etched diamond membranes,* Nano Lett. **19**, 3987 (2019).

[70] D. Bluvstein, Z. Zhang and A. C. B. Jayich, *Identifying and mitigating charge instabilities in shallow diamond nitrogen-vacancy centers,* Phys. Rev. Lett. **122**, 076101 (2019).

[71] S. Sangtawesin *et al.*, *Origins of diamond surface noise probed by correlating single-spin measurements with surface spectroscopy,* Phys. Rev. X **9**, 031052 (2019).

[72] H. Fotso, A. Feiguin, D. Awschalom and V. Dobrovitski, *Suppressing spectral diffusion of emitted photons with optical pulses,* Phys. Rev. Lett. **116**, 033603 (2016).

[73] E. Janitz *et al.*, *Fabry-perot microcavity for diamond-based photonics,* Phys. Rev. A **92**, 043844 (2015).

[74] S. Bogdanović *et al.*, *Design and low-temperature characterization of a tunable microcavity for diamond-based quantum networks,* Appl. Phys. Lett. **110**, 171103 (2017).

[75] D. Riedel *et al.*, *Deterministic enhancement of coherent photon generation from a nitrogen-vacancy center in ultrapure diamond,* Phys. Rev. X **7**, 031040 (2017).

[76] M. Ruf, M. J. Weaver, S. B. van Dam and R. Hanson, *Resonant excitation and purcell enhancement of coherent nitrogen-vacancy centers coupled to a fabry-perot microcavity,* Phys. Rev. Appl. **15**, 024049 (2021).

[77] J.-H. Kim, S. Aghaeimeibodi, J. Carolan, D. Englund and E. Waks, *Hybrid integration methods for on-chip quantum photonics,* Optica **7**, 291 (2020).

[78] A. W. Elshaari, W. Pernice, K. Srinivasan, O. Benson and V. Zwiller, *Hybrid integrated quantum photonic circuits,* Nat. Photonics **14**, 285 (2020).

[79] N. H. Wan *et al.*, *Large-scale integration of artificial atoms in hybrid photonic circuits,* Nature **583**, 226 (2020).

[80] C. Bradac, W. Gao, J. Forneris, M. E. Trusheim and I. Aharonovich, *Quantum nanophotonics with group iv defects in diamond,* Nat. Commun. **10**, 1 (2019).

[81] T. Iwasaki *et al.*, *Germanium-vacancy single color centers in diamond,* Sci. Rep. **5**, 12882 (2015).

[82] R. E. Evans, A. Sipahigil, D. D. Sukachev, A. S. Zibrov and M. D. Lukin, *Narrow-linewidth homogeneous optical emitters in diamond nanostructures via silicon ion implantation,* Phys. Rev. Appl. **5**, 044010 (2016).

[83] G. Thiering and A. Gali, *Ab initio magneto-optical spectrum of group-iv vacancy color centers in diamond,* Phys. Rev. X **8**, 021063 (2018).

[84] M. E. Trusheim *et al.*, *Lead-related quantum emitters in diamond,* Phys. Rev. B **99**, 075430 (2019).

[85] M. E. Trusheim *et al.*, *Transform-limited photons from a coherent tin-vacancy spin in diamond,* Phys. Rev. Lett **124**, 023602 (2020).

[86] C. Nguyen *et al.*, *Quantum network nodes based on diamond qubits with an efficient nanophotonic interface,* Phys. Rev. Lett. **123**, 183602 (2019).

[87] M. K. Bhaskar *et al.*, *Experimental demonstration of memory-enhanced quantum communication,* Nature **580**, 60 (2020).

[88] S. Daiss *et al.*, *A quantum-logic gate between distant quantum-network modules,* Science **371**, 614 (2021).

[89] C. Hepp *et al.*, *Electronic structure of the silicon vacancy color center in diamond,* Phys. Rev. Lett. **112**, 036405 (2014).

[90] D. D. Sukachev *et al.*, *Silicon-vacancy spin qubit in diamond: a quantum memory exceeding 10 ms with single-shot state readout,* Phys. Rev. Lett. **119**, 223602 (2017).

[91] E. Takou and S. E. Economou, *Optical control protocols for high-fidelity spin rotations of single siv$^-$ and snv$^-$ centers in diamond,* arXiv:2105.08594 (2021).

[92] R. Debroux *et al.*, *Quantum control of the tin-vacancy spin qubit in diamond,* arXiv:2106.00723 (2021).

[93] D. D. Awschalom, R. Hanson, J. Wrachtrup and B. B. Zhou, *Quantum technologies with optically interfaced solid-state spins,* Nat. Photonics **12**, 516 (2018).

[94] L. C. Bassett, A. Alkauskas, A. L. Exarhos and K.-M. C. Fu, *Quantum defects by design,* Nanophotonics **8**, 1867 (2019).

[95] R. Nagy *et al.*, *High-fidelity spin and optical control of single silicon-vacancy centres in silicon carbide,* Nat. Commun. **10**, 1 (2019).

[96] D. M. Lukin, M. A. Guidry and J. Vučković, *Integrated quantum photonics with silicon carbide: challenges and prospects,* PRX Quantum **1**, 020102 (2020).

[97] A. Bourassa *et al.*, *Entanglement and control of single nuclear spins in isotopically engineered silicon carbide,* Nat. Mater. **19**, 1319 (2020).

[98] J. M. Kindem *et al.*, *Control and single-shot readout of an ion embedded in a nanophotonic cavity,* Nature **580**, 201 (2020).

[99] B. Merkel, A. Ulanowski and A. Reiserer, *Coherent and purcell-enhanced emission from erbium dopants in a cryogenic high-q resonator,* Phys. Rev. X **10**, 041025 (2020).

[100] N. T. Son *et al.*, *Developing silicon carbide for quantum spintronics,* Appl. Phys. Lett. **116**, 190501 (2020).

[101] S. Yang *et al.*, *High-fidelity transfer and storage of photon states in a single nuclear spin,* Nat. Photonics **10**, 507 (2016).

[102] G. Wolfowicz *et al.*, *29si nuclear spins as a resource for donor spin qubits in silicon,* New J. Phys. **18**, 023021 (2016).

[103] J. T. Muhonen *et al.*, *Storing quantum information for 30 seconds in a nanoelectronic device,* Nat. Nanotechnol. **9**, 986 (2014).

[104] P. Tamarat *et al.*, *Spin-flip and spin-conserving optical transitions of the nitrogen-vacancy centre in diamond,* New J. Phys. **10**, 045004 (2008).

[105] L. Bassett, F. Heremans, C. Yale, B. Buckley and D. Awschalom, *Electrical tuning of single nitrogen-vacancy center optical transitions enhanced by photoinduced fields,* Phys. Rev. Lett. **107**, 266403 (2011).

[106] H. Bernien *et al.*, *Two-photon quantum interference from separate nitrogen vacancy centers in diamond,* Phys. Rev. Lett. **108**, 043604 (2012).

[107] C. Yang *et al.*, *Silicon qubit fidelities approaching incoherent noise limits via pulse engineering,* Nat. Electron. **2**, 151 (2019).

[108] D. A. Lidar, I. L. Chuang and K. B. Whaley, *Decoherence-free subspaces for quantum computation,* Phys. Rev. Lett. **81**, 2594 (1998).

[109] A. Reiserer *et al.*, *Robust quantum-network memory using decoherence-protected subspaces of nuclear spins,* Phys. Rev. X **6**, 021040 (2016).

[110] F. Dolde *et al.*, *Room-temperature entanglement between single defect spins in diamond,* Nat. Phys. **9**, 139 (2013).

[111] M. J. Degen, *On the creation, coherence and entanglement of multi-defect quantum registers in diamond,* Ph.D. Thesis, TUDelft (2021).

[112] G. Khutsishvili, *Spin diffusion and magnetic relaxation of nuclei,* Sov. Phys. JETP **15**, 909 (1962).

[113] R. Guichard, S. Balian, G. Wolfowicz, P. Mortemousque and T. Monteiro, *Decoherence of nuclear spins in the frozen core of an electron spin,* Phys. Rev. B **91**, 214303 (2015).

[114] E. Kawakami *et al.*, *Electrical control of a long-lived spin qubit in a si/sige quantum dot,* Nat. Nanotechnol. **9**, 666 (2014).

[115] B. Hensen, *Measurement-based quantum computation with the nitrogen-vacancy centre in diamond,* M.Sc. Thesis, TUDelft (2011).

[116] S. Loenen, *Improving single-shot readout for diamond quantum processors,* M.Sc. Thesis, TUEindhoven (2019).

[117] S. B. van Dam *et al.*, *Optical coherence of diamond nitrogen-vacancy centers formed by ion implantation and annealing,* Phys. Rev. B **99**, 161203 (2019).

[118] A. E. Rugar *et al.*, *Generation of tin-vacancy centers in diamond via shallow ion implantation and subsequent diamond overgrowth,* Nano Lett. **20**, 1614 (2020).

[119] M. Degen *et al.*, *Entanglement of dark electron-nuclear spin defects in diamond,* Nat. Commun. **12**, 1 (2021).

[120] S. de Bone, R. Ouyang, K. Goodenough and D. Elkouss, *Protocols for creating and distilling multipartite ghz states with bell pairs,* IEEE Trans. Quantum Eng. **1**, 1 (2020).

ACKNOWLEDGEMENTS

Writing these final few pages of my thesis culminates a journey which began with a visit to Delft on a bitterly cold morning in December 2016. The warm welcome I received — and the QuTech Christmas party that evening — convinced me that there would be no better place to do my PhD. I am grateful to all who made this journey such a fun one.

First, **Tim Taminiau**. Tim, just a few weeks after our first meeting in Delft, we had a second discussion. This time I was back in London, and you'd just managed to get into a temporary apartment in Colombia after the unexpected early arrival of Samuel. Despite clearly having hardly slept, you patiently explained all sorts of wonderful possibilities with carbon spins and NV centres. That patience and enthusiasm have been recurring themes throughout my PhD. I have learnt so much from you over these years, both of quantum physics, but also of the right way to 'do' science. Most of all, I'm grateful for all the spontaneous discussions of spins and new ideas. I'm sure the group will continue to prosper under your guidance. Thank you for everything!

Ronald Hanson, thank you for being my promotor, and for all the advice, guidance and support. Thanks also for letting me join the NV^0 project, and for all the fun discussions from it. The environment that you created in both Team Diamond and then in QuTech as scientific director was a big part of my enjoyment during my time here. The *'problem = challenge'* mantra will live long in my mind!

To the remainder of my committee, **Fedor Jelezko**, **Michel Orrit**, **Leo DiCarlo**, and **Simon Gröblacher**, thank you for making the time to read and assess this thesis, and for joining the defence ceremony. **Lieven Vandersypen**, thank you for agreeing to be on stand-by, and for all that you continue to do for QuTech as the new scientific director.

Slava Dobrovitski, your quantum dynamics seminars served as my crash-course into the world of spins. Thanks for all the discussions, be it of language, culture, or, of course, science (especially your insights into NV^0). Though I often wonder if *I* should be the one visiting *your* office to ask about the nuances of English, I'm glad you do it nevertheless!

The wonderful group of people which form **Team Diamond** have made up a good chunk of my colleagues and friends here in the Netherlands. **Joe Randall**, you joined just a couple of months after me, and we will now finish just a couple of months apart. The contents of this thesis reflect a lot of hours spent together in the lab, and, more recently, on Zoom. I think we formed a pretty good 'British contingent'. Thanks for all that you taught me in the lab, the insights that you brought, and the Mathematica wizardry. Getting the first DDrf gate working was a special moment, and it's been great to work on the quantum simulations effort. Thanks also for all the fun times, either armed with a cuppa or beer in hand! All the best to you and Lucy for the UK. Be it in academia or industry, I'm sure you'll do a brilliant job.

Mohamed Abobeih, we also spent many hours together in the lab and the office. Thanks for teaching me how to use the setup, and for everything else that followed. I'm always grateful for your laid-back outlook on life, and for the discussions of science, its

politics, and all the gossip you somehow picked up on the grapevine. Finding good food is never hard when you're around (apart from the WB lunches)! Good luck in Boston, I'm quite sure our paths will overlap again before too long.

Maarten Degen, we shared a lot of experiences together, from our first attempts trying to code up laser scans, to an epic trip around the Norwegian fjords, and *that* night at ADE. Thanks for the help with M2 and for your all-round kindness. I'm excited to see what you decide to do next.

Simon Baier, we had fun adventures both in the cleanroom (blind leading the blind?!) and then trying to unravel the mysteries of NV^0. After several months building a new setup, it was incredibly motivating to join a project in which every run of the experiment added new intrigue. Your positivity is infectious - everything will be 'fan-tas-tik' for your future students! All the best for you, Katrin, Florian and David in Innsbruck.

I had the pleasure to supervise two Master's students, **Remon Berrevoets** and **Asier Galicia**. I learnt a lot from both of you: I hope the feeling is at least somewhat mutual! Remon, designing funky new gate sequences was a lot of fun, and your simulations proved to be an enlightening result in the DDrf work. I'm glad that you're still around at QuTech, and excited to see what comes next out of the QKD demonstrator. Asier, PulsePol turned out to be a real beast of a topic! The insights you found are really neat, while working with ever-more spins was a fun challenge that continues to keep me busy. You write far better code than the rest of us put together, so thanks for the beautiful simulations.

Hans Bartling, we've overlapped for a long while now. It's been great to share an office; thanks for all the discussions of spin pairs, unexpected coherence times, or any sport that happens to be ongoing. I hope that the p****s survive until we're both long gone! **Sjoerd Loenen**, your drive to understand detail is astounding. The help in finishing M2 was much appreciated. It was pretty exciting to come back from a Christmas holiday to find that you and Maarten had started taking actual useful data. Thanks for the fun times too, especially the Belgian beer night in that Delft student house!

Guido van der Stolpe and **Damian Kwiatkowski**, it's been great to see your progress over the last year. The ENES measurements are beautiful, and I'm excited to see what will follow. Thank you both for your positivity and enthusiasm! **Nicolas Demetriou**, we haven't worked much together, but I'm excited to see the next steps with networks. Good luck! **Benjamin Pingault**, **Aletta Meinsma**, **Alex Breitweiser**, **Floris van der Gronden**, and **Nico Zutt**, thanks for all you contributed in the time you spent with us in Tim's group.

There are many members of Ronald's group that I haven't directly worked with, but that made a big contribution to my time here. **Max Ruf**, we will finish our PhDs just a couple of weeks apart. Teaching the RP together was a lot of fun, though perhaps not for all the students: you are an excellent plagiarism detector! I deeply admire the way you managed the cavity project. Thanks for the times at conferences (*"I don't like champagne, but let's get another one!"*), at Casa Ruf-Milner, and that bar in Rotterdam. I hope all goes well for you and Siobhan with your next steps!

Matteo Pompili and **Sophie Hermans**, you will both also finish your PhDs before long. Thanks for involving me in the discussions about carbon control for the network setups. It was really great to see your perseverance pay off as the 3-node experiments came together. Thanks also for all the fun times together, and those two great diamond dinners, way back when Team Diamond could (almost) fit in one house! **Arian Stolk**,

sorry for poisoning you before ADE, though I think it's fair to say you got your revenge. The trip to Norway with Maarten is a special memory from my time here. Good luck making entanglement! **Matthew Weaver**, thanks for all the lunchtime chats, your hard work as a guide in Boston, and for our climbing sessions (alongside Simon). Good luck at QPhox! **Takashi Yamamoto**, setting up diamond growth in Delft is one of the coolest things I've witnessed here. I look forward to seeing your future creations.

Matteo Pasini and **Yanik Herrmann**, it's been great to see your progress building the SnV and Cav2 setups. Good luck with your respective journeys! **Hans Beukers** and **Marie-Christine Roehsner**, I'm glad you came back for your PhD and post-doc respectively. I am sure you will both do great things. **Nina Codreanu**, I love seeing the progress on diamond nanofabrication, and your enthusiasm for it (and everything else!). **Kian van der Enden**, you ooze chill! Good luck propelling the demonstrator project to new heights. **Thomas Middelburg**, thanks for all the hard work on the NV^0 project.

Julia Brevoord, **Valeria Cimini**, **Wouter Westerveld**, **Lorenzo de Santis**, **Anna Tchebotareva**, **Jesse Slim**, **Airat Galiullin**, **Romy van Es**, **Guus Evers**, **Chris van Egmond**, **Santi Sager la Ganga**, **Marianne Teng**, **Stein Faes**, **Laura dos Santos Martins**, **Annick Tepe**, **Kamiel Dankers**, **Lisa de Kluijver** and **Laurens Feije**: thank you all for making Team Diamond such a fun place to work!

There are also number of former diamonds who had a big impact on my time here. **Toeno van der Sar**, your PhD work underlies the principles of the ^{13}C DDrf gates. Thanks for those early discussions. It's great that you're back here in Delft leading your own team. **Norbert Kalb**, your knowledge of DD2 and diamond fab were both saving graces during my first months! **Julia Cramer**, your efforts in preparing M1 made working on that setup far too easy! **Peter Humphreys, Suzanne van Dam** and **Stefan Bogdanovic**, thanks for being so welcoming. **Hannes Bernien**, I'm excited to join the team!

Outside Team Diamond, I am grateful to many others for their contributions to this thesis. **David Elkouss, Sébastian de Bone**, and **Paul Möller**, it was a pleasure to work on the ^{13}C memory project together. Thanks for developing those great network simulations, and for all your insights into distributed quantum computing. **Norman Yao** and **Francisco Machado**, your insights into time crystals really sharpened my understanding.

To the management assistants of QuTech, particularly **Marja Plas** and **Chantal Smith**: thank you for saving me from all the paperwork, and for handling any request so efficiently. **Raymond Schouten** and **Raymond Vermeulen**, thanks for patiently explaining so much about electronics, and then just making some fancy component anyway! **Martin Eschen**, the temperature controller works beautifully, and our discovery of the power of bubble wrap is a fond memory. **Nora Fahrenfort** and **Henk Polinder**, thanks for the work towards making a truly stable magnetic field. Thanks also to **Remco Roeleveld, Jelle Haanstra, Mark Ammerlaan, Siebe Visser, Jason Mensigh, Olaf Benningshof** and **Nico Alberts** for the many hours saved by your help and advice. **Mariya Sholkina**, thanks for keeping the laser labs running safely and for all the coffee-table chats.

The efforts towards recreating SIL diamond fab were aided by many. First, thanks go to Max for his training. I think the fact that Simon, Sjoerd and Guido passed their wet-bench tests under my tutelage says more about your expertise than mine (to the 'dirty boys', I hope you remember to clean your beakers!). The guidance of Norbert, **Nick de Jong, Ruud Schmits, Hans van den Berg, Jasper Flipse** and **Paul Alkemade** was also

an immense help. A special thank-you goes to **Saurabh Karwal**, for saving my devices at critical moments! I am grateful to the staff at the Kavli Nanolab Delft, in particular **Eugene Straver, Pauline Stevic, Marc Zuiddam** and **Hozanna Miro**. **René Vollmer**, the new SILs look great! **Brecht Simon**, thanks for the much improved tri-acid process.

There are a number of others who made the QuTech environment so positive. **Anta Das**, it's good to know someone else is following the cricket! **Josh Slater**, it was fun having you across the corridor the last few months. **Greg Mazur**, thanks for warning me when you were going to ruin my data! **Jelmer Boter** and **Chien-An Wang**, it was a pleasure sharing F027 with you. **Andrea Cornea, Nima Kalhor, Gertjan Eenink, Luca Petit** and **Mohammad Mehmandoost**, the same goes for my early days in B106. Thanks to **Alberto Bordin, Bas Hensen, Christian Möhle, Clara Osorio, Filip Rozpedek, Guoji Zheng, Gustavo Castro do Amaral, Hanifa Tidjani, Hany Ali, Jaco Morits, Jake Davidson, James Kroll, Jorge Marques, Mohsen Falamarzi Askarani, Nir Alfasi, Nodar Samkharadze, Sara Marzban, Sjaak van Diepen, Stephan Philips, Thijs Stevenga, Tim Coopmans, Xiao Xue,** and **Yang Wang** for all the coffee-table and food-truck meetings!

Playing with Q2 was a great excuse to get out of the lab on a Wednesday evening. I fear our music video will live on for eternity. Thanks to **Floor van Riggelen, Will Lawrie, Anne-Marije Zwerver, Marina Quintero Pérez, Christian Dickel, Pablo Cova Fariña**, Joe, Leo, Ruud, Romy, Hans, Matteo Sr., Matteo Jr., Remco and Jelle for all the fun! Likewise, thanks to the mighty Kavli Warriors for letting me disgrace myself on the football pitch from time to time.

As I come to the end of my formal education, I am grateful to a number of former mentors, including **Ray Healy, David Smith**, and **Chris Clare** at DCGS, **Jonathan Coleman** and **Zahra Gholamvand** at TCD, **Ferruccio Renzoni** and **Luca Marmugi** at UCL, and **Vlatko Vedral** and **Tristan Farrow** at Oxford. **Roy Taylor** and the rest of the FOG group at Imperial: thanks for all that you taught me during my Master's project, and for always welcoming me back when I'm in London.

To all my friends and family, thanks for all the support and the fun on my return visits! I hope to see you all again soon. To my sisters and their partners, **Amelia** and **Jae**, and **Eliza** and **Sean**, thanks for putting up with me for all these years! To my parents-in-law, **Helen** and **Andrew**, thank you for your kindness and love. I hope that we can meet again before long. **Mum** and **Dad**, it's been hard being barely able to see you over the last two years. Thank you for supporting everything I choose to do, and for all your love along the way.

Effy, thank you for your unwavering love, for keeping me sane over these four years, and for all our adventures. I look forward to the next one in Chicago, together with our grumpy cat, **Freja**.

Conor Bradley
Delft, August 2021

LIST OF PUBLICATIONS

9. *Fault-tolerant operation of a logical qubit in a diamond quantum processor.*
M. H. Abobeih, Y. Wang, J. Randall, S. J. H. Loenen, **C. E. Bradley**, M. Markham, D. J. Twitchen, B. M. Terhal & T. H. Taminiau,
arXiv:2108.01646.

8. *Robust quantum-network memory based on spin qubits in isotopically engineered diamond.*
C. E. Bradley, S. W. de Bone, P. F. W. Möller, S. Baier, M. J. Degen, S. J. H. Loenen, H. P. Bartling, M. Markham, D. J. Twitchen, R. Hanson, D. Elkouss & T. H. Taminiau,
In preparation (Ch. 4 of this thesis).

7. *Observation of a many-body-localized discrete time crystal with a programmable spin-based quantum simulator.*
J. Randall*, **C. E. Bradley***, F. V. van der Gronden, A. Galicia, M. H. Abobeih, M. Markham, D. J. Twitchen, F. Machado, N. Y. Yao & T. H. Taminiau,
arXiv:2107.00736.

6. *Coherence and entanglement of inherently long-lived spin pairs in diamond.*
H. P. Bartling, M. H. Abobeih, B. Pingault, M. J. Degen, S. J. H. Loenen, **C. E. Bradley**, J. Randall, M. Markham, D. J. Twitchen & T. H. Taminiau,
arXiv:2103.07961.

5. *Entanglement of dark electron-nuclear spin defects in diamond.*
M. J. Degen*, S. J. H. Loenen*, H. P. Bartling, **C. E. Bradley**, A. L. Meinsma, M. Markham, D. J. Twitchen, & T. H. Taminiau,
Nat. Commun. **12**, 3470 (2021)

4. *Orbital and spin dynamics of single neutrally-charged nitrogen-vacancy centers in diamond.*
S. Baier*, **C. E. Bradley***, T. Middelburg, V. V. Dobrovitski, T. H. Taminiau & R. Hanson,
Phys. Rev. Lett. **125**, 193601 (2020).

3. *Atomic-scale imaging of a 27-nuclear-spin cluster using a quantum sensor.*
M. H. Abobeih, J. Randall, **C. E. Bradley**, H. P. Bartling, M. A. Bakker, M. J. Degen, M. Markham, D. J. Twitchen & T. H. Taminiau,
Nature **576**, 411 (2019).

2. *A ten-qubit solid-state spin register with quantum memory up to one minute.*
C. E. Bradley*, J. Randall*, M. H. Abobeih, R. C. Berrevoets, M. J. Degen, M. A. Bakker, M. Markham, D. J. Twitchen & T. H. Taminiau,
Phys. Rev. X **9**, 031045 (2019).

1. *Comparison of liquid exfoliated transition metal dichalcogenides reveals $MoSe_2$ to be the most effective hydrogen evolution catalyst.*
Z. Gholamvand, D. McAteer, C. Backes, N. McEvoy, A. Harvey, N. C. Berner, D. Hanlon, **C. Bradley**, I. Godwin, A. Rovetta, M. E. G. Lyons, G. S. Duesberg & J. N. Coleman,
Nanoscale **8**, 5737-5749 (2016).

* Equally contributing authors

Conor Eliot Bradley

February 2nd, 1995
Sheffield
United Kingdom

2007 - 2013	**Secondary school**
	Dr. Challoner's Grammar School, Amersham, UK
2013 - 2017	**MSci in Physics** (First class honours)
	Imperial College London, UK
	Thesis: *"An all-fibre integrated Yb-doped 'Figure-of-eight' laser"*
	Supervisor: Prof. J. Roy Taylor FRS
Summer 2014	Research Student, Coleman Group, Trinity College Dublin, Ireland
Summer 2015	Research Student, Renzoni Group, University College London, UK
Summer 2016	Research Student, Vedral Group, University of Oxford, UK
2017 - 2021	**PhD in Physics**
	Delft University of Technology, The Netherlands
	Thesis: *"Order from disorder: Control of multi-qubit spin registers in diamond"*
	Group: Taminiau Lab, QuTech and Kavli Institute of Nanoscience
	Promotor: Prof. dr. ir. Ronald Hanson
	Co-promotor: Dr. ir. Tim H. Taminiau